Unveiling the Structure of Active Galactic Nuclei with Hard X-ray Spectroscopy

Thesis by
Mislav Baloković

In Partial Fulfillment of the Requirements for the
degree of
Doctor of Philosophy

CALIFORNIA INSTITUTE OF TECHNOLOGY
Pasadena, California

2017
Defended May 25, 2017

Mislav Baloković
ORCID: 0000-0003-0476-6647

ACKNOWLEDGEMENTS

Many good people helped me on my way to this point in life. First and foremost, my loving family, Snježana, Darije, Jakov and Luka Baloković, and my amazing wife, Antonija Oklopčić. I am in great debt of gratitude to my parents for their unconditional support stretching over (more than!) 30 years and across more than one continent. They taught me to be inquisitive, open-minded, persistent, and hard-working in my pursuit of knowledge. I will always be grateful for their encouragement and their unwavering belief in me.

I owe so much of my success and happiness to Antonija that I cannot mention her in just a single paragraph. Words cannot fairly express how grateful I am that our lives are intertwined in their every aspect. I am truly thankful her continued love, support, encouragement, and understanding since before we even considered going to graduate school. She made the last 6 years in Pasadena, our home away from home, the most wonderful in my life.

I would not have made it all the way to Pasadena without my many friends, teachers and mentors. Special thanks go to Mario Pallua, my best-est man, for introducing me to the wonders of the night sky and amateur astronomy, in addition to the music and the resulting life-long friendships. Our shared enthusiasm fueled our many nights under the open sky with a telescope, our small astronomy projects, and our early efforts to share the excitement of astronomy with everyone around us.

Ana Bedalov, Dejan Vinković, Mario Jurić, Željko Ivezić, and others have helped me more than they know in defining my path toward a career in astronomy. Their encouragement and support led me to spend my undergraduate summers at top-class astronomy institutions around the world, which I enjoyed immensely. I am indebted to Martin Kürster, Anton Koekemoer, and Dominik Riechers, for investing their time to show me what it means to be a professional astronomer. Along the way I met Vernesa Smolčić, to whom I owe many thanks for being my undergraduate thesis advisor, and for providing valuable support in preparing both Antonija and me for graduate school abroad.

I am sincerely grateful to my thesis advisor, Fiona Harrison, for her sustained support, and the freedom I was given to explore scientific questions outside of my thesis topic. I consider myself fortunate to have had an advisor who provided help and guidance whenever it was needed despite her countless other responsibilities,

while letting me develop my own research plan and set my own pace. I appreciate learning from her about the importance of being concise and clear, both in expressing scientific ideas, as well as in being an efficient leader.

Thanks to Fiona and *NuSTAR* I had the privilege to work with some of the greatest experts in my field, Andrea Comastri, Greg Madejski, Dave Alexander, Giorgio Matt, and Mike Koss, among others. It continues to be a pleasure to share research ideas with such excellent scientists. Much of my work would not have been possible without the dedication and hard work of many people in the *NuSTAR* collaboration, at Caltech and around the world. I appreciate the help, patience, and kindness from all who have been a part of Fiona's research group over the past 6 years, especially Dan Stern, Brian Grefenstette, Kristin Madsen, Dom Walton, Felix Fürst, Murray Brightman, Karl Forster, Liz Rivers, and Marianne Heida. I learned so much about so many different things from them.

My time in graduate school would have been much less fun without the good friends I found there. I really appreciate the many times spent with Ben Montet, Allison Strom, Trevor David, Yi Cao, Abhilash Mishra, and Antonija, be it at work (working or not) or far from campus, discussing greatest scientific achievements or airline miles, studying or partying, celebrating or commiserating... I am also grateful for company, advice, and shared experiences with many other Caltech students; in particular, older colleagues like Gwen Rudie and Drew Newman, who helped me a lot in navigating the graduate school life and the postdoc job market.

I would also like to thank the rest of my thesis committee: Phil Hopkins, the committee chair, Lynne Hillenbrand, Tony Readhead, and Nick Scoville. I admire their foresight in giving me good advice on my thesis plan at my candidacy exam 3 years prior, which came to be crucial in the end although to me it did not appear so at the time. More generally, along with other faculty, staff, and administrators, I thank them for keeping the life in the Astronomy Department so supportive and enjoyable.

Finally, I gratefully acknowledge the Fulbright International Science and Technology Fellowship, which generously supported my first three years in graduate school, and led to many good times spent getting to know Fulbright fellows from all corners of the world. I also acknowledge the NASA Earth and Space Science Fellowship for the support of the latter three years in graduate school. At the very end, I would like to thank Caltech as a whole, and the many people who make it such a magnificent place to do science!

ABSTRACT

Despite the long history of studies of active galactic nuclei (AGN), details of the structure of the accretion flow onto supermassive black holes are far from clear. Work presented in this thesis is directed at unveiling properties of AGN structure through broadband X-ray spectroscopy, with particular emphasis on the hard X-ray band (photon energies $> 10\,\mathrm{keV}$). With its unprecedented sensitivity in this energy band, the *NuSTAR* telescope provides the key observational diagnostics of the properties of the AGN X-ray source, the corona, and the surrounding gas in the accretion disk, the broad-line region, and the torus.

The first study presented in this thesis focuses on measurements of the optical depth and the temperature of the plasma in the corona of an obscured AGN. Fitting theoretical spectral models for coronal emission to the *NuSTAR* data constrained these two basic physical parameters under the assumption of either spherical or disk-like geometry for the corona.

The remainder of the thesis is dedicated to studies of the anisotropic obscuring structure broadly referred to as the *torus*. One of them is a case study of three heavily obscured AGN with spectra dominated by the X-ray light scattered and reprocessed in the torus, where it is possible to constrain one of the basic torus properties – its globally averaged column density. The following study presents the calculation of a new spectral model for reprocessing of the intrinsic X-ray continuum within the torus. Its added flexibility compared to previously available models allows for both the average column density of the torus and its covering factor to be constrained from broadband X-ray spectra of a wide variety of AGN.

The final part of the thesis in based on a large survey of the local obscured AGN population performed with *NuSTAR*. Spectral modeling of more than a hundred individual AGN, including both old and new spectral models, is presented. From analyses of the X-ray data for a large and representative AGN sample, for the first time, it is found that their tori preferentially have high covering factors and average column densities close to unity optical depth for Compton scattering.

PUBLISHED CONTENT AND CONTRIBUTIONS

Baloković, M., Brightman, M., Harrison, F. A., et al., 2017,
New Spectral Model for Measuring Torus Covering Factors from Broadband X-ray Spectra of Active Galactic Nuclei,
submitted to The Astrophysical Journal (in peer review as of May 25, 2017)
Contributions: I formulated the idea for this project, wrote the computer code for calculation of the new model, selected the data to demonstrate the application of the model, performed spectral analyses, and wrote the paper. The second author contributed to computation of the new model, while the third author helped with writing the paper. All authors were involved in discussions, and provided advice on various aspects of model building and application of the model to real data.

Baloković, M., Matt, G., Harrison, F. A., et al., 2015,
Coronal Properties of the Seyfert 1.9 Galaxy MCG-05-23-016 Determined from Hard X-Ray Spectroscopy with NuSTAR,
The Astrophysical Journal, 800, 62, DOI: 10.1088/0004-637X/800/1/62
Contributions: The project was conceived by the second and the third author. I performed the majority of the data processing and analysis with input from these two authors. I wrote the paper reporting the observational results and their interpretation. The rest of the authors contributed to discussion of the results, and/or to the *NuSTAR* mission in general.

Baloković, M., Comastri, A., Harrison, F. A., et al., 2014,
The NuSTAR View of Nearby Compton-thick Active Galactic Nuclei: The Cases of NGC 424, NGC 1320, and IC 2560,
The Astrophysical Journal, 798, 111, DOI: 10.1088/0004-637X/794/2/111
Contributions: The first three authors collaborated on the selection of the *NuSTAR* data for this publication. I performed all data processing and spectral analyses, and I wrote the paper with help from the second and third authors. The rest of the authors contributed to discussion of the results and their implications, and/or to the *NuSTAR* mission in general.

TABLE OF CONTENTS

LIST OF ILLUSTRATIONS

LIST OF TABLES

Chapter 1

INTRODUCTION

1.1 Unified Model of Active Galactic Nuclei (AGN)

1.1.1 From the Discovery of Quasars to the Basic Unified Model

During my graduate program at Caltech, we celebrated the 50-year anniversary of Maarten Schmidt's realization (Schmidt, 1963) that the radio source 3C 273 was associated with a star-like source with the *enormous* redshift of 16 %.[1] Although radio sources had been found to be associated with distant galaxies before (e.g., Baade & Minkowski 1954), the origin of the large-scale radio emission, which had no obvious connection to the galaxy nucleus, was unclear at the time. Identification of a population of quasi-stellar radio sources (quasars) was soon followed by the discovery of a more numerous population of radio-quiet quasi-stellar galaxies (Sandage, 1965). Qualitatively similar objects had been found much earlier in the nuclei of some relatively nearby galaxies by Seyfert (1943), but the first investigation into the nature of Seyfert galaxies came long after their initial discovery (Burbidge et al., 1959).

The idea that vigorous accretion onto a supermassive black hole (SMBH) is the central engine powering quasars was proposed soon after their discovery. Given their large distances, the enormous luminosity of quasars had to be due to physical processes significantly more efficient than those powering stars (Hoyle & Fowler, 1963). With is mass-to-energy conversion efficiency of $\sim 10\,\%$, accretion onto SMBHs offered a viable option (Salpeter, 1964). Interestingly, while there is abundant indirect evidence for the existence of black holes (e.g., Eckart et al. 2017), the first direct confirmation of their existence was provided by the detection of gravitational waves from a black hole merger only last year (Abbott et al., 2016). Furthermore, the first direct image of a SMBH event horizon may be expected within a year from now from the Event Horizon Telescope (Doeleman et al., 2008).

Theory of the thin accretion disk (Shakura & Sunyaev, 1973) provided the basic working model for the structure of the inward accretion flow around the SMBH

[1] I shall always remember with fondness that, in the lecture Prof. Schmidt gave to my class on the history related to his discovery of quasars, he quantified redshifts in *percentages*.

in a typical active galactic nucleus (AGN), which we still use today. However, AGN phenomenology is very rich, challenging the early idea that AGN are a single population. Early AGN studies focused on trying to understand the nature of differences in their radio-band morphology (Fanaroff & Riley, 1974). Diversity was also noticed in optical spectra of AGN, resulting in the broad- and narrow-line taxonomy that we still use today (Osterbrock, 1978). Insight from optical spectropolarimetric observations (e.g., Antonucci & Miller 1985, Tran et al. 1992), was instrumental for the development of the idea in that different types of AGN could be unified into a single multi-component system viewed from different angles, which resulted in the formulation of the basic unified model of AGN (Antonucci, 1993; Urry & Padovani, 1995).

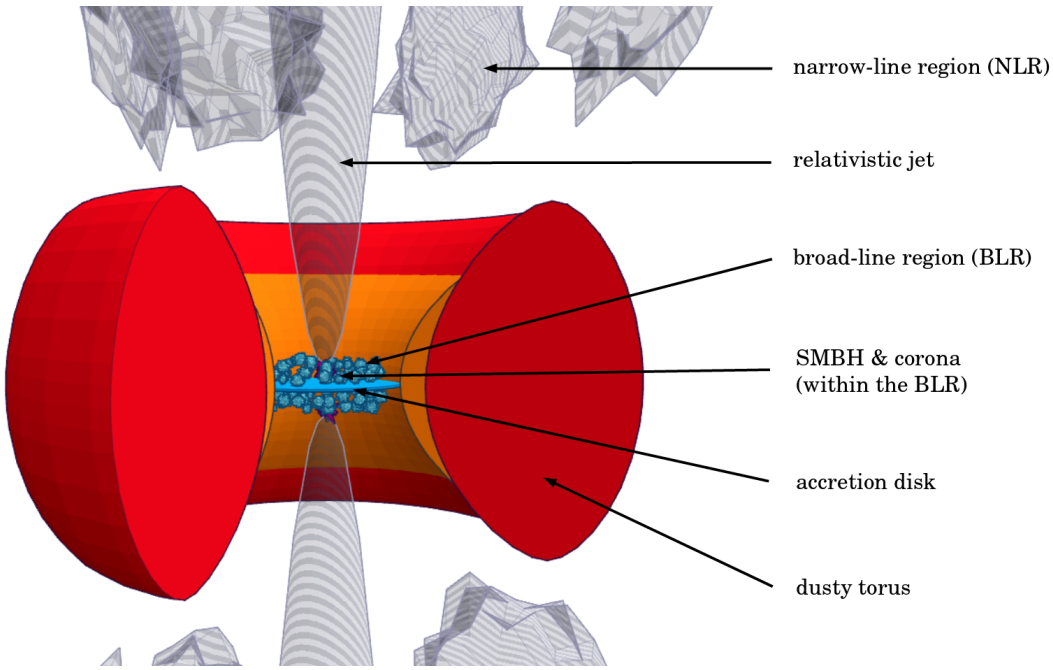

Figure 1.1: Illustration of the main components of the basic unified model of AGN. Based on the sketch I made for Farrah et al. (2016).

1.1.2 The Basic Unified Model of AGN

The idea behind the basic unified model of AGN is that phenomenological differences can (largely) be accounted for by changing only the orientation of the observer with respect to a multi-component system surrounding essentially every SMBH. Granted, at the time of the formulation of the basic unified model (Antonucci, 1993; Urry & Padovani, 1995), it was already known that some phenomenological classes do not fit the same picture. The model was an attempt to coherently organize most of

the observed AGN classes, and it was supposed to be applicable to the bulk of active SMBH systems. A sketch of the basic unified model, with its main components highlighted, is shown in Figure 1.1.

The main components of a typical AGN in the framework of the basic unified model, from the smallest scales outward, are:

- Supermassive black hole (SMBH): the source of gravity powering the nuclear activity. Mass range is generally accepted to be between 10^5 and 10^{10} $M_\odot$. Linear size of the event horizon is directly proportional to the SMBH mass and roughly ranges between 10^{10} and 10^{15} cm (between a few light-seconds and a few light-days).

- Accretion disk: optically thick and geometrically thin rotating disk formed from in-falling material which looses its angular momentum through friction within the disk. It radiates thermally (with the innermost regions being hottest) and is the primary source of electromagnetic radiation due to accretion.

- Corona: low-density, high-temperature plasma present around the SMBH and the accretion disk, containing high-velocity electrons which up-scatter ultraviolet photons from the accretion disk to high energies, primarily to the X-ray band. Its linear size is commensurable with that of the event horizon.

- Broad-line region (BLR): a sphere-like or disk-like arrangement of partially ionized high-density clouds of dust-free gas surrounding the SMBH, emitting broad emission lines (FWHM $> 1000\,\mathrm{km\,s^{-1}}$) of permitted atomic transitions. The bulk of these clouds is located light-days to light-months from the SMBH.

- Obscuring torus: geometrically thick structure, inflated in the direction perpendicular to the accretion disk, that provides covering of a significant fraction of the sky as seen from the SMBH. Its radial extent ranges roughly from the dust sublimation radius (which scales with AGN luminosity; roughly 0.1 pc, or just under a light-year) out to $\gtrsim 10$ pc (tens to hundreds of light-years).

- Narrow-line region (NLR): a bi-conical structure of low-density ionized clouds emitting narrow permitted and forbidden emission lines (FWHM $< 1000\,\mathrm{km\,s^{-1}}$). They reside at ~kpc distances, and have a direct line of sight to the innermost parts of the system, which provides the high ionization potential.

- Relativistic jet: a high-velocity stream of particles launched in opposite directions perpendicularly to the accretion disk and radiating non-thermally via synchrotron and inverse-Compton processes. In about 10 % of AGN, the relativistic jet is so strong and so well collimated that it propagates out to distances of ∼100 kpc. Majority of AGN either exhibit a much weaker and shorter jet, or have no detectable jet emission.

This basic model provides an explanation for why narrow (permitted and forbidden) lines are observed in nearly all AGN, while broad lines are not: the former are emitted from larger spatial scales and are therefore observable from any orientation, while the latter originate from small scales and can therefore be hidden by the obscuring torus, depending on the observers' orientation with respect to the AGN. When the viewing angle is such that the innermost regions are seen directly, the observer sees a broad-line (type I) spectrum. If the same system is observed closer to edge-on orientation, where the obscuring torus hides emission from the accretion disk and the BLR, only a narrow-line (type II) spectrum will be observed. However, broad lines are, at least in principle, still observable in polarized light due to scattering on free electrons associated with the ionized NLR bi-cone.

Numerous observational results were folded into the unified model picture. Orientation of radio jets, the ionized bi-cones, and the polarization position angle, provided evidence for co-alignment of the main structures that comprise the model outlined here (e.g., Pogge 1988, Evans et al. 1991, Storchi-Bergmann et al. 1992a). Furthermore, direct observations of the obscuring torus in a small number of nearby galaxies (e.g., Jaffe et al. 1993) had shown that it extends in the direction perpendicular to the jet and to the direction in which the NLR opens. Kinney et al. (1991) argued that the NLR emission has to be powered by a source of ultraviolet photons that is not observed directly due to very high extinction in the obscuring torus. Around the same time, the first focusing X-ray telescopes yielded measurements of obscuration columns in sizeable samples of bright AGN, providing evidence for higher obscuration in type II compared to type I AGN (e.g., Awaki et al. 1991, Mulchaey et al. 1992). Early infrared observations successfully detected thermal emission from the warm dust in the obscuring torus (e.g., Storchi-Bergmann et al. 1992b).

Many studies to this day interpret their data in the sense of being either consistent or inconsistent with the unified model. While in some cases this may indeed refer to the basic unified model described above, it mostly refers to the broader family of "weaker" unification models. These models recognize at least several classes that

differ in their physical properties (and may change in time), and they unify only some of the diverse AGN phenomenology into orientation-based effects.

1.1.3 Contemporary View of AGN Unification

The idea of accretion onto SMBHs is central to all AGN. However, both theory and observations indicate that the structure of the accretion flow changes with luminosity and the Eddington ratio[2] ($\lambda_{\rm Edd}$). When the accretion rate falls below a critical level, the standard accretion disk (Shakura & Sunyaev, 1973) is predicted to be replaced with an optically-thin radiatively inefficient accretion flow (e.g., Narayan & Yi 1994, Blandford & Begelman 1999). In Seyferts and quasars, at high $\lambda_{\rm Edd}$, the accretion disk extends down to the innermost stable circular orbit (ISCO) at a few gravitational radii[3] (R_G). In AGN with low $\lambda_{\rm Edd}$, studies of spectral energy distributions (SEDs) from the radio to X-ray bands show that the standard accretion disk may be truncated at $\sim 100\,R_G$ (e.g., Ho 2008, Mason et al. 2012, Nemmen et al. 2014).

Different $\lambda_{\rm Edd}$, which represent different accretion rates for SMBHs of similar mass, have also been associated with the excitation mode dichotomy in the NLR emission of radio-loud AGN (e.g., Chiaberge et al. 1999, Smolčić 2009, Best & Heckman 2012). High-excitation AGN are thought to be radiatively efficient and dominated by energy output from the accretion disk, while low-excitation AGN are radiatively inefficient and dissipate most of their energy kinetically, through relativistic jets. The latter is more conducive to formation of powerful large-scale radio jets, while in the former category approximately 10 % of the population shows strong radio emission from a relativistic jet (e.g., Jiang et al. 2007, Baloković et al. 2012, Padovani 2016).

The focus of this thesis is on the active nuclei of Seyfert galaxies (Seyferts hereafter), which represent the bulk of radiative-mode AGN both in the local universe and at high redshift (e.g., Ueda et al. 2014, Aird et al. 2015). They typically have SMBH masses in the $10^7 - 10^8\,M_\odot$ range, Eddington ratios between 1 % and 10 %, and bolometric luminosity $10^{42} - 10^{45}\,{\rm erg\,s^{-1}}$. The structure of their accretion flow is thought to be most similar to the basic unified model described in § 1.1.2. The primary source of radiation in these AGN is the thermally radiating accretion disk, heated though viscous forces as matter spirals inward toward the SMBH. X-ray emission is thought to be produced via inverse Compton scattering of the ultraviolet

[2]Defined as $\lambda_{\rm Edd} = L_{\rm bol}/L_{\rm Edd}$, where $L_{\rm bol}$ is the bolometric luminosity of the AGN and $L_{\rm Edd}$ is the maximum luminosity attainable through spherical accretion of dust-free gas, $L_{\rm Edd} = 1.26 \times 10^{38}\,(M_{\rm SMBH}/M_\odot)\,{\rm erg\,s^{-1}}$.

[3]Gravitational radius is defined as $R_G = GM/c^2 = 1.48 \times 10^{21}\,(M_{\rm SMBH}/M_\odot)\,{\rm cm}$. ISCO radius depends on the spin of the SMBH, but is always or the order of unity in units of R_G.

and optical photons from the accretion disk in the hot coronal plasma (e.g., Haardt & Maraschi 1991, Haardt et al. 1994, Titarchuk 1994).

Emission from the disk and the corona is partially absorbed and reprocessed by larger-scale structures – in particular, the torus. The modern view of the torus has moved beyond the simple donut-like structure depicted in Figure 1.1: it is more likely to be an anisotropic, clumpy, dynamical structure of gas and dust extending roughly from sub-pc to 10-pc scales, and emitting primarily through relatively cold dust (e.g., Nenkova et al. 2008a, Schartmann et al. 2008). For extreme Seyferts, and non-Seyfert AGN, the torus may either disappear due to the lack of radiative support at low luminosity (e.g., Elitzur & Shlosman 2006, Hönig & Beckert 2007), or be dispersed on a short timescale and related to transient outflows in the chaotic environment of a high-redshift high-luminosity quasar, likely hosted in a galaxy merger (e.g., Di Matteo et al. 2005, Hopkins et al. 2006).

Over the last decade, the notion of the coevolution of galaxies and AGN has become inextricably ingrained in our view of both galaxy evolution and the nature of the AGN phenomenon (e.g., Fabian 2012, Heckman & Best 2014, Brandt & Alexander 2015). Evidence for past interaction between SMBHs and their host galaxies has been found in the form of scaling relations between the SMBH mass and the mass of the spheroidal component of galaxies in the local universe, suggesting a common evolution (Ferrarese & Merritt, 2000; Gebhardt et al., 2000; McConnell & Ma, 2013).

Many studies have shown that nuclear obscuration is less common among luminous AGN (e.g., Tozzi et al. 2006, Ebrero et al. 2009, Buchner et al. 2015), suggesting that AGN-driven outflows may efficiently sweep gas and dust away from its surroundings, possibly affecting star formation in their hosts (e.g., Silk & Rees 1998, King 2003, Hopkins & Elvis 2010). Recent theoretical work supports the idea that these outflows are driven by fast accretion-disk winds, although it is still unclear how they couple to the larger-scale galactic environment (e.g., Faucher-Giguère & Quataert 2012, Wagner et al. 2013, Zubovas & Nayakshin 2014). Outflows at a range of distances from the SMBH have been observed in many AGN (e.g., Sturm et al. 2011, Tombesi et al. 2012, Cicone et al. 2014); however, the connection across the vastly different spatial scales is difficult to establish (Tombesi et al., 2015). While it is becoming clear that winds and outflows are integral parts of the accretion flow and the modern AGN paradigm, our knowledge of their properties, structure, and key physical mechanisms is currently limited.

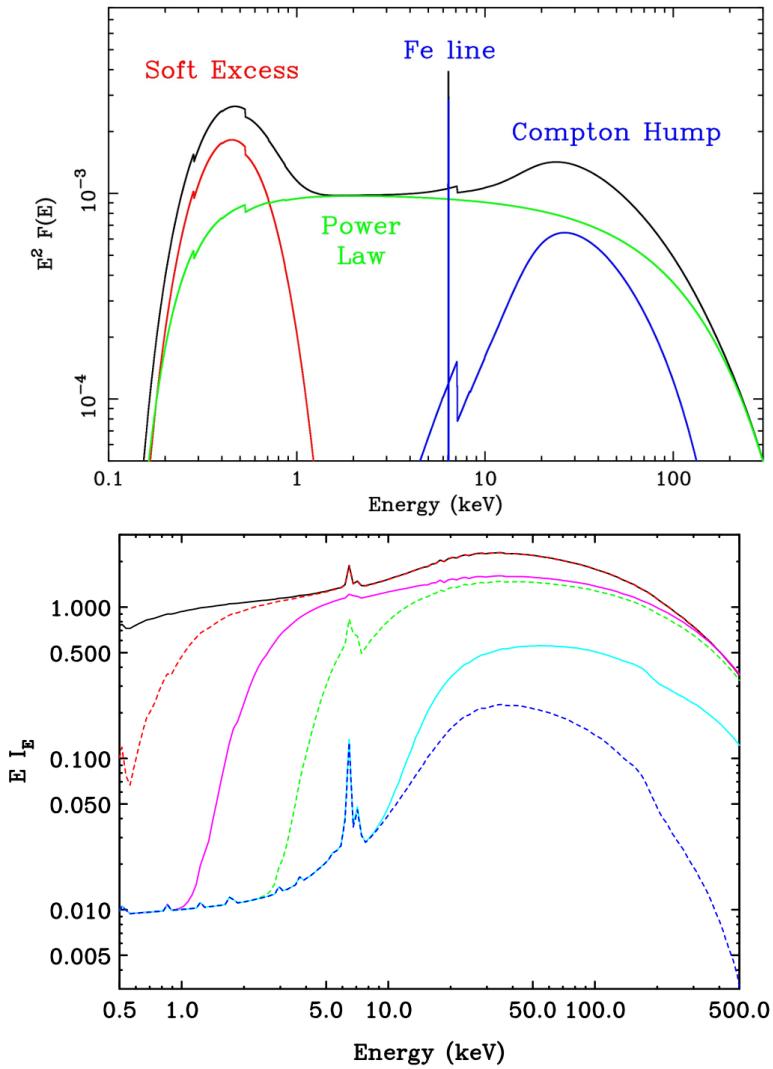

Figure 1.2: Example X-ray spectra of AGN. *Upper panel:* Typical components in the X-ray spectrum of an unobscured AGN are labeled: the coronal continuum shown as a power law with a high-energy exponential cutoff (green), an black-body component representing the soft excess (red), and main features due to reprocessing, the Fe Kα line and the Compton hump (blue). Note that in the case of reprocessing in a rapidly rotating accretion disk, the blue components would be smeared out, unlike in the case of reprocessing in larger-scale structures such as the torus. *Lower panel:* The effect of line-of-sight absorption assuming a range of column densities, log $N_{\rm H}/{\rm cm}^{-2} =$ 20.5, 21.5, 22.5, 23.5, 24.5, 25.5 shown in black, red, magenta, green, cyan, and blue, respectively. Note that with increasing $N_{\rm H}$, the features due to reprocessing become more prominent, and dominate at the high-$N_{\rm H}$ end.

1.2 Studies of AGN in the X-ray Band

1.2.1 Main Components of an AGN X-ray Spectrum

Emission of the non-thermal X-ray continuum in typical Seyferts is ascribed to tenuous plasma in the innermost region of the accretion flow, which up-scatters ultraviolet photons from the accretion disk into the X-ray band. By analogy with the outermost part of the atmosphere of the Sun, this component is called the corona. The main physical mechanism that shapes the coronal X-ray spectrum is comptonization: inverse Compton scattering of optical and ultraviolet accretion-disk photons on fast electrons. The geometry of the corona is not well constrained: it could be a thin outermost layer of the accretion disk (Haardt & Maraschi, 1991), the ionized inner edge of the accretion disk (Gardner & Done, 2014), or a compact source extending perpendicularly above the disk, like the base of a jet (e.g., Matt et al. 1991, Dauser et al. 2013).

The details of the coronal spectrum depend on physical conditions in the plasma, its geometry, and the seed photon spectrum (e.g., Haardt & Maraschi 1993, Titarchuk 1994, Poutanen & Svensson 1996). For a broad range of conditions it can be approximated well with a power-law continuum with a high-energy exponential cutoff: $n(E) = dN/dE \propto E^{-\Gamma} \times \exp(E/E_{\rm cut})$, where $n(E)$ is the number of photons per unit energy, E is photon energy, Γ is the photon index and $E_{\rm cut}$ is the e-folding energy scale. X-ray emission can also be produced by the larger-scale relativistic jet; in non-blazar[4] AGN with strong and favorably oriented jets, both the coronal and the jet continuum can contribute in the X-ray band (e.g., Madsen et al. 2015a).

Some typical AGN X-ray spectra are shown in Figure 1.2. The upper panel shows the main features of an unobscured AGN spectrum, while the lower one shows the effect of increasing line-of-sight obscuration. Obscured AGN are the focus of this thesis; however, unobscured AGN have been studied in significantly more detail (thanks to a slew of highly sensitive soft X-ray instruments) as they allow us to directly probe the innermost regions around SMBHs with spectroscopic and variability studies. The lack of absorption makes it possible to observe detailed spectral signatures of the accretion disk imprinted onto the featureless coronal continuum.

As a result of Compton scattering, absorption, and fluorescence in the optically thick disk, the observed spectrum exhibits a series of emission lines in the soft

[4] In blazars, the X-ray band is typically dominated by relativistic beaming effects due to the small viewing angle with respect to the jet (e.g., Urry & Padovani 1995, Fossati et al. 1998, Ghisellini 2016).

X-ray band (< 10 keV), and a broad Compton hump peaking in the hard X-ray part of the spectrum (∼30 keV). The strongest emission lines are those of Fe, due to a combination of its high relative abundance and high fluorescent yield. Being dominant, the Fe Kα line (a blend of several lines corresponding to transitions of electrons to the innermost shell of Fe) is typically the only line considered relevant in modeling AGN spectra. Because of the high circular velocities in the innermost part of the accretion disk, and the effects of strong gravity in the immediate vicinity of the SMBH, the fluorescent lines, as well as the Compton hump, typically get smeared out by the Doppler shift and the gravitational redshift into the typical spectral signature of the so-called relativistic reflection[5] (e.g., Fabian et al. 1989, Reynolds & Nowak 2003, Garcia et al. 2014).

Physical conditions within the accretion disk, where the bulk of the X-ray reprocessing takes place, are such that matter can mostly be considered neutral. However, its outermost layer or its edge toward the SMBH, possibly due to direct interaction with the coronal plasma, can be ionized. This alters absorption and scattering cross-sections and adds features due to fluorescence as well as recombination of ionized species, modifying the reprocessed spectrum (e.g., Ross & Fabian 2005, García et al. 2013). The forest of blended soft X-ray lines due to ionized line emission has been suggested as the physical origin of the commonly observed spectral feature in unobscured AGN, phenomenologically named the "soft excess". The nature of this spectral component is currently not well understood: instead of relativistically blurred lines, it has also been proposed to be due to comptonization of accretion disk photons by a particular population of hot electrons (e.g., Gardner & Done 2014, Matt et al. 2014), or due to ionized absorption with respect to a continuum that is not observed directly (e.g., Middleton et al. 2007, Vasudevan et al. 2014).

Line emission from regions photoionized by the AGN continuum and absorption due to ionized gas in the line of sight to the X-ray source (often called "warm absorption" in the literature) is commonly observed in soft X-ray spectra of AGN (e.g., Turner & Miller 2009, Detmers et al. 2011, Longinotti et al. 2013). The latter includes broad absorption troughs interpreted as signatures of "ultra-fast outflows" due to highly ionized clouds traveling along our line of sight at velocities exceeding 10 % of the speed of light (Tombesi et al., 2012).

The main difference between the model spectra shown in the upper and lower panels

[5]The popular term "reflection" is a misnomer: the reprocessed spectrum has a completely different shape then the input spectrum. In this thesis, an effort was made to refer to this physical process as "reprocessing" rather than "reflection".

of Figure 1.2 is the low-energy exponential cutoff due to photoelectric absorption in the intervening material that obscures the innermost part of the AGN and dominates over the spectral signatures produced there. The obscuration, predominantly by neutral gas, can be due to a number of structures surrounding the inner $\sim$ 100 gravitational radii from the SMBH; within a modern unified scheme, this could be the BLR (Risaliti et al., 2005), the dusty torus (e.g., Markowitz et al. 2014, Marinucci et al. 2016), clumpy wind (Elitzur & Shlosman, 2006), or any interface between these components. Some part of the line-of-sight column density can be due to the host galaxy (e.g., Goulding et al. 2011, Buchner & Bauer 2017).

Reprocessing of the intrinsic X-ray continuum in these larger-scale structures is an important diagnostic of obscuration averaged over all lines of sight from the SMBH, as opposed to the single line of sight to the observer (e.g., Awaki et al. 1991, Krolik et al. 1994, Murphy & Yaqoob 2009). The physical processes are identical to those forming the fluorescent lines and the Compton hump in the reprocessed spectrum of the accretion disk. The distinguishing features are the fact that the reprocessed spectrum of the larger-scale obscurer is not relativistically broadened, that the spectral shape depends on geometry, and that the reprocessed spectrum cannot respond to changes in the intrinsic continuum on timescales shorter than a few light-crossing times[6] (e.g., Madejski et al. 2000, Yaqoob 2012). While disk reprocessing features are difficult to detect in obscured AGN, unobscured ones typically show a mix of both reprocessing signatures.

1.2.2 X-ray Spectroscopy of AGN in the Local Universe

Progress in X-ray astronomy has largely been driven by technological advances over the last several decades. Nearly 30 years ago, data from the *Ariel V* satellite showed that X-ray emission is a common property of AGN, and that the X-ray flux significantly varied down to timescales shorter than one day in some sources (e.g., Elvis et al. 1978, Marshall et al. 1981). The *Einstein* observatory, launched in 1978, provided focusing X-ray optics and high sensitivity, which increased the number of X-ray detections of AGN by an order of magnitude, and enabled sizable samples of nearby AGN to be studied in the X-ray band.

A series of instruments with increasing sensitivity followed, including *Ginga*, *ASCA*, *EXOSAT*, *ROSAT*, *RXTE*, *BeppoSAX*, *Suzaku*, and the currently active observatories, *XMM-Newton*, *Chandra*, *INTEGRAL*, *Swift*, *NuSTAR*, and *ASTROSAT*. Despite the

[6] In analogy with the relativistic inner-disk reflection, reprocessing on large spatial scale is often called "distant reflection" in the literature.

unfortunately short lifetime of the recently launched *Hitomi* observatory, excellent facilities are currently available in Earth orbit for studies of AGN in the X-ray band. Note should be taken of the fact that due to technical limitations, of all these X-ray observatories only *Chandra* has the capability to resolve the central regions of at most a few nearby AGN down to a spatial scale of $\simeq 20\,\mathrm{pc}$ (Marinucci et al., 2013; Bauer et al., 2015); all other AGN are unresolved, so the information on their structure and properties has to be extracted from their spectra and variability.

Using detailed spectroscopy and timing we have learned a tremendous amount about the innermost region surrounding SMBHs, yet many details are still unclear. Some open issues in X-ray spectroscopy of unobscured AGN include the unknown origin of the soft X-ray excess, and the unknown geometry and physical properties of the corona. While much of our knowledge relies on modeling of the spectral signatures briefly described in § 1.2.1, some results have received more independent confirmation than others over the years.

For example, the interpretation of the broad red wing of the Fe Kα line, first observed by Tanaka et al. (1995) and subsequently by many others, has been debated in the literature (e.g., Miller et al. 2008, Turner & Miller 2009, Miller & Turner 2013) until very recently. Measurements enabled by the high-sensitivity broadband observations with *XMM-Newton*, *Suzaku*, and *NuSTAR* (e.g., Risaliti et al. 2013, Zoghbi et al. 2017), as well as characterization of energy-dependent and frequency-dependent time lags due to reverberation (e.g., Zoghbi et al. 2014, Kara et al. 2015a), make it difficult to explain the observational data in terms of theories other than the relativistic broadening of the reprocessing features due to a rapidly rotating accretion disk. This lends credibility to many SMBH spin measurements based on broad Fe Kα modeling in more than a dozen nearby AGN (e.g., Brenneman & Reynolds 2006, Reynolds 2014).

As the soft X-ray spectrum of obscured AGN is dominated by absorption, these objects have been studied in less detail, despite being more numerous than unobscured AGN ($\simeq 60\,\%$; e.g., Risaliti et al. 1999, Panessa et al. 2006, Brightman & Nandra 2011a). Obscured AGN are usually defined with a cut in the line-of-sight column density (N_H) at $10^{22}\,\mathrm{cm}^{-2}$, with a special category being Compton-thick (CT) AGN, for which N_H exceeds unity optical depth for Compton scattering at roughly $10^{24}\,\mathrm{cm}^{-2}$. Out of three AGN in our immediate neighborhood (within 4 Mpc), NGC 4945 and NGC 1068 are CT AGN, and Cen A is heavily obscured (Matt et al., 1999). The difficulty in studying X-ray spectra of these objects is that most of their

soft X-ray flux is extinguished, which, first of all, makes it difficult to select large and complete samples, and also leaves only a limited amount of absorbed intrinsic X-ray continuum observable in the soft X-ray band.

A new window for studies of obscured AGN opened up with the large-area surveys with IBIS/ISGRI on board *INTEGRAL* (Winkler et al., 2003), and BAT on board *Swift* (Barthelmy et al., 2005), both operating in the hard X-ray band (approximately 15–200 keV). While their instantaneous sensitivity is low, their very wide fields of view and sky-scanning operation mode result in detections of large samples of AGN less biased against heavily obscured AGN than any soft X-ray survey. These surveys enabled selection of the brightest hard X-ray AGN to follow up with *Suzaku* and its pointed hard X-ray detector (PIN). Used in parallel to the soft X-ray instrument on board *Suzaku* (XIS), it provided an additional 15–55 keV constraints on spectra of several dozen obscured AGN (e.g., Eguchi et al. 2009, Tazaki et al. 2011, Comastri et al. 2010; see Figure 1.3), despite its low sensitivity and narrow bandpass compared to *NuSTAR*.

Theoretical models for interpretation of X-ray spectra of obscured AGN were initially motivated by the growing number of good-quality X-ray spectra from *Einstein* and its successors (e.g., George & Fabian 1991, Ghisellini et al. 1994, Krolik et al. 1994). At that time it was established that the absorption seen in the X-ray spectra of obscured AGN is consistent with the gas located in the BLR or the obscuring torus. Detection of a narrow Fe Kα line in virtually every AGN X-ray spectrum with sufficient data quality (e.g., Awaki et al. 1991, Nandra & Pounds 1994, Turner et al. 1997) was interpreted as evidence for a significant covering factor of CT material outside of our line of sight, likely associated with the obscuring torus.

Features in the reprocessed spectrum, such as the Compton hump, fluorescent lines of atomic species, their secondary K-shell and L-shell lines, and down-scattered Compton shoulders (Matt et al., 1991; Matt, 2002; Yaqoob & Murphy, 2011), can be used to study the properties of the torus. However, detection of these lines requires soft X-ray spectra of the highest quality (e.g., Yaqoob & Padmanabhan 2004, Shu et al. 2010a, Liu et al. 2016). The Compton hump was within reach of previous X-ray instruments with bandpass extending above 10 keV (*BeppoSAX*, *RXTE*, *Suzaku*), but the sensitivity of those instruments was typically insufficient to strongly constrain the shape of this broad feature, except in a few cases of the brightest sources (e.g., Yaqoob 2012). Several sample studies (Dadina, 2008; Vasudevan et al., 2013; Rivers et al., 2013), as well as studies of stacked spectra (Malizia et al., 2003; Ricci

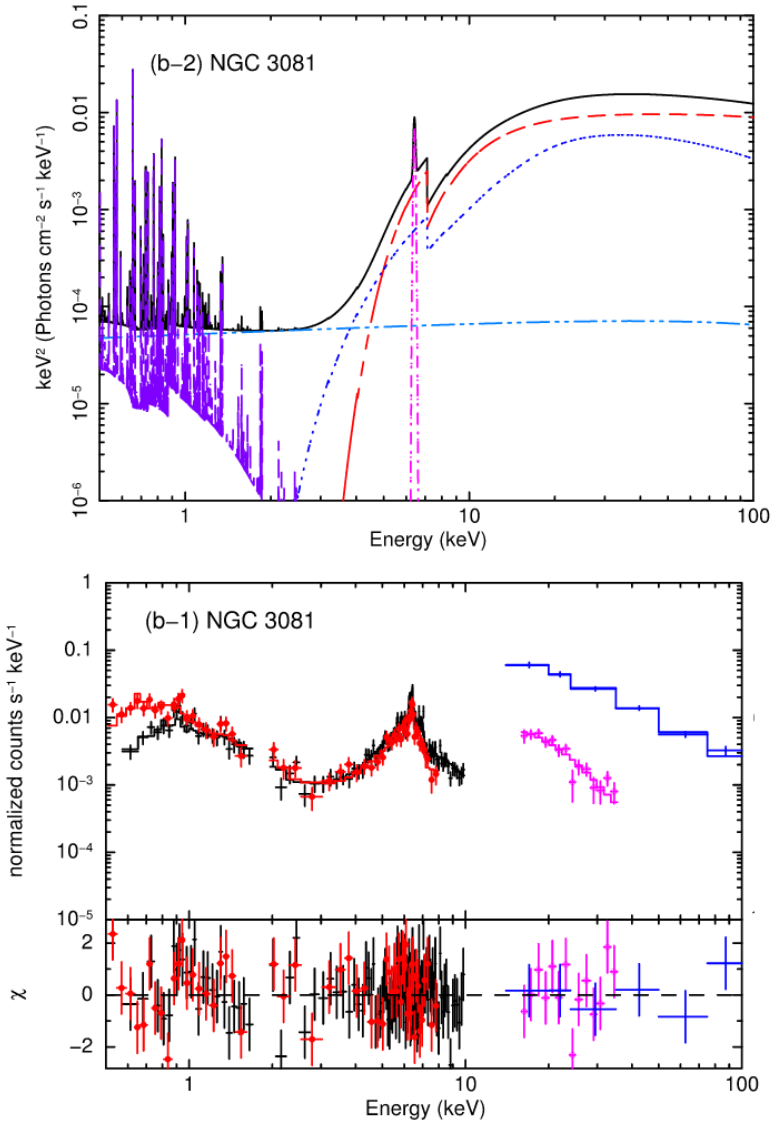

Figure 1.3: Model X-ray spectrum of the heavily obscured AGN NGC 3081 (upper panel) fitted to the *Suzaku* and *Swift*/BAT data (lower panel) by Eguchi et al. (2011). The model consists of photoionized plasma (dark purple), Thomson-scattered continuum (light blue), reprocessed continuum from the torus (dark blue), reprocessed Fe Kα emission from the torus (magenta), and the absorbed intrinsic continuum (red). The torus model used here is from Ikeda et al. (2009). In the lower panel *Suzaku*/XIS data is shown in red and black, while magenta and blue show *Suzaku*/PIN and *Swift*/BAT data, respectively. Note the narrow energy range of the *Suzaku*/PIN instrument, the low energy resolution of the *Swift*/BAT data, and the fact that neither have any overlap with the soft X-ray data that could provide robust relative offsets.

et al., 2011), found evidence for strong Compton humps in subsets of their sources, arguing indirectly that this could be related to the properties of their torus.

Prior to the *NuSTAR* launch in 2012, only a small number of studies focused on constraining the properties of the torus in individual AGN using the latest generation of X-ray reprocessing models (Murphy & Yaqoob, 2009; Ikeda et al., 2009; Brightman & Nandra, 2011a): e.g., Braito et al. (2013), Yaqoob (2012), Marchese et al. (2012). In contrast to many studies finding that a CT torus model can generally reproduce observed Fe Kα lines and broadband X-ray spectra of obscured AGN (e.g., Eguchi et al. 2009, Fukazawa et al. 2011, Tazaki et al. 2011), they found that at least some AGN may have a torus with average column density below the CT threshold. Studies of large samples selected from the *Swift*/BAT and *INTEGRAL* catalogs (e.g., Winter et al. 2009, Burlon et al. 2011, Malizia et al. 2012) generally focused on constraining the intrinsic distribution of $N_{\rm H}$ in the local AGN population. They typically found CT AGN at a rate of a few percent, having to rely on model-based estimates of survey completeness to evaluate their intrinsic fraction in the broad range of 10–50 % of the local AGN population.

1.2.3 AGN at High Redshift and The Cosmic X-ray Background

Although work presented in this thesis is based on detailed spectroscopy of nearby obscured AGN, an important part of motivation for these studies comes from the high-redshift universe, where they are thought to be more abundant (e.g., La Franca et al. 2005, Treister et al. 2008, Buchner et al. 2015). X-ray spectra of distant AGN cannot be directly studied at the same level of detail as those of their local counterparts due to limited data quality. However, some part of what we learn from nearby AGN may be applicable to the high-redshift AGN population. Understanding AGN obscuration is an essential ingredient in understanding the details of the accretion history of the Universe and the relation between SMBH growth and galaxy evolution (Brandt & Alexander, 2015).

Deep X-ray surveys with *Chandra* and *XMM-Newton* have revolutionized our understanding of AGN evolution. Identification of AGN by their X-ray signature leads to less contaminated and more complete AGN samples in comparison with optical and infrared selection: host galaxies only weakly contribute to the hard X-ray band[7] even at high star-formation rates, and X-rays penetrate significantly higher absorption columns than visible light. An important finding enabled by deep X-

[7]It is worth noticing that the effect of redshift is such that for sources at higher redshift, soft X-ray telescopes observe more penetrating, hard X-ray photons.

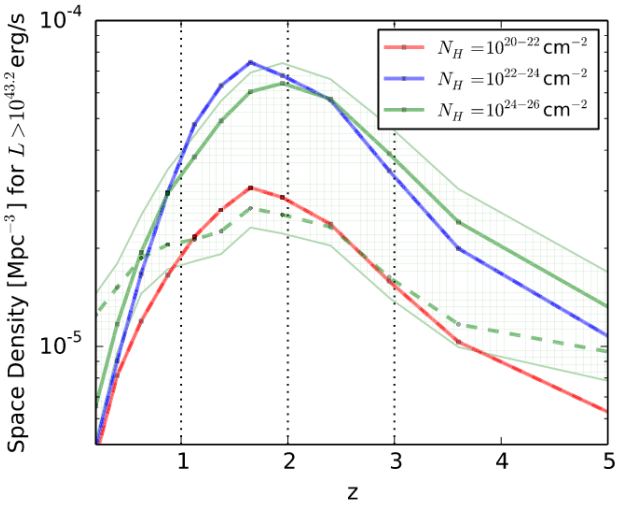

Figure 1.4: The evolution of the space density of unobscured (red), non-CT obscured (blue) and CT AGN (green; area showing uncertainties), from the work of Buchner et al. (2015). Note that the rise from $z = 0$ to $z \sim 2$ is steeper for obscured than unobscured AGN, resulting in a larger obscured AGN fraction at $z > 0$. © AAS. Reproduced with permission.

ray surveys is the anti-hierarchical luminosity-dependent evolution of AGN number density, now known as "cosmic downsizing" (e.g., Cowie et al. 2003, Silverman et al. 2008, Ueda et al. 2014). Though limited in the number of targets and data quality, spectroscopy of AGN detected in these surveys indicates that obscuration properties of AGN also evolve: for example, Brightman et al. (2014) found that the AGN torus covering factor decreases with luminosity at all redshifts, and that torus covering factors are on average higher for higher-redshift AGN – consistent with population studies finding an increase of the obscured AGN fraction with redshift.

The integrated signature of the growth of SMBH through cosmic history is observed today as the cosmic X-ray background (CXB). Many studies of the CXB spectrum (Madau et al. 1994, Gilli et al. 2007, Akylas et al. 2012, among others) have found it necessary to assume that a large portion is produced by heavily obscured AGN and CT AGN, albeit with severe degeneracy with their assumed average spectral shape. AGN populations found in deep surveys with *XMM-Newton* and *Chandra* account for $\simeq 80\,\%$ of the soft X-ray CXB spectrum (Brandt & Alexander, 2015); however, only a few percent of the population contributing to the peak of the CXB spectrum at $\simeq 30$ keV has been resolved directly before the launch of *NuSTAR*. While *NuSTAR* is expected to directly resolve 50–60 % of the CXB (see Harrison et al. 2016 for

intermediate results), studies of obscured AGN spectra can help greatly in removing an important degeneracy in constraining this elusive population through spectral modeling of the CXB spectrum.

1.3 The Context and the Focus of This Thesis

This thesis is focused on studies of obscured AGN in the local universe using broadband X-ray spectroscopy. The key instrument providing the sensitive data above 10 keV, where all previous instruments had significantly lower sensitivity is the Nuclear Spectroscopic Telescope Array (*NuSTAR*; Harrison et al. 2013). *NuSTAR* is the first orbiting hard X-ray observatory (covering the 3–79 keV band) to feature focusing optics, which enables it to efficiently reject the high background that limited the sensitivity of collimated or coded-aperture instruments. With its unprecedented sensitivity above 10 keV, good energy resolution, as well as spatial resolution, *NuSTAR* is ideally suited for detailed studies of obscured AGN in the local universe, and up to $z \sim 1$ in deep surveys.

The first study, presented in Chapter II, is motivated by the unknown geometry and properties of the AGN corona. I performed a detailed spectroscopic analysis of two *NuSTAR* observations of the obscured Seyfert MCG –05-23-016 (optical type 1.9), which has been published in Baloković et al. (2015). The main result of our spectral modeling was one of the first reliable measurements of the optical depth and the coronal temperature for an obscured AGN. Using theoretical models for coronal emission, it was possible to constrain these two basic physical parameters independently assuming two simple coronal geometries. Similar measurements have been performed on about a dozen AGN observed with *NuSTAR* (e.g., Matt et al. 2015; see Fabian et al. 2015 for a summary), but reliable constraints remain scarce for obscured AGN.

Both because of the lack of contiguous sensitive coverage extending into the hard X-ray band, broadband X-ray spectra of CT AGN other than the few brightest examples, have not been studied in detail. Chapter III presents a spectroscopic study of three CT AGN, NGC 424, NGC 1320, and IC 2560, using *NuSTAR*, *Swift*, and *XMM-Newton* data. Using both phenomenological spectral models and an empirically motivated model for the torus, we arrive at a conclusion that the intrinsic continuum is completely extinguished in all three spectra, leaving them dominated by light reprocessed by the torus with a large but finite optical depth to Compton scattering

and likely non-uniform structure. As one of the first CT AGN studies with *NuSTAR* (published in Baloković et al. 2014), the study discusses selection of AGN with similar spectra in deeper *NuSTAR* surveys. The predicted X-ray "colors" were subsequently used by Lansbury et al. (2015) and Lansbury et al. (2017) to identify faint, highly obscured AGN.

After a number of completed studies of heavily obscured AGN observed with *NuSTAR*, some of which I directly contributed to (e.g., Brightman et al. 2015, Rivers et al. 2015a, Masini et al. 2016), and the initial spectral analyses of the growing sample of *Swift*/BAT-selected AGN observed with short *NuSTAR* exposures, it became apparent that a new model for X-ray reprocessing in the AGN torus is needed. Chapter IV presents the first in a suite of spectral fitting models computed in approximately toroidal geometry with a new Monte Carlo radiative transfer code I built for this purpose. This particular model adopts the geometry of the popular model by Brightman & Nandra (2011a), which was found not to reproduce more recent calculations by Liu & Li (2015). In order to highlight its features, the new fitting model is applied to *NuSTAR* spectra of four nearby AGN, 3C 390.3, NGC 2110, IC 5063, and NGC 7582, showing that each one has a distinct spectral signature of the torus in its X-ray spectrum.

Chapters V and VI present my work on the large sample of AGN selected in the hard X-ray band (14–195 keV) from the flux-limited all-sky survey with *Swift*/BAT. They were observed nearly simultaneously with short *NuSTAR* and *Swift*/XRT exposures, generating an atlas of good-quality broadband X-ray spectra for over 130 obscured AGN in the local universe. Such a survey provides, for the first time, a complete picture of the spectral diversity exhibited by obscured AGN at the level comparable to that of unobscured AGN. Furthermore, it provides new insight into obscuration-unbiased properties of the local AGN population, such as the distribution of $N_{\rm H}$, and the properties of the obscuring torus. A phenomenological spectral analysis of this sample is presented in Chapter V. Chapter VI present spectral analyses based on torus reprocessing models, including the new model presented in Chapter IV.

Chapter VII provides an overview of the findings presented in this thesis, as well as those from other related studies carried out in the last few years, mostly using *NuSTAR*. In this final chapter I also present possible future extensions of my work, and some prospects for moving the field forward using the planned next generation of X-ray telescopes.

Chapter 2

CORONAL PROPERTIES OF THE SEYFERT 1.9 GALAXY MCG –05-23-016 DETERMINED FROM HARD X-RAY SPECTROSCOPY WITH *NUSTAR*

Abstract

Measurements of the high-energy cut-off in the coronal continuum of active galactic nuclei have long been elusive for all but a small number of the brightest examples. We present a direct measurement of the cut-off energy in the nuclear continuum of the nearby Seyfert 1.9 galaxy MCG –05-23-016 with unprecedented precision. The high sensitivity of *NuSTAR* up to 79 keV allows us to clearly disentangle the spectral curvature of the primary continuum from that of its reflection component. Using a simple phenomenological model for the hard X-ray spectrum, we constrain the cut-off energy to 116^{+6}_{-5} keV with 90 % confidence. Testing for more complex models and nuisance parameters that could potentially influence the measurement, we find that the cut-off is detected robustly. We further use simple Comptonized plasma models to provide independent constraints for both the kinetic temperature of the electrons in the corona and its optical depth. At the 90% confidence level, we find $kT_e = 29 \pm 2$ keV and $\tau_e = 1.23 \pm 0.08$ assuming a slab (disk-like) geometry, and $kT_e = 25 \pm 2$ keV and $\tau_e = 3.5 \pm 0.2$ assuming a spherical geometry. Both geometries are found to fit the data equally well and their two principal physical parameters are correlated in both cases. With the optical depth in the $\tau_e \gtrsim 1$ regime, the data are pushing the currently available theoretical models of the Comptonized plasma to the limits of their validity. Since the spectral features and variability arising from the inner accretion disk have been observed previously in MCG –05-23-016, the inferred high optical depth implies that a spherical or disk-like corona cannot be homogeneous.

Material presented in this chapter has been published as Baloković et al. 2015, ApJ, 800, 62.

2.1 Introduction

The intrinsic X-ray continuum of active galactic nuclei (AGN) is thought to be produced in the immediate vicinity of the central black hole. Phenomenologically, the nuclear continuum can be described as a power law, typically with a photon index of 1.8–2.0, with an exponential cut-off at 150–350 keV (Dadina, 2007; Burlon et al., 2011; Molina et al., 2013; Vasudevan et al., 2013; Malizia et al., 2014; Ballantyne, 2014). The currently accepted model for formation of this spectral component is the inverse Compton scattering of the thermal radiation from the accretion disk by relativistic electrons distributed around the black hole in a structure referred to as the corona (e.g., Rybicki & Lightman 1979; Titarchuk 1994; Zdziarski et al. 2000). The shape of the coronal spectrum is a function of the seed photon field, the kinetic temperature of the plasma, the geometry of the corona, and the observer orientation.

Previous studies suggest that the corona does not uniformly cover the surface of the accretion disk (Haardt et al., 1994), and that it is likely compact (Reis & Miller, 2013). Microlensing measurements on distant quasars confirm the compactness of the X-ray-emitting region (e.g. Dai et al. 2010; Mosquera et al. 2013). However, other physical parameters of AGN coronae are currently poorly constrained due to the lack of direct observations in the hard X-ray band, as well as the degeneracy introduced by contributions from the processed (reflected) spectra from the inner regions of the accretion disk and the dusty molecular torus at larger distances (e.g., George & Fabian 1991; Ghisellini et al. 1994). Disentangling those spectral components requires high-quality hard X-ray data.

We report on the high-energy cut-off measurement and coronal parameters of the active nucleus of the nearby ($z = 0.0085$; 36 Mpc) Seyfert 1.9 galaxy MCG–05-23-016 (Véron et al., 1980; Wegner et al., 2003), using *NuSTAR* data in the 3–79 keV band (Harrison et al., 2013). This AGN has been extensively observed in the soft X-ray band (Weaver et al., 1997; Mattson & Weaver, 2004; Balestra et al., 2004; Braito et al., 2007; Reeves et al., 2007; Zoghbi et al., 2014), revealing a complex structure of the flourescent line emission, including both broad and narrow components produced by the disk and the torus reflection, respectively. The high-energy spectrum, however, has been only poorly constrained thus far: e.g., Perola et al. (2002) and Dadina (2007) found high-energy cut-offs at 147^{+70}_{-40} keV and 190^{+110}_{-60} keV from *BeppoSAX* data, Molina et al. (2013) found it at 85^{+35}_{-20} keV using *INTEGRAL* data, Beckmann et al. (2008) combined *Swift*/BAT and *INTEGRAL* to support a variable cut-off between 50 keV and $\gtrsim$100 keV, while other results in the

literature only placed lower limits in the 100–200 keV range.

The main reason for the discrepant measurements in the past is likely the degeneracy between a cut-off at $\lesssim 200$ keV and a strong reflection continuum. The high signal-to-noise ratio achieved in the observations of MCG –05-23-016 with *NuSTAR* allows us to clearly separate the spectral curvature due to the reflection continuum from the spectral curvature due to the coronal cut-off. In § 2.2 we report on the *NuSTAR* observations and in § 2.3 we present our spectral analysis. In § 2.4 we discuss the potential issues and the physical properties of the corona, and briefly summarize our results in § 2.5.

2.2 Observations and Data

NuSTAR observed MCG –05-23-016 on two occasions: on 2012 July 11–12 (OBSID 10002019), and on 2013 June 3–7 (OBSID 60001046). The first observation was conducted as a part of the *NuSTAR* calibration campaign. The second observation was a science observation carried out simultaneously with a long *Suzaku* observation. We defer the broadband (0.5–79 keV) spectral analysis of the simultaneous *NuSTAR* and *Suzaku* data taken in 2013 to a forthcoming paper (Zoghbi et al., in preparation).[1] Hereafter, we refer to the 2012 and 2013 observations as the *calibration* and *science* observations, respectively.

The event files were cleaned and processed using the NuSTARDAS software package (version 1.2.1) and the scripts `nupipeline` and `nuproducts`. After the automated processing by the pipeline, the total source exposure is 34 ks for the calibration observation, and 160 ks for the science observation. We extracted the source spectra from circular regions 120 arcseconds in radius, centered on the peak of the source image. Corresponding background spectra were extracted from polygonal regions encompassing the same detector, but avoiding the region within 140″ from the source image peak. We estimate that at most 2 % of the background counts above 25 keV can be due to contamination by the source. The response matrices were generated using the calibration database (CALDB) version 20131223.

The analysis presented here is based predominantly on the higher-quality science observation, while the calibration observation is used to investigate the spectral variability on the timescale of one year. The count rate was variable at the level

[1] This analysis, which included additional observations of MCG –05-23-016 in 2015 was published in Zoghbi et al. (2017).

of $\lesssim$ 30 % during the long *NuSTAR* science observation, and $\lesssim$20 % during the calibration observation. The variability on timescales of $\lesssim$1-ks is addressed in detail in a separate publication (Zoghbi et al., 2014). For the analysis presented in this paper, we use the observation-averaged spectra from each of the two *NuSTAR* focal plane modules (FPMA and FPMB), and fit them jointly for each of the two observations, allowing for the cross-normalization constant to vary freely in all fits. The normalization offset is found to be smaller than 5 % in all cases, as expected from instrument calibration (Madsen et al., 2015b).

2.3 Spectral Modeling

We model the *NuSTAR* data in `Xspec` (version 12.8.1; Arnaud 1996) using χ^2 statistics. In order for χ^2 statistics to provide unbiased results we group the data to have a signal-to-noise ratio of at least 10 per bin after background subtraction. All uncertainties on spectral parameters are reported as 90 % confidence intervals from marginalized probability distributions determined using the Markov Chain Monte Carlo (MCMC) algorithm available in `Xspec`.

2.3.1 Phenomenological Models

We start the analysis with a simple absorbed power-law model: `TBabs×zTBabs×pow` in `Xspec`. The first absorption component (`TBabs`; Wilms et al. 2000) represents Galactic absorption fixed to a column density of $N_{\rm H,Gal} = 8 \times 10^{20}\,{\rm cm}^{-2}$ (Kalberla et al., 2005), while the redshifted component (`zTBabs`) accounts for additional absorption by the host galaxy. The redshift is fixed to $z = 0.0085$ (Wegner et al., 2003), and the host column density is a free parameter in the fit. This model fits the data from the science observation very poorly, with a reduced χ^2 (χ^2/ν, where ν is the number of degrees of freedom), in excess of 3. The best-fit model for the science observation data and the residuals are shown in Figure 2.1, in order to highlight the main features that hint towards more appropriate models.

The residuals in the top right panel of Figure 2.1 show signatures of a reprocessed (reflected) component: a neutral iron Kα emission line (6.4 keV) and a broad Compton hump peaking at 20–30 keV. We therefore replace the continuum of the previous model with a `pexrav` component (Magdziarz & Zdziarski, 1995), and add two Gaussian components (one broad and one unresolved; following Zoghbi et al. 2013) to model the line. `pexrav` includes both the intrinsic power-law continuum and the reflection of that continuum from optically thick material. We keep the

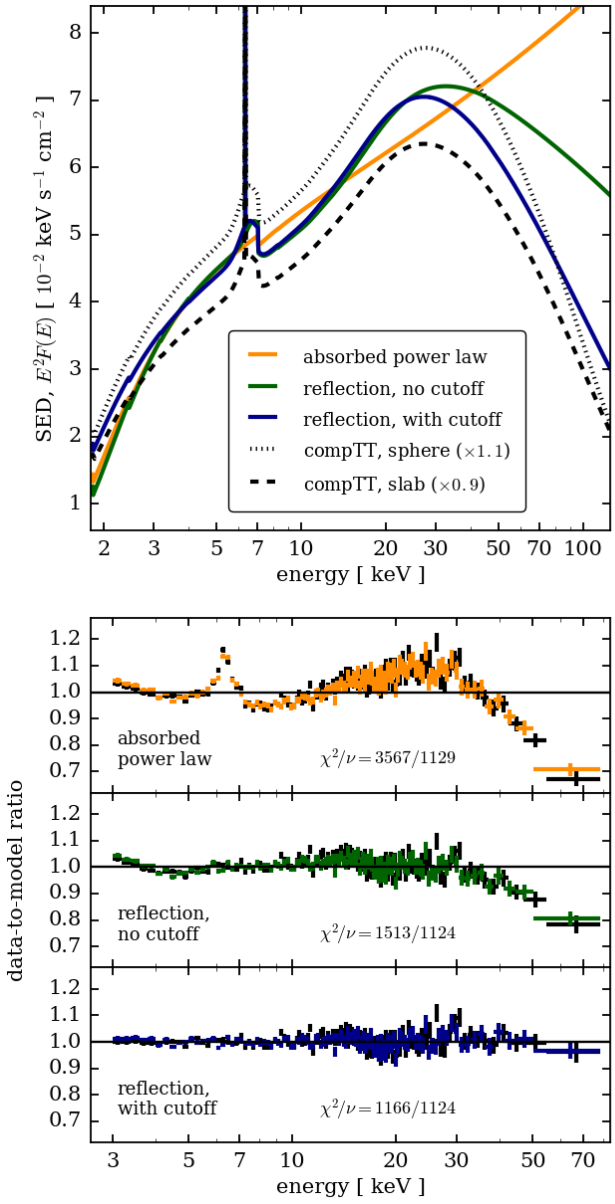

Figure 2.1: *Top:* The model spectral curves for the best-fit models considered in this work: phenomenological ones in solid colored lines and physical ones in dotted and dashed black lines. The physical `compTT` model for spherical (slab) geometry has been moved up (down) by 10 % for clarity. *Bottom:* The data-to-model ratios for the *NuSTAR* science observation data, and the three phenomenological models discussed in § 2.3.1. For clarity, the data are binned in excess of the signal-to-noise ratio of 10 per bin which was used for the modeling. Residuals are shown with colored lines (matching the models in the left panel) for FPMA and in black lines for FPMB. The residuals of the `compTT` models in either geometry are indistinguishable from those in the bottom panel, and are therefore not shown here.

inclination angle fixed at the default value ($\cos\theta_{\rm inc} = 0.45$, $\theta_{\rm inc} \approx 60°$) and leave chemical abundances fixed at Solar values. For the initial fit, we also keep the energy of the power-law cut-off fixed far above the upper end of the *NuSTAR* bandpass at 1000 keV.

This model fits the science observation data much better than the previous one (χ^2/ν=1513/1124=1.35). The best-fit photon index and absorption column density are $\Gamma = 2.00 \pm 0.01$ and $N_{\rm H} = (2.5 \pm 0.2) \times 10^{22}\,{\rm cm}^{-2}$, respectively. The broad Gaussian line component ($\sigma_1 = 0.35 \pm 0.03$ keV) is best fitted at a slightly higher energy than the neutral iron Kα line: $E_1 = 6.7 \pm 0.2$ keV. Fitting for the energy of the narrow line component does not improve the best fit significantly ($\Delta\chi^2/\Delta\nu = -1/-1$), so we leave it fixed at 6.4 keV. The reflection is found to be strong, with a relative normalization $R_{\rm pex} = 0.93 \pm 0.04$, but clearly insufficient to account for all the curvature present in the hard X-ray spectrum – as indicated by the residuals of the best fit displayed in the middle right panel of Figure 2.1.

Letting the cut-off energy vary in the optimization results in a significant improvement of the best fit: χ^2/ν=1163/1124=1.03 ($\Delta\chi^2 = -349$ for one additional free parameter). This verifies that a cut-off at $E_{\rm cut} \approx 115$ keV is robustly detected within the *NuSTAR* band. The best fit column density is $N_{\rm H} = (1.1 \pm 0.2) \times 10^{22}\,{\rm cm}^{-2}$, which is consistent with the much more precise measurement, $N_{\rm H} = (1.32 \pm 0.02) \times 10^{22}\,{\rm cm}^{-2}$, from the joint modeling of the simultaneous *NuSTAR* and *Suzaku* data (Zoghbi et al., 2013). Freezing $N_{\rm H}$ to $1.32 \times 10^{22}\,{\rm cm}^{-2}$results in $\Delta\chi^2/\Delta\nu = +3/+1$. For consistency with our work on the joint dataset, we keep $N_{\rm H}$ fixed hereafter. The best-fit parameters of the `pexrav` component are $\Gamma = 1.85 \pm 0.01$, $R_{\rm pex} = 0.87 \pm 0.04$ and $E_{\rm cut} = 116^{+6}_{-5}$ keV. The broad iron line is best fitted with $E_1 = 6.43 \pm 0.05$ keV and $\sigma_1 = 0.46 \pm 0.06$ keV. The model curve and the residuals are plotted in comparison to the previous ones in Figure 2.1.

The final form of our phenomenological model is `TBabs`×`zTBabs`×(`zgauss`[×2] +`pexrav`). Applying this model to the data from the calibration observation, we find that most of the best-fit spectral parameters are consistent with those of the longer science observation (the exception being $R_{\rm pex}$), albeit less well constrained due to lower photon statistics. The best-fit parameters and their 90 % confidence intervals are given in Table 2.1 for both observations. The flux was (12 ± 1) % lower in the 2–10 keV band during the calibration observation, but the two observations can be modeled self-consistently with just the normalization of the primary continuum and the relative reflection normalization changing significantly between the

observations. Although we explored other models suggested in the literature, we find that neither adding a second reflection component, nor replacing the `pexrav` and the line components with `pexmon` (linking those components self-consistently; Nandra et al. 2007), nor modeling the broad iron line with a relativistic broadening model, reaches lower χ^2/ν. More importantly, those alternative models confirm the measurement of $E_{\rm cut}$ to be robust and, in the worst case, marginally consistent with the 90 % confidence interval based on the phenomenological model presented here. This is discussed further in § 2.4.2.

2.3.2 Physical Models of the Corona

In the previous section we established that the coronal continuum can be approximated as a power law with an exponential cut-off at high energies. More physical models (such as the `compTT` model of Titarchuk 1994) assume a geometry for the corona and allow for determination of its physical parameters from the data. In such models, low-energy (~UV) photons from the accretion disk are Compton-scattered by hot electrons in the plasma. The spatial distribution of the coronal plasma can be approximated with simple geometrical shapes, such as a sphere centered on the black hole, or a slab covering the surface of the accretion disk. In `Xspec` terminology, we replace the `pexrav` continuum with a `refl(compTT)` component: `compTT` models the intrinsic coronal continuum for either a slab (disk-like) or a spherical geometry, and `refl` convolves it with reflection features. We fix the thermal photon temperature to 30 eV, which is appropriate for an AGN accretion disk and does not influence the output spectrum much. We leave the reflector inclination fixed at $\cos i = 0.45$ and iron abundance fixed at the Solar value.

We find that both geometries can provide a good description of the science observation data: the best-fit χ^2 is 1163 for the slab model, and 1161 for the spherical model, both with 1124 degrees of freedom. In either geometry the coronal temperature (kT_e) and the optical depth (τ_e) are very well constrained and strongly correlated, as shown in Figure 2.2. In the case of a slab geometry we find $kT_e = 29 \pm 2$ keV and $\tau_e = 1.23 \pm 0.08$, while for the spherical one the best fit is found for $kT_e = 25 \pm 2$ keV and $\tau_e = 3.5 \pm 0.2$. All other parameters are found to be consistent with values determined from the simpler phenomenological models. We find qualitatively and quantitatively similar results for the calibration observation data. Finally, we also verify that consistent results are obtained with a more elaborate coronal model, `compPS` (Poutanen & Svensson, 1996). While the best-fit parameters may not agree with the `compTT` values within the uncertainties in all cases, the results are

qualitatively the same. A complete summary of the best-fit parameters is given in Table 2.2.

Table 2.1: Summary of best-fit model parameters for MCG –05-23-016 using the phenomenological continuum model, and parameters independent of the choice of the continuum model.

Observation:		science	calibration
independent of the continuum model			
Start–stop Date:		2013 June 3–7	2012 July 11–12
$F\,(2-10\,\mathrm{keV})$ [a]		10.49 ± 0.02	9.13 ± 0.03
$L\,(2-10\,\mathrm{keV})$ [b]		1.781 ± 0.003	1.530 ± 0.005
Number of d.o.f.		1124	703
C_{FPMB} [c]		1.032 ± 0.002	1.045 ± 0.005
$E_{\mathrm{line\,1}}$	[keV]	6.43 ± 0.05	$6.5^{+0.2}_{-0.1}$
$\sigma_{\mathrm{line\,1}}$	[keV]	0.46 ± 0.06	0.5 ± 0.2
$\mathrm{EW}_{\mathrm{line\,1}}$	[eV]	80 ± 10	80 ± 20
$\mathrm{EW}_{\mathrm{line\,2}}$	[eV]	40 ± 10	50 ± 20
phenomenological continuum model: `pexrav`			
χ^2		1163	687
Γ		1.85 ± 0.01	1.83 ± 0.02
R_{pex}		0.87 ± 0.04	1.1 ± 0.1
E_{cut}	[keV]	116^{+6}_{-5}	119^{+16}_{-13}

Notes: Uncertainties listed here are 90 % confidence intervals derived from MCMC chains.

[a] Flux in the 2–10 keV band in units of $10^{-11}\,\mathrm{erg\,s^{-1}\,cm^{-2}}$, calculated from the best-fit phenomenological model. Note that this is an extrapolation down to 2 keV, but we provide it here for comparison with the literature.

[b] Intrinsic continuum luminosity (de-absorbed and excluding reflection components) in the 2–10 keV band in units of $10^{43}\,\mathrm{erg\,s^{-1}}$, calculated from the best-fit phenomenological model. Note that this is an extrapolation down to 2 keV.

[c] Cross-normalization factor for *NuSTAR* module FPMB, assuming $C_{\mathrm{FPMA}} = 1$.

Table 2.2: Summary of best-fit model parameters for MCG –05-23-016 using the physical continuum models in slab and sphere geometries.

Observation:		science	calibration
Comptonized continuum model: `refl(compTT)`			
1) assumed corona geometry: slab			
χ^2		1163	688
$R_{\rm pex}$		0.84 ± 0.04	1.1 ± 0.1
kT_e	[keV]	29 ± 2	30 ± 3
τ_e		1.23 ± 0.08	1.2 ± 0.1
2) assumed corona geometry: sphere			
χ^2		1161	688
$R_{\rm pex}$		0.82 ± 0.04	1.0 ± 0.1
kT_e	[keV]	25 ± 2	26 ± 3
τ_e		3.5 ± 0.2	3.5 ± 0.3
Comptonized continuum model: `compPS`			
1) assumed corona geometry: slab			
χ^2		1159	690
$R_{\rm pex}$		0.65 ± 0.05	0.83 ± 0.09
kT_e	[keV]	26 ± 2	26 ± 3
τ_e		2.2 ± 0.1	2.2 ± 0.2
2) assumed corona geometry: sphere			
χ^2		1161	691
$R_{\rm pex}$		0.69 ± 0.04	0.89 ± 0.08
kT_e	[keV]	25 ± 2	25 ± 3
τ_e		3.2 ± 0.2	3.3 ± 0.3

Notes: Uncertainties listed here are 90 % confidence intervals derived from MCMC chains.

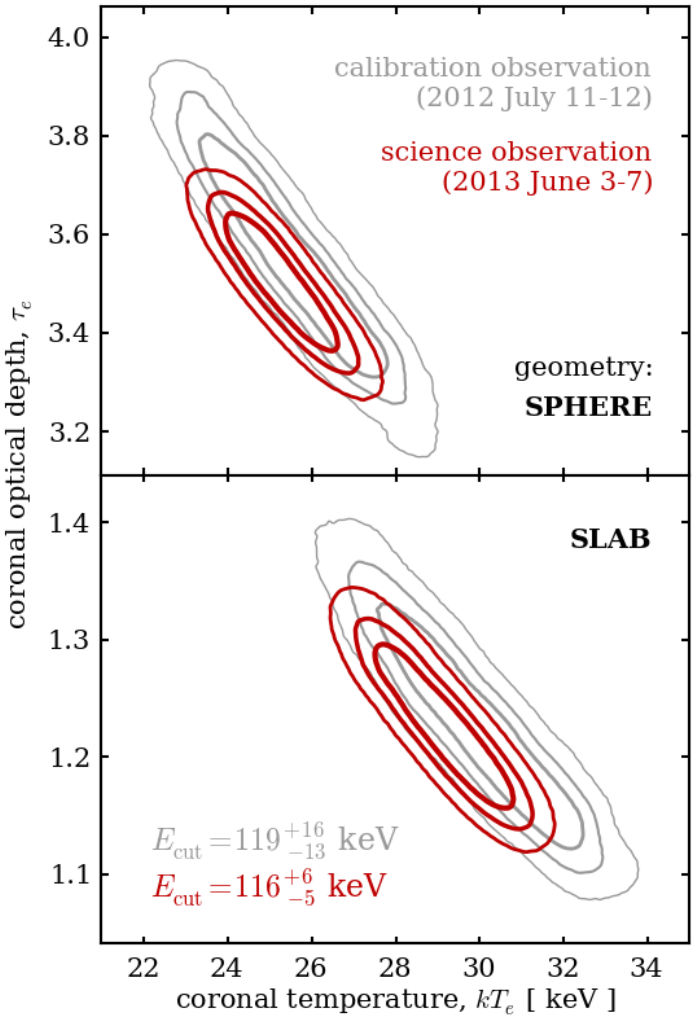

Figure 2.2: Marginal probability distributions for parameters τ_e and kT_e of the `compTT` model in the spherical geometry (top panel) and slab geometry (bottom panel). The distributions are derived from MCMC chains computed with `Xspec` and normalized separately. The red (gray) contours are based on fits to the science (calibration) observation data, marking enclosed probability of 68, 90, and 99 % with the solid, dashed, and dotted lines, respectively.

2.4 Discussion

2.4.1 The Hard X-ray Spectrum and Its Variability

Our spectral modeling results are generally consistent with previous findings, and confirm that the X-ray spectrum of MCG –05-23-016 resembles that of a classical Compton-thin Seyfert 2 nucleus (e.g., Walton et al. 2013). The high-energy cut-off has been previously measured in MCG –05-23-016 with the *BeppoSAX*, *INTEGRAL*

and *Swift* hard X-ray instruments: 147^{+70}_{-40} keV (Perola et al., 2002), 190^{+110}_{-60} keV (Dadina, 2007), 85^{+35}_{-20} keV (Molina et al., 2013). Beckmann et al. (2008) claimed that the cut-off energy is variable within the 50∼100 keV range, but did not highlight any clear trends. It is important to stress that these inferences required assumptions about the photon index and reflection normalization in most cases, while we determine these spectral parameters directly from the data. The phenomenological model presented in § 2.3.1 is the simplest model accounting for the key spectral features observed in the *NuSTAR* bandpass: the iron lines, the Compton hump, and the high-energy cut-off. We emphasize that it should not be taken too literally, as we exploit its simplicity only to highlight the precision of the $E_{\rm cut}$ measurement and the issues that it raises.

More complicated models are clearly needed to fully explain the high-quality soft X-ray observations (e.g., Reeves et al. 2007; Zoghbi et al. 2013). Although *NuSTAR* does not have sufficient spectral resolution to resolve details in the iron line complex, we compute equivalent widths of the two Gaussian components used in our modeling (80 ± 10 eV for the broad and 40 ± 10 eV for the narrow component; see Table 2.1) and find that they are consistent with the highest-quality soft X-ray data. We also test a two-component reflection model, in which the distant reflection is separated from the relativistically broadened and partially ionized reflection off the inner accretion disk. For the disk reflection component we use `reflionx_hc`—an updated version of `reflionx` (Ross & Fabian, 2005) with a variable $E_{\rm cut}$—and relativistic broadening modeled by a convolution with the `Xspec` model `kdblur`. We find that the *NuSTAR* data are not sensitive to the accretion disk parameters as long as its ionization is low ($\xi \lesssim 50\,{\rm erg\,s\,cm^{-1}}$), which is suggested by the best fit. Although the exact best-fit $E_{\rm cut}$ depends on the nuisance parameters, in all cases it is found to be marginally consistent (at the 90 % confidence level) with $E_{\rm cut} = 116^{+6}_{-5}$ keV.

The variability on the ≲1-ks timescale has been shown to be due to reverberation of the primary continuum on the inner accretion disk (Zoghbi et al., 2014). Evaluation of the spectral variability between the two *NuSTAR* observations (approximately one year apart) is limited by the possible variability of the absorbing column. Our analysis of the joint *NuSTAR* and *Suzaku* dataset from 2013 gives a relatively low absorption column density compared to the average taken from the literature ($1.32 \times 10^{22}\,{\rm cm^{-2}}$ compared to $\approx 1.6 \times 10^{22}\,{\rm cm^{-2}}$, excluding the Galactic contribution), which might or might not have persisted since the calibration observation in 2012. In our modeling, summarized in Tables 2.1 and 2.2, we assume the same

absorption column for both observations. If we instead adopt the long-term average column for the calibration observation,[2] we find a cut-off at ≈130 keV, which is only marginally different from the science observation. With no soft X-ray coverage for the calibration observation, the claim that $E_{\rm cut}$ is variable is therefore not statistically significant.

With the column density kept constant, only the absolute flux and the relative reflection normalization (R) seem to have changed significantly. If we separate the reflection from the coronal continuum,[3] we find that the normalization of the former does not change significantly between the two observations and conclude that the change is due to the relative increase of the coronal continuum flux. The flux of the broad iron line component is constant between the observations within the 90 % confidence interval. The spectral variability may be due to the time delay between variations in the coronal continuum and its reflection by the distant torus. Alternatively, an effective change in R may be due to a long-term physical change in the coronal geometry, such as its height above the accretion disk, or in the innermost region of the accretion disk itself.

2.4.2 Robustness of the Cut-off Measurement

As demonstrated in § 2.3.1 (see Figure 2.1), a high-energy cut-off is clearly required by the *NuSTAR* data. Even though the cut-off energy ($E_{\rm cut}$) is above the upper end of the *NuSTAR* bandpass, strong curvature is apparent below 79 keV and allows for determination of $E_{\rm cut}$ to $\lesssim$ 5 % (statistical uncertainty; 90 % confidence). The best-fit value of $E_{\rm cut}$, however, depends on the assumptions that go into the simple model we fit to the data. One example is the inclination: if left free to vary in optimization, the best fit tends to $i \approx 80°$ and $E_{\rm cut} \approx 130$ keV, whereas adopting a value from the recent literature[4] ($i \approx 45°$; Braito et al. 2007; Reeves et al. 2007; Zoghbi et al. 2013) leads to $E_{\rm cut} \approx 110$ keV. Likewise, if we leave the iron abundance to vary freely, the best fit is found for $A_{\rm Fe} = 0.9 \pm 0.2$. This is consistent with our assumption of $A_{\rm Fe} = 1$, but implies $E_{\rm cut} = 122$ keV, which is at the upper end of the

[2] Due to the lack of coverage below 3 keV, *NuSTAR* alone cannot constrain strongly column densities as low as 1×10^{22} cm^{-2}. With $N_{\rm H}$ left free to vary, the best fit for the calibration observation is found for $(1.3 \pm 0.4) \times 10^{22}$ cm^{-2}.

[3] This is achieved by setting the `pexrav` component to produce only the reflection continuum (formally, $R < 0$ in `Xspec`) and adding a separate cut-off power law continuum component, where the photon index and the cut-off energy are shared by both components and their normalizations are free to vary independently.

[4] Note that Weaver et al. (1997) and Mattson & Weaver (2004) advocated a nearly face-on inclination ($i \approx 80°$); however, more recent data do not favor that value.

90 % confidence interval found in § 2.3.1.

A two-component reflection model leads to best-fit $E_{\rm cut}$ between 110 and 124 keV, depending on different assumptions. The typical statistical uncertainty on the best-fit $E_{\rm cut}$ in any particular fit to the science observation data is approximately 7 keV (20–30 keV for the calibration observation), with the iron abundance left free to vary and the ionization and the relativistic broadening parameters fixed close to values found in previous work (e.g., Zoghbi et al. 2013). We emphasize, however, that the systematics introduced by assuming a particular model are comparable to the statistical uncertainties in the case of the science observation of MCG –05-23-016, and are therefore important to consider. With the full flexibility in the shape of the complex reflection continuum, the *NuSTAR* data robustly constrain $E_{\rm cut}$ to the slightly broader 105–130 keV interval, skewed towards the lower end and centered around 115 keV (when marginalized over different assumptions).

For high-quality data systematic uncertainty comparable to statistical uncertainty may also arise from arbitrary choices of the source and background extraction regions, and the choice of binning. For the $E_{\rm cut}$ measurement presented in this paper, we have verified that different choices give results consistent with those discussed above. Systematics are clearly less of an issue with lower-quality data, as demonstrated by the calibration observation data presented here: in that case the constraints on spectral parameters are weakened, and the systematic uncertainty gets absorbed in the statistical uncertainty. This has been the case for the majority of the similar measurements on other AGN published so far, including the recent ones based on the *NuSTAR* data (Brenneman et al., 2014a; Marinucci et al., 2014; Ballantyne et al., 2014). As in the case of IC 4329a (Brenneman et al., 2014b), additional constraints come from joint analyses of simultaneous soft and hard X-ray datasets, leading to further improvement in constraining $E_{\rm cut}$.

2.4.3 Toward a Physical Model of the AGN Corona

The high-energy cut-offs have been measured with a relative uncertainty of $\gtrsim$30 % for a relatively small sample of bright nearby AGN; most of the AGN observed with previous generation of hard X-ray instruments provide lower limits on this parameter (e.g., Dadina 2007; Malizia et al. 2014). Using the *NuSTAR* data, the cut-off energies have recently been measured for IC 4329a ($E_{\rm cut} = 184 \pm 14$ keV; Brenneman et al. 2014a), SWIFT J2127.4+5654 ($E_{\rm cut} = 108^{+11}_{-10}$ keV; Marinucci et al. 2014) and 3C 382 ($E_{\rm cut} = 214^{+147}_{-63}$ keV, and > 190 keV in two distinct spectral

states; Ballantyne et al. 2014). The high quality of the *NuSTAR* spectra in the hard X-ray band up to 79 keV enable reliable independent measurements of the physical parameters of the corona: its temperature, kT_e, and optical depth, τ_e. In this paper we present the most precise measurement thus far, with relative uncertainty of 5 % (at the 90 % confidence level), although, as discussed in § 2.4.2, the exact value depends somewhat on nuisance parameters.

We find that, even though the physical parameters such as kT_e and τ_e are very well constrained by the data, it is still impossible to formally distinguish the geometry. The slab (disk-like) and the spherical geometries, as parametrized by the `compTT` and `compPS` models used here, both describe the MCG –05-23-016 spectrum equally well. We note that a similar result was found in observations of the Seyfert 1.2 IC 4329a and the narrow-line Seyfert 1 SWIFT J2127.4+5654 with *NuSTAR* (Brenneman et al., 2014a; Brenneman et al., 2014b; Marinucci et al., 2014). Both of these AGN and MCG –05-23-016 are radio-quiet, however, they differ in other properties. With a mass of the super-massive black hole of $\sim 5\times10^7\ M_\odot$ (Wandel & Mushotzky, 1986), the mean intrinsic 2–10 keV luminosity of 1.66×10^{43} erg s^{-1} (see Table 2.1) and a bolometric correction from Marconi et al. (2004), MCG –05-23-016 is accreting at approximately 5 % of the Eddington rate. This is almost an order of magnitude less than the other two AGN.

Interestingly, SWIFT J2127.4+5654 has the lowest black hole mass and the lowest cut-off, followed by MCG –05-23-016 in the middle, and IC 4329a with highest mass and cut-off energy. In a number of other AGN, a stringent lower limit on the cut-off energy was placed using the *NuSTAR* data, indicating a generally higher coronal temperature and lower optical depths, e.g., $E_{\rm cut} > 190$ keV in 3C 382 (Ballantyne et al., 2014) and in Ark 120 (Matt et al., 2014), and $E_{\rm cut} > 210$ keV in NGC 2110 (Marinucci et al., 2015). Using long-term averaged data from *INTEGRAL*, Malizia et al. (2014) constrained cut-off energies for 26 AGN in the range between 50 and 200 keV, some of which have been or will be observed with *NuSTAR*. With more high-quality measurements in the near future, covering a wide range of physical properties, it will be possible to directly probe the physics of the AGN corona. In order to distinguish the fine differences due to the coronal geometry, longer observations of sources with a weaker reflection continuum will be needed.

The difference between the optical depth in the two geometries tested here is partially due to the different geometrical definition: whereas in the spherical case it is taken in the radial direction, in the case of slab geometry it is taken vertically, creating

a natural offset by a factor of $\cos\theta_{\rm inc}$. For $\cos\theta_{\rm inc} = 0.45$ used here, the radial optical depth for the slab geometry becomes almost equal to the one of the spherical corona. The important result we point out in this paper is that the $E_{\rm cut}$ <200 keV measurements with *NuSTAR*pressure the theoretical models towards the high-τ_e regime where their validity falls off. The approximations used in the `compPS` model hold only for low optical depth and the formal limits are $\tau_e < 1.5$ for the slab, and $\tau_e < 3$ for the sphere geometry (Poutanen & Svensson, 1996).

The limits of the simpler `compTT` model are even more stringent, although good agreement is found between the analytical model and Monte Carlo simulations in the $\tau_e \sim 1$ regime (Titarchuk, 1994). It is therefore not surprising that the best-fit optical depth in the two models differs somewhat. If the high optical depth derived from the currently available models can be interpreted directly, our results imply that the corona must be inhomogeneous. Spectral features and variability signatures of reflection from the inner accretion disk are clearly detectable in MCG –05-23-016 (Zoghbi et al., 2014) and therefore the corona, which covers the disk in either geometry, cannot be completely opaque. Homogeneity is one of the assumptions of the coronal models used here; pressing against their limits may be indicative of that assumption not being satisfied. Alternatively, our result may simply indicate a geometry different from the ones assumed in this work. In either case, we are drawn to the conclusion that new models are needed in order to better understand the physical implications of our result.

2.5 Summary and Conclusions

In this paper we focus on modeling the hard X-ray spectrum of MCG –05-23-016 in order to constrain models of the AGN corona. We first robustly establish that a cut-off is present in the spectrum at 116^{+6}_{-5} keV (statistical uncertainty; 90 % confidence), despite the non-negligible reflection component contributing to curvature of the hard X-ray spectrum. The ability to disentangle a $\lesssim 200$ keV cut-off from the reflection continuum is essentially unique to *NuSTAR*.

Modeling the spectrum with physical models, we find that both slab and spherical geometries of the corona provide equally good fits to the data, albeit for different physical parameters. Assuming a simple coronal model (`compTT`), we find the kinetic temperature of electrons in the corona and its optical depth, kT_e and τ_e, to be 29 ± 2 keV (25 ± 2 keV) and 1.23 ± 0.08 (3.5 ± 0.2) for the slab (spherical) geometry.

Similar results are found for a different, less approximate model (`compPS`). It is important to note that in all cases the data push the models towards high-τ_e values, where their validity drops off.

The relative statistical uncertainty of 5 % (quoted here as a 90 % confidence interval) has never been achieved before and we show that the new level of precision enabled by *NuSTAR* requires careful consideration of possible systematic uncertainties arising from simplifying assumptions. With further measurements at comparable precision for AGN with a wide range of properties, and the extension of Comptonization models towards the high-opacity regime, it should be possible to construct a clearer physical picture of the AGN corona in the near future.

Acknowledgements

M. B. acknowledges support from the International Fulbright Science and Technology Award. A. M. and G. M. acknowledge financial support from Italian Space Agency under grant ASI/INAF I/037/12/0-011/13 and from the European Union Seventh Framework Programme (FP7/2007-2013) under grant agreement n. 312789. C. S. R. thanks NASA for support under ADAP grant NNX14AF86G.

This work was supported under NASA Contract No. NNG08FD60C, and made use of data from the *NuSTAR* mission, a project led by the California Institute of Technology, managed by the Jet Propulsion Laboratory, and funded by the National Aeronautics and Space Administration. We thank the *NuSTAR* Operations, Software and Calibration teams for support with the execution and analysis of these observations. This research has made use of the *NuSTAR* Data Analysis Software (NuSTARDAS) jointly developed by the ASI Science Data Center (ASDC, Italy) and the California Institute of Technology (USA). This research has made use of NASA's Astrophysics Data System.

Chapter 3

THE *NUSTAR* VIEW OF NEARBY COMPTON-THICK AGN: THE CASES OF NGC 424, NGC 1320 AND IC 2560

Abstract

We present X-ray spectral analyses for three Seyfert 2 active galactic nuclei, NGC 424, NGC 1320, and IC 2560, observed by *NuSTAR* in the 3–79 keV band. The high quality hard X-ray spectra allow detailed modeling of the Compton reflection component for the first time in these sources. Using quasi-simultaneous *NuSTAR* and *Swift*/XRT data, as well as archival *XMM-Newton* data, we find that all three nuclei are obscured by Compton-thick material with column densities in excess of $\sim 5 \times 10^{24}$ cm^{-2}, and that their X-ray spectra above 3 keV are dominated by reflection of the intrinsic continuum on Compton-thick material. Due to the very high obscuration, absorbed intrinsic continuum components are not formally required by the data in any of the sources. We constrain the intrinsic photon indices and the column density of the reflecting medium through the shape of the reflection spectra. Using archival multi-wavelength data we recover the intrinsic X-ray luminosities consistent with the broadband spectral energy distributions. Our results are consistent with the reflecting medium being an edge-on clumpy torus with a relatively large global covering factor and overall reflection efficiency of the order of 1 %. Given the unambiguous confirmation of the Compton-thick nature of the sources, we investigate whether similar sources are likely to be missed by commonly used selection criteria for Compton-thick AGN, and explore the possibility of finding their high-redshift counterparts.

Material presented in this chapter has been published as Baloković et al. 2014, ApJ, 794, 111.

3.1 Introduction

It is well established that a significant fraction of active galactic nuclei (AGN) are intrinsically obscured by gas and dust surrounding the central supermassive black holes (SMBH). Obscured AGN are needed to explain the ~30 keV peak of the Cosmic X-ray Background (CXB; e.g., Churazov et al. 2007; Frontera et al. 2007; Ajello et al. 2008; Moretti et al. 2009); however, their space density is observationally poorly constrained. AGN obscured by gas with column density of $N_{\rm H} \lesssim 1.5 \times 10^{24}\,{\rm cm}^{-2}$ have been identified in large numbers in deep soft X-ray (< 10 keV) surveys (Brandt & Hasinger, 2005), which are powerful means for identifying the bulk of the AGN population at high redshift and thus providing valuable constraints on the growth history of SMBH (e.g. La Franca et al. 2005; Aird et al. 2010). However, the heavily obscured, Compton-thick sources ($N_{\rm H} > 1.5 \times 10^{24}\,{\rm cm}^{-2}$; see, e.g. Comastri 2004 for a review) required by the CXB models remain elusive.

Recent surveys with the hard X-ray (> 10 keV) telescopes *Swift*/BAT (*Burst Alert Telescope*; Gehrels et al. 2004) and *INTEGRAL* (*International Gamma-Ray Astrophysics Laboratory*; Winkler et al. 2003) indicate that in the local Universe the fraction of obscured AGN (with $N_{\rm H} > 10^{22}\,{\rm cm}^{-2}$) is approximately 80 %, while Compton-thick sources likely contribute about 20 % of the total number of AGN (estimated from the observed $\lesssim$10 % fraction corrected for survey completeness, e.g., Malizia et al. 2009, Burlon et al. 2011). Obscured AGN therefore contribute significantly to the local supermassive black hole space density (Marconi et al., 2004) and may be even more important at earlier epochs (La Franca et al., 2005; Ballantyne et al., 2006; Treister & Urry, 2006; Brightman & Ueda, 2012; Iwasawa et al., 2012). The peak of the CXB at ~30 keV can be reproduced by invoking a significant number of Compton-thick sources at moderate redshift (e.g., Gilli et al. 2007; Treister et al. 2009; Ballantyne et al. 2011; Akylas et al. 2012); however, to date only a few percent of the CXB has actually been resolved at its peak energy (e.g., Ajello et al. 2008, Bottacini et al. 2012). The distribution of the obscuring column density and the degeneracy in relative contributions of absorption- and reflection-dominated hard X-ray spectra are therefore poorly constrained with the current data.

A primary goal of the *NuSTAR* (*Nuclear Spectroscopic Telescope Array*; Harrison et al. 2013) hard X-ray mission is to study the evolution of obscuration in AGN at $0 < z < 2$ through its comprehensive extragalactic survey program. In addition to blank-field observations, the program includes a survey of known sources selected

from the *Swift*/BAT catalog with two goals: (i) obtain high-quality spectroscopy of the nearby *Swift*/BAT-selected AGN, and (ii) perform a wide-field search for serendipitous background sources (Alexander et al., 2013). In this chapter we present observations and modeling of the hard X-ray spectra of three local AGN: NGC 424, NGC 1320, and IC 2560, two of which are selected from the program outlined above. All three show spectra dominated by reflection from cold, distant, Compton-thick material, the properties of which are impossible to fully constrain using only soft X-ray data. These Compton-thick AGN demonstrate how *NuSTAR* spectroscopy of the nearby targets can characterize their X-ray properties better than previously possible, and how the new constraints may lead to improved understanding of both local AGN and their distant counterparts. Ultimately, the *NuSTAR* surveys will allow us to directly determine the fraction of Compton-thick sources in the AGN population and the distribution of the obscuring column density for heavily obscured AGN.

The chapter is organized as follows. In § 3.2 we present the target selection, and the new data obtained from quasi-simultaneous observations with *NuSTAR* and *Swift*. § 3.3.1 and § 3.3.2 demonstrate that reflection is the dominant component of the hard X-ray spectra of these three AGN. § 3.3.3 provides a more detailed spectral analysis including the *XMM* data. A comparison with the previously published X-ray results, as well as a discussion of the multi-wavelength properties and constraints on the AGN geometry, is presented in § 3.4. We summarize our results in § 3.5. In this work we use standard cosmological parameters ($h_0 = 0.7$, $\Omega_\Lambda = 0.73$) to calculate distances. Unless noted otherwise, all uncertainties are given as 90 % confidence intervals.

3.2 Target Selection and Observations

3.2.1 Target Selection

The *NuSTAR* Extragalactic Survey program includes a wide-field shallow component (average exposure of 20 ks) in which the observatory is pointed towards a known AGN previously detected with *Swift*/BAT or selected because of high obscuration inferred from soft X-ray (< 10 keV) observations. The wide field of view of the *Swift*/BAT instrument and its nearly uniform coverage of the whole sky down to a sensitivity of $\gtrsim 1.0 \times 10^{-11}$ erg s^{-1} cm^{-2} in the 14–195 keV band (Baumgartner et al., 2013), provide a reasonable sample of predominantly local ($z \sim 0.03$) AGN. Its more uniform and deeper exposure of the sky away from the Galactic plane

compared to *INTEGRAL* makes the *Swift*/BAT survey source catalog an excellent starting point for selecting targets for more detailed spectroscopic studies, such as possible with *NuSTAR*. The targets were selected for *NuSTAR* observations from the catalog utilizing 54 months of BAT operation (Cusumano et al., 2010). Unless prevented by technical constraints, all *NuSTAR* targets in this program receive on average 7 ks of quasi-simultaneous coverage (with delay of $\lesssim$1 day) in the soft X-ray band from the *Swift*/XRT in order to enable spectral analysis over the broad 0.3–79 keV band.

Two of the targets presented here, NGC 424 (Tololo 0109–383) and NGC 1320, were selected from the 54-month *Swift*/BAT catalog.[1] The third target, IC 2560, was selected from a sample of relatively faint AGN with some indication of Compton-thick obscuration from previous observations (e.g., Risaliti et al. 1999, Tilak et al. 2008). Soft X-ray spectroscopy, as well as multi-wavelength data, indirectly suggest that NGC 424 and NGC 1320 are also likely to be Compton-thick (Collinge & Brandt, 2000; Marinucci et al., 2011; Brightman & Nandra, 2011a). The selection of the sample presented here is based on a basic spectral analysis of all *NuSTAR* 20-ks snapshot observations of AGN up to May 2013. Out of 34 observed AGN we selected three that show the most prominent Compton reflection component signature: very hard spectrum ($\Gamma < 1$, assuming a simple power law model), strong Compton hump (high reflection fraction, $R > 10$, assuming the simplest reflection model) and iron emission (large equivalent width of the neutral iron Kα line, $\gtrsim$ 1 keV). This is not a uniformly selected, statistically complete sample – we will address such samples in future work. However, the hard X-ray properties of these three targets can be considered representative of a larger class of heavily obscured AGN, which make up approximately 10 % of the sample of nearby AGN being surveyed with *NuSTAR*. The observed spectra of all three sources are shown in Figure 3.1. Some basic data on the targets is summarized in Table 3.1.

[1] Due to different methodology and low significance, NGC 1320 is not included in the latest 70-month catalog (Baumgartner et al., 2013)

Table 3.1: Basic data for the AGN discussed in this chapter

	NGC 424	NGC 1320	IC 2560
Galaxy Type [a]	SB0/a	Sa	SBb
AGN Type [a]	Sy 1/Sy 2	Sy 2	Sy 2
M_{SMBH} / $M_{\odot}$ [b]	6.0×10^7	1.5×10^7	2.9×10^6
Redshift (z) [c]	0.0117	0.0091	0.0096
d_L / Mpc [c]	50.6	39.1	41.4
$N_{\mathrm{H,G}}$ / cm^{-2} [d]	1.7×10^{20}	4.3×10^{20}	6.8×10^{20}

[a] Summary of classifications from the NASA Extragalactic Database (NED; `http://ned.ipac.caltech.edu/`).

[b] Black hole mass from Greenhill et al. (2008) and Bian & Gu (2007).

[c] Adopted redshift and luminosity distance (calculated assuming $h_0 = 0.7, \Omega_\Lambda = 0.73$) based on published measurements available through NED. Note that the distances used in the literature differ $\lesssim 10$ % for NGC 424 and NGC 1320, and up to 40 % for IC 2560.

[d] Galactic column density averaged between Dickey & Lockman (1990) and Kalberla et al. (2005).

3.2.2 *NuSTAR* Data

NGC 1320 was observed on two occasions: an initial 15-ks snapshot and additional follow-up to improve the signal-to-noise ratio for detailed spectral analysis. As a first step in our analysis we check for variability between the observations and find that they are consistent with no change; hereafter we analyse them jointly, but without co-adding. The other two sources were observed once each. Table 3.2 gives a summary of all *NuSTAR* observations. The raw data were reduced using the `NuSTARDAS` software package (version 1.2.1), distributed with the `HEASOFT` package by the NASA High Energy Astrophysics Archive Research Center (HEASARC). The raw events were cleaned and filtered for South Atlantic Anomaly (SAA) passages using the `nupipeline` task. The cleaned events were further processed for each of the two focal plane modules (FPMA and FPMB) using the `nuproducts` task, which generates the spectra and the corresponding response files. These procedures are presented in detail in the *NuSTAR* user's guide.[2]

[2] `http://heasarc.gsfc.nasa.gov/docs/nustar/analysis/nustar_swguide.pdf`

Spectra for all of the sources were extracted from circular regions 40″ in radius, centered on the peaks of the point-source images. The background spectra were extracted from regions encompassing the same detector as the source,[3] excluding the circular region 50″ around the source. The background region sampling the same detector as the source provides the best estimate of the underlying background. For IC 2560 the background was extracted from two adjacent detectors due to its position in the focal plane. All fluxes reported here have been automatically corrected for the finite extraction aperture using the best point spread function model currently available. We do not use *NuSTAR* data below 3 keV, since the calibration is currently uncertain in that energy range. The upper end of the bandpass is mostly limited by photon statistics and the *NuSTAR* instrumental background. All *NuSTAR* spectra are binned to a minimum of 20 photons per bin using `HEASOFT` task `grppha`.

3.2.3 *Swift*/XRT Data

Each *NuSTAR* observation was accompanied by a short observation with *Swift*, typically delayed by less than 24 hours. The purpose of these observations was to provide coverage on the soft X-ray end of the spectrum, where the *NuSTAR* sensitivity drops off, and to facilitate a comparison of the soft X-ray flux with the data available in the literature. Since the sources are not expected to be highly variable on timescales of hours, quasi-simultaneous exposures with *NuSTAR* and *Swift*/XRT provide a broadband snapshot covering the range from approximately 0.5 to 70 keV. The *Swift*/XRT observations were performed in the Photon Counting mode (Burrows et al., 2005). The data were reduced using the task `xrtpipeline` (version 0.12.6), which is a part of the XRT Data Analysis Software (`XRTDAS`) within `HEASOFT`. Spectra were extracted from circular regions 20″ in radius centered on the targets, and the backgrounds were extracted from large annular source-free regions around them. We used response file `swxpc0to12s6_20010101v013.rmf` from the *Swift*/XRT calibration database, while auxiliary response files were generated using the task `xrtmkarf`. Table 3.2 provides the complete list of observations. Unfortunately, the observation of IC 2560 was too short to yield a detection in the *Swift*/XRT band, so we use it here only to place an upper limit on the soft X-ray emission. Due to low count statistics, the *Swift*/XRT spectra are binned to a minimum of 10 photons per bin.

[3] In each module the focal plane consists of 4 detectors; for details, see Harrison et al. (2013).

3.2.4 Archival *XMM-Newton* Data

In addition to the quasi-simultaneous *NuSTAR* and *Swift*/XRT data, we use archival data from *XMM-Newton* to additionally verify our models. The *XMM* spectra are the highest-quality soft X-ray spectra currently available for these sources. Descriptions of the data and details regarding their reduction can be found in Marinucci et al. (2011), Brightman & Nandra (2011a), and Tilak et al. (2008) for NGC 424, NGC 1320, and IC 2560, respectively.

Table 3.2: Summary of the quasi-simultaneous *NuSTAR* and *Swift* observations

Target	Sequence ID	Start Time [UTC]	Duration [ks]	Exposure [ks]	Count Rate [a] [10^{-2} counts s^{-1}]
***NuSTAR* Observations**					
NGC 1320	60061036002	2012-Oct-25 21:50	25.7	14.5	2.8±0.2 / 2.4±0.2
NGC 424	60061007002	2013-Jan-26 06:35	26.7	15.5	4.7±0.2 / 4.6±0.2
IC 2560	50001039002	2013-Jan-28 22:05	43.5	23.4	1.1±0.1 / 1.1±0.1
NGC 1320	60061036004	2013-Feb-10 07:15	49.9	28.0	3.0±0.1 / 2.6±0.1
***Swift*/XRT Observations**					
NGC 1320	00080314001	2012-Oct-26 02:48	75.6	6.8	1.04±0.03
NGC 424	00080014001	2013-Jan-26 06:34	23.9	6.6	2.55±0.03
IC 2560	00080034001	2013 Jan 29 17:50	2.0	2.0	<0.42
NGC 1320	00080314002	2013-Feb-10 07:19	23.9	6.6	1.04±0.03

[a] Count rates for *NuSTAR* modules FPMA / FPMB (3–79 keV), or *Swift*/XRT (0.3–10 keV).

3.3 Modeling of the X-ray Spectra

The *NuSTAR* hard X-ray spectra (3–70 keV) of NGC 424, NGC 1320, and IC 2560 are qualitatively similar, as demonstrated in Figure 3.1. In the lower panel the figure we also show the ratios of the spectra to their respective best-fit power law model simply to highlight the most important features. The best-fit photon indices in all three cases are lower than unity; these fits are rather poor (reduced $\chi^2 \gtrsim 3$) and intended only for demonstration. The spectra exhibit very hard continua with a convex shape broadly peaking around 20 keV, and a prominent emission feature at 6.4 keV, matching the rest-frame energy of the neutral iron Kα emission line. The hard effective photon indices and the structure of the residuals reveal the presence of a strong X-ray reflection component in the *NuSTAR* spectra. The prominent neutral iron line arising from fluorescence and the broadly peaked Compton hump in the

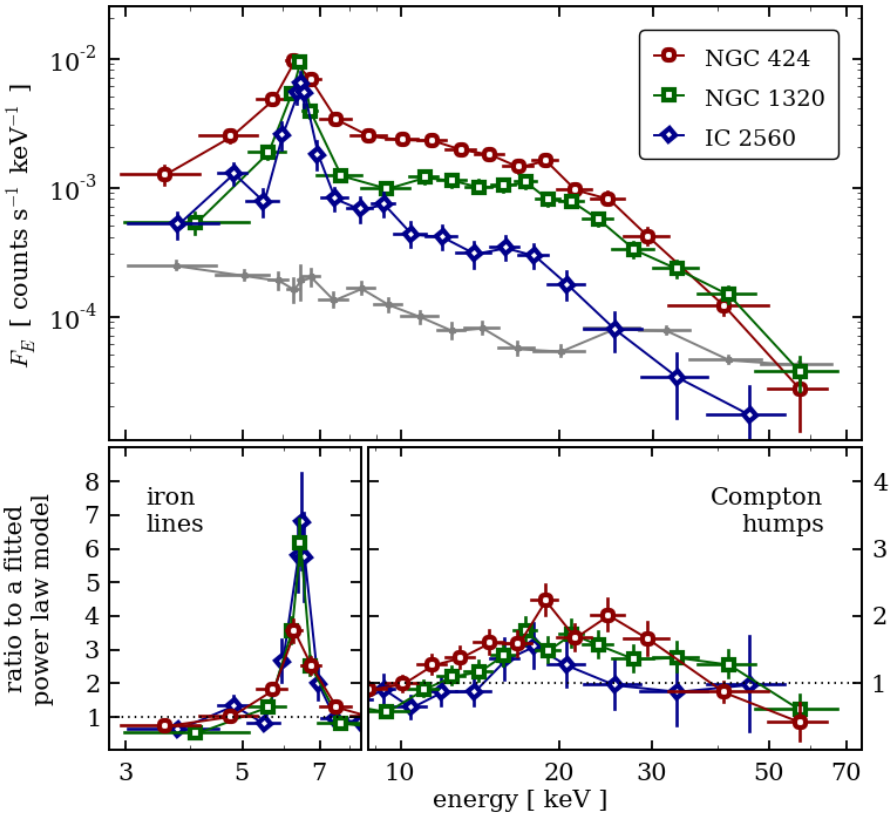

Figure 3.1: *Upper panel:* Observed *NuSTAR* spectra of NGC 424 (red circles), NGC 1320 (green rectangles), and IC 2560 (blue diamonds). Spectra for two focal plane modules have been co-added, and only the longer observation of NGC 1320 is shown here for clarity. The typical background level and its uncertainty are shown by the filled grey symbols and lines. *Lower panels:* Ratio of the spectra and a simple power-law model fitted to each spectrum (symbols as in the panel above). Note that the right panel is rescaled vertically with respect to the left panel by a factor of 2 in order to better show the Compton humps.

20–30 keV region are typical signatures of such a component (e.g., Ghisellini et al. 1994; Matt et al. 2000; Matt et al. 2003a).

Detailed models of the soft X-ray spectra, which is composed of a combination of Thomson-scattered AGN light, plasma ionized by the AGN and star formation, are not the focus of the work presented here. We refer the reader to Marinucci et al. (2012), Brightman & Nandra (2011b), and Tilak et al. (2008) for more details on such models. In the analysis presented here, a simple power law is used to approximate the contribution of the soft component(s) to the spectra above 3 keV. A good phenomenological model for the *Swift*/XRT soft X-ray data (0.3–3 keV) for

both NGC 424 and NGC 1320 is a power law with $\Gamma_s \approx 2.7$ ($\Gamma_s = 2.5 \pm 0.8$ and $\Gamma_s = 2.7 \pm 0.4$, respectively). We adopt this average value and keep it fixed in all models, varying only the normalization, in order to avoid the degeneracy associated with its large uncertainty. For all three targets we verify that this value is consistent with the higher-quality *XMM-Newton* data. The *XMM* data clearly require a more complex spectral model in order to fit the data well, as additional fine structure on top of the slope is apparent in the < 3 keV residuals. However, the simple power law represents a good approximation. More detailed modeling is not warranted for the hard X-ray analysis presented in this chapter.

In the following subsections we present results from applying three different types of hard X-ray spectral models. First we apply simple, phenomenological models, which have been extensively used in previous work (§ 3.3.1). We also apply physically motivated torus models (§ 3.3.2) and reflection-only models (§ 3.3.3). We use `Xspec` version 12.8.1 (Arnaud, 1996) for all our modeling. In addition, we: (i) take into account redshifts and Galactic absorption column density listed in Table 3.1, (ii) assume a contribution from a soft power law component ($\Gamma_s = 2.6$) with free normalization, (iii) assume Solar abundances, (iv) assume a high-energy cutoff in the nuclear continuum at 200 keV,[4] and (v) leave the cross-normalization constants between instruments to vary freely. We perform all parameter optimizations using the Cash statistic (Cash, 1979), but report the χ^2 values of each best fit due to their straightforward interpretability.

3.3.1 Phenomenological Models

We first fit an absorbed power law model using the `Xspec` component `plcabs` (Yaqoob, 1997). This model represents an absorbed power-law spectrum including the effects of Compton scattering. This model is approximated in order to be computationally fast, and it is also limited to $N_{\rm H} < 5 \times 10^{24}\,{\rm cm}^{-2}$. In all three cases the fits are poor and show a strong narrow residual feature around 6.4 keV. The addition of two unresolved Gaussian components ($\sigma = 10^{-3}$ keV) at 6.40 and 7.06 keV, corresponding to neutral iron Kα and Kβ lines, improves the fits significantly.

Although the reduced χ^2 (χ^2/ν, where ν is the number of degrees of freedom) reaches $\simeq$1 for the case of IC 2560 and $\simeq$1.5 for the other two AGN, the fits are

[4] We show later in § 3.4.1 that the NGC 424 data are consistent with this value; for the other two targets this parameter is unconstrained. This choice is consistent with the recent literature, e.g., Ballantyne (2014) and Malizia et al. (2014).

difficult to justify physically. The best fits are all qualitatively the same: the intrinsic power law with a photon index which tends to $\Gamma \lesssim 1$ is absorbed by a column density of $10^{23-24}\,\mathrm{cm}^{-2}$, and the equivalent width of the Gaussian component at the energy of the iron Kα line exceeds 2 keV. These values of Γ are much harder than typical for the coronal continuum of AGN, while the equivalent width of the iron line strongly indicates presence of a reflection component. The photon indices can be assumed to take on a typical value of 1.9 at a cost of increasing the χ^2; however, the best fits remain qualitatively the same. They are shown for each of the three AGN in the top panels of Figure 3.2.

We next add a reflection component, which we approximate using the `pexrav` model (Magdziarz & Zdziarski, 1995). This model produces the reflected continuum of an infinite slab of infinite optical depth, and is therefore only an approximation for the reflection off a distant torus. We apply this component to produce only the reflected continuum. The incident spectrum is set to be the same intrinsic cut-off power law as in the `plcabs` component. We start our fitting procedure with both the transmitted and the reflected component. We also include narrow Gaussian components at 6.40 and 7.06 keV and the soft $\Gamma = 2.7$ power law. The basic result of the fitting is that the contribution of the transmitted components are minor for all three AGN: the data requires either very high absorption column ($N_{\mathrm{H,A}} \gtrsim 5 \times 10^{24}\,\mathrm{cm}^{-2}$, which is the upper limit of the `plcabs` model), or zero normalization.

For NGC 424 the best-fit column density is $N_{\mathrm{H,A}} \gtrsim 5 \times 10^{24}\,\mathrm{cm}^{-2}$ and the intrinsic power law continuum slope is $\Gamma = 2.1^{+0.3}_{-0.2}$ ($\chi^2/\nu = 58/60$). If we fix the absorption column density at a lower value, the normalization of the transmitted component decreases until it becomes consistent with zero for $N_{\mathrm{H,A}} = 2 \times 10^{24}\,\mathrm{cm}^{-2}$. If the transmitted component is removed from the model altogether, the best fit ($\chi^2/\nu = 59/61$) is found for $\Gamma = 1.71 \pm 0.09$. We find qualitatively similar results for IC 2560. For a fixed $N_{\mathrm{H,A}} = 5 \times 10^{24}\,\mathrm{cm}^{-2}$ the best-fit photon index is $2.5^{+0.5}_{-0.7}$ ($\chi^2/\nu = 21/28$). For either a lower $N_{\mathrm{H,A}}$ or a lower Γ, the `plcabs` component vanishes, and the best fit is found for a `pexrav`-only model ($\chi^2/\nu = 22/29$) with $\Gamma = 2.2^{+0.3}_{-0.4}$. In the case of NGC 1320 the best-fit model ($\chi^2/\nu = 149/121$) is dominated by the reflection component, but does include a transmitted power-law component with $\Gamma = 1.3^{+0.3}_{-0.2}$ and $N_{\mathrm{H,A}} = (2^{+2}_{-1}) \times 10^{24}\,\mathrm{cm}^{-2}$. Simply removing the latter component degrades the fit only to $\chi^2/\nu = 152/123$. An alternative model, dominated by the `plcabs` component above 10 keV, can be found with the assumption of $\Gamma = 1.9$ ($\chi^2/\nu = 163/122$).

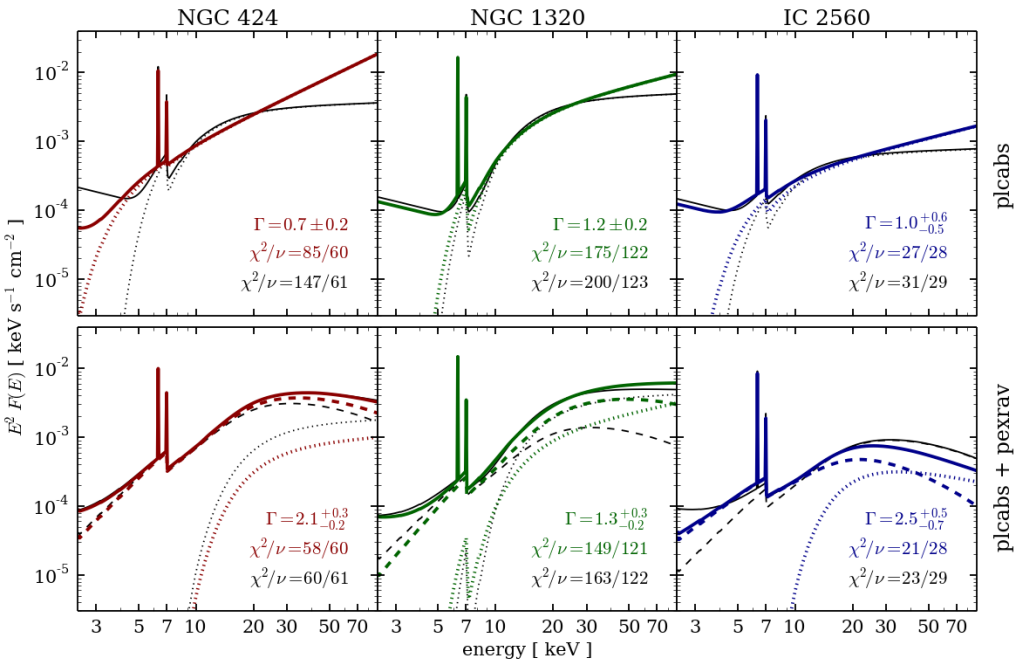

Figure 3.2: Simple approximate models fitted to the NGC 424, NGC 1320, and IC 2560 *Swift*/XRT and *NuSTAR* data (see § 3.3.1 for details). Thick colored lines show models for which the photon index was determined from the data; the best-fit value, its 90 % confidence interval and the best fit χ^2 are given in the lower right corner of each panel. The thin black lines show the same models with the assumption of $\Gamma = 1.9$; its χ^2 is given in black letters. With the solid lines we show the total model, while the dashed and dotted lines show the reflection and the transmission components, respectively. *Upper panels:* Transmission-only models based on `plcabs`. *Lower panels:* Two-component models based on the `plcabs` and `pexrav` components.

The models presented in this subsection are summarized in Figure 3.2. For all three AGN we find that a statistically good description of their hard X-ray spectra can be achieved using models consisting almost entirely of reflection components. However, with the quality of the data acquired in short 20-ks exposures it is not possible to exclude a minor contribution from a transmitted intrinsic continuum. The large equivalent width of the iron lines point towards strong reflection, and essentially rule out the possibility that the hard X-ray spectrum is primarily due to the transmission of the intrinsic continuum through mildly Compton-thick material. We further examine a set of more appropriate physically motivated models.

3.3.2 Torus Models

An improvement over the `pexrav` approximation, which assumes infinite optical depth, is offered by theoretical models that use Monte Carlo simulations of the propagation of X-ray photons through material of finite optical depth in a physically motivated geometry. The first `Xspec` model of that kind is `MYtorus` (Murphy & Yaqoob, 2009; Yaqoob, 2012).[5] The basis of the `MYtorus` model is a literal torus with a 60° half-opening angle. It consists of two main spectral components: a transmitted continuum component (formally called zeroth-order continuum, `MYTZ`, by the authors of the model) and a scattered one (`MYTS`; also referred to as reprocessed, or reflected). The former is produced by scattering photons *away* from the line of sight, while the latter is formed by photons scattered *into* the line of sight of the distant observer.

We start with the complete `MYtorus` model, which is characterized by a single column density ($N_{\rm H,R} = N_{\rm H,A} = N_{\rm H}$, corresponding to the column density in the equatorial plane of the torus). The internal normalizations between the components are fixed. The first model we test is an edge-on torus with inclination fixed at 90°. This model does not fit any of the *NuSTAR* and *Swift* data considered here: the reduced χ^2 values do not get any lower than 2–3. Note that these models are transmission-dominated and therefore formally similar (but physically more appropriate) to the `plcabs`-only model examined in § 3.3.1.

Next we fit for the inclination angle of the torus under different assumptions of the equatorial column density, $N_{\rm H}$, since a straightforward fit for both of those parameters is highly degenerate. The results are again qualitatively the same for all three AGN, regardless of $N_{\rm H}$: the best-fit inclination angles are found to be close to 60°, matching the opening angle of the torus. For example, at $N_{\rm H} = 5 \times 10^{24}\,{\rm cm}^{-2}$ (shown in the upper panels of Figure 3.3), the best-fit inclinations are 69^{+5}_{-4}, 68^{+3}_{-2}, and 66^{+7}_{-4} degrees for NGC 424, NGC 1320, and IC 2560, respectively. The best-fit photon indices are 2.1 ± 0.1 for NGC 424 and 2.0 ± 0.1 for NGC 1320, while for IC 2560 the fit runs into the upper domain limit of `MYtorus` at $\Gamma = 2.6$. The fits are slightly better for higher assumed $N_{\rm H}$, but they never reach $\chi^2/\nu < 1.5$. Most of the χ^2 contribution comes from the iron line region, which we treat in more detail in § 3.3.3.

These results can easily be understood as the tendency of the fit to maximize the con-

[5] We use the version of `MYtorus` model that is publicly available at `http://www.mytorus.com`. Specifically, we use the tables with reprocessing calculated up to 200 keV.

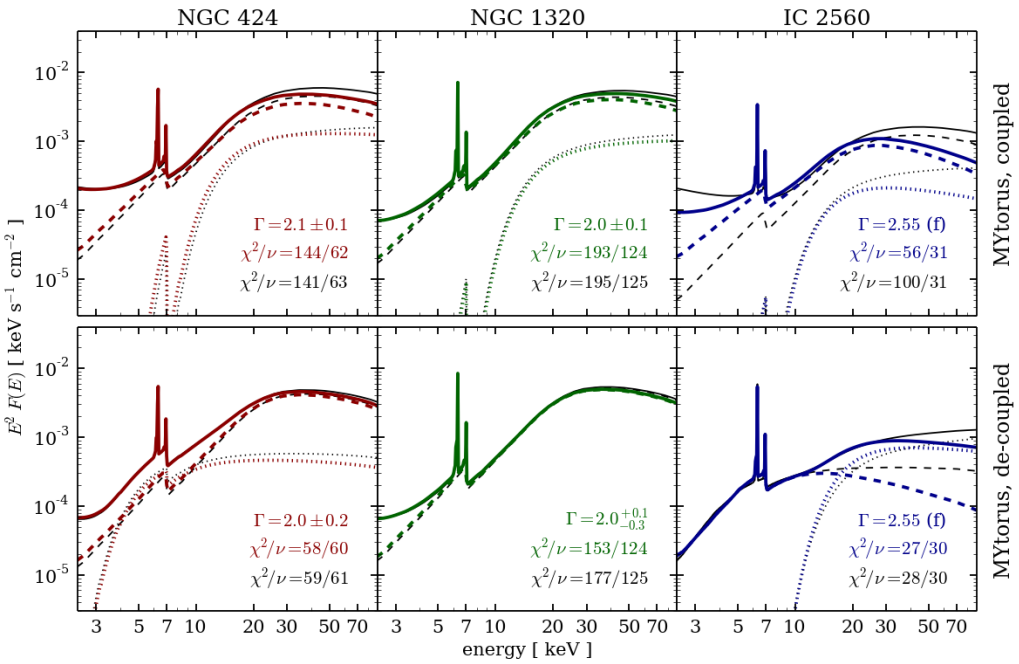

Figure 3.3: Torus models fitted to the NGC 424, NGC 1320, and IC 2560 *Swift*/XRT and *NuSTAR* data (see § 3.3.2 for details). Thick colored lines show models for which the photon index was determined from the data; the best-fit value, its 90 % confidence interval and the best fit χ^2 are given in the lower right corner of each panel. The thin black lines show the same models with the assumption of $\Gamma = 1.9$; its χ^2 is given in black letters. With the solid lines we show the total model, while the dashed and dotted lines show the reflection and the transmission components, respectively. *Upper panels:* Literal torus models represented by `MYtorus` in the coupled mode, with equatorial column density fixed to 5×10^{24} cm^{-2}. *Lower panels:* Generalized two-component models based on de-coupled components of `MYtorus`.

tribution of the reflected component (which increases with decreasing inclination, as the observer sees more of the inner far side of the torus), while not completely uncovering the source of the continuum at the center (since in the line of sight the light suffers significant absorption by passing through the edge of the torus for any inclination greater than 60°). In all cases the spectra are dominated by the reflection component, with only a minor contribution from transmission of the nuclear continuum along the line of sight.

Finally, we try a model in which the two spectral components of the `MYtorus` model are treated independently.[6] In this case, the transmitted zeroth-order continuum, `MYTZ`, and the scattered/reflection component, `MYTS`, have fixed inclination param-

[6]This is the *de-coupled* mode, after Yaqoob (2012).

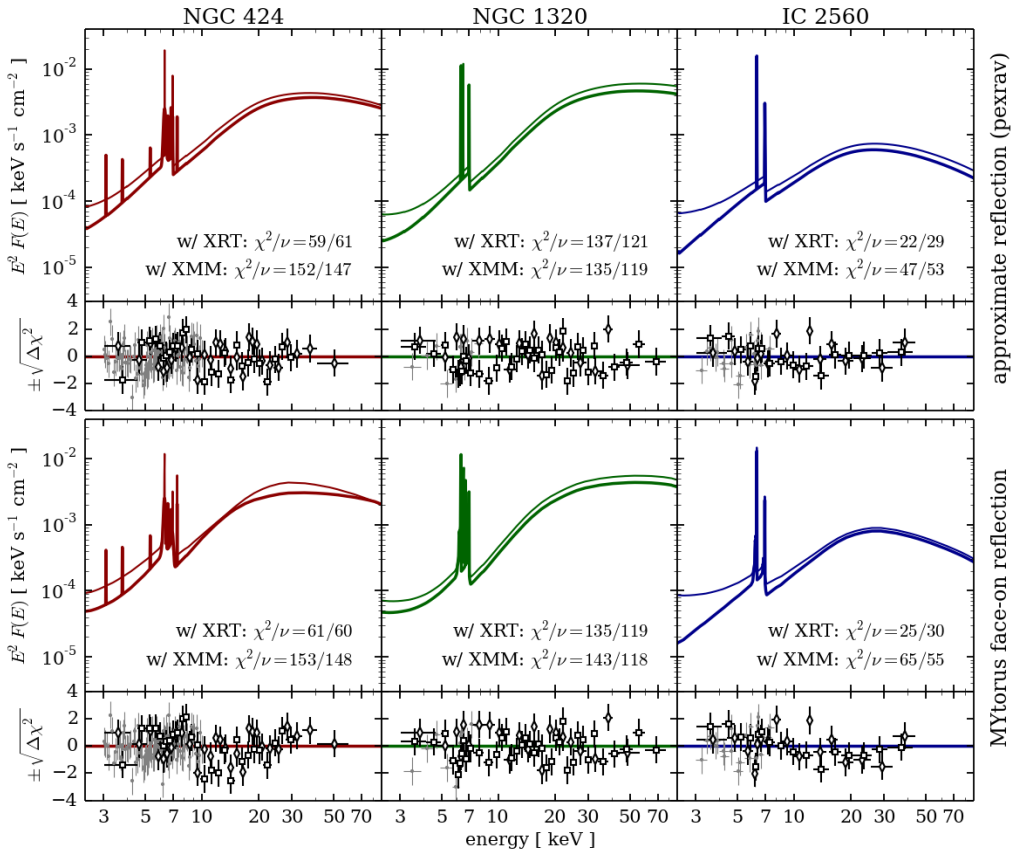

Figure 3.4: Reflection-only models fitted to the NGC 424, NGC 1320, and IC 2560 *NuSTAR* data jointly with simultaneous *Swift*/XRT and non-simultaneous archival *XMM-Newton* data (see § 3.3.3 for details). Thin colored lines show best fits to the *NuSTAR* and *Swift*/XRT data (except for IC 2560, where only the *NuSTAR* data was used), while the thick lines show the same for the *NuSTAR* and *XMM* data lowered by 20 % for clarity. χ^2 values for the best fits are given in each panel. Smaller panels show the residuals: black empty symbols for *NuSTAR* (diamonds for FPMA and squares for FPMB), and grey filled symbols for *XMM*. *Upper panels:* Models with the reflection continuum approximated by the `pexrav` component. *Lower panels:* Models in which the reflection spectrum is represented by the face-on component of `MYtorus`.

eters (90° for the former and 0° for the latter), separate column densities ($N_{\rm H,A}$ and $N_{\rm H,R}$, respectively), and a relative normalization ($A_{\rm rel}$) different from unity. This again leads to solutions in which the reflection component dominates over the transmission component (by a factor of $A_{\rm rel} = 5 - 20$, compared to the internal normalization of the complete `MYtorus` model). However, the fit parameters are different for each AGN, as shown in the lower panels of Figure 3.3.

For NGC 424 we find that a transmission component with $N_{\rm H,A} = (3 \pm 1) \times 10^{23}$ cm^{-2} contributes significantly in the iron line region, while the reflection continuum dominates above 10 keV. In the case of NGC 1320 the normalization of the transmitted component is consistent with zero. The lower quality of the IC 2560 spectum allows for a number of degenerate solutions that sensitively depend on the choice of assumptions. Assuming $\Gamma = 2.55$ as before, one interesting possible solution ($\chi^2/\nu = 27/30$) is reflection from Compton-thin material ($N_{\rm H,R} \approx 5 \times 10^{23}$ cm^{-2}) dominating below 10 keV with a direct power law absorbed by $N_{\rm H,A} \approx 5 \times 10^{24}$ cm^{-2} dominating above that. Removal of the latter component, however, leads to a slightly better reflection-only model ($\chi^2/\nu = 25/30$), which we elaborate on in § 3.3.3. In conclusion, the physically motivated models of the AGN torus, in addition to the phenomenological models presented in § 3.3.1, demonstrate that the observed *NuSTAR* spectra are consistent with being reflection-dominated.

3.3.3 Reflection-dominated Models

The conclusion of both of the preceding two subsections is that the reflection-dominated models provide either better, or statistically equivalent but simpler, descriptions of the observed hard X-ray spectra compared to transmission-dominated or two-component models. Here we summarize the results obtained with the simultaneous *Swift* and *NuSTAR* data, and also consider the higher-quality, non-simultaneous, archival *XMM-Newton* data. In order to avoid the complexities associated with the detailed modeling of the soft X-ray emission unrelated to the AGN, we only use the *XMM* data above 3 keV. The model parameters of interest are listed in Tables 3.3 and 3.4.

NGC 424

Before using the *XMM* data from Marinucci et al. (2011) jointly with the *NuSTAR* data, we first checked whether the target changed dramatically in flux between the two observations. We construct a simple phenomenological model for the 3–

10 keV region by fitting the *XMM* spectrum with a `pexrav` continuum and Gaussian components for 8 emission lines, fixed to the following energies:[7] 3.13, 3.83, 5.37, 6.40, 6.65, 6.93, 7.06, and 7.47 keV. None of the lines are resolved by *XMM*, except the iron Kα line at 6.4 keV with width of $\sigma = 0.09 \pm 0.01$ keV. The 3–10 keV flux calculated for this model fitted to the *XMM* data is $8.4 \pm 0.2 \times 10^{-13}$ erg s^{-1} cm^{-2}, which is $\lesssim 20$ % lower than the $1.1 \pm 0.1 \times 10^{-12}$ erg s^{-1} cm^{-2} derived for the quasi-simultaneous *Swift*/XRT and *NuSTAR*/FPMA data fitted with the same model (all parameters fixed, except for the overall normalization factor). Given the cross-calibration uncertainty between *NuSTAR* and *XMM* of 10 % (Madsen et al., 2015b), the fluxes can be considered almost consistent. We therefore conclude that the flux variability is not severe, and proceed with a joint spectral analysis.

The best-fit approximate reflection-only model (using `pexrav`) for the NGC 424 data from *Swift* and *NuSTAR* is found for $\Gamma = 1.71 \pm 0.09$, with $\chi^2/\nu = 59/61$. The *XMM* data require the Fe Kα line to be broadened ($\sigma = 0.09 \pm 0.01$ keV, $\Delta\chi^2 = 109$ for one additional free parameter), but lead to a very similar result: $\Gamma = 1.64 \pm 0.09$ with $\chi^2/\nu = 152/147$. Strong Fe Kα lines with equivalent width of $\approx$1 keV are found in both cases. The `MYtorus` model fits the *NuSTAR* and *Swift*/XRT data well ($\chi^2/\nu = 61/60$) for $\Gamma = 2.28^{+0.03}_{-0.09}$. The best fit is achieved for reflector column density ($N_{\rm H,R}$) at the upper limit of the range covered by `MYtorus`, 10^{25} cm^{-2}, with a 90 % confidence lower limit of 5×10^{24} cm^{-2}. We find that the line component normalization is marginally lower than unity and that the data favor addition of a narrow Ni Kα line at 7.47 keV ($\Delta\chi^2 = 7$ for one additional free parameter). The best fit parameters and their uncertainties at the 90 % confidence level are listed in Table 3.3. Model curves and residuals are shown in Figure 3.4.

A straightforward fit of the reflection-only `MYtorus` model does not find a statistically acceptable solution ($\chi^2/\nu = 195/148$) for the joint *NuSTAR* and *XMM* data. The *XMM* residuals point towards a disagreement in the region surrounding the prominent iron lines between 6 and 8 keV. We show this energy range in more detail in Figure 3.5, with several different modeling solutions. We first attempt fitting for the energy of the ionized iron line otherwise fixed at 6.65 keV: in this case (Case A) the fit is improved to $\chi^2/\nu = 179/147$ for $E = 6.57^{+0.01}_{-0.03}$ keV. Letting the width of the line vary in the fit (Case B) leads to $E = 6.54 \pm 0.06$ keV and $\sigma = 0.33 \pm 0.08$, removing the need for the previously included line at 6.93 keV. Although this is a

[7] This is a somewhat simpler model than the one used in the original analysis, but it describes the 3–10 keV spectrum very well, with $\chi^2/\nu = 0.95$. For identification of the various emission lines, see Marinucci et al. (2011).

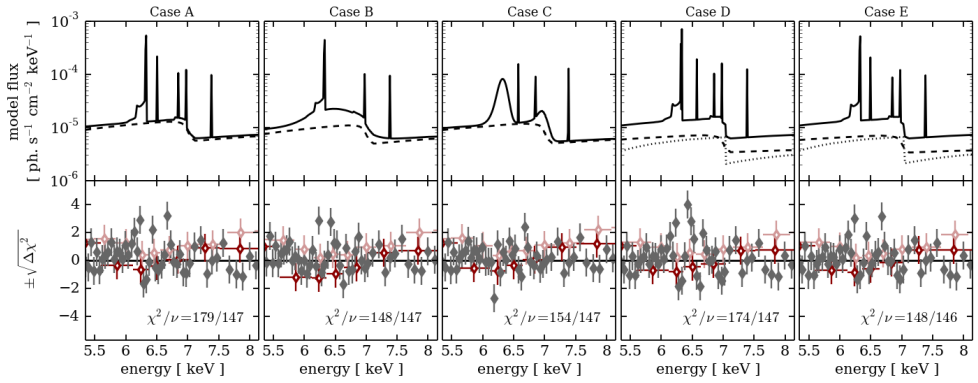

Figure 3.5: Demonstration of the spectral modeling of NGC 424 data in the energy range containing prominent iron lines. Different columns show the model curves (upper panel) and *XMM* and *NuSTAR* residuals (lower panel) for specific cases discussed in § 3.3.3. The solid black lines in the upper panel show the sum of all model components, dashed lines show the reflection continuum, and dotted lines show the absorbed/transmitted component in the rightmost two panels. In the lower panels we show the *NuSTAR* FPMA (FPMB) residuals with dark (light) red symbols, and *XMM* EPIC-pn residuals with grey symbols. In Case A we fit for the energy of the ionized iron line at ≈ 6.6 keV, keeping energies of all other lines fixed; in Case B, we let the width of that line to vary as well. In Case C we broaden the Fe Kα and Kβ lines while keeping line energies fixed at their expected values. Table 3.3 lists the model parameters for Case C. In Cases D and E we add a transmitted component with $N_{\rm H,A} \approx 7\times10^{23}$ cm^{-2}, and fit for the energy of the ionized iron line in the latter.

statistically good model ($\chi^2/\nu = 148/147$), it is difficult the interpret the broad Gaussian feature that it includes. We find an equally good fit ($\chi^2/\nu = 153/147$, Case C) by broadening the `MYtorus` line component, which includes neutral Fe Kα and Kβ lines, using a Gaussian kernel with $\sigma = 0.06 \pm 0.01$ keV. Letting ionized iron line energy vary does not significantly improve the fit. The best-fit photon index is $\Gamma = 2.07^{+0.11}_{-0.09}$ and the reflector column density is well constrained to $N_{\rm H,R} = (3 \pm 1)\times10^{23}$ cm^{-2}. The model parameters listed in Table 3.4 represent this particular case.

An alternative two-component model is suggested by our modeling in § 3.3.2, as well as the literature (Iwasawa et al., 2001; Marinucci et al., 2011). We add a second `MYtorus` component to describe the intrinsic continuum contribution transmitted through the absorbing torus (`MYTZ×pow` in `Xspec`), since the sharp iron edge of an absorbed power-law component ($N_{\rm H,A} \approx 1\times10^{24}$ cm^{-2}) could significantly contribute to the 6–8 keV line region. We find that with emission line energies kept fixed (Case D) the best fit occurs at $\chi^2/\nu = 174/147$. The model is improved

($\chi^2/\nu = 148/146$) if we additionally let one of the ionized iron lines' energy to vary in the fit; the best-fit energy in that case (Case E) is $6.57^{+0.02}_{-0.05}$ keV. The photon index found in Cases D and E, which include component transmitted through a column density of $N_{\rm H,A} = (7 \pm 3) \times 10^{23}\,{\rm cm}^{-2}$, is consistent with the one found in Case C. The reflector column density is at the upper boundary of the model at $10^{25}\,{\rm cm}^{-2}$ for Cases D and E, with a 90 % confidence lower limit of $5 \times 10^{24}\,{\rm cm}^{-2}$. In § 3.4 we discuss the physical plausibility of the simple solutions proposed here. We stress that the details of the iron line region modeling are entirely driven by the high-quality *XMM* data, which are not the focus of this analysis. Although some contribution of a heavily absorbed component cannot be completely ruled out, all of the X-ray data considered here support the reflection-dominated spectrum hypothesis within the statistical uncertainties.

NGC 1320

NGC 1320 was simultaneously observed with *NuSTAR* and *Swift* twice. As no significant differences are apparent between the two observations, we model both epochs simultaneously and list the best-fit parameters of those fits in Tables 3.3 and 3.4. The best-fit photon index is hard ($\Gamma = 1.3 \pm 0.1$); however, assuming a higher cut-off energy for the intrinsic continuum brings it closer to the typical value: e.g., for a cut-off at 500 keV, the best fit is obtained for $\Gamma = 1.5 \pm 0.1$. As in the case of NGC 424, we find that in the `MYtorus` reflection-only model the best-fit photon index is steeper ($\Gamma = 1.9^{+0.1}_{-0.3}$) than the photon index derived from the `pexrav` modeling. The joint fit of the approximate reflection-only model with `pexrav` is significantly improved upon adding a narrow line component at $6.57^{+0.16}_{-0.08}$ keV, which is most likely an Fe XXV Kα line.

Using the `MYtorus` reflection-only model, a line is required at 6.6 ± 0.1 keV. In both cases, the equivalent width of the line is 0.3 ± 0.2 keV. All other spectral parameters are consistent between the two. Addition of the ionized iron line is essentially the only improvement needed over the reflection-dominated models already mentioned in § 3.3.1 and § 3.3.2. We find that the normalization of the lines component of the `MYtorus` model is mildly elevated, but consistent with unity ($1.2^{+0.3}_{-0.4}$). The `MYtorus` model additionally provides a constraint on the column density of the reflecting material, instead of assuming it to be infinite. The reflector column density, $N_{\rm H,R}$, is mildly degenerate with the intrinsic photon index, but it can be constrained independently to $N_{\rm H,R} = (4^{+4}_{-2}) \times 10^{24}\,{\rm cm}^{-2}$ with 90 % confidence.

The only soft X-ray data available for NGC 1320 besides our quasi-simultaneous *Swift*/XRT data is from a relatively short 12-ks *XMM-Newton* observation in 2006 (Brightman & Nandra, 2011a). Only a minor difference of $\lesssim 30\,\%$ in the 3–10 keV flux is observed between the *XMM* and the simultaneous *Swift*/XRT and *NuSTAR* observations, so we proceed with a joint analysis. No significant difference is found between the best-fit intrinsic photon indices based on the *Swift* or *XMM* data for either the `pexrav` or `MYtorus` models. A significant improvement in either case is found if a narrow line corresponding to ionized iron is added to the model. The best fit energy is $6.55^{+0.10}_{-0.09}$ keV for the `pexrav` model and $E = 6.77^{+0.06}_{-0.23}$ keV for the `MYtorus` model, with equivalent widths of 0.2 ± 0.1 keV and $0.3^{+0.1}_{-0.2}$ keV, respectively. Addition of a Ni Kα line at 7.47 keV does not significantly improve the fit. The *XMM* data further constrain the column density of the reflector: $N_{\mathrm{H,R}} = (4^{+2}_{-1}) \times 10^{24}\,\mathrm{cm}^{-2}$ with 90 % confidence. Both best-fit models and their respective residuals are shown in the middle column of Figure 3.4.

IC 2560

IC 2560 is the faintest target considered in this chapter, and correspondingly has the poorest photon statistics. The quasi-simultaneous *Swift*/XRT observation is too short to provide useful soft X-ray data, so for the initial modeling we use the *NuSTAR* data alone. From the best fit of the approximate `pexrav` model we find that the intrinsic photon index is steeper than in the other two targets ($\Gamma = 2.2^{+0.3}_{-0.4}$), and that the iron lines are strong; the equivalent widths of the Fe Kα and Kβ lines are $2.1^{+1.3}_{-0.5}$ keV and $0.6^{+0.6}_{-0.4}$ keV, respectively. In the case of the `MYtorus` reflection-only model we find that the normalization of the line component is significantly elevated, $2.2^{+0.7}_{-0.5}$. The intrinsic photon index is somewhat degenerate with the reflector column density; both are best fitted by parameter values on the edge of the validity domain of the model. Formally, we are able to derive only the lower limits on the best-fit parameters: $\Gamma > 2.6$ and $N_{\mathrm{H,R}} > 10^{25}\,\mathrm{cm}^{-2}$. By fixing the photon index to 2.55 (which is statistically acceptable, with $\chi^2/\nu = 25/30$), we can estimate a 90 % confidence lower limit on $N_{\mathrm{H,R}}$ to be $7{\times}10^{24}\,\mathrm{cm}^{-2}$ based on the *NuSTAR* data alone.

The *XMM* data we use are MOS1 and MOS2 spectra (above 3 keV) from an 80-ks observation published in Tilak et al. (2008). By calculating 3–10 keV fluxes based on a simple reflection model represented by a sum of a `pexrav` continuum and a Gaussian line component we find that the flux did not change between the *XMM* and *NuSTAR* observation by more than 20 %. The joint fits to the *NuSTAR* and

XMM data result in best-fit parameters entirely consistent with those found with the *NuSTAR* data alone. Again, the best-fit photon index and column density in the `MYtorus` model is formally outside of its validity domain. By assuming statistically acceptable $\Gamma = 2.55$ ($\chi^2/\nu = 65/55$) we can constrain $N_{\mathrm{H,R}}$ to be greater than $7{\times}10^{24}\,\mathrm{cm}^{-2}$ with 90 % confidence. Both models and their residuals are shown in the rightmost column of Figure 3.4. Tables 3.3 and 3.4 provide an overview of the best-fit values for all relevant model parameters.

Table 3.3: Summary of model parameters for the phenomenological (`pexrav`-based) reflection-only model fitted to the quasi-simultaneous *NuSTAR* and *Swift*/XRT data, and non-simultaneous *NuSTAR* and *XMM-Newton* data

Fitted Data	NGC 424		NGC 1320		IC 2560	
	NuSTAR+ *Swift*/XRT	*NuSTAR*+ *XMM-Newton* [a]	*NuSTAR*+ *Swift*/XRT	*NuSTAR*+ *XMM-Newton* [a]	*NuSTAR*	*NuSTAR*+ *XMM-Newton* [a]
χ^2/ν	59 / 61	152 / 147	137 / 121	135 / 119	22 / 29	47 / 54
Γ (`pexrav`) [b]	1.71 ± 0.09	1.66 ± 0.09	1.3 ± 0.1	1.3 ± 0.1	$2.2^{+0.3}_{-0.4}$	$2.2^{+0.1}_{-0.2}$
$EW_{\mathrm{Fe\ K}\alpha}$ / keV	1.0 ± 0.3	$1.07^{+0.13}_{-0.09}$ [c]	$0.7^{+1.7}_{-0.5}$	$1.1^{+0.9}_{-0.4}$	$2.1^{+1.3}_{-0.5}$	$2.5^{+0.6}_{-0.4}$
$EW_{\mathrm{Fe\ K}\beta}$ / keV	$0.4^{+0.3}_{-0.2}$	0.13 ± 0.04	0.5 ± 0.3	$0.6^{+0.6}_{-0.4}$	0.8 ± 0.6	0.7 ± 0.3
$EW_{\mathrm{Ni\ K}\alpha}$ / keV	—	0.16 ± 0.06	—	—	—	—
$EW_{\mathrm{ion.Fe}}$ / keV	—	0.05 ± 0.02, $0.10^{+0.05}_{-0.04}$	0.3 ± 0.2	0.2 ± 0.1	—	—
$E_{\mathrm{ion.Fe}}$ / keV	—	6.65 (f), 6.93 (f)	$6.57^{+0.16}_{-0.08}$	$6.54^{+0.10}_{-0.09}$	—	—
C (FPMB/FPMA)	1.1 ± 0.1	1.1 ± 0.1	0.93 ± 0.07	0.9 ± 0.1	1.1 ± 0.2	$1.1^{+0.1}_{-0.2}$
C (SOFT/FPMA)	1.4 ± 0.4	1.1 ± 0.1	1.1 ± 0.3	0.8 ± 0.1	—	$0.9^{+0.2}_{-0.1}$

Notes: Uncertainties listed here are 90 % confidence intervals, and (f) marks fixed parameters.

[a] EPIC/pn data for NGC 424, and NGC 1320, MOS1/2 data for IC 2560, used only above 3 keV.

[b] Set to produce only the reflection continuum (i.e. no contribution from the intrinsic power law continuum).

[c] Iron Kα line width was determined by fitting, $\sigma = 0.09 \pm 0.01$ keV.

Table 3.4: Summary of model parameters for the `MYtorus`-based face-on reflection model fitted to the quasi-simultaneous *NuSTAR* and *Swift*/XRT data, and non-simultaneous *NuSTAR* and *XMM-Newton* data

Fitted Data	NGC 424		NGC 1320		IC 2560	
	NuSTAR+ *Swift*/XRT	*NuSTAR*+ *XMM-Newton* [a]	*NuSTAR*+ *Swift*/XRT	*NuSTAR*+ *XMM-Newton* [a]	*NuSTAR*	*NuSTAR*+ *XMM-Newton* [a]
χ^2/ν	61 / 60	153 / 148 [b]	135 / 121	143 / 118	25 / 30	65 / 55
Γ (`MYtorus`)	$2.28^{+0.03}_{-0.09}$	$2.07^{+0.11}_{-0.09}$	1.7 ± 0.2	1.6 ± 0.2	2.55 (f)	2.55 (f)
$N_{\rm H,R}$ / (10^{24} cm^{-2}) [c]	10^{+u}_{-5}	3 ± 1	4^{+4}_{-2}	4^{+2}_{-1}	10^{+u}_{-3}	10^{+u}_{-3}
line norm. (`K`) [d]	0.7 ± 0.2	$0.68^{+0.09}_{-0.07}$	$1.2^{+0.3}_{-0.4}$	1.6 ± 0.2	$2.2^{+0.7}_{-0.5}$	2.1 ± 0.3
$EW_{\rm Ni\ K\alpha}$ / keV	0.5 ± 0.4	0.04 ± 0.01	—	—	—	—
$EW_{\rm ion.Fe}$ / keV	—	0.04 ± 0.02, 0.05 ± 0.03	0.3 ± 0.2	$0.3^{+0.1}_{-0.2}$	—	—
$E_{\rm ion.Fe}$ / keV	—	6.65 (f), 6.93 (f)	6.6 ± 0.1	$6.77^{+0.06}_{-0.23}$	—	—
`C` (FPMB/FPMA)	1.1 ± 0.1	1.1 ± 0.1	0.93 ± 0.08	0.93 ± 0.07	1.1 ± 0.2	1.1 ± 0.2
`C` (SOFT/FPMA)	1.4 ± 0.4	1.1 ± 0.1	$0.9^{+0.4}_{-0.3}$	0.8 ± 0.1	—	1.0 ± 0.2

Notes: Uncertainties listed here are 90 % confidence intervals, and (f) marks fixed parameters.

[a] EPIC/pn data for NGC 424 and NGC 1320, MOS1/2 data for IC 2560, used only above 3 keV.

[b] In this fit the line component is Gaussian-smoothed with $\sigma = 0.06 \pm 0.01$ keV.

[c] Hydrogen column density of the material producing the reflection spectrum. Values with uncertainty marked with $+u$ denote 90 % confidence upper limits in excess of 10^{25} cm^{-2}, which is outside of the domain of the `MYtorus` model.

[d] Relative normalization of the emission lines component with respect to its corresponding reflection continuum.

3.4 Discussion

3.4.1 Comparison with Previously Published X-ray Spectral Analyses

The earliest X-ray spectrum of NGC 424 came from an *ASCA* observation, which revealed a prominent iron line and a hard spectrum suggestive of Compton-thick reflection of the nuclear continuum (Collinge & Brandt, 2000). This result has been confirmed in later observations, by *BeppoSAX*, *Chandra* and *XMM-Newton* (Iwasawa et al., 2001; Matt et al., 2003a). The soft X-ray spectrum has most recently been analysed in depth by Marinucci et al. (2011), using a long ∼100-ks *XMM-Newton* observation. The focus of that work was on detailed modeling of the physical state of the plasma dominating below 2 keV, but the data were also used to model the X-ray continuum and line emission up to 10 keV. In agreement with earlier results, they found support for a strong reflection component and a heavily absorbed power-law continuum obscured by nearly Compton-thick material with $N_{\rm H,A} = 1.1 \times 10^{24}\,{\rm cm}^{-2}$ contributing only above 5 keV.

With the hard X-ray coverage of *BeppoSAX* (Iwasawa et al., 2001) it was possible to infer that the intrinsic power-law continuum is absorbed by a column density of $\gtrsim 2 \times 10^{24}\,{\rm cm}^{-2}$. Note, however, that only the simple approximate models were used in the spectral analyses leading to the inference of the column density, and that they required assuming a photon index ($\Gamma = 2$), since it was not possible to constrain it directly from the data. Using the simultaneous *Swift*/XRT and *NuSTAR* data, we firmly establish that the hard X-ray spectrum of NGC 424 can be described as being dominated by reflection. A contribution from a heavily absorbed component cannot be completely ruled out, but it is not formally required by any of the data considered in this work.

Burlon et al. (2011) analyzed the first three years of *Swift*/BAT data on NGC 424 and modeled it simply as a heavily absorbed power law with $N_{\rm H,A} = (2.0^{+0.3}_{-0.4}) \times 10^{24}\,{\rm cm}^{-2}$ and $\Gamma = 1.9 \pm 0.3$. Since that model does not include any contribution from a reflection component, it is not directly comparable to our results. The *Swift*/BAT spectrum from the 70-month survey (Baumgartner et al., 2013) is entirely consistent with the *NuSTAR* and *XMM* data ($\chi^2/\nu = 153/153$; see Figure 3.6) for a cross-normalization constant of 1.5 ± 0.3 relative to *NuSTAR*/FPMA. We also verify that our models are consistent with the *BeppoSAX*data from Iwasawa et al. (2001). With the photon index fixed at its best-fit value for that model, $\Gamma = 1.68$, we find that the cutoff energy is $E_{\rm cut} = 120^{+50}_{-30}$ keV. A slightly higher cut-off energy, $E_{\rm cut} = 190^{+260}_{-80}$ keV, is inferred from the equivalent fit using the *Swift*/XRT instead

of the *XMM* data.

The 14–195 keV luminosity published in the 70-month *Swift*/BAT catalog (6.5×10^{42} erg s^{-1}) is calculated by assuming a relatively flat $\Gamma \approx 2$ spectrum; if we use our model instead, the 14–195 keV luminosity based on *Swift*/BAT data alone is 5.5×10^{42} erg s^{-1}. The apparently significant normalization offset and its uncertainty are likely due to the limited statistics and long-term averaging of the *Swift*/BAT data, in addition to simple flux calibration differences. In the rest of the discussion we assume $\sim$ 30 % lower luminosity as inferred from the *NuSTAR* data, as listed in Table 3.5.

No dedicated long X-ray observations of NGC 1320 exist in the literature: the only previously available soft X-ray data was taken with *XMM-Newton* as part of a recent survey of infrared-bright AGN (Brightman & Nandra, 2011a). The original modeling by those authors and later re-analyses (e.g., Georgantopoulos et al. 2011; Severgnini et al. 2012; Marinucci et al. 2012) agree that the nucleus of NGC 1320 is heavily obscured ($N_{\rm H,A} \gtrsim 1 \times 10^{24}$ cm^{-2}), and infer the presence of a considerable reflection component on the basis of a strong iron line with an equivalent width of $\simeq$1 keV. Gilli et al. (2010) assert that both reflected and transmitted components contribute to the spectrum, but provide very few details on the modeling as the model parameters are largely unconstrained by the data.

Our analysis of NGC 1320 (which includes the same *XMM* data in addition to the *NuSTAR* data) confirms most of the earlier results and solidifies the dominance of the reflection spectrum above 2 keV. A transmitted component is not formally required by our data. A hard X-ray source was detected by *Swift*/BAT at the coordinates of NGC 1320, but the low significance of that detection does not provide any additional spectral constraints (Cusumano et al., 2010). The published 15–150 keV luminosity, 2.8×10^{42} erg s^{-1} (observed, uncorrected for absorption), agrees well with the luminosity calculated from our spectral model in the slightly wider 14–195 keV band (Table 3.5).

Prior X-ray observations of IC 2560 have been performed by *ASCA* (Risaliti et al., 1999), *Chandra* (Iwasawa et al., 2002; Madejski et al., 2006) and *XMM-Newton* (Tilak et al., 2008). The earliest observation already showed that the source was likely Compton-thick, with a very strong iron line indicating the presence of a reflection component. More sensitive observations with *Chandra* and later *XMM* confirmed that the 2–10 keV spectrum can be well described as a cold neutral reflection from a Compton-thick medium, including a particularly strong iron line

with an equivalent width in excess of 2 keV.

The lack of a heavily absorbed intrinsic continuum component in all observations has been explained by invoking Compton-thick nuclear obscuration. The most stringent constraint on the absorption column density is provided by a 80-ks *XMM* observation: $N_{\rm H,A} > 3 \times 10^{24}\,{\rm cm}^{-2}$ (Tilak et al., 2008). This source is very faint at hard X-ray energies, as confirmed by our *NuSTAR* data, and has never previously been detected by any hard X-ray instrument above 10 keV. This is partly due to the heavy obscuration, but possibly also due to the atypically steep intrinsic photon index ($\Gamma > 2.2$) suggested by our modeling. Owing to the lack of high-energy coverage, previous studies could not constrain the photon index. The lack of detection of a heavily absorbed transmitted component in the *NuSTAR* band satisfies all previous lower limits on the line-of-sight column density, and pushes it further toward the $\sim 10^{25}\,{\rm cm}^{-2}$ regime.

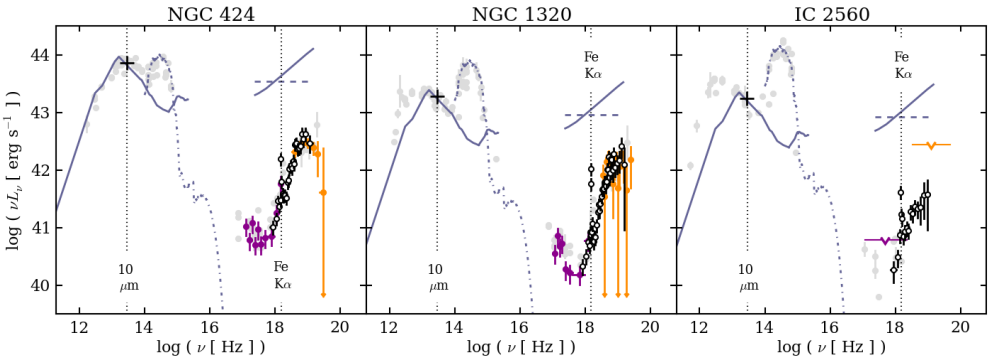

Figure 3.6: Observed SEDs of NGC 424 (left), NGC 1320 (middle), and IC 2560 (right panel) constructed using archival data (grey points) acquired using the ASDC SED Tool. The minor vertical spread in the data in the optical and infrared, only reflects the fact that different finite apertures had been used for photometry in different publicly available catalogs. The black crosses mark the luminosities at 10 μm, considered as representative mid-infrared luminosities ($L_{\rm MIR}$) in this work. The frequency of the prominent neutral Fe Kα line at 6.4 keV is marked in all panels. We show an Sa/b galaxy template with a dark grey line as a proxy for the host galaxy SED. The *Swift* spectra are shown in magenta and orange symbols for the XRT and the BAT instruments, respectively. For IC 2560 only upper limits are available (marked with empty downward arrows; see text for details). The errorbars on some *Swift*/BAT bins extend below the the y-axis limit, and are marked with small filled downward arrows. The *NuSTAR* data are plotted in black.

3.4.2 Multi-wavelength Data and Spectral Energy Distributions

All three of our sources have been previously observed in a wide range of spectral bands. We use publicly available archival data from the ASDC SED Tool[8] to construct the rough spectral energy distributions shown in Figure 3.6. Note that the distance uncertainties translate into a systematic uncertainty of approximately 0.1 dex in the vertical direction. As it is not important for our work, we do not concern ourselves with the various aperture diameters allowing differing levels of host stellar contamination in the optical and near-infrared photometry. We filter out small-aperture measurements, and those with large and unspecified uncertainties.

All three galaxies are morphologically classified to be at a transition between S0 and Sa/b type (see Table 3.1). The starlight dominates the optical output (the nuclei are heavily extincted in the optical), but most of the mid-infrared luminosity can be ascribed to the AGN (as thermal radiation from the torus), since there are no indications of significant starburst activity in any of the sources. By averaging over the wealth of mid-infrared data available for each of the sources, we estimate their mid-infrared luminosities ($L_{\rm MIR} = \nu L_\nu$ at $\sim$10 μm) to be 7×10^{43} erg s^{-1} for NGC 424 and 2×10^{43} erg s^{-1} for both NGC 1320 and IC 2560 (see Table 3.5). These values are expected to be different by no more than a factor of $\sim$2 from the luminosities in any of the mid-infrared bands between 5 and 25 μm commonly used in the literature, which is acceptable for the purposes of our order-of-magnitude calculations in § 3.4.3.

The quasi-simultaneous *Swift* and *NuSTAR* data for all sources are plotted together with the multi-wavelength archival data in Figure 3.6. The short 2-ks *Swift*/XRT observation of IC 2560 did not provide useful data for spectral modeling, so we show only the 3σ upper limit on the 0.3–10 keV flux of $\sim 2 \times 10^{-13}$ erg s^{-1} cm^{-2}. This corresponds to the luminosity upper limit plotted as a downward arrow in the soft X-ray range of Figure 3.6 (rightmost panel). The *Swift*/XRT and *NuSTAR* data for NGC 424 and NGC 1320, as well as the *NuSTAR* data for IC 2560, were unfolded in `Xspec` using their respective best-fit models. The same models were used to unfold the *Swift*/BAT spectra, since they fit those data well. The highest-quality *Swift*/BAT spectrum of NGC 424 was taken from the 70-month catalog (Baumgartner et al., 2013). The NGC 1320 data is only available as a part of the 54-month catalog (Cusumano et al., 2010), since it is undetected in the 70-month catalog due to low statistics and different methodology.

[8] `http://tools.asdc.asi.it/SED/`

IC 2560 is not listed in any of the published *Swift*/BAT source catalogs. The detection threshold of the 70-month catalog at 5σ can be calculated from Equation (9) in Baumgartner et al. (2013) using an estimate of the exposure time in the part of the sky surrounding IC 2560. Based on their Figure 1, we estimate the exposure time to be approximately 12 Ms, implying sensitivity of 9×10^{-12} erg s^{-1} cm^{-2} in the 14–195 keV band. This upper limit is displayed as an orange downward arrow in Figure 3.6. The highest-energy *NuSTAR* data points are almost an order of magnitude below this limit.

All three sources are relatively faint in the radio, with none of their radio luminosities ($L_{\rm rad} = \nu L_\nu$, for $\nu = 5$ GHz) exceeding 2×10^{38} erg s^{-1}, based on archival flux densities (see Table 3.5). Terashima & Wilson (2003) defined that radio-loud AGN have $R_{\rm X} > -4.5$, where $R_{\rm X} = \log(L_{\rm rad}/L_{\rm X})$, $L_{\rm rad}$ is as defined above, and $L_{\rm X}$ is the intrinsic 2–10 keV luminosity. Despite the latter being uncertain due to obscuration, as we elaborate in the following section, all three AGN may at best straddle the dividing line between the radio-quiet and radio-loud objects, but they are not strong radio sources. Using the empirical relations of Bell (2003) to convert the radio luminosity into star formation rate, we find $\sim 1\, M_\odot\, {\rm yr}^{-1}$ in each case. The radio luminosity is thus consistent with being due to star formation typical for the S0–Sa/b morphology of the host galaxies (Bendo et al., 2002).

Table 3.5: Estimated luminosities of the targets in different spectral bands

Spectral Band	NGC 424	NGC 1320	IC 2560
14–195 keV [a]	36	27	5.0
15–55 keV [a]	23	14	3.6
2–10 keV [a]	2.5	0.90	0.80
[O III] λ5007 [b]	1.7	0.20	0.25
MIR (10 μm) [b]	710	190	170
5 GHz [c]	0.0018	0.0003	0.0016

Notes: Luminosities are given in units of 10^{41} erg s^{-1}. All values refer to observed luminosities, i.e., they are not corrected for absorption or reddening.

[a] Calculated from our best-fit models. Typical statistical uncertainty is $\lesssim 20\,\%$.

[b] Average value based on published measurements in Murayama et al. (1998), Gu et al. (2006), LaMassa et al. (2010), and Kraemer et al. (2011). Overall uncertainties in absolute values are estimated to be about a factor of two.

[c] Calculated from NVSS flux density at 1.4 GHz (Condon et al., 1998), assuming a $f_\nu \propto \nu^{-0.7}$ spectrum.

3.4.3 Intrinsic X-ray Luminosities

The three AGN considered in this work are all heavily obscured, as previously suggested by their relatively faint soft X-ray spectra with strong fluorescent iron lines, and strong mid-infrared and [O III] emission (e.g., Risaliti et al. 1999; Collinge & Brandt 2000; Brightman & Nandra 2011b). The *NuSTAR* data presented here confirm that their intrinsic continua are heavily suppressed by obscuration and thus not directly observable. For a column density of the order of 10^{24} cm^{-2} (and particular obscuring material geometry) the intrinsic X-ray continua would significantly contribute to the flux in the *NuSTAR* 3–79 keV band despite the heavy obscuration. However, our modeling suggests that the hard X-ray spectra of NGC 424, NGC 1320 and IC 2560 are dominated by a reflected component in each case, indicating that along the line of sight towards those nuclei the absorption column is well above the Compton-thick threshold at 1.4×10^{24} cm^{-2} and likely in the 10^{25} cm^{-2} regime.

Without a direct constraint on the transmission of the intrinsic continuum along the line of sight, we can only indirectly infer the intrinsic X-ray luminosity through other SED components. NGC 1320 and IC 2560 have very similar mid-infrared, [O III] and 2–10 keV luminosities (see Table 3.5). We note that star formation may be contributing a part of the luminosity in these bands, but we ignore it in the simple estimates performed here. In comparison with empirical correlations from the literature, we find that without any correction for absorption NGC 1320 and IC 2560 fall at least an order of magnitude below the distribution of intrinsic $L_{2\text{-}10\,\mathrm{keV}}/L_{\mathrm{MIR}}$ and $L_{2\text{-}10\,\mathrm{keV}}/L_{[\mathrm{O\,III}]}$ ratios. For example, for NGC 1320 (IC 2560) $\log(L_{2\text{-}10\,\mathrm{keV}}/L_{\mathrm{MIR}}) = -2.3$ (-2.4) compared to -0.63 ± 0.69 (Lutz et al., 2004), and $\log(L_{2\text{-}10\,\mathrm{keV}}/L_{[\mathrm{O\,III}]}) = 0.6$ (0.5) compared to 1.76 ± 0.38 (Mulchaey et al., 1994). The quoted median log-ratios and their standard deviations were derived empirically from sample studies of nearby Seyfert 2 nuclei. Simply assuming that these intrinsic ratios hold for our AGN leads to a conservative lower limit on the intrinsic 2–10 keV luminosity of $> 2 \times 10^{42}$ erg s^{-1}.

In the case of obscuration by a column density of $\lesssim 1.4 \times 10^{24}$ cm^{-2} the transmitted continuum in the 2–10 keV band is $\sim$10 % of the intrinsic flux (e.g., Burlon et al. 2011), but in order for the reflection to dominate the X-ray spectrum, a suppression by a factor of $\sim$100 is typically needed (e.g., Matt et al. 2004). We therefore assume that the intrinsic 2–10 keV luminosity of both sources is roughly a factor of 100 greater than the observed one, estimating it at $\lesssim 1 \times 10^{43}$ erg s^{-1}. With this luminosity and the mid-infrared luminosities of almost 2×10^{43} erg s^{-1}, NGC 1320 and IC 2560 fall right onto the tight relation between $L_{2\text{-}10\,\mathrm{keV}}$ and L_{MIR} from Gandhi et al. (2009), where both quantities are intrinsic (i.e. the infrared luminosity directly measures the torus emission) and the relation is directly applicable to heavily obscured AGN. For comparison, Tilak et al. (2008) derive $\sim 6 \times 10^{42}$ erg s^{-1} from the mid-infrared luminosity of IC 2560, however, they also arrive at an order of magnitude lower estimate based on the [O III] luminosity[9]. For NGC 1320 Brightman & Nandra (2011a) derive an intrinsic 2–10 keV luminosity of 5×10^{42} erg s^{-1}. Our best estimate is therefore 7×10^{42} erg s^{-1} for both sources, with an uncertainty of about a factor of 2. In Figure 3.7 we show the observed and intrinsic 2–10 keV luminosities in the context of empirical correlations between $L_{2\text{-}10\,\mathrm{keV}}$ and L_{MIR} (Lutz et al., 2004; Fiore et al., 2009; Gandhi et al., 2009).

[9]Note that earlier estimates of the intrinsic luminosity (Ishihara et al., 2001; Iwasawa et al., 2002; Madejski et al., 2006) generally yielded lower values, which is partly due to significantly lower assumed distance to IC 2560: 26 Mpc, compared to 41.4 Mpc used in this work.

One notable difference between NGC 1320 and IC 2560 is that the latter is significantly less luminous in the hard X-ray bands, likely due to the much steeper intrinsic continuum suggested by our best-fit reflection model. Partly because of the obscuration so high that even the hard X-ray continuum is substantially suppressed and partly due to the steepness of the continuum, IC 2560 deviates significantly from the empirically determined distribution of observed luminosity ratios for Seyfert 2 nuclei with hard X-ray fluxes from *Swift*/BAT. For example, LaMassa et al. (2010) find[10] $\log(L_{14\text{-}195\,\mathrm{keV}}/L_{\mathrm{MIR}}) = -0.8 \pm 0.3$ and $\log(L_{14\text{-}195\,\mathrm{keV}}/L_{[\mathrm{O\,III}]}) = 2.7 \pm 0.6$, compared to -1.6 and 1.3 for IC 2560, respectively. NGC 424 and NGC 1320 deviate from those distributions by no more than 1.5 standard deviations, except for the case of $L_{14\text{-}195\,\mathrm{keV}}/L_{[\mathrm{O\,III}]}$ for NGC 424. Again, this may be due to the photon index being steeper than the population mean, though it may also be related to the unusual optical spectrum of NGC 424, which shows features of both type 1 and type 2 AGN (see Table 3.1 and § 3.4.4).

NGC 424 is the most luminous of the three AGN in our sample. One of the spectral models that fully accounts for the features in its joint *XMM-Newton* and *NuSTAR* spectrum is a two-component `MYtorus` model consisting of an absorbed power law in addition to the reflected component. However, simple consideration of energetics essentially rules out the possibility that the absorbed power law represents the intrinsic continuum observed directly, absorbed along the line of sight to the nucleus. In the broad 14–195 keV band the de-absorbed intrinsic continuum luminosity is less than half of the reflected component luminosity ($1.3 \times 10^{42}\,\mathrm{erg\,s^{-1}}$ compared to $2.9 \times 10^{42}\,\mathrm{erg\,s^{-1}}$).Such a continuum simply cannot provide sufficient photon flux to produce the observed spectrum. Furthermore, the infrared data, the internal normalization of the `MYtorus` model components, and a comparison to similar obscured AGN from the literature (e.g., Matt et al. 2004; Burlon et al. 2011; Yaqoob 2012; Arévalo et al. 2014) suggest that the intrinsic continuum should be nearly two orders of magnitude stronger in order to produce the observed reflected emission. This absorbed power law component could be well explained in a scenario in which the absorbed continuum comes from optically thin Thomson scattering of the nuclear continuum by free electrons, seen through an off-nuclear "window" of lower column density than that of the predominantly Compton-thick material. Such a scattered component is expected to contain ∼1–10 % of the power of the intrinsic continuum (e.g., Moran et al. 2000), which agrees well with our model.

[10]No standard deviation was given, so we roughly estimate it based on standard deviations of other similar samples.

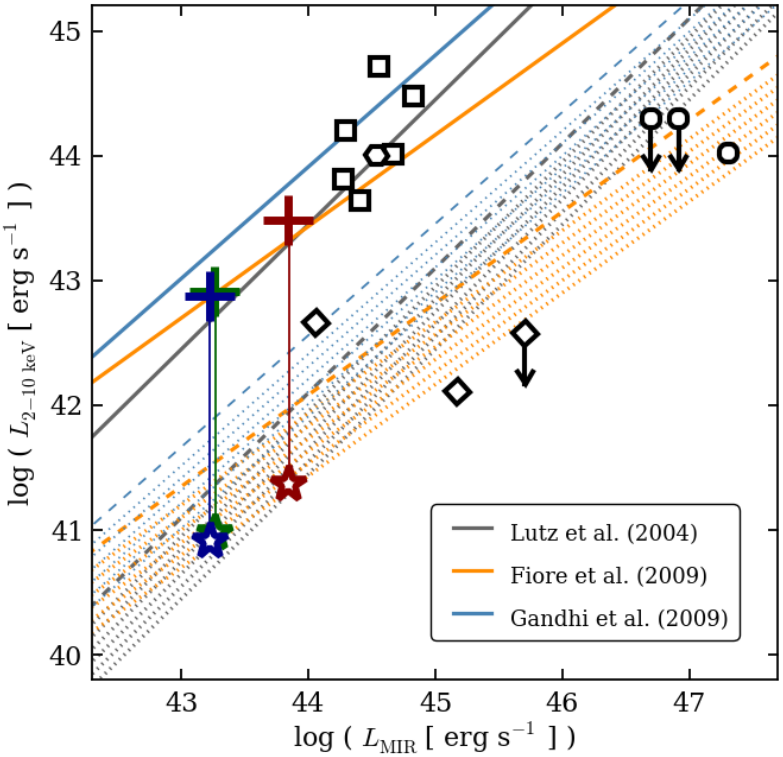

Figure 3.7: The solid lines show empirical $L_{2\text{-}10\,\mathrm{keV}} - L_{\mathrm{MIR}}$ correlations from the literature: Lutz et al. (2004) in dark grey, Fiore et al. (2009) in yellow, and Gandhi et al. (2009) in light blue. With dashed lines we show the same relations for sources absorbed by a column density $N_{\mathrm{H,A}} = 1.4 \times 10^{24}$ cm^{-2}, i.e. for borderline Compton-thick absorption. The dotted lines mark regions occupied by reflection-dominated sources (i.e., the absorbed continuum component is not observable at all below 10 keV) with reflection efficiency between 1 and 3 %, calculated from the `MYtorus` model. NGC 424, NGC 1320, and IC 2560 are plotted in dark red, green and blue, respectively. Their observed 2–10 keV luminosities are marked with star symbols, while the crosses show the adopted intrinsic values (with their size approximating the uncertainty). Overplotted in empty black symbols we show other AGN observed with *NuSTAR* in the extragalactic surveys program: serendipitously discovered non-beamed AGN from Alexander et al. (2013) with squares, SDSS-selected obscured quasars from Lansbury et al. (2014) with diamonds, WISE-selected ultra-lumninous $z = 2$ quasars from Stern et al. (2014) with circles, and a $z = 2$ quasar identified in the ECDFS field from Del Moro et al. (2014) with a hexagon.

The hypothesis that the intrinsic power law continuum is significantly stronger than what the absorbed power law component of `MYtorus` would imply is fully consistent with multi-wavelength properties of NGC 424 and its mid-infrared and [O III] luminosities in particular. In comparison with the published distributions for Seyfert 2 AGN samples, $\log(L_{2\text{-}10\,\mathrm{keV}}/L_{\mathrm{MIR}}) = -2.4$ and $\log(L_{2\text{-}10\,\mathrm{keV}}/L_{[\mathrm{O\,III}]}) = 0.2$ make NGC 424 a severe outlier and suggest that it would take a boost of nearly two orders of magnitude from the observed luminosity to make its properties typical for a Seyfert 2 nucleus. We therefore estimate that the intrinsic 2–10 keV luminosity of NGC 424 is $\gtrsim 2 \times 10^{43}\,\mathrm{erg\,s^{-1}}$. Based only on data below 10 keV, Marinucci et al. (2011) infer a somewhat lower luminosity of $4 \times 10^{42}\,\mathrm{erg\,s^{-1}}$. Using broad-band data from *ASCA* and *BeppoSAX* (0.6–100 keV) Iwasawa et al. (2001) argued that under reasonable assumptions on geometry the intrinsic 2–10 keV luminosity could be as high as $2 \times 10^{43}\,\mathrm{erg\,s^{-1}}$. With that luminosity NGC 424 would closely match the intrinsic relation between $L_{2\text{-}10\,\mathrm{keV}}$ and L_{MIR} from Lutz et al. (2004), Fiore et al. (2009) and Gandhi et al. (2009); see Figure 3.7.

The adopted intrinsic luminosities may be converted to bolometric ones using empirical calibrations (e.g., Marconi et al. 2004; Lusso et al. 2012). We estimate the bolometric correction factors for both the mid-IR and 2–10 keV bands to be 10–20, not including the considerable intrinsic uncertainty of a factor ≃3. The bolometric luminosity is then $\sim 7 \times 10^{44}\,\mathrm{erg\,s^{-1}}$ for NGC 424 and $\sim 2 \times 10^{44}\,\mathrm{erg\,s^{-1}}$ for NGC 1320, and IC 2560. Combined with the measured masses of the SMBH harbored by the AGN we can estimate their Eddington fraction, $L_{\mathrm{bol}}/L_{\mathrm{Edd}}$, where L_{bol} is the bolometric luminosity and L_{Edd} is the Eddington luminosity. The mass of the SMBH in IC 2560 has been measured dynamically using the water megamasers (Ishihara et al., 2001), while for NGC 424 and NGC 1320 it was infered from measurements of stellar velocity dispersion via the M_{SMBH}–σ_* relation (Bian & Gu, 2007). Using those values we infer Eddington fractions of ∼5 % for NGC 424 ($M_{\mathrm{SMBH}} = 6.0 \times 10^7\,M_\odot$) and NGC 1320 ($M_{\mathrm{SMBH}} = 1.5 \times 10^7\,M_\odot$), and ∼30 % for IC 2560 ($M_{\mathrm{SMBH}} = 2.9 \times 10^6\,M_\odot$). The uncertainties on these values are likely up to a factor of 5, but it is encouraging that the quantities are consistent with empirical correlations observed in large AGN samples (e.g., Vasudevan & Fabian 2009; Lusso et al. 2012). We also find that the AGN with the highest Eddington fraction, IC 2560, has the steepest photon index, in accordance with the statistical relation found by Brightman et al. (2013) and consistent with the spread observed for individual sources in their sample.

3.4.4 Constraints on the Geometry of the Obscuring Material

By modeling the hard X-ray spectra of NGC 424, NGC 1320, and IC 2560 we have unambigously confirmed that the dominant component in their hard X-ray spectra is a reflection of the nuclear continuum from distant, cold material. Although minor contributions from heavily absorbed intrinsic continua (at the $\lesssim$10 % level) cannot be completely ruled out with the data from short *NuSTAR* exposures presented here, it is clear that the sources are reflection-dominated; their nuclear regions therefore must be heavily obscured by Compton-thick material. The type of reflection spectrum that fits all of the data best is the "face-on" component of the `MYtorus` model, which can be envisioned as the component that remains when the observer looks down the axis of symmetry of the torus, but with the central region, from where the intrinsic continuum is emitted, blocked by a completely opaque patch. According to Yaqoob (2012), this component closely approximates the spectrum one would observe in the case of a uniform Compton-thick torus being tilted towards the observer just enough for the far side of the torus to be visible in reflected light, but not enough to allow the nuclear continuum to be observable over the closer edge of the torus (e.g. Matt et al. 2003b).

Although the inclination limits for the situation described above depend on the scale height of the gas and dust distribution, one can argue that if the obscuring material really does reside in a toroidal structure, its orientation with respect to the observer would need to be close to edge-on. This orientation is indeed plausible given that water megamaser emission has been observed in two out of three targets (Braatz et al., 1996; Ishihara et al., 2001; Kondratko, 2007; Zhang et al., 2010), with IC 2560 being well established as a classical disk megamaser (see, e.g., Tilak et al. 2008 for a discussion of the possible disk/torus and masing clouds' geometry). It is worth noting that the type of reflection spectrum that fits the *NuSTAR* data (both "face-on" `MYtorus` and `pexrav` models) is more characteristic of surface scattering than scattering through dense material, which argues towards a tilted edge-on and possibly clumpy torus scenario, rather than complete enclosure in a spherical distribution of material. The `MYtorus` model used here is uniform, has sharp edges and a fixed covering fraction of $1/2$. These are approximations made in order to simplify the model calculation – astrophysical tori are likely neither uniform, nor have an outer solid surface. For those reasons, a blind application of the literal torus in which one would fit for all free parameters of the model (especially inclination) may not be reasonable or even recommended (Yaqoob, 2012).

From the multi-wavelength data presented in § 3.4.3 we infer a reflection efficiency in the 2–10 keV band of the order of 1 %, broadly consistent with any torus orientation (Ghisellini et al., 1994). In order to achieve the observed reflection dominance, the material surrounding the source must intercept a relatively large fraction of the nuclear luminosity (i.e., large covering fraction), while the side of the torus closer to the observer covers the direct line of sight with only a small global covering fraction – letting the bulk of the backside reflection spectrum pass through unimpeded. A compelling physical scenario may be that of a clumpy torus (Nenkova et al., 2008b; Elitzur, 2012). In that case the central source would be surrounded by a large number of individual high-column-density clouds with a large global covering factor, but also plenty of essentially clear lines of sight for their reflection spectra to reach the observer. In the clumpy torus picture the complete extinction of the intrinsic continuum along the line of sight to the nucleus could be explained by a large inclination angle and larger density of clouds in the equatorial plane of the system, which is again consistent with the observations of megamasers.

Torus clumpiness also offers a natural explanation for the weak absorbed power law component required to model the NGC 424 spectrum: along some off-nuclear lines of sight there could be openings with relatively low column density ($\sim 10^{23-24}$ cm^{-2}, compared to the surrounding $\gtrsim 10^{25}$ cm^{-2}), through which we observe a weak continuum produced by optically thin Thomson scattering of the nuclear continuum on free electrons. Those free electrons are located in, or above, the opening of the torus and scatter the intrinsic continuum and the broad line region photons into our line of sight. This mechanism has already been invoked to explain the weak broad lines (e.g., Hα, Hβ, Fe II) seen in the optical spectrum of NGC 424, which is otherwise typical of a Seyfert 2 AGN (Murayama et al., 1998), and the broad emission lines detected in polarized light (Moran et al., 2000), typical of type 1 AGN with a "hidden" broad-line region. With newer data it is becoming possible to go beyond the simplistic type 1 and type 2 classification and more directly probe the geometry of the obscuring material. We have shown in previous sections that the infrared and the soft X-ray data, and especially the hard X-ray data from *NuSTAR*, unambiguously confirm the heavy obscuration of the central source in NGC 424 regardless of the optical classification.

Using high angular resolution interferometric data, Hönig et al. (2012) find that the dominant contribution to the nuclear mid-infrared flux comes from relatively cold optically-thin dust in a structure elongated in the direction of the torus axis of

symmetry (as determined from the spectropolarimetric data of Moran et al. 2000). This observation suggests an interesting dust distribution in which optically thin clouds line the torus opening and possibly reach out to the narrow-line region (see Figure 9 in Hönig et al. 2012). There is a possibility that a fraction of the optically thick clumps that predominantly reside in the torus get entrained in a wind together with the optically thin clouds that dominate the mid-infrared output; this is broadly consistent with our spectral modeling (i.e., symmetrically broadened neutral, and Doppler-shifted ionized iron lines; see § 3.3.3).

The example of NGC 424 highlights the importance of modeling the hard X-ray spectra of Compton-thick AGN in synergy between data from different spectral bands in order to probe the unresolved AGN structure. The high degree of similarity with the Circinus Galaxy and NGC 1068 in both the interferometric mid-infrared data (Mason et al., 2006; Reunanen et al., 2010; Hönig et al., 2012) and the hard X-ray spectra from *NuSTAR* (Arévalo et al. 2014; Bauer et al. (2015)) may be indicating that these objects are not merely isolated special cases. Due to the lack of similar data for NGC 1320 and IC 2560, at this point we can only speculate that they may exhibit a similar sort of geometry as NGC 1068, Circinus and NGC 424, which are brighter and have higher-quality broadband data.

Further evidence for clumpiness of the obscuring matter surrounding the nuclei in general can be found in observations of dramatically changing column density in some nearby AGN (e.g., Matt et al. 2003b; Risaliti et al. 2010; Rivers et al. 2011; Walton et al. 2014), as well as the optical classification changes observed in at least a dozen AGN up to date (see, e.g., Shappee et al. 2014). For NGC 424 and IC 2560 no significant variability in absorption has been observed in the literature, but an optically thin scattering medium has been invoked in modeling of their soft X-ray spectra in some observations (Matt et al., 2003a; Tilak et al., 2008). We observe no spectral changes between three epochs of NGC 1320 observations and the data are currently not of sufficient quality to constrain a possible Thomson-scattered continuum component. Hard X-ray variability could in principle be used to further constrain the physical size of the torus (e.g., Mattson & Weaver 2004), which might be possible with future repeated observations. The moderately large sample of nearby heavily obscured AGN currently surveyed with *NuSTAR* will provide the high-quality hard X-ray data needed for such work in the near future.

3.4.5 Broader Context: Identification and Properties of Obscured AGN

The three sources presented here join a relatively small sample of nearby Compton-thick AGN that have been studied spectroscopically in some detail over the broad 0.2–200 keV energy range (e.g., Maiolino et al. 1998; Matt et al. 2000). *NuSTAR* opens up an opportunity to extend our empirical knowledge towards less luminous and more distant Compton-thick AGN, and ultimately understand their properties better. Early results from the *NuSTAR* extragalactic surveys (Alexander et al. 2013, Mullaney et al. 2015, Civano et al. 2015) already include candidate counterparts to these local AGN at higher redshift (e.g., $z \approx 0.5$, Lansbury et al. 2014; $z \approx 2$, Del Moro et al. 2014, Stern et al. 2014). Short ∼20-ks *NuSTAR* observations of obscured luminous quasars at low redshift ($L_{\rm bol} \gtrsim 10^{45}\,{\rm erg\,s^{-1}}$, $z \lesssim 0.2$; Gandhi et al. 2014) may reach sufficient photon statistics to enable modeling similar to that presented here.

However, for most of the high-redshift sources one is limited to using band ratios as indicators of their spectral shape. In Figure 3.8 we show the ratio of counts in the *NuSTAR* 3–8 and 8–24 keV bands for $z > 0$ Compton-thick reflection-dominated AGN ($N_{\rm H,A} > 10^{25}\,{\rm cm^{-2}}$) with X-ray spectra equal to those of the three AGN presented in this chapter. Their tracks cross those of Compton-thin AGN (obscured by $N_{\rm H,A} \sim 10^{23-24}\,{\rm cm^{-2}}$), showing that information beyond the band ratio is needed in order to isolate Compton-thick AGN. The distinction between Compton-thick and Compton-thin obscuration is of key importance in population studies (e.g., the distribution of $N_{\rm H,A}$ in obscured AGN) and understanding of the CXB, since the AGN obscured by $N_{\rm H,A} \lesssim 10^{24}\,{\rm cm^{-2}}$ contribute significantly more hard X-ray radiation per source (Comastri, 2004; Gilli et al., 2007).

A three-band X-ray approach, similar to the one recently proposed by Iwasawa et al. (2012), or Brightman & Nandra (2012), would provide better means of discrimination between the levels of obscuration. However, at low number counts the uncertainties on band ratios in two bands can already be large, and dividing the data into three bands may not be beneficial. The possible confusion outlined in Figure 3.8 is aggravated by the fact that a spread in intrinsic photon indices exists in the population, as demonstrated by the differing photon indices of the three AGN presented here. Compared to the observed distribution of Γ with a mean of 1.9 and an intrinsic width of a 0.3 (e.g. Brightman & Nandra 2011a; Burlon et al. 2011; Ballantyne 2014), the photon indices determined from spectral analysis of the *NuSTAR* data span almost the full observed range, but do not represent extreme sources.

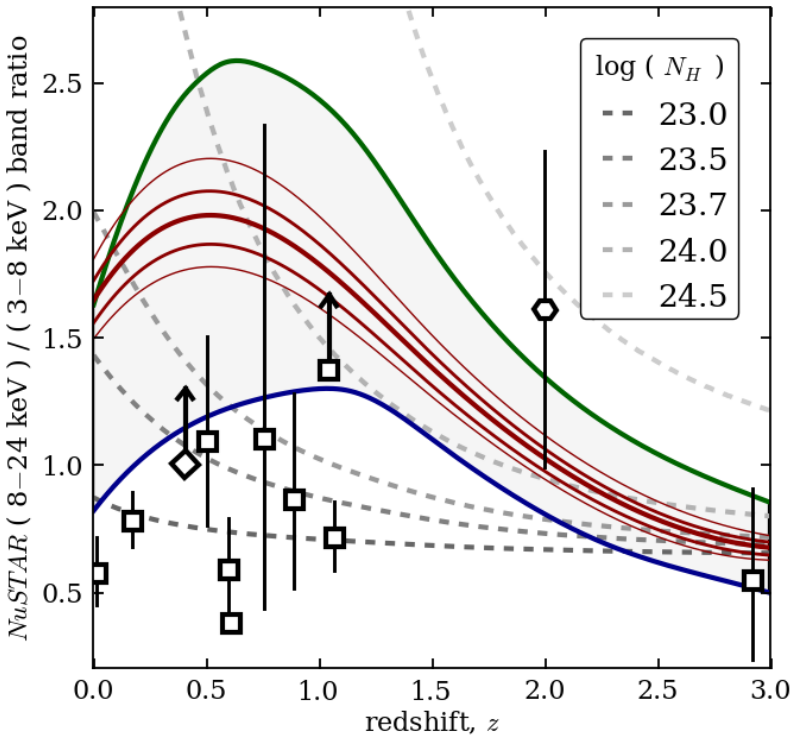

Figure 3.8: Predicted count rate ratio for the *NuSTAR* 3–8 and 8–24 keV bands for some simple models as a function of redshift. The dashed lines in the background show tracks for a simple absorbed power law model (assuming $\Gamma = 1.8$) for a range of column densities along the line of sight to the nucleus. Thick colored lines correspond to tracks of best-fit models for NGC 424 (red), NGC 1320 (green) and IC 2560 (blue). The differences between the three thick colored tracks are mostly due to different intrinsic photon indices; from 1.9 for NGC 1320 to 2.55 for IC 2560 (2.3 for NGC 424). With thinner red lines we show the effect of changing the intrinsic photon index of NGC 424 by 0.05 and 0.1 in either direction. Overplotted are data for the first 10 detected *NuSTAR* serendipitous sources (squares, from Alexander et al. 2013) and a lower limit for a heavily obscured SDSS quasar (diamond) presented in (Lansbury et al., 2014). Any source with a low count rate and a band ratio within the shaded grey area (or higher) may be considered a Compton-thick AGN candidate. However, the obscuration would need to be inferred from the mid-infrared, or other multi-wavelength data.

The constant difference of approximately 0.4 between photon indices determined using the `pexrav` models and those determined using `MYtorus` can be understood as arising from the different geometries and parameters assumed; we explore those differences in detail in Brightman et al. (2015). As obscured AGN studies expand to higher redshifts and lower luminosities, the variance of different systems will only increase, which further motivates establishing good spectral templates based on nearby objects such as the ones presented here.

The typically low signal-to-noise ratio of sources identified in the blank-field *NuSTAR* surveys makes it difficult to distinguish different AGN types based only on band ratios and it is therefore crucial to consider multi-wavelength data. For example, any source found to occupy the grey area in Figure 3.8 has a spectral slope consistent with a heavily Compton-thick AGN, but only those with an extreme $L_{2\text{-}10\,\mathrm{keV}}/L_{\mathrm{MIR}}$ (as discussed in § 3.4.3) should be considered true candidates. A similar concept of Compton-thick AGN selection was employed by Severgnini et al. (2012). Many other studies of empirical multi-wavelength correlations and indirect obscuration indicators have been conducted in the past (e.g., Mulchaey et al. 1994; Lutz et al. 2004; Alexander et al. 2008; Fiore et al. 2009; LaMassa et al. 2010; Zhang et al. 2010; Georgantopoulos et al. 2011; Goulding et al. 2011; Iwasawa et al. 2012), directly or indirectly leading towards better selection criteria. With our small sample of three, we can identify the megamaser-biased selection of Compton-thick AGN in Zhang et al. (2010) as potentially inadequate, as none of our sources (despite two of them hosting water megamasers), would be classified as Compton-thick based on their multi-wavelength selection criteria. Perhaps owing to the similarity and simplicity of their spectra, all three sources generally pass the selection criteria proposed in the literature.

In this chapter we used the empirical correlations, mainly between $L_{2\text{-}10\,\mathrm{keV}}$ and L_{MIR}, in two ways: (i) assuming they hold for our sources, we infer that the intrinsic 2–10 keV luminosity has been suppressed by a factor of $\sim$100, and (ii) having determined that the X-ray spectra are dominated by reflection, which is typically assumed to be of the order of 1 % efficient in the 2–10 keV band, we verify that our sources still match the intrinsic relations and the Compton-thick AGN selection criteria. In that process we construct a complete self-consistent picture for each of our targets in order to provide a valuable benchmark for future multi-wavelength studies. With more precise measurements, better selection, tighter correlations, and larger samples it will become possible to constrain the geometry of the circumnuclear

material on statistical grounds and provide new tests for the contending AGN models (e.g., Ghisellini et al. 1994; Urry & Padovani 1995; Elitzur 2012).

3.5 Summary and Conclusions

This chapter presents hard X-ray spectroscopy of three highly obscured, nearby Seyfert nuclei: NGC 424, NGC 1320, and IC 2560. *NuSTAR* observations unambiguously confirm that they are among the most obscured AGN in the local universe: the obscuration of the nuclei is well into the Compton-thick regime, where the nuclear continuum is suppressed to the extent that the distant/cold reflection component dominates the X-ray spectrum above 3 keV. Although hard X-ray data from nearly obscuration-unbiased surveys with *Swift*/BAT and *INTEGRAL* were previously able to provide basic fluxes and spectral shapes, with *NuSTAR* it is possible study moderately large samples of hard X-ray selected AGN spectroscopically. With better understanding of local heavily obscured examples and their multi-wavelength properties we aim to achieve greater reliability in identifying their more distant counterparts. This will ultimately lead to improved indirect indicators that are often the only tools available for high-redshift AGN studies.

From the analysis of the quasi-simultaneous *NuSTAR* and *Swift*/XRT observations, as well as archival *XMM-Newton* and multi-wavelength data, we find the following:

- All three sources show strong fluorescent iron lines and prominent Compton humps, as expected for reflection spectra. They stand out from the *NuSTAR* sample of local hard X-ray selected AGN by their hard effective photon indices and very high reflection strength, if modeled with simple spectral models. From a preliminary analysis of the ongoing *NuSTAR* survey of nearby AGN, we estimate that similar sources constitute approximately 10 % of that currently incomplete sample.

- Detailed modeling reveals that the X-ray spectra above 3 keV are dominated by reflection components and that no contributions from heavily absorbed intrinsic continua are formally required by the data. We thus infer that in all three cases the intrinsic continuum is obscured by $N_{\mathrm{H,A}} > 5 \times 10^{24}\,\mathrm{cm}^{-2}$ and find $N_{\mathrm{H,R}} \gtrsim 3 \times 10^{24}\,\mathrm{cm}^{-2}$ for the column density of the reflecting material. The dominance of the reflection component is further supported by the strong fluorescent Fe Kα lines with equivalent width of 1–2.5 keV.

- As the intrinsic X-ray continua are not observed in transmission, we estimate their luminosities from multi-wavelength data, and infer a reflection efficiency of the order of 1 % in the 2–10 keV band. Based on that efficiency and the surface-type reflection that fits the data best we argue for an edge-on clumpy torus geometry. Further studies of statistically representative samples of Compton-thick AGN are needed to constrain the typical reflection efficiency, which is currently only assumed to be of the order of 1 % in CXB models.

- Considering the extension of Compton-thick AGN studies to the high-redshift, low-count regime, we show that the band count ratio in the *NuSTAR* bandpass is not a good discriminator between mildly and heavily Compton-thick sources at $z > 0$ and advocate usage of mid-infrared data to infer obscuration or reflection dominance. In that context, we use archival multi-wavelength data to verify that (i) our sources obey intrinsic luminosity relations derived empirically from large AGN samples, and (ii) they would not miss being classified as Compton-thick AGN using most of the selection techniques proposed in the literature.

Acknowledgements

The authors thank the anonymous referee for useful comments which have improved the manuscript. M. B. acknowledges support from the International Fulbright Science and Technology Award. A. C. acknowledges support from ASI-INAF grant I/037/012/0-011/13. M. K. gratefully acknowledges support from Swiss National Science Foundation Grant PP00P2_138979/1.

This work was supported under NASA Contract No. NNG08FD60C, and made use of data from the *NuSTAR* mission, a project led by the California Institute of Technology, managed by the Jet Propulsion Laboratory, and funded by the National Aeronautics and Space Administration. We thank the *NuSTAR* Operations, Software and Calibration teams for support with the execution and analysis of these observations. This research has made use of the *NuSTAR* Data Analysis Software (`NuSTARDAS`) jointly developed by the ASI Science Data Center (ASDC, Italy) and the California Institute of Technology (USA). This research made use of the XRT Data Analysis Software (`XRTDAS`), archival data, software, and on-line services provided by the ASDC. This research has made use of NASA's Astrophysics Data System.

Chapter 4

NEW SPECTRAL MODEL FOR MEASURING TORUS COVERING FACTORS FROM BROADBAND X-RAY SPECTRA OF ACTIVE GALACTIC NUCLEI

Abstract

The basic unified model of active galactic nuclei (AGN) invokes an anisotropic obscuring structure, usually referred to as a torus, to explain the diverse phenomenology of AGN as an angle-dependent effect. We present a new grid of X-ray spectral templates based on radiative transfer calculations in neutral gas in an approximately toroidal geometry. Fitting the templates to broadband X-ray spectra of AGN provides constraints on two important geometrical parameters of the gas distribution around the supermassive black hole: the average column density and the covering factor. Compared to the currently available spectral templates, our model is more flexible, and capable of providing constraints on the main torus parameters in a wider range of AGN. We demonstrate the application of this model using hard X-ray spectra from *NuSTAR* (3–79 keV) for four AGN covering a variety of classifications: 3C 390.3, NGC 2110, IC 5063 and NGC 7582. This small set of examples was chosen to illustrate the range of possible torus configurations, from disk-like to sphere-like geometries with column densities below, as well as above, the Compton-thick threshold. This diversity of torus properties challenges the simple assumption of a standard geometrically and optically thick toroidal structure commonly invoked in the basic form of the unified model of AGN. Finding broad consistency between the constraints from the *NuSTAR* data and those from infrared modeling, we discuss how the approach from the X-ray band complements similar measurements of AGN structures at other wavelengths.

Material presented in this chapter has been submitted for publication in AAS Journals.

4.1 Introduction

According to the simple unification model of active galactic nuclei (AGN), a toroid-like structure (popularly, *torus*) provides the anisotropic obscuration needed to explain the diversity of AGN observed across the electromagnetic spectrum (Antonucci 1993, Urry & Padovani 1995). The torus absorbs and reprocesses radiation from the accretion disk and the innermost regions around the supermassive black hole (SMBH). Reprocessed thermal emission from dust in the torus is observed primarily in the infrared part of the spectrum (see, e.g., Hönig 2013, Netzer 2015 for recent reviews). Signatures of reprocessing in the X-ray band—narrow fluorescent emission lines (most notably, neutral iron lines around 6.4 keV) and the Compton hump broadly peaking at 10–30 keV—arrise primarily from interaction of X-ray photons with the surrounding gas (e.g., Leahy & Creighton 1993, Ghisellini et al. 1994, Krolik et al. 1994). These spectral features have been observed in nearly all X-ray spectra of non-blazar AGN with sufficient energy coverage and data quality (e.g., Nandra & Pounds 1994, Turner et al. 1997, Risaliti 2002, Dadina 2008, Rivers et al. 2013, Vasudevan et al. 2013, Kawamuro et al. 2016a).

A large body of literature on X-ray spectroscopy of AGN is based on models computed for reprocessing in a semi-infinite plane geometry, the most popular of which is `pexrav` (Magdziarz & Zdziarski, 1995). Spectral models in which the signature of the torus is approximated with `pexrav` have been popular for describing the phenomenology of broadband X-ray spectra of AGN because this simple geometry is easily parametrized, and because the quality of hard X-ray data (> 10 keV) was such that deviations from this assumption were generally not considered significant. Reprocessed continua are known to vary as a function of geometry of the reprocessing material (e.g., Nandra & George 1994, Yaqoob 1997, Murphy & Yaqoob 2009, Ikeda et al. 2009, Brightman & Nandra 2011a, Liu & Li 2014, Furui et al. 2016); however, the ability to constrain the geometry of the reprocessing material is clearly lacking in the `pexrav`-based phenomenological approach. The 100-fold increase in sensitivity in the hard X-ray band (> 10 keV) brought by *NuSTAR* (Harrison et al., 2013) made it possible to study the spectral signatures of the torus in detail.

Empirically motivated spectral models with approximately toroidal geometry have been calculated by Murphy & Yaqoob (2009, `MYtorus` hereafter), Ikeda et al. (2009), Brightman & Nandra (2011a, `BNtorus` hereafter), Liu & Li (2014, `Ctorus` hereafter), and Furui et al. (2016). Some of these models were made available to

the community; `MYtorus` and `BNtorus` in particular have been used extensively for detailed spectroscopic studies of nearby obscured AGN observed with *NuSTAR* (e.g., Arévalo et al. 2014, Baloković et al. 2014, Annuar et al. 2015, Rivers et al. 2015a, Ricci et al. 2016, Boorman et al. 2016, Gandhi et al. 2017), as well as studies using broadband data with hard X-ray coverage from *Suzaku*/PIN, *Swift*/BAT, and *INTEGRAL* instruments (e.g., Fukazawa et al. 2011, Tazaki et al. 2011, Yaqoob 2012, Braito et al. 2013, Vasylenko et al. 2013, Miniutti et al. 2014, Yaqoob et al. 2015).

These torus models are limited in the range of physical scenarios they describe. In `MYtorus`, with a geometry of an actual torus, the covering factor is fixed (50 % of the sky covered as seen from the SMBH). This assumption limits the range of spectral shapes that the model can reproduce without *decoupling* it into independent transmitted and reprocessed spectral components, therefore introducing ambiguity into its interpretation (Yaqoob, 2012). Such a decoupling is often required in spectral analyses of high-quality broadband X-ray spectra (e.g., Puccetti et al. 2014, Bauer et al. 2015, Guainazzi et al. 2016).

In the `BNtorus` model, the torus opening angle is a free parameter, but the torus column density is assumed to be equal to the line-of-sight column density ($N_{\mathrm{H,los}}$) for any obscured AGN. While this assumption does not hold in general, it does describe some AGN well: Compton-thick (CT; $N_{\mathrm{H}} > 10^{24}\,\mathrm{cm}^{-2}$) AGN represent 20–50 % of the local AGN population (e.g., Risaliti et al. 1999, Ricci et al. 2015, Akylas et al. 2016, Koss et al. 2016a) and it is widely believed that our line of sight crosses their tori in most cases. `BNtorus` is therefore applicable to CT AGN spectra, and Brightman et al. (2015) used it to measure the torus covering factors in a sample of 10 *NuSTAR*-observed CT AGN.

Many multi-epoch X-ray studies have shown that $N_{\mathrm{H,los}}$ varies on timescales of hours to months, as clouds of gas pass in and out of our line of sight (e.g., Risaliti et al. 2002, Lamer et al. 2003, Risaliti et al. 2010, Marchese et al. 2012, Braito et al. 2013, Markowitz et al. 2014, Rivers et al. 2015a, Guainazzi et al. 2016, Marinucci et al. 2016, Ricci et al. 2016). The *average* column density of the torus, which is a large parsec-scale structure, can only vary over significantly longer timescales (~years). The ability to decouple the line-of-sight component from reprocessing in the spatially extended torus is essential for multi-epoch modeling of a wide variety of AGN. While this is possible with `MYtorus` and `Ctorus`, they do not feature the covering factor as a free parameter.

The covering factor of the torus is one of its most basic geometric parameters. It may be affected by winds and outflows from the innermost regions around the SMBH, therefore providing insight into physics of AGN feedback and the interaction of SMBHs with their host galaxies (e.g., Elvis 2000, Hopkins et al. 2006, Fabian 2012, Heckman & Best 2014, Netzer 2015). Studies in the infrared band indicate that the torus covering factor may be a function of luminosity (e.g., Maiolino et al. 2007, Treister et al. 2008, Assef et al. 2013), and may correlate with other measurable properties (e.g., presence of broad lines in optical spectra; Mateos et al. 2016). It has been suggested that the covering factor depends on the Eddington ratio (e.g., Ezhikode et al. 2016, Buchner & Bauer 2017), and that its dependence on luminosity or the Eddington ratio changes with redshift (e.g., Aird et al. 2015, Buchner et al. 2015). AGN population studies in the X-ray band suggest that the fraction of obscured AGN drops as a function of luminosity (e.g., Sazonov & Revnivtsev 2004, Hasinger 2008, Burlon et al. 2011, Vasudevan et al. 2013). A tentative trend for lower covering factors at higher luminosity was also found from analyses of individual AGN both in the infrared (Alonso-Herrero et al., 2011) and in the X-ray band (Brightman et al., 2015).

The next step toward systematically probing the properties of the torus from the X-ray band will be analyses of AGN samples with good-quality hard X-ray data. A large, representative sample of nearby obscured AGN observed with *NuSTAR* is presented in Chapters V and VI of this thesis. This study reveals that the local AGN population exhibits a broad range of Compton hump strengths when modeled with `pexrav`[1], including a significant fraction with high values (e.g., Ricci et al. 2011, Rivers et al. 2013, Vasudevan et al. 2013, Kawamuro et al. 2016a, also Chapter V), which may be indicative of the increased (or decreased) prominence of the Compton hump as a function of the covering factor of the torus and its average column density. While this idea is not new (e.g., Madejski et al. 2000; Krolik et al. 1994; Ghisellini et al. 1994), the operational tool for measuring the covering factor from X-ray spectra independently from the line-of-sight component has thus far not been available.

In this chapter we present a new tool for probing the torus structure from the X-ray

[1] In `pexrav` and `pexmon` (extension of `pexrav`, including fluorescent line emission; Nandra et al. 2007), the contribution of reprocessed continuum is parametrized with the spectral parameter R. To avoid confusion, because this parameter can formally take on negative values, we define $R_{\rm pex} = |R|$. $R_{\rm pex} = 1$ corresponds to the amount of reprocessing created by an infinitely optically thick plane covering one half of the sky as seen from the X-ray source. While small deviations from unity can be interpreted as the reprocessing medium covering a solid angle of $\simeq 2\pi\, R_{\rm pex}$, this interpretation clearly fails for deviations greater than a factor of $\simeq 2$, which are often found in X-ray spectral analyses.

band. With its increased flexibility in comparison with currently available models, we aim to enable studies of the main torus parameters in AGN of any class. Our grid of spectral templates is made available to the community in the form of a new `Xspec` table model (Arnaud, 1996). Construction of the spectral template grid is presented in § 4.2. In § 4.3 we demonstrate its use on *NuSTAR* spectra of four different AGN in order to highlight its features and capabilities. In § 4.4 we briefly discuss the results for this small and diverse set of examples, and their interpretation. We also make a comparison to relevant measurements from the literature, with particular emphasis on the infrared, and discuss the prospect for future synergy with other methods of constraining torus geometry.

4.2 New Spectral Templates

Reprocessed components of AGN X-ray spectra are formed in interaction of the intrinsic X-ray continuum of AGN with the surrounding medium. In order to investigate the details of the complex relationship between the geometry of this material and the observed spectra, we have built a new Monte Carlo radiative transfer code `BORUS` (Baloković et al., in preparation). Radiative transfer simulations using this code can be performed in an arbitrary geometry, and at energy resolution matching high-resolution X-ray calorimeters similar to *Hitomi* Soft X-ray Spectrometer (Mitsuda et al., 2014), e.g., *Athena* X-ray Integral Field Unit (Barret et al., 2016), and the *Hitomi* replacement, X-ray Astronomy Recovery Mission (XARM). Details of these calculations will be presented in a dedicated paper; here we only outline the main properties, and then focus on the particular subset of low-resolution spectral templates used in this chapter and Chapter VI. The spectral templates are available on the Web[2], and can be obtained directly from the authors.

4.2.1 Model Setup

The `BORUS` radiative transfer code is capable of computation in an arbitrary 3-dimensional space within which matter density can be represented as a mathematical function of position, or as a data cube. It is therefore possible to calculate output spectra for complex matter distributions expected from hydrodynamical simulations of the circumnuclear environment (e.g., Wada 2012). However, for fitting limited-quality X-ray data, these structures need to be simplified and parametrized. For

[2]Temporarily at `www.astro.caltech.edu/~mislavb/download`; if the link is no longer functional, contact the author for an update.

the spectral templates presented here, we choose the same simple, approximately toroidal geometry employed in Brightman & Nandra (2011a). They used a uniform-density sphere with two conical polar cutouts with the opening angle as a free parameter of the model.[3] This simplification should be thought of as a smoothed distribution of individual clouds comprising the torus, as illustrated in Figure 4.1. Although we used the same geometry as Brightman & Nandra (2011a), our new calculation is more detailed, flexible, includes features that the original calculation lacks, and resolves some known problems. We directly compare our new spectral templates with those from `BNtorus` in § 4.2.3.

`BORUS` calculates Green's functions for initial photon energies between 1 keV and 1 MeV. These functions are convolved with a parametrized intrinsic continuum in post-processing. The medium is assumed to be cold, neutral, and static. Photons are propagated through this medium until they are absorbed without fluorescent re-emission or until they escape the system. At each step, relative probabilities of photoelectric absorption and Compton scattering are computed based on photoelectric absorption cross-sections from NIST/XCOM[4], elemental abundances from Anders & Grevesse (1989), and the Klein-Nishina scattering cross-section formula. In the case of absorption, fluorescent photons are emitted according to fluorescent yields for Kα_1, Kα_2, and Kβ lines from Krause (1979), for all elements up to zinc ($A = 30$).

We compute spectral templates with a range of relative abundance of iron between 1/10 and 10. Changing the iron abundance parameter results in a self-consistent modification of iron fluorescent line intensity and of the shape of the reprocessed continuum, which is affected by the change in the total photoelectric cross-section. Compton scattering for the spectral templates presented here does depend on atomic species, but we neglect the internal structure of the scattering atoms for the low-resolution templates discussed in this thesis (see Furui et al. 2016 for a calculation that includes these effects). The Compton shoulder is computed for all fluorescent spectral lines.

4.2.2 `Xspec` Table Model `borus02`

The grid of spectral templates computed using `BORUS` in the particular geometry shown in Figure 4.1 is named `borus02`. The covering factor of the torus, as seen

[3] Specifically, this geometry is assumed for the `Xspec` table model `torus1006.fits`.

[4] Available on the Web at `https://www.nist.gov/pml/xcom-photon-cross-sections-database`; originally, Berger & Hubbell (1987).

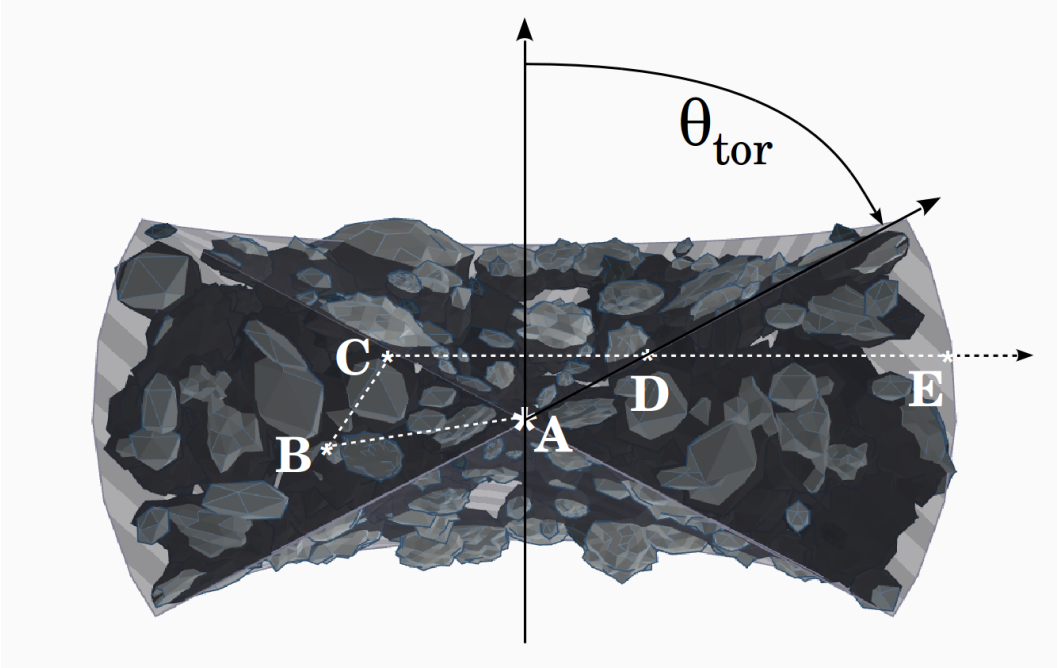

Figure 4.1: Cross-section of the approximately toroidal geometry adopted for our model. Though the torus may be composed of individual clouds in reality (shown as light grey blobs), we approximate it with a uniform density sphere with two conical cutouts (shown as striped semi-transparent geometrical shape). The half-opening angle of the torus, $\theta_{\rm tor}$ (or, equivalently, the covering factor, $C_{\rm tor} = \cos\theta_{\rm tor}$) is a free parameter of our model. The white asterisk in the middle (point A) represents the X-ray source. White dashed lines and letters trace a particular photon ray which exits the system in the direction of the observer to the right (looking at the system edge-on). Note that in a clumpy torus it may happen that photons scattered toward the observer at point C (near the inner edge of the torus) can escape without absorption if they pass between individual clouds. However, in a torus with uniform density, such photons will undergo absorption and scattering between points D and E. The difference in resulting reprocessed spectra is illustrated in Figure 4.2.

from the X-ray source in the center, is simply related to the half-opening angle of the torus, $\theta_{\rm tor}$, as $C_{\rm tor} = \cos\theta_{\rm tor}$. Angles $\theta_{\rm tor}$ and $\theta_{\rm inc}$ (inclination) both increase away from the axis of symmetry of the torus. We calculate the spectral templates for covering factors at 10 points equally spaced in $\cos\theta_{\rm tor}$. The minimal and maximal values of $\theta_{\rm tor}$, corresponding to the covering factors of 100 % and 10 %, are zero and 84.1°, respectively. The output of the radiative transfer simulation is arranged so that exit angles of each photon are separated into 10 bins in $\cos\theta_{\rm inc}$, each with a width of 0.1. The centers of the first and the last bins are at $\cos\theta_{\rm inc}$ equal to 0.05 and 0.95, which corresponds to inclination angles of 87.1° and 18.2°, respectively. Note

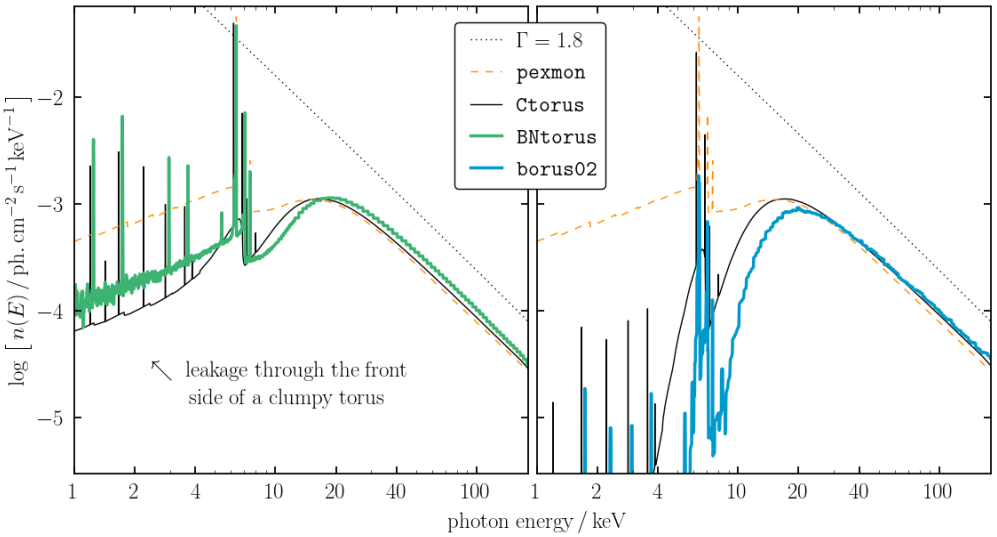

Figure 4.2: Comparison of reprocessed spectra from `pexmon` (Nandra et al. 2007; dashed orange line), `Ctorus` (Liu & Li 2014; thin, black, solid line), `BNtorus` (Brightman & Nandra 2011a; thick, green, solid line in the left panel), and `borus02` (thick, solid, blue line in the right panel). Intrinsic power-law continuum with $\Gamma = 1.8$, assumed for each of the models, is shown with a grey, dashed line. For all models we assume an edge-on view ($\theta_{\rm inc} \approx 85°$), and assume that the line-of-sight column density is equal to the average column density of the torus ($\log N_{\rm H,los}/{\rm cm}^{-2} = \log N_{\rm H,tor}/{\rm cm}^{-2} = 24.5$). For comparison, `pexmon` is plotted with normalization formally corresponding to a covering factor of 50 % ($R_{\rm pex} = 1$; infinite plane geometry), and all other models have a 50 % covering factor ($\theta_{\rm tor} = 60°$). In the left panel, `Ctorus` is plotted with a small number of clouds in the line of sight along the equatorial plane ($N_{\rm clo} = 2$). `BNtorus`, also plotted in the left panel, matches this porous torus model relatively well. In the right panel, we compare `borus02` to `Ctorus` with a larger number of clouds ($N_{\rm clo} = 10$), approximating a more uniform torus. In reference to Figure 4.1, the right and left panel mainly show the effects of absorption and scattering between points D and E, and lack thereof, respectively.

that $\theta_{\rm inc} \approx 0°$ corresponds to a pole-on and $\theta_{\rm inc} \approx 90°$ corresponds to an edge-on view. Azimuthal angles are averaged over because of axial symmetry.

We utilize the additive table model option available in `Xspec` to enable fitting our parametrized grid of spectral templates to X-ray data. The basic FITS-format table containing the spectra for the full range of parameters is named `borus02.fits`. For simplicity and convenience, we also make available additional tables with a reduced number of parameters, and versions with parameters in different units ($\theta_{\rm tor}$,

$\theta_{\rm inc}$, or their cosines).[5] The `borus02_afe1.fits` table, which we use for fitting examples in § 4.3, has the relative abundance of iron fixed at unity. In all cases, the tables contain *only* the spectral components arising from reprocessing in the torus; the component transmitted directly (absorbed in some cases, unabsorbed in others) is *not* included.

In the set of templates presented in this chapter, the intrinsic continuum is assumed to be a power law with an exponential cutoff, $n(E) \propto E^{-\Gamma} \exp(-E/E_{\rm cut})$. The photon index ($\Gamma$) can be varied between 1.4 and 2.6, and the high-energy cutoff ($E_{\rm cut}$) has a range between 20 keV and 2 MeV. Normalization of the intrinsic continuum follows the `Xspec` convention and is therefore defined in units of photons $\rm s^{-1}\,cm^{-2}\,keV^{-1}$ at 1 keV. These parameters can be linked to other basic spectral components in `Xspec` in order to construct a complete spectral model for fitting AGN X-ray spectra.

A basic model may be defined with the following command sequence in `Xspec`:

$$\begin{aligned} \texttt{m} \;&=\; \texttt{c}_1 \times \texttt{phabs} \times (\texttt{atable\{borus02.fits\}} \\ &+\; \texttt{zphabs} \times \texttt{cabs} \times \texttt{cutoffpl} \\ &+\; \texttt{c}_2 \times \texttt{cutoffpl}\,) \end{aligned}$$

In the expression above, $\texttt{c}_1$ and $\texttt{c}_2$ stand for instrument cross-normalization and the relative normalization of a leaked or scattered unabsorbed reflection of the intrinsic continuum, respectively. `phabs` accounts for foreground Galactic absorption, while `zphabs`×`cabs` represents line-of-sight absorption at the redshift of the X-ray source (generally independent from the average column density of the torus), including Compton scattering losses out of the line of sight.[6] `cutoffpl` represents the intrinsic continuum, and its parameters should be linked to the Γ, $E_{\rm cut}$, and normalization parameters of the `borus02` table. We recommend formulating the model so that the `borus02` table is the first additive component. In that case the allowed parameter range for Γ and $E_{\rm cut}$ will be read from the table, ensuring that in parameter optimization `Xspec` will not step out of the limited parameter space.

[5] In particular, the `borus01.fits` model represents a spherical absorber (covering factor fixed at unity, which is included in `borus02` tables). It can be directly compared to the Brightman & Nandra (2011a) model with the uniform sphere geometry (`Xspec` table `sphere0708.fits`), and the `plcabs` model (Yaqoob, 1997), which is a limited analytic approximation of radiative transfer in the same geometry. Note that the table naming scheme corresponds to a wider set of torus geometries computed using `BORUS`, but not discussed here.

[6] The line-of sight absorption model `phabs` may be freely replaced with a more updated absorption model, such as `tbabs` Wilms et al., 2000. Here we use `phabs` in order to consistently use elemental abundances adopted for calculation of the reprocessed spectra.

The line-of-sight column density, $N_{\rm H,los}$, and the torus column density, $N_{\rm H,tor}$, should generally not be linked – the main feature of our new table model is that the equality of these two quantities can be tested with the data. However, the user may still choose to make the assumption that $N_{\rm H,tor} = N_{\rm H,los}$ in order to reduce the number of free parameters. For increased linearity of the parameter space, it is often better to use logarithmic units for $N_{\rm H,tor}$, fitting for log $N_{\rm H,tor}$ instead. Likewise, we recommend fitting for the torus covering factor, $C_{\rm tor} = \cos\theta_{\rm tor}$, and the cosine of the inclination angle, instead of fitting for $\theta_{\rm tor}$ and $\theta_{\rm inc}$ directly. Due to the likely complex landscape of the parameter space, the use of Markov chain Monte Carlo (MCMC) sampling or more advanced Bayesian methods (Buchner et al., 2014) should be preferred over the straightforward χ^2 minimization with many free parameters. In order to facilitate the application of our new `Xspec` table model to X-ray data, in § 4.3 we present a two-step approach demonstrated on four AGN with *NuSTAR* data of different quality.

4.2.3 Direct Comparison with `BNtorus`

In this section we highlight the differences between our new set of X-ray spectral templates and the frequently used, publicly available `Xspec` table model `BORUS`. The physics of radiative transfer employed in both calculations is nearly the same; the `BORUS` code is more versatile in terms of geometry, operates at higher energy resolution, and takes into account a greater number of atomic species and their fluorescent lines. For `borus02` we adopted the same approximately toroidal geometry assumed in calculating the `BNtorus` spectral templates, at least in principle.

As Liu & Li (2015) recently pointed out, there is significant disagreement between `BNtorus` and their simulations for the same geometry. Their calculated spectra are in qualitative agreement with previously published calculations such as Ghisellini et al. (1994), Krolik et al. (1994), Ikeda et al. (2009) and Murphy & Yaqoob (2009). A comparison of `BNtorus` spectra to our new calculations (see Figure 4.2) confirms this discrepancy. We trace the problem back to a deficiency in the original calculation of the `BNtorus` model.

The issue with the Brightman & Nandra (2011a) calculation arises from absorption not being applied to the reprocessed light emitted from the inner side of the torus (the side opposite the observer). All obscured sightlines are affected by this to some degree. The photon path shown with white dashed lines in Figure 4.1 exemplifies the issue: by error, photons scattered toward an edge-on observer at point C (near the inner surface of the torus) reach the observer without any further absorption or

scattering. In the assumed geometry, these photons should additionally interact with the torus material between points D and E. As a result of the missing absorption, within the `BNtorus` model there is very little difference in the spectral shapes of reprocessed components for pole-on and edge-on inclinations.

The disagreement between `BNtorus` and our new calculation is demonstrated in Figure 4.2. In order for the reprocessed component to dominate below $\simeq$30 keV, we compare model spectra for $\log N_{\rm H,los}/{\rm cm}^{-2} = \log N_{\rm H,tor}/{\rm cm}^{-2} = 24.5$. The `BNtorus` spectrum shows an excess of soft X-ray flux ($\lesssim$20 keV), which should be heavily absorbed for an edge-on view of a uniform-density torus. We further compare the spectra to the clumpy `Ctorus` model, which features the average number of clouds along and equatorial line of sight ($N_{\rm clo}$, ranging from 2 to 10) as a free parameter. For $N_{\rm clo} = 2$, it emulates a torus sparsely populated with clouds, which results in less absorption and scattering on the side of the torus closer to the observer. In the other extreme, for $N_{\rm clo} = 10$, the torus volume is filled out more and therefore more similar to a uniform-density torus. The former situation matches `BNtorus` well, while the latter is closer to `borus02`. Figure 4.2 shows the difference only for $\log N_{\rm H,tor}/{\rm cm}^{-2} = 24.5$; for higher and lower $N_{\rm H,tor}$, the differences are more and less severe, respectively.

While `BNtorus` does not correctly reproduce spectra for the geometry described in Brightman & Nandra (2011a), it may approximate spectral features produced by the more general and more realistic class of clumpy tori. In the example given in Figure 4.1, the photon path passes the cross-section of the torus (between points D and E) through a region with no clouds. This is a physically plausible scenario in which photons emitted from the inner side of the torus would be able to escape unimpeded toward an edge-on observer. The inner-side reprocessed component, which shows some similarity to that reproduced by `BNtorus` (see Figure 4.2), could in principle be directly observable through the front side of the torus as long as the gas distribution is not uniform, i.e., is clumpy. Evidence that this is a possible, if not likely, scenario in AGN is abundant from detailed spectroscopy (e.g., Arévalo et al. 2014, Baloković et al. 2014, Annuar et al. 2015) and studies of line-of-sight absorption variability (e.g., Risaliti et al. 2002, Torricelli-Ciamponi et al. 2014, Markowitz et al. 2014).

In addition to resolving the issue of missing absorption, `borus02` has additional features which make it significantly more flexible than `BNtorus`. Separation of the line-of-sight and reprocessed components is not possible with `BNtorus`. This

limits its application only to AGN for which it is justified to assume that the line-of-sight column density ($N_{\rm H,los}$) is equal to the average column density of the torus ($N_{\rm H,tor}$). With `borus02` one can self-consistently model multi-epoch data assuming that the $N_{\rm H,los}$ varies, while $N_{\rm H,tor}$ does not, as observed in many AGN with multi-epoch X-ray data (e.g., Marchese et al. 2012, Braito et al. 2013, Ricci et al. 2016). Furthermore, `borus02` includes the high-energy cutoff ($E_{\rm cut}$) and the relative abundance of iron ($A_{\rm Fe}$) as additional model parameters. They enable complex spectral models to be used with a greater degree self-consistency. These parameters will also make it possible to include torus reprocessing components in spectral models of AGN in which these parameters appear to have extreme values (e.g., Brenneman et al. 2011, Kara et al. 2015b, Xu et al. 2017).

4.3 Examples of Application for Fitting Hard X-ray Spectra

In order to demonstrate the usage and potential of our model, we choose four AGN observed with *NuSTAR*: 3C 390.3, NGC 2110, IC 5063 and NGC 7582. This is by no means a complete or representative sample – the targets are primarily chosen for the diversity of their physical properties. 3C 390.3 is a broad-line radio galaxy (a radio-loud type 1 Seyfert), IC 5063 is a radio-loud type 2 Seyfert, and NGC 2110 and NGC 7582 are radio-quiet type 2 Seyferts. Except for IC 5063, which is part of a large sample presented in Chapters V and VI (as are NGC 2110 and NGC 7582), detailed spectral analyses of the *NuSTAR* spectra of these sources have already been published: 3C 390.3 by Lohfink et al. (2015), NGC 2110 by Marinucci et al. (2015) and NGC 7582 by Rivers et al. (2015a). In the case of NGC 7582, we additionally include a new *NuSTAR* observation taken in 2016 (obsID 60201003002), which has not yet been published elsewhere. The reader is referred to the references listed above for the description of the observations, data processing procedures, and spectral analyses using spectral models commonly employed in the literature. For simplicity, in this chapter we use only the *NuSTAR* data (3–79 keV) for fitting our model.

We performed spectral analyses in `Xspec`, fitting FPMA and FPMB spectra simultaneously, without coadding. Our basic model is defined as in § 4.2.2, but with the factor $\mathtt{c}_2$ (relative normalization of the secondary continuum) fixed to zero, and $E_{\rm cut}$ fixed to 300 keV, unless explicitly stated otherwise. Parameter optimization is based on the χ^2 statistic. We use 5 % as the threshold in null-hypothesis probability ($p_{\rm null}$; the probability of the observed data being drawn from a particular model, given its

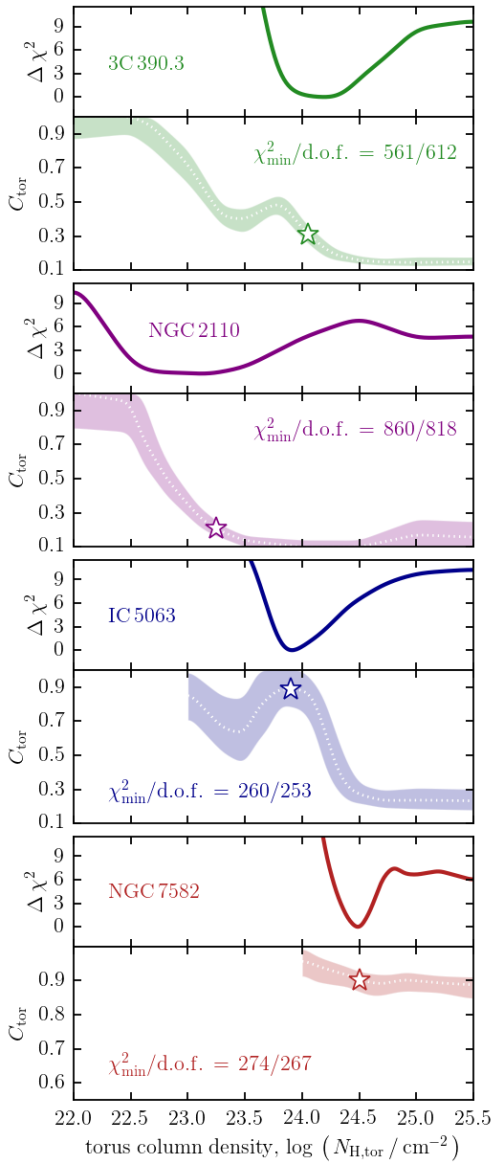

Figure 4.3: Constraints on the torus covering factor ($C_{\rm tor}$) as a function of the torus column density ($N_{\rm H,tor}$) for 3C 390.3, NGC 2110, IC 5063, and NGC 7582. Inclination is a free parameter in all fits. The solid lines in the upper panels for each source show minimum χ^2 as a function of $N_{\rm H,tor}$ normalized to the best-fit χ^2. The dashed lines in the lower panels show medians of the probability distribution of $C_{\rm tor}$ at each $N_{\rm H,tor}$ and the shaded regions enclose 68 % (1 σ) of the probability. Curves are plotted only for the range of $N_{\rm H,tor}$ for which a statistically acceptable fit was found. They have been smoothed with a Gaussian kernel with standard deviation equal to half of the step size over the parameter space, $\Delta \log N_{\rm H,tor}/{\rm cm}^{-2} = 0.1$. Stars mark the $N_{\rm H,tor}$ with the lowest χ^2 for each AGN.

χ^2 and the number of degrees of freedom) for a model to be formally acceptable as a good representation of the data; i.e., models with $p_{\rm null} < 5\,\%$ are rejected.

If a parameter can be limited to a range that is smaller than its domain, so that there is a gradient in χ^2 exceeding $\delta\chi^2 = 1$ from the best fit while all other parameters are free to vary, we consider that parameter constrained. We base our constraints on marginalized probability distributions derived from converged MCMC chains produced with the built-in Goodman & Weare (2010) MCMC algorithm in `Xspec`. They can be two-sided or one-sided. For two-sided constraints uncertainty is quoted as the interval containing 68 % of the total probability, equivalent to $1\,\sigma$ uncertainty for a Gaussian probability distribution. When $\delta\chi^2$ between the best fit and the edge of the domain is less than unity, we quote a $1\,\sigma$ limit, so that 84 % of the total probability is enclosed (conversely, 16 % is left out). We verified that the best-fit parameters are always within the uncertainty interval, although they often do not exactly match the distribution medians.

In § 4.3.1 we first present results based on a single epoch of *NuSTAR* data for each source (the first epochs for NGC 2110 and NGC 7582). Then, in § 4.3.2 we show how single-epoch constraints may be influenced by variability, and discuss how multi-epoch X-ray data and some justifiable assumptions can be leveraged to derive more robust self-consistent constraints and assess possible systematics.

4.3.1 Single-epoch Constraints on the Torus Parameters

We first run a set of fits with the $N_{\rm H,tor}$ parameter kept fixed in order to determine whether any assumptions on this parameter result in statistically unacceptable solutions (i.e., $p_{\rm null} < 5\,\%$). The pairs of panels in Figure 4.3 show the constrains on $C_{\rm tor}$ for a range of assumed values of $N_{\rm H,tor}$, and the associated χ^2 curve. Other model parameters are left free to vary in these fits. Spectral models for each of the sources are shown in Figure 4.4. In Figure 4.5 we show two-dimensional constraints on $N_{\rm H,tor}$ and $C_{\rm tor}$, where $N_{\rm H,tor}$ is also left free to vary in the fit.

3C 390.3

The unobscured 3C 390.3 is our simplest example, since the lack of line-of-sight absorption in the *NuSTAR* band allows us to set $N_{\rm H,los}$ to zero. The top two panels in Figure 4.3 show that a good fit can be found for any assumed $N_{\rm H,tor}$, but that there is a clear minimum in χ^2 around the best fit at $N_{\rm H,tor} = 1.1 \times 10^{24}\,{\rm cm}^{-2}$. For the best fit, $\chi^2 = 561.0$ for 612 degrees of freedom (d.o.f.). This model is shown in the

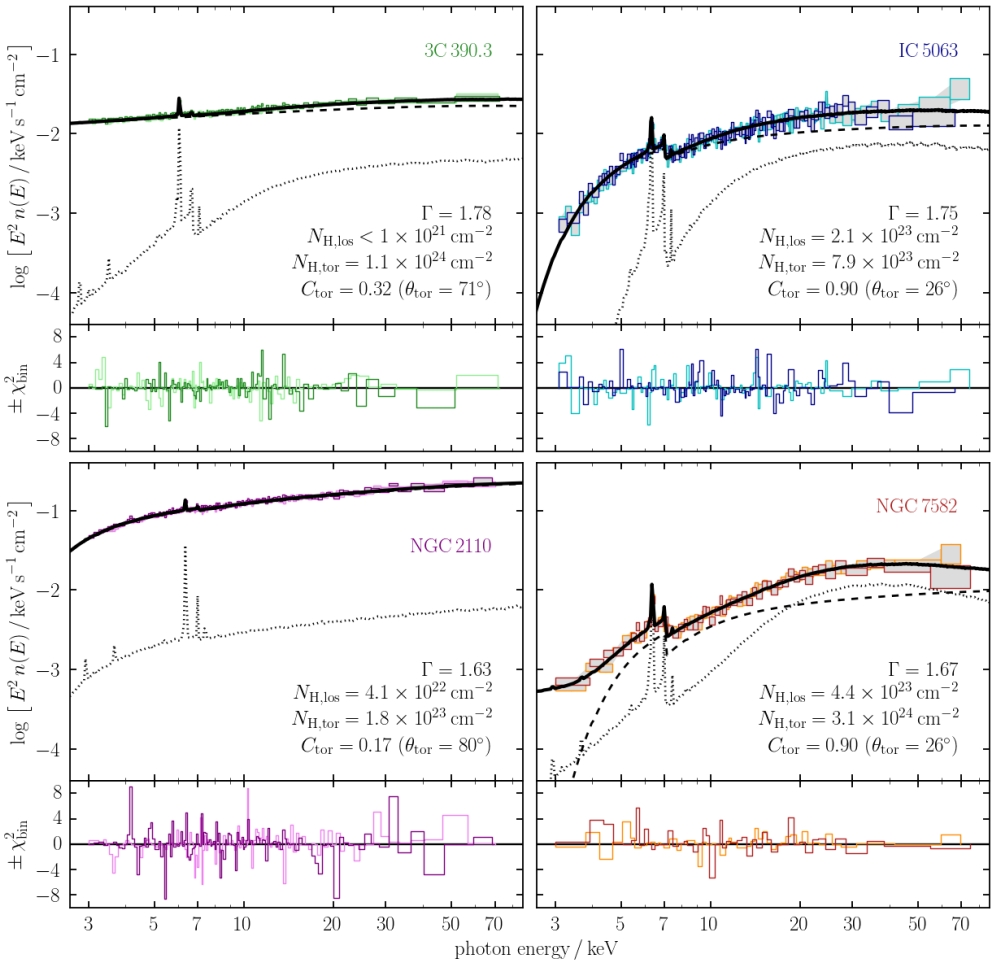

Figure 4.4: Best-fit spectral models for 3C 390.3, NGC 2110, IC 5063, and NGC 7582. We show the total spectrum in solid lines, the absorbed power-law components with dashed lines, and the reprocessed component (including fluorescent emission lines) with dotted lines. In the lower right of each panel showing the model spectra, we list its main parameters. FPMA and FPMB residuals in terms of χ^2 contributions per bin are plotted below each spectrum (in darker and lighter colors, respectively); they are binned to improve clarity.

top left panel of Figure 4.4; the flat residuals suggest that all features in the data are accounted for by this spectral solution. With $N_{H,tor}$ fixed at the best-fit value, we find $C_{tor} = 0.32^{+0.05}_{-0.07}$. The inclination angle is constrained so that $\cos\theta_{tor} > 0.3$, so that our line of sight does not intercept any of the reprocessing material, consistent with the type 1 optical classification of 3C 390.3. Figure 4.5 shows the probability density distribution in the two-dimensional plane spanned by $N_{H,tor}$ and C_{tor}, obtained from a fit in which $N_{H,tor}$ is left free to vary. In this case, the covering factor constraint is slightly broader: $C_{tor} = 0.3^{+0.2}_{-0.1}$. The possibility that the reprocessed component is

due to the accretion disk rather than the torus is discussed in § 4.3.2.

NGC 2110

NGC 2110 is mildly obscured by $N_{\rm H,los} = (4.0 \pm 0.2) \times 10^{22}$ cm^{-2}, which is detectable as an exponential roll-off of the power-law continuum ($\Gamma = 1.628 \pm 0.007$) at the lower end of the *NuSTAR* band. Its spectrum is remarkably featureless, except for a narrow Fe Kα line with an equivalent width of 33 ± 6 eV. Stepping through the range of log $N_{\rm H,tor}/{\rm cm}^{-2}$ between 22.0 and 25.5 we find that acceptable model include tori with very small covering factors, $C_{\rm tor} < 0.2$ for log $N_{\rm H,tor}/{\rm cm}^{-2} > 23.5$, as well as tori with high covering but low $N_{\rm H,tor}$. The difference in the best-fit χ^2 over the whole range is very small (< 10, for 819 d.o.f.). A broad minimum in χ^2 at $22.5 <$ log $N_{\rm H,tor}/{\rm cm}^{-2} < 23.5$ covers nearly the full range of covering factors (0.1–1.0). The best fit, with χ^2/d.o.f.= 860.4/818, is found for log $N_{\rm H,tor}/{\rm cm}^{-2} \approx 23.3$. With log $N_{\rm H,tor}$ fixed at this value, $C_{\rm tor} < 0.24$ and $\cos\theta_{\rm inc} > 0.28$. The lower left pair of panels in Figure 4.4 show this model and the residuals. Note that a number of narrow, isolated bins contribute substantially to the total χ^2 without corresponding to any real but unmodeled spectral features. With $N_{\rm H,tor}$ as a free parameter in the fit, the constraints are much broader, as shown in Figure 4.5. The probability density distribution in the $N_{\rm H,tor}$–$C_{\rm tor}$ plane is highly elongated and reaches log $N_{\rm H,tor}/{\rm cm}^{-2} \approx 22.6$ and $C_{\rm tor} \approx 0.8$ within $1\,\sigma$ contours. No constraint on inclination can be given in this case.

IC 5063

Partly due to higher line-of-sight absorption in comparison with 3C 390.3 and NGC 2110, the *NuSTAR* data for IC 5063 have the constraining power to reject a part of the parameter space on statistical grounds, despite lower photon statistics. As the third pair of panels in Figure 4.3 shows with the lack of $C_{\rm tor}$ constraints for $N_{\rm H,tor} < 10^{23}$ cm^{-2}, no model with $p_{\rm null} > 5$ % can be found for a lower torus column density. χ^2 as a function of log $N_{\rm H,tor}$ has a minimum (χ^2/d.o.f.= 259.6/253) around log $N_{\rm H,tor}/{\rm cm}^{-2} = 23.9$. With log $N_{\rm H,tor}$ fixed at this value, $C_{\rm tor} > 0.77$ and $\cos\theta_{\rm inc} < 0.62$. This model is shown in the upper right panels of Figure 4.4. Fitting for the torus column density, we find that it is very well constrained, log $N_{\rm H,tor}/{\rm cm}^{-2} = 23.95 \pm 0.07$, and that there is almost no degeneracy with the covering factor. Unlike the cases of 3C 390.3 and NGC 2110, the contours in the $N_{\rm H,tor}$–$C_{\rm tor}$ plane are elongated along the axes, predominantly vertically. Constraints

on $C_{\rm tor}$ and $\cos\theta_{\rm inc}$ are therefore no different than those obtained with $N_{\rm H,tor}$ fixed. With a high $C_{\rm tor}$ and $N_{\rm H,tor}$ near the CT threshold, the reprocessed component contributes $\sim 20\,\%$ of the flux in the 10–50 keV band.

NGC 7582

NGC 7582 exhibits the most complex X-ray spectrum of the AGN discussed here. Its $N_{\rm H,los}$ is known to be variable and multiple layers of absorption have been invoked in previous spectral analyses (Rivers et al., 2015a). We find it necessary to include a non-zero parameter $\mathtt{c}_2$ (as defined in § 4.2.2) in order to account for partial absorption along the line of sight; without it, the residuals show a significant excess below 4.5 keV. For the first *NuSTAR* observation considered here, under different assumptions for $N_{\rm H,tor}$, we always find $N_{\rm H,los}$ consistent with $(3.6 \pm 0.4) \times 10^{23}$ cm^{-2} and $\mathtt{c}_2 = 0.10 \pm 0.04$ (i.e. $\approx 90\,\%$ line-of-sight covering, or $\approx 10\,\%$ Thompson-scattered fraction). The 3–15 keV continuum is dominated by the transmitted component, while the Compton hump dominates in the 15–60 keV range (see the lower right panels of Figure 4.4). Stepping through the $N_{\rm H,tor}$ parameter space we first find that no models with $\log N_{\rm H,tor}/{\rm cm}^{-2} < 24.0$ are acceptable according to our $p_{\rm null} > 5\,\%$ threshold. The χ^2 curve shown in the lowest pair of panels in Figure 4.3 shows a very well defined minimum at $\log N_{\rm H,tor}/{\rm cm}^{-2} \approx 24.5$. At this $N_{\rm H,tor}$, both $C_{\rm tor}$ and $\cos\theta_{\rm inc}$ are narrowly constrained to 0.90 ± 0.03. Additionally fitting for the torus column density yields $\log N_{\rm H,tor}/{\rm cm}^{-2} = 24.0 \pm 0.1$, and does not affect the other model parameters. NGC 7582 therefore seems to have a CT torus that covers $\approx 90\,\%$ of the sky as seen from the SMBH, yet we observe it through a hole with roughly an order of magnitude lower column density. We further test this result with additional data in the following section, and discuss its interpretation in § 4.4.

4.3.2 Additional Constraints and Considerations

Line-of-sight and Torus Column Density

The flexibility of `borus02` allows us to test the common assumption that the line-of-sight column density matches the average column density of the torus. For 3C 390.3 and NGC 7582, with $\log N_{\rm H,los}/{\rm cm}^{-2} < 21$ and $\log N_{\rm H,los}/{\rm cm}^{-2} \approx 23.3$, respectively, this assumption cannot yield a good fit for any combination of other model parameters. Both AGN clearly require presence of CT material out of our line of sight. This is not necessarily true for IC 5063 and NGC 2110, since statistically acceptable models with $p_{\rm null} > 5\,\%$ can be found for both AGN. For NGC 2110,

such a solution ($\log N_{\rm H,tor}/{\rm cm}^{-2} = \log N_{\rm H,los}/{\rm cm}^{-2} \approx 22.6$, $C_{\rm tor} > 0.7$) is within the $1\,\sigma$ contour for the single epoch constraints shown in Figure 4.5, and within the $3\,\sigma$ contour based on two epochs. Fitting the IC 5063 data with the assumption that $N_{\rm H,tor} = \log N_{\rm H,los}/{\rm cm}^{-2} \approx 23.3$ increases χ^2 with respect to the fit featuring independent column densities ($\Delta\chi^2 = 16.0$) and results in $C_{\rm tor} = 0.5 \pm 0.1$. In this case, we also find $\Gamma = 1.51 \pm 0.03$, which implies a harder intrinsic continuum than the bulk of local Seyferts (for which the distribution of Γ is roughly Gaussian with a mean $\simeq$1.8 and standard deviation $\simeq$0.2; e.g., Dadina 2008, Rivers et al. 2013, also Chapter V), unlike $\Gamma = 1.75 \pm 0.04$ obtained in § 4.3.1.

External Constraints and Additional Spectral Components

Because 3C 390.3 is a powerful radio galaxy, the orientation of its jet can be measured in order to better constrain the inclination (e.g., Alef et al. 1988). Assumption of co-alignment can then be employed to infer the inclination of the accretion disk and the torus. Based on this and constraints from other measurements, which yield similar values (e.g., Flohic & Eracleous 2008), Dietrich et al. (2012) found that the inclination of the symmetry axis of the AGN to our line of sight is 27 ± 2 degrees. If we fix the inclination and perform the fitting as in § 4.3.1, we obtain $\log N_{\rm H,tor}/{\rm cm}^{-2} = 24.4 \pm 0.3$ and $C_{\rm tor} = 0.22^{+0.13}_{-0.07}$. While these constraints still overlap with those obtained with $\theta_{\rm inc}$ as a free parameter, the two-dimensional probability distribution is shifted appreciably toward higher $N_{\rm H,tor}$ and lower $C_{\rm tor}$.

If we additionally allow that the intrinsic continuum has a high-energy cutoff ($E_{\rm cut}$) lower than 300 keV, as assumed in § 4.3.1, the constraints shift further to $\log N_{\rm H,tor}/{\rm cm}^{-2} > 24.5$ and $C_{\rm tor} = 0.14 \pm 0.02$. $E_{\rm cut}$ is found to be 155^{+11}_{-8} keV; however, the decrease in χ^2 with respect to a fixed value at 300 keV too small to consider it as a significant spectral feature ($\Delta\chi^2 < 1.0$). This was not the case in the analysis of Lohfink et al. (2015), where the reprocessed continuum was assumed to have a different spectral shape. The constraints on $N_{\rm H,tor}$ and $C_{\rm tor}$ under the assumption of fixed inclination and free $E_{\rm cut}$ are shown in the right panel of Figure 4.5, as an example of how different assumptions may systematically shift constraints on the torus parameters.

Finally, we also tested for the presence of relativistically broadened reprocessing in the innermost part of the accretion disk by adding a `relxill` component (Garcia et al., 2014) to our `Xspec` model. Over a variety of assumptions for the parameters of the `relxill` component, we find that its contribution to the iron line emission

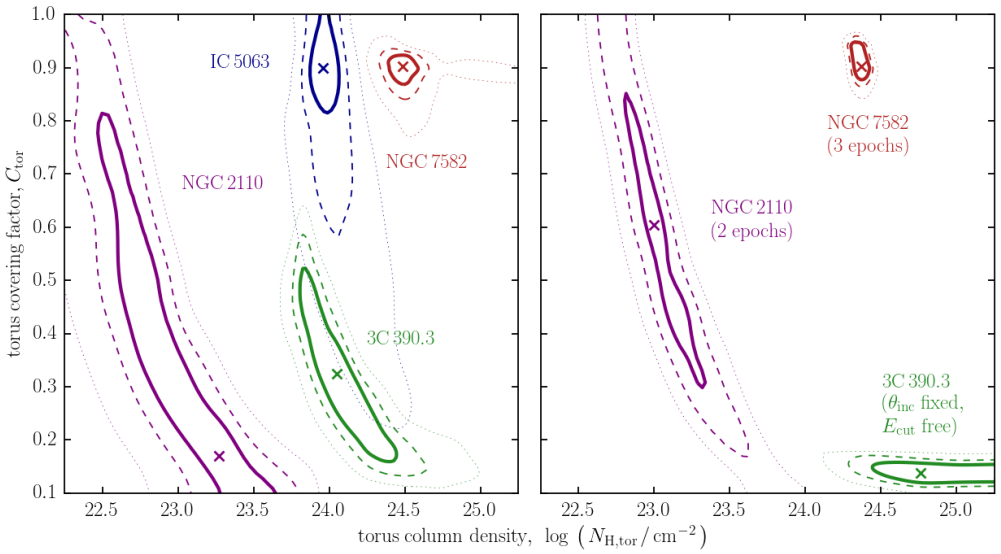

Figure 4.5: Two-dimensional $\Delta\chi^2$ contours for torus column density and covering factor for 3C 390.3, IC 5063, NGC 2110, and NGC 7582. The left panel shows basic single-epoch fits with inclination as a free parameter and fixed $E_{\rm cut} = 300$ keV. The right panel shows contours for the three AGN with additional constraints introduced in § 4.3.2: two and three epochs fitted simultaneously for NGC 2110 and NGC 7582, respectively, and fixed inclination, $\theta_{\rm inc} = 27°$ (Dietrich et al., 2012), and fitted high-energy cutoff, $E_{\rm cut} = 115^{-8}_{+11}$ keV, for 3C 390.3. Solid, dashed, and dotted lines mark 1, 2, and 3 σ contours ($\Delta\chi^2 = 2.3$, 4.6 and 9.2 from the best-fit value). Crosses mark the best-fit values.

and the Compton hump is always sub-dominant. In all cases, $C_{\rm tor}$ is found to be consistent within 2 σ with the region outlined by contours in the two panels of Figure 4.5. Having additionally included higher-energy-resolution data from *Suzaku*, Lohfink et al. (2015) found no evidence for relativistically broadened features, further strengthening our conclusion that the reprocessed component is dominated by material which may have a disk-like geometry, but is located at distances not affected by general relativistic effects.

Multi-epoch X-ray Data

NGC 2110 and NGC 7582 have been observed with *NuSTAR* two and three times, respectively.[7] The advantage of multi-epoch observations is that the effects of variability in luminosity or other spectral components can be taken into account self-consistently. AGN are known to vary in luminosity of the intrinsic continuum

[7] 3C 390.3 has formally been observed twice, but because those observations are consecutive, we treat them as a single observation here.

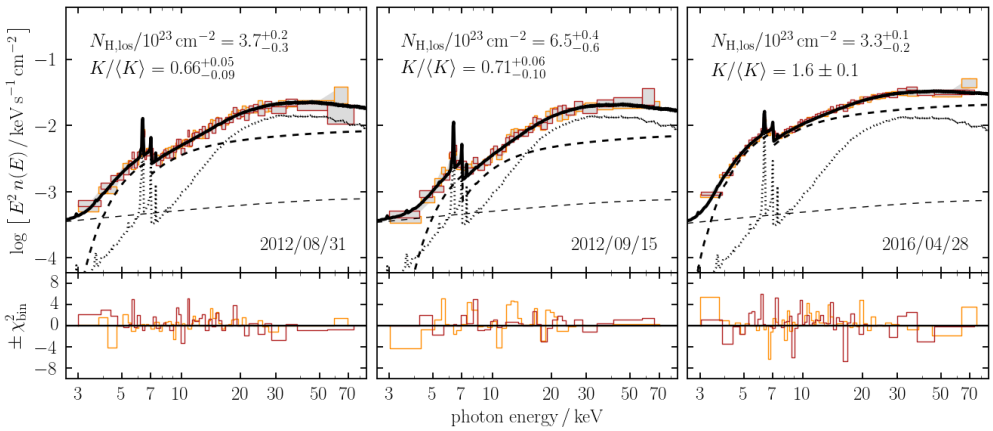

Figure 4.6: Self-consistent spectral model for three epochs of *NuSTAR* observations of NGC 7582. The spectra can be self-consistently modeled under the assumption that the normalization of the intrinsic continuum (K) and the line-of-sight column density ($N_{\rm H,los}$) vary between observations, and that the scattered components' normalization is determined by the average intrinsic continuum normalization ($\langle K\rangle$). See § 4.3.2 for details.

down to very short timescales. However, the torus is expected to be a parsec-scale structure and hence the reprocessed spectral components cannot follow fast changes in the intrinsic continuum. The reprocessed components should therefore be normalized not with respect to the intrinsic continuum luminosity within a given observation, but with respect to the average luminosity. Multiple observations provide additional photon statistics that reduce statistical uncertainties, and they also provide a better estimate of the average, rather than instantaneous intrinsic luminosity of the AGN.

We first consider NGC 2110, which did vary in flux between the two *NuSTAR* observations in 2012. For the first observation, analyzed in § 4.3.1, Marinucci et al. (2015) found that the 2–10 keV flux was elevated with respect to the long-term average. The second observation, during which the 2–10 keV flux was closer to the average, is therefore a better representation of the typical intrinsic luminosity, which sets the normalization of the reprocessed component. In effect, we assumed that the increase in flux during the first observation was temporary and did not have an immediate effect on the reprocessed component. We further assumed that the line-of-sight column density and the photon index did not change between two observations, as suggested by single-epoch spectral analyses.

A joint fit yields results similar to those from our single-epoch analysis in § 4.3.1,

with $\log N_{\rm H,tor} = 23.0 \pm 0.3$, $C_{\rm tor} = 0.6^{+0.2}_{-0.3}$, and no constraint on $\theta_{\rm inc}$. The two-dimensional probability distributions shown in Figure 4.5 seem marginally inconsistent with each other. However, it must be noted that the two-epoch analysis is significantly more robust; not only does it have better photon statistics, but it also avoids the erroneous normalization of the reprocessed components with an intrinsic continuum that is atypically luminous.

A joint fit yields results similar to those from our single-epoch analysis in § 4.3.1, with $\log N_{\rm H,tor} = 23.0 \pm 0.3$, $C_{\rm tor} = 0.6^{+0.2}_{-0.3}$, and no constraint on $\theta_{\rm inc}$. The two-dimensional probability distributions shown in Figure 4.5 seem marginally inconsistent with each other. However, it must be noted that the two-epoch analysis is significantly more robust; not only does it have better photon statistics, but it also avoids the erroneous normalization of the reprocessed components with an intrinsic continuum that is atypically luminous.

In addition to the variability of the intrinsic continuum luminosity, some AGN, like NGC 7582, also vary in the line-of-sight column density. In modeling multiple epochs of observation of such an object, we therefore allow for $N_{\rm H,los}$ to be fitted to each observation in addition to the intrinsic continuum amplitude. We assume that a good representation of the average intrinsic continuum luminosity, which sets the normalization of the reprocessed components, is provided by the average of continuum luminosities between the three observations. We found no evidence that the photon index changed between observations, while $N_{\rm H,los}$ and intrinsic continuum amplitude did.

We show our best-fit spectral model for NGC 7582 in all three epochs of *NuSTAR* observations in Figure 4.6. Each of the three panels lists $N_{\rm H,los}$ and the continuum normalization with respect to the mean ($\langle K \rangle$). It is worth noting that in the first two epochs the Compton hump dominates the 15–60 keV band, while in the third epoch the increased intrinsic continuum dominates instead. This self-consistent three-epoch fit confirms our torus constraints from § 4.3.1, and makes them even tighter: $\log N_{\rm H,tor}/{\rm cm}^{-2} = 24.39 \pm 0.06$, $C_{\rm tor} = 0.90^{+0.07}_{-0.03}$, and $\cos\theta_{\rm inc} = 0.87 \pm 0.05$.

4.4 Discussion

4.4.1 New Tool for Studying the AGN Torus

In recent years, `MYtorus`, `BNtorus`, and, to a more limited extent, the torus model by Ikeda et al. (2009), have been used to probe the basic parameters of AGN tori—

their average column densities ($N_{\rm H,tor}$) and covering factors ($C_{\rm tor}$)—from the hard X-ray band. While the average column density can be estimated using the `MYtorus` model assuming its particular geometry with a fixed 50 % covering factor (e.g., Braito et al. 2013, Baloković et al. 2014, Yaqoob et al. 2015), our new model is the only reliable publicly available tool for constraining the torus covering factor from X-ray data. `BNtorus` has been used to provide covering factor estimates in previous studies (e.g., Gandhi et al. 2014, Brightman et al. 2015, Koss et al. 2015), but they may need reassessment in the light of issues with missing absorption that we identified in § 4.2.3. More complex torus models will become available in the near future (e.g., Liu & Li 2014, Furui et al. 2016), motivated by the high energy resolution of X-ray calorimeters. `borus02`, as an updated and extended version of the already popular `BNtorus` model, may be an effective tool for better understanding the relation between new results and those already in the literature.

The `BORUS` radiative transfer code, on which our `borus02` spectral templates are based, is a versatile tool for investigating the observable effects of torus geometry and clumpiness in the X-ray band in future studies (Baloković et al., in preparation). The parametrization of geometry adopted for `borus02` was chosen in particular to match the `BNtorus` model, in order to extend its flexibility and enable more detailed studies of torus parameters in a wider population of AGN than previously possible.

In terms of additional model parameters, `borus02` tables include the high-energy cutoff and the relative abundance of iron. More importantly, it combines the best features of `BNtorus` and `MYtorus` by having a variable covering factor, as well as the reprocessed component separated from the transmitted (absorbed) component. The line-of-sight column density therefore does not need to be assumed equal to the average over the whole torus. The scenario in which these quantities differ is supported by the *NuSTAR* data in the fitting examples presented in § 4.3, as well as the literature.

4.4.2 Interpretation of Fitting Results

In interpretation of the results from spectral analyses employing `borus02` tables, one needs to keep in mind that the uniform-density torus is just an approximation of a non-uniform (clumpy) distribution of matter around the SMBH. This idea is illustrated in Figure 4.1. It is possible to define a covering factor (e.g., fraction of the sky covered with column density above some threshold, as seen from the SMBH at the center) and a typical column density (e.g., average over all obscured

sightlines to the SMBH) for a wide variety of possible geometries. For any torus, the line-of-sight column density ($N_{\rm H,los}$) can differ widely depending on its orientation with respect to the observer at a given time. Parameters $N_{\rm H,tor}$ and $C_{\rm tor}$ therefore provide information on the material *outside* of our line of sight.

In the paradigm described above, it is not difficult to understand how the tori in NGC 7582 and IC 5063 can simultaneously have a high $C_{\rm tor}$ and $N_{\rm H,tor}$ in the CT regime, without CT absorption in the line of sight. NGC 7582 may have a clumpy torus with $N_{\rm H} \sim 10^{25}\,{\rm cm}^{-2}$ clumps covering $\lesssim$20 % of the sky and the rest covered with $N_{\rm H} \approx 5 \times 10^{23}\,{\rm cm}^{-2}$, which averages to $\approx 3 \times 10^{24}\,{\rm cm}^{-2}$, in agreement with our modeling in § 4.3. This configuration can explain the previously observed CT state, as well as the average line-of-sight column density (see Rivers et al. 2015a for a summary of previous X-ray observations of NGC 7582). Our modeling also constrains the inclination so that $\cos\theta_{\rm inc} \approx C_{\rm tor} \approx 0.9$, implying that we are viewing at the torus close to its edge. In the uniform torus model, reprocessed emission from the inner side of the torus can only be observed for $\cos\theta_{\rm inc} > C_{\rm tor}$, but a clumpy torus would have such lines of sight even for $\cos\theta_{\rm inc} < C_{\rm tor}$ (see Figures 4.1 and 4.2). Constraints on $\theta_{\rm inc}$ from fitting `borus02` should be interpreted in relation to $C_{\rm tor}$, rather than in absolute terms.

The *NuSTAR* data robustly exclude the possibility that the torus in 3C 390.3 has a high covering factor; with $C_{\rm tor} \lesssim 0.3$, its reprocessed component may simply be due to the outer part of the accretion disk. The NGC 7582 torus is unlikely to be ring-like ($C_{\rm tor} \simeq 0.1$) or even disk-like ($C_{\rm tor} \simeq 0.5$). In § 4.3.2 we presented fitting results for NGC 2110 and IC 5063 under the assumption that $N_{\rm H,tor} = N_{\rm H,los}$, which yields acceptable, though not preferred, models for their *NuSTAR* spectra. With this assumption, the NGC 2110 torus appears to be sphere-like but has two orders of magnitude lower average column density than the CT torus of NGC 7582. The torus in IC 5063 fits in between the other three, with its likely high covering factor and borderline CT average column density. This is already a step forward in testing the common assumption that all Seyfert-like AGN possess essentially the same kind of a torus.

We stress that the constraints presented in this study are based on *NuSTAR* data alone, and can therefore be significantly improved in more detailed studies in the future. The data used for demonstration in this study are representative of a long *NuSTAR* observation in the case of 3C 390.3 (100 ks), a short snapshot observation of a very bright AGN in the case of NGC 2110 (≈20 ks, but with photon statistics typical of

a long exposure on an typical local Seyfert), and short observations of IC 5063 and NGC 7582, characteristic of the *NuSTAR* snapshot survey of the *Swift*/BAT-selected AGN (see Chapters V and VI). Inclusion of good-quality soft X-ray data, as well as self-consistently modeled additional epochs, can help constrain the torus parameters even further (see Yaqoob et al. 2015 and Guainazzi et al. 2016, for the case of Mrk 3 without and with *NuSTAR* data, respectively). We anticipate that many such studies will be done within the operational lifetime of *NuSTAR*.

4.4.3 Implications for Previous Results Based on Phenomenological Models

Despite the availability of empirically motivated torus models in recent years, a large fraction of the literature, and especially studies of large AGN samples, made use of disk reprocessing models such as `pexrav` to approximate the torus contribution to AGN spectra. The spectral fitting examples presented in § 4.3 already suggest a natural explanation for the very low Compton hump strengths measured using `pexrav` in some AGN (notably, radio galaxies; Ballantyne 2007, Tazaki et al. 2011). Very strong non-relativistic reprocessing signatures have been observed both in stacked hard X-ray data (Malizia et al. 2003, Ricci et al. 2011, Esposito & Walter 2016) and in spectral analyses of particular AGN (e.g., Rivers et al. 2013, Vasudevan et al. 2013, Chapter V). Within our model, scaling of the Compton hump amplitude and shape corresponds to scaling of the torus covering factor.

Models for fitting torus SEDs in the infrared band have been available for a long time (see, e.g., Netzer 2015 for a recent review). The best results are obtained where it is possible to resolve out the nuclear emission, or spectroscopically isolate AGN emission, thus minimizing contamination from star formation in the central regions of the host galaxies. These models have been used extensively for constraining torus properties in bright local AGN (e.g., Alonso-Herrero et al. 2011, Lira et al. 2013, Ichikawa et al. 2015), as well as higher-redshift sources (e.g., Efstathiou et al. 2013, Roseboom et al. 2013, Podigachoski et al. 2016), to the extent possible with limited unresolved photometry. Most of them include a parameter such as the opening angle or, equivalently, the covering factor, though the assumed geometries do differ.

Directly comparing our $C_{\rm tor}$ constraints to the results from Alonso-Herrero et al. (2011), we find that they are broadly consistent for all three AGN included in both studies, NGC 2110, IC 5063, and NGC 7582. In all three cases, infrared-derived covering factors are high, 80 – 95 %. Our $C_{\rm tor} > 0.8$ constraint for IC 5063 is entirely consistent with this, as is $C_{\rm tor} \approx 0.9$ for NGC 7582. The covering factor for

NGC 2110 torus based on infrared data is nearly 100 %, which is an acceptable solution for the X-ray data, although the *NuSTAR* spectra indicate a preference for a lower value. Near-complete covering is obtained under the assumption that $N_{\mathrm{H,tor}} = N_{\mathrm{H,los}}$ for both NGC 2110 and IC 5063. While Ichikawa et al. (2015) also find a high dust covering factor for NGC 2110 ($\approx$ 90 %) from infrared SED modeling, Lira et al. (2013) find a significantly lower dust covering factor ($\approx$ 50 %) for NGC 7582, in disagreement with Alonso-Herrero et al. (2011) and our apparently very tight X-ray constraint. Torus column densities are very different between these three AGN, and may be indicative of a different spatial scale or nature of the reprocessing material (i.e., compact, possibly clumpy, torus versus gas and dust in the host galaxy).

Despite the fact that most infrared SED models include a geometrical measure such as the torus opening angle or, equivalently, covering factor, it is unclear to what extent this is comparable to C_{tor} of the X-ray torus. Discrepancies may be expected because the infrared emission comes predominantly from dust, whereas X-rays are mostly affected by the much more abundant gas. There is little doubt that dust-free gas exists in the innermost regions of typical Seyferts (e.g., in the broad-line region; Gaskell et al. 1981). Comparing X-ray and infrared size estimates, Gandhi et al. (2015) have found that the bulk of fluorescent emission of iron likely originates from within the dust sublimation radius. The dust/infrared and gas/X-ray covering factors may therefore naturally differ depending on the overall geometry of the SMBH surroundings. Our model will enable some of the first systematic comparisons between the gas covering factor from the X-ray band and the constraints on dusty torus geometry derived from infrared modeling for single sources with high-quality data on the one hand, and large samples with lower-quality data on the other.

4.4.4 Multi-wavelength Synergy in Future Studies

Thus far, only a small number of studies in the literature combine multi-wavelength probes of torus parameters with geometric constraints from high-quality hard X-ray spectroscopy; e.g., Bauer et al. (2015), Koss et al. (2015), Masini et al. (2016). In a recent study of the obscured quasar IRAS 09104+4109, Farrah et al. (2016) combined X-ray, optical and infrared data in order to construct a self-consistent picture of its torus. While the short *NuSTAR* observation (15 ks) did not provide constraints as tight as those derived from the infrared data, it is encouraging that both spectral bands independently yield results in agreement with optical (spectroscopic and polarimetric) and radio data. It would certainly be better to have an internally self-consistent model including both gas and dust distributions for spectra in both

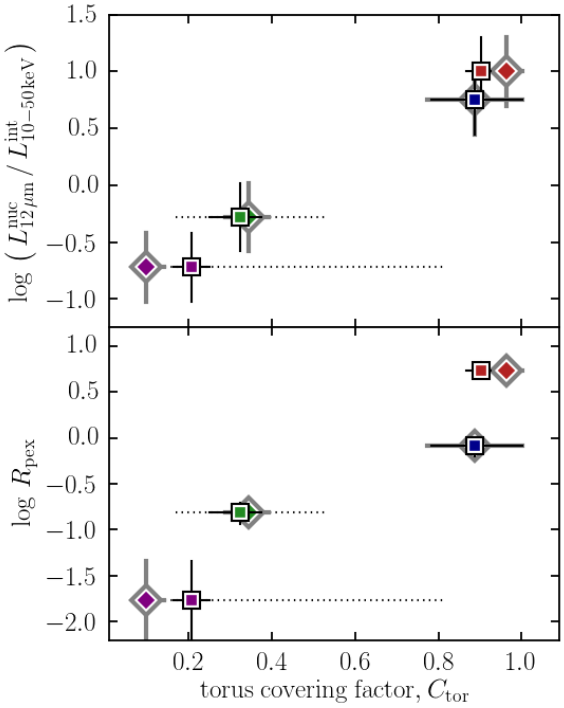

Figure 4.7: Relationship between the fitted torus covering factor ($C_{\rm tor}$) and two possible indicators of the covering factor. The upper panel shows the ratio of mid-infrared to X-ray luminosity, and the lower shows the relative normalization of the reprocessed continuum ($R_{\rm pex}$ parameter of the `pexrav` model) from a phenomenological model fit to broadband X-ray spectrum. Marker colors correspond to different AGN, as in other figures. Marker edges and errorbars in plotted black correspond to $C_{\rm tor}$ constraints with best-fit torus column density ($N_{\rm H,tor}$) for each source. Dotted errorbars for 3C 390.3 and NGC 2110 illustrate how the uncertainty increases when $N_{\rm H,tor}$ is left free to vary instead of being fixed at the best-fit value. Grey edges and diamond markers show $C_{\rm tor}$ constraints with the assumption that all tori are borderline CT, so that $\log\ N_{\rm H,tor}/{\rm cm}^{-2}$ is fixed at 24.0.

the infrared and X-ray bands; however, no such models have been published yet. In future work, `BORUS` will be used to construct grids of spectral templates that enable simultaneous fitting of both infrared and X-ray data, including those with high energy resolution from an instrument similar to *Hitomi*/SXS (Mitsuda et al., 2014), such as *Athena*/XIFU (Barret et al., 2016), and XARM.

Placing constraints on the geometrical and physical torus parameters for single objects is possible from optical, infrared and radio observations. Ionization cone opening angles can be constrained from optical observations with the high spatial resolution of the *Hubble Space Telescope* (e.g., Schmitt et al. 2003, Fischer et al. 2013), and may be expected to correlate to some degree with the torus opening

angle. For IC 5063, Schmitt et al. (2003) found that the ionization cone has a half-opening angle of $\simeq 30°$, and that it is aligned well with the jet observed at radio frequencies. The broad-line region of IC 5063 has been observed in polarized light (Inglis et al., 1993), indicating that it is present but hidden by intervening extinction. The torus geometry favored by our spectral modeling ($\theta_{\rm tor} < 40°$, $\theta_{\rm inc} > 50°$, $\log N_{\rm H,tor}/{\rm cm}^{-2} \approx 23.9$) is remarkably consistent with these completely independent constraints.

Additional constraints from resolved ionization cone observations may be expected in the near future from *Chandra* (Maksym et al., 2016) and the *James Webb Space Telescope*. Infrared photometry and spectroscopy at high spatial resolution (Ichikawa et al., 2015), interferometry (Burtscher et al., 2013) and polarimetry (Lopez-Rodriguez et al., 2015) have significantly contributed to recent advances in probing AGN structures. Molecular gas observations resolving the torus scales in nearby AGN with ALMA are able to probe torus kinematics (Garcia-Burillo et al., 2016). Some radio observations directly measure the orientation of the AGN structures with respect to the observer (e.g., jet, megamaser disk), while others are more indirect and model-dependent (Marin, 2016). Compared to these more traditional probes, constraints from the X-ray band have thus far been poorly explored, but they show promise for unique new insights into the nature of the AGN torus in the near future.

4.5 Summary

With the recent improvement in hard X-ray data quality brought about by *NuSTAR*, and the flexible empirically motivated spectral models, measuring the torus covering factor from the X-ray band is now possible for large samples of AGN. In this chapter we presented a new set of parametrized spectral templates, named `borus02`, made available to the public in the form of an `Xspec` table model, in order to facilitate studies of the torus geometry through X-ray spectroscopy. In calculation of the model spectra we assumed an approximately toroidal geometry with conical polar cutouts, following the popular `BNtorus` model of Brightman & Nandra (2011a). Our new model may be considered an updated, expanded and more flexible version of `BNtorus`.

Because `borus02` represents only the reprocessed spectral component (separated from the line-of-sight component), while featuring both the average column density

and the covering factor as free parameters, it is applicable to a wide variety of AGN. In order to highlight its capabilities, we presented its application on four AGN observed with *NuSTAR*. These four examples cover different parts of the parameter space spanned by the column density ($22 < \log N_{\rm H,tor}/{\rm cm}^{-2} < 25.5$) and the covering factor ($0.1 < C_{\rm tor} < 1.0$). Furthermore, we demonstrated how inclusion of multi-epoch data, external constraints and various assumptions can help with evaluating or alleviating some systematic uncertainties.

Finally, we compared our constraints on the torus covering factor with dust covering factors derived from modeling of infrared data, and found encouraging consistency. More detailed work will be required in order to understand the relationship between constraints from different wavelength regimes in terms of a physical interpretation. When combined self-consistently, the joint leverage of these different probes of torus geometry and orientation (not limited only to X-ray and infrared spectral modeling) should enable us to better characterize the complex geometry of the unresolvable innermost region surrounding SMBHs, and replace the proverbial donut-like AGN torus with a more realistic structure.

Acknowledgements

This work made use of data from the *NuSTAR* mission, a project led by the California Institute of Technology, managed by the Jet Propulsion Laboratory, and funded by the National Aeronautics and Space Administration. We thank the *NuSTAR* Operations, Software and Calibration teams for support with the execution and analysis of these observations. Furthermore, this research has made use of the following resources: the NASA/IPAC Extragalactic Database (NED), operated by the Jet Propulsion Laboratory, California Institute of Technology, under contract with the National Aeronautics and Space Administration; the High Energy Astrophysics Science Archive Research Center Online Service, provided by the NASA/Goddard Space Flight Center; NASA's Astrophysics Data System; `matplotlib`, a Python library for publication quality graphics (Hunter, 2007).

We acknowledge financial support from NASA Headquarters under the NASA Earth and Space Science Fellowship Program, grant NNX14AQ07H (M. B.), the ASI/INAF grant I/037/12/0–011/13 (A. C.), the Caltech Kingsley visitor program (A. C.), FONDECYT 1141218 (C. R.), Basal-CATA PFB–06/2007 (C. R.) and the China-CONICYT fund (C. R.).

Chapter 5

NUSTAR SURVEY OF THE LOCAL SEYFERT II POPULATION: PHENOMENOLOGY OF BROADBAND X-RAY SPECTRA

Abstract

Selection of active galactic nuclei (AGN) in the hard X-ray band (> 10 keV) results in both the least contaminated and the least obscuration-biased samples of AGN in the local universe. In the work presented here we make use of the flux-limited all-sky survey with the *Swift*/BAT instrument to select a large sample of type II (optical type 2, 1.9, and 1.8) Seyfert nuclei for short simultaneous observations with *NuSTAR* and *Swift*. The resulting sample of 124 AGN with simultaneous broadband X-ray spectra in the 0.3–79 keV band represents a unique dataset for constraining properties of the local obscured AGN population ($z < 0.1$). In the first part of this study we present the observations, data processing and analysis methods, and spectral modeling based on simple phenomenological models often used for obscured AGN in the literature. We characterize the spectral properties in terms of distributions of the main spectral parameters, and examine trends in the strength of the signatures of X-ray reprocessing (fluorescent Fe Kα line and the Compton hump), with column density and intrinsic luminosity. Limitations of the phenomenological approach to constraining the torus properties are discussed, but more detailed modeling is deferred to a follow-up study (Chapter VI). We employ these phenomenological findings to improve on the selection of Compton-thick AGN in *Swift*/BAT and *NuSTAR* surveys, and discuss how our results inform the synthesis models of the cosmic X-ray background.

Material presented in this chapter will be submitted for publication in AAS Journals.

5.1 Introduction

The standard basic picture of broadband X-ray spectra of AGN consists of the intrinsic continuum (usually approximated by a power-law continuum) originating from immediate surroundings of the SMBH, photoelectrically absorbed along the line of sight to the observer by the intervening material. Due to low quality of the data, this simple model may describe X-ray spectra of distant AGN sufficiently well (Brandt & Alexander, 2015), however, high-quality spectra often reveal additional spectral components. The Comptonized X-ray continuum can deviate from a power-law shape and its high-energy cutoff encodes information about the physical conditions in the emitting coronal plasma (e.g., Fabian et al. 2015). As photons propagate outwards, they are not only absorbed but also Compton-scattered in the surrounding gas associated with the accretion disk, the broad-line region (BLR), winds, outflows, and the putative molecular torus invoked by the Unified Model of AGN (Antonucci 1993, Urry & Padovani 1995). Fitting spectral models to the X-ray data provides insight into the geometry, the physical conditions, and the dynamics of these structures.

Within the Unified Model of AGN, our line of sight toward a type II object crosses the anisotropic, possibly toroidal obscuring structure (*torus* hereafter), causing the BLR and the innermost parts of the accretion flow to be unobservable.[1] Most type II AGN therefore display absorption in their X-ray spectra, caused by a line-of-sight column density of $10^{22} - 10^{24}\,\mathrm{cm}^{-2}$ in moderately obscured sources and in excess of $10^{24}\,\mathrm{cm}^{-2}$ in Compton-thick (CT) AGN. Scattering in the torus produces a continuum with a prominent broad Compton hump at $\sim$30 keV and narrow fluorescent line emission, with the strongest emission line being the Kα line of iron at 6.4 keV (e.g., Matt et al. 1991, Nandra & George 1994, Murphy & Yaqoob 2009). Signatures of reprocessed radiation, often referred to as *reflection*, have been ubiquitously observed in X-ray spectra of non-blazar AGN (e.g., Nandra & Pounds 1994, Turner et al. 1997, Risaliti 2002, Dadina 2008, Rivers et al. 2013, Vasudevan et al. 2013).

Studies with *BeppoSAX* (e.g., Risaliti 2002, Dadina 2008), *RXTE* (Rivers et al., 2013) and *Suzaku* (e.g., Fukazawa et al. 2011, Kawamuro et al. 2016a), all of which had pointed hard X-ray instruments of limited sensitivity, were fundamental in making important steps toward understanding both the phenomenology of broadband

[1] With the caveats that in some cases a reflection of the BLR can be seen indirectly in scattered polarized light (e.g., Ramos Almeida et al. 2016), and that some AGN may be intrinsically missing a BLR (e.g., Elitzur & Netzer 2016).

X-ray spectra and the physics they probe. The advent of wide-field hard X-ray surveys using *Swift*/BAT (Barthelmy et al. 2005, Baumgartner et al. 2013) and *INTEGRAL* (Beckmann et al. 2006, Bird et al. 2016), enabled large samples to be selected and studied statistically, however, with low-resolution and low signal-to-noise ratio hard X-ray spectra averaged over long timescales (e.g., Winter et al. 2009, Burlon et al. 2011, Ricci et al. 2011, Malizia et al. 2012, Vasudevan et al. 2013, Vasylenko et al. 2015). With the 100-fold increase in sensitivity in the hard X-ray band (> 10 keV) enabled by the *Nuclear Spectroscopic Telescope Array* (*NuSTAR*; Harrison et al. 2013), we now have the opportunity to probe the broadband X-ray spectra of obscured AGN with a continuous bandpass and high photon statistics from 3 keV up to ~ 75 keV. Paired with the uniform and nearly unbiased selection of the brightest hard X-ray sources with the *Swift*/BAT instrument, the *NuSTAR* survey presented here provides the largest atlas of high-quality hard X-ray spectra available to study the local population of obscured AGN in the X-ray band. As such, our sample has an immense value for constraining AGN structures such as the corona and the torus.

A large body of literature on X-ray spectroscopy of obscured AGN is based on models computed for reprocessing in a semi-infinite plane geometry, the most popular of which is `pexrav` (Magdziarz & Zdziarski, 1995). Reflection spectra vary as a function of geometry of the reprocessing material (e.g., Leahy & Creighton 1993, Ghisellini et al. 1994, Krolik et al. 1994, Nandra & George 1994), however, because of the popularity of `pexrav` in the past, in this study we focus on phenomenological modeling based on spectral templates using `pexrav` to represent the torus features. In a follow-up study (Baloković et al., in preparation; see Chapter VI), we will present an analysis of geometrical constraints for the torus from the more modern models based on approximately toroidal geometry for the same sample. These models, especially `MYtorus` (Murphy & Yaqoob, 2009) and `BNtorus` (Brightman & Nandra, 2011a), have already been used extensively for detailed spectral analyses from *NuSTAR* data on nearby heavily obscured AGN, e.g., Arévalo et al. (2014), Baloković et al. (2014), Gandhi et al. (2014), Puccetti et al. 2014, Annuar et al. (2015), Bauer et al. (2015), Brightman et al. (2015), Rivers et al. (2015a), Guainazzi et al. (2016), Masini et al. (2016), Ricci et al. (2016); however, a population study on a statistically significant and representative sample of AGN observed with *NuSTAR* has not been presented to this date.

In this chapter we present the *NuSTAR* survey of *Swift*/BAT-selected AGN, and the

resulting sample(s) of Seyfert II AGN (§ 5.2). In § 5.3 we describe our methods of data processing and analysis, and provide an overview of definitions and conventions we employ. We proceed to present our spectral modeling in § 5.4, and the results in § 5.5. A discussion of spectral constraints for various groups of AGN, a comparison with the literature and more advanced models, are given in § 5.6. We summarize our findings in § 5.7. The Appendix provides additional details on spectral modeling of some particular AGN.

5.2 Sample Selection and Observations

In the following subsections we first describe the *NuSTAR* survey of *Swift*/BAT-selected AGN. We then define the main sample, for which we perform a uniform spectroscopic analysis in § 5.4, and several smaller subsamples used for comparisons. In the remainder of this chapter, as well as the following one, we define *Sy II* as a group of AGN optically classified as types 2, 1.9, 1.8, including some narrow-line LINERs, with a range of luminosity between low-luminosity AGN ($L_{\rm bol} \lesssim 10^{41}\,{\rm erg\,s^{-1}}$) and quasars ($L_{\rm bol} \gtrsim 10^{45}\,{\rm erg\,s^{-1}}$), i.e., a broadly defined class of narrow-line Seyfert nuclei. In order to emphasize the difference between this group and the more formally defined type-2 Seyfert class, we employ roman numerals (Sy II) in contrast to decimal notation (Sy 2.0) akin to the intermediate optical types 1.8 and 1.9. Discussion of type-2 subclasses with hidden/polarized optical broad lines and infrared-only broad lines is beyond the scope of this study.

5.2.1 The *NuSTAR* Survey of *Swift*/BAT-selected AGN

Extragalactic survey of the hard X-ray sky, aimed at understanding the AGN population and its evolution, is one of the primary goals of the *NuSTAR* mission (Harrison et al., 2013). In addition to observations of deep fields, which are limited to small areas of the sky, the *NuSTAR* Extragalactic Survey includes a shallow and wide component, where serendipitous sources are identified in the field of view in targeted observations of brighter sources (Alexander et al., 2013; Lansbury et al., 2017). The *NuSTAR* survey of *Swift*/BAT-selected AGN has a two-fold goal: one is to acquire an unprecedented atlas of high-quality hard X-ray spectra of local AGN, and the other one is to search a large (non-contiguous) area of the sky to shallow depth in pursuit of faint serendipitous sources. Both of these goals can be readily achieved with short observations of bright AGN selected from the *Swift*/BAT survey.

Because of the 100-fold increase in sensitivity between *Swift*/BAT and *NuSTAR*, for

any source detected in the *Swift*/BAT all-sky survey, an observation with the minimal *NuSTAR* exposure of ≃20 ks (*snapshot*) is essentially guaranteed to generate data with signal-to-noise ratio (SNR) high enough for basic spectral modeling (i.e., beyond the hardness ratio methods that deep surveys are limited to; e.g., Civano et al. 2015, Mullaney et al. 2015). Despite the short exposures compared to long observations aimed at detailed spectroscopic studies of particularly interesting AGN (e.g., Arévalo et al. 2014, Ballantyne et al. 2014, Puccetti et al. 2014, Baloković et al. 2015, Bauer et al. 2015, Lohfink et al. 2015, Guainazzi et al. 2016), the survey has led to a number of interesting studies of heavily obscured local AGN based on *NuSTAR* snapshots (e.g., Baloković et al. 2014, Annuar et al. 2015, Rivers et al. 2015a, Koss et al. 2016b, Masini et al. 2016, Puccetti et al. 2016). Many of the AGN observed with long exposures are among the brightest local AGN, and hence have *Swift*/BAT counterpart although they were formally not observed as a part of the *NuSTAR* snapshot survey. For the sample presented here we mainly use the short observations, but also employ longer exposures where it is beneficial for making the data set more uniform in quality.

The survey utilizes the latest publicly available catalog of *Swift*/BAT AGN, compiled using 70 months of BAT exposure (Baumgartner et al., 2013). The 70-month catalog classifies AGN into five different categories, one of which ("class 5") contains AGN of optical type 1.8, 1.9 and 2.0. We refer to this group of AGN as *Sy II* hereafter. The prevalence of obscured AGN observed in the survey is due to prioritization of that class over others, because the high sensitivity of *NuSTAR* can be most uniquely exploited for studying AGN with the heaviest obscuration. The snapshot survey of *Swift*/BAT-selected AGN has proven to be valuable for studies of both local and higher-redshift AGN population, and continues to provide data to the community thought the *NuSTAR* Extragalactic Legacy Survey program.[2] The program is further enriched with follow-up observations with *Swift*/XRT, which provide valuable quasi-simultaneous spectral coverage below the lower end of the *NuSTAR* bandpass (< 3 keV). The combination of *Swift* and *NuSTAR* instruments therefore provides continuous (in fact, overlapping) broadband spectra over nearly four decades in photon energy, from ≃ 0.5 keV up to ≃ 200 keV.

5.2.2 The Main Sample

In order to get a more uniform selection, we apply a cut in flux in the *Swift*/BAT band (14–195 keV), $f_{\rm BAT} > 10^{-11}$ erg s^{-1} cm^{-2}, and a cut in redshift, $z < 0.1$. The total

[2] `http://www.nustar.caltech.edu/page/legacy_surveys`

number of Sy II in the *Swift*/BAT 70-month catalog with these cuts applied is 230. Of those, *NuSTAR* data are publicly available for more than 135 *Swift*/BAT AGN observed before mid-2017, with multiple observations available for approximately 10 % of the targets. From this initial selection we removed a number of bright sources that received long exposures because the observations were done as part of other *NuSTAR* programs. By excluding them we decrease the extreme range of data quality within our sample, so that the spectral analysis could be done more uniformly. We do, however, consider these AGN to be parts of the full *Swift*/BAT-selected sample (see § 5.2.3), as they are important for population statistics, and their high-quality spectra help with understanding the lower-quality spectra of the main sample targets. Basic data for 124 targets selected for our main sample is listed in Table C1. In order to improve readability, this table, and other tables exceeding a single page in length, is placed in the Appendix.

Due to the significantly better spatial resolution of *NuSTAR*, a number of *Swift*/BAT sources are resolved into two or more individual sources. In most cases one of the sources is significantly brighter while the other(s) would likely be undetectable with *Swift*/BAT if they were further apart. Lansbury et al. (2017) present the analysis of serendipitously detected sources in the field of view during observations targeting *Swift*/BAT AGN. We have verified that in all cases the *NuSTAR* source associated with the optically-detected Sy II is the brightest. Two exceptions are the observations of SWIFT J0209.5−1010 and SWIFT J2028.5+2543, where in both cases we find two sources of nearly equal brightness and both fit the Sy II classification. The former includes NGC 833 and NGC 835 (both narrow-line low-luminosity AGN in the HCG 16 group; O'Sullivan et al. 2014, González-Martín et al. 2016), while the latter consists of NGC 6921 and MCG +04-48-002 in a triple interacting system (Koss et al., 2016b). We consider each of the four AGN separately as parts of our sample.

Our main sample covers more than 50 % of the parent sample, and it is statistically consistent with a random draw. We compare the main sample to its parent sample in terms of distributions of flux ($f_{\rm BAT}$), redshift (z) and luminosity ($L_{\rm BAT}$) taken from the *Swift*/BAT 70-month catalog. Although these three quantities are not independent, matching three distributions provides additional assurance of good representation of the redshift-luminosity plane. According to a two-sample Kolmogorov-Smirnov test, all three distributions are consistent between our main sample and the parent *Swift*/BAT sample. Our sample is therefore statistically representative of the

larger *Swift*/BAT-selected sample of Sy II in the local Universe. In Figure 5.1 we show the coverage of the redshift-luminosity plane down to the *Swift*/BAT flux cut at 1×10^{-11} erg s^{-1} cm^{-2} and up to $z = 0.1$. Sources observed with *NuSTAR* as part of the sample presented here are marked with circles, demonstrating the uniformity in *NuSTAR* coverage of the parent sample.

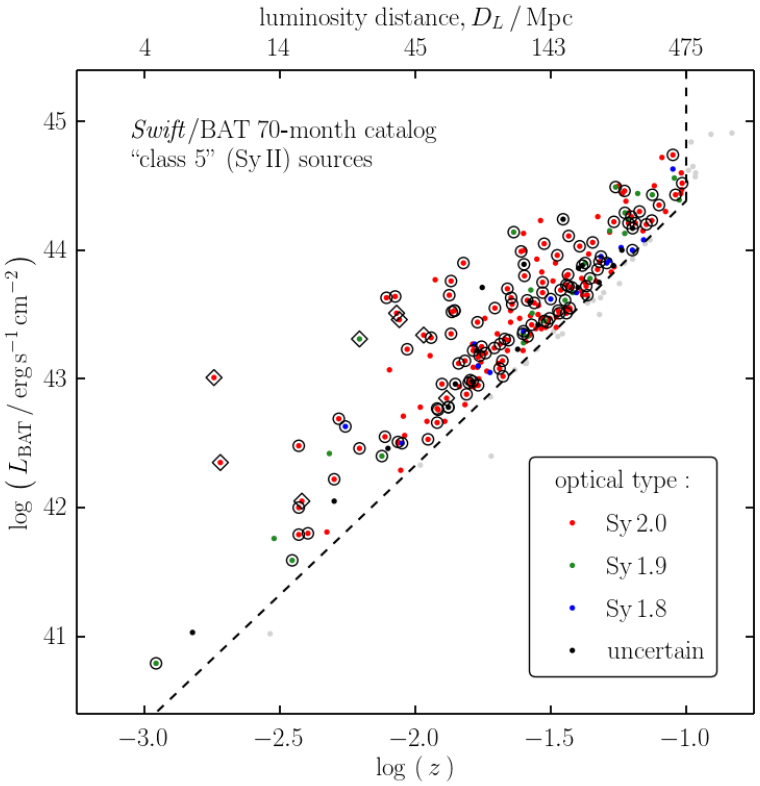

Figure 5.1: Redshift-luminosity plane covered by the parent sample of *Swift*/BAT-selected Sy II sources ("class 5" in the *Swift*/BAT 70-month catalog). The 230 sources that satisfy cuts in flux and redshift described in § 5.2.2 (shown with black dashed lines) are plotted in colors that correspond to their cataloged optical type. Grey points show *Swift*/BAT sources excluded by our cuts. We mark the sources targeted with *NuSTAR* and presented in our main sample with black circles, or with a black diamond if they are listed in the excluded sample.

5.2.3 Targets Excluded from the Main Sample

We compile a list of sources excluded from the main sample despite meeting our selection criteria, because they require spectral modeling outside of the scope of the study presented here. *NuSTAR* observations of *Swift*/BAT-selected Sy II with the highest total number of counts were acquired in targeted observations and not as part of the snapshot survey, which is described in § 5.2.1. For this reason, their

simultaneous *Swift*/XRT data are lacking, or are piled-up in some cases, and require special treatment. We exclude them from the uniform spectral analysis performed on the main sample because the simple models considered in this work do not fit their observed spectra. The *NuSTAR* data for these AGN have been analyzed in detail in dedicated publications. We report on previous results from the literature and or own modeling of these sources in Appendix B.

To the list of excluded targets we also add AGN with spectra that require special treatment despite moderate SNR (e.g., inseparable pair of AGN in SWIFT J0350.1−5019, or atypically steep spectra of ESO 383-G018 and IRAS 05189−2524), and AGN with good-quality *NuSTAR* data that formally do not meet the *Swift*/BAT 70-month catalog optical selection criteria although part of the literature classifies them as Sy II. This way we keep the selection of the main sample as simple as possible, yet also discuss spectra of AGN that arguably should have been included if the classification methodology of the *Swift*/BAT 70-month catalog were different in details. For example, CT AGN NGC 424 (see Chapter III) is usually optically classed as a Sy 2, but is assigned to the Sy I group in the *Swift*/BAT catalog, most likely because broad lines have been detected at a low level in some observations (Murayama et al. 1998, Moran et al. 2000). Although spectral parameters of these sources do not enter our analysis of the sample, it is important to consider them in population statistics.

5.3 Data Reduction and Analysis Methods

5.3.1 Data Selection and Processing

NuSTAR Data

The data for all targets in the main sample (listed in Table C1) was processed as uniformly as possible. However, the *NuSTAR* survey of *Swift*/BAT AGN covers a factor of $\simeq 50$ in X-ray flux, and the exposures do not scale with the targets' apparent brightness. Some very bright objects have been observed with significantly more exposure because the observations were intended for detailed multi-epoch studies: e.g., NGC 1365 (Rivers et al., 2015b) and Mrk 3 (Guainazzi et al., 2016) in the main sample, and most of the targets in the excluded sample. In those cases, we chose observations for which quasi-simultaneous *Swift*/XRT data were taken, since typically only one epoch would be followed-up with *Swift*. In other cases, fainter targets were observed more than once to study variability (e.g., IC 751; Ricci et al. 2016), or to increase data quality (e.g., NGC 5643; Annuar et al. 2015). If no

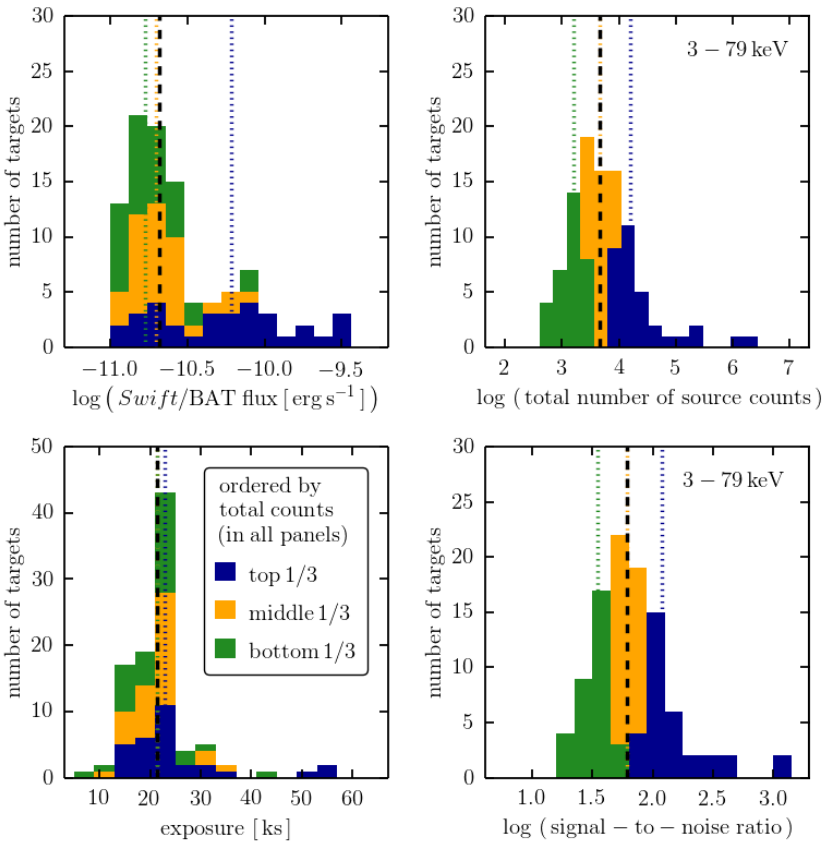

Figure 5.2: Distributions of the *Swift*/BAT 70-month catalog flux, *NuSTAR* exposure times, total number of source counts, and signal-to-noise ratio in the full *NuSTAR* band, 3–79 keV. The histograms are colored according to the total number of source counts so that the third of the sample with the highest number of counts is shown in blue, while the middle and the bottom third are shown with yellow and green, respectively. Dashed vertical lines denote distribution medians and dotted lines enclose 68 % of the distributions.

significant variability was detected, we coadded data from multiple observations, otherwise we chose the observations which either had quasi-simultaneous *Swift*/XRT coverage or represents a closer match to the typical data quality of the main sample.

The data for each of the 124 targets in the main sample was uniformly reduced with the same basic procedure. To this end we developed an automated approach that reduces the number of arbitrary human choices in data processing to a minimum, and at the same time maximizes the high-energy signal-to-noise ratio of the spectra for the short exposure times typical for this survey. Basic information regarding observation IDs, times of observation, exposures, and data quality is given in Table C2. A graphical representation of data quality is given in Figure 5.2.

For 116 targets we use single *NuSTAR* obsIDs, while for the rest we coadd two or more. For four targets (IC 1663, 3C 105, 2MASX J04234080+0408017 and LEDA 3097193) multiple obsIDs represent essentially a single-epoch observation: the obsIDs were separated because telescope pointing needed to be refined mid-observation early on in the *NuSTAR* mission, or they were interspersed between Target of Opportunity or calibration observations. CGCG 420-015 was observed three times in total, including one ∼100-ks observation, for a detailed study presented in a dedicated paper (Marinucci et al., in preparation); here we coadd the two short observations in order to improve data quality but not make it significantly higher than the sample median. For NGC 5643 two observations were taken in order to improve the data quality (Annuar et al., 2015). For the targets discussed above we find no variability between the observations for which we coadded the data. The coadded data from multiple observations represent the longest exposures in our data set, ranging up to 42 ks. The shortest exposure time is just 3 ks (MCG +11-11-032). Most targets were observed for 15–25 ks, the average being 20.0 ks.

We processed the raw data using the standard *NuSTAR* data processing package, `NuSTARDAS`, generally following the procedures described in the *NuSTAR* user's guide.[3] We used a range of software editions (`HEASOFT` 6.14–6.16, `NuSTARDAS` 1.4–1.6) and versions of the calibration database (between 20130909 and 20150316). No significant changes were noted in updating from an older to a newer version. Event filtering was performed with the `nupipeline` script, generally following the recommendations of the *NuSTAR* Science Operations Center regarding the filtering level and leaning toward stricter filtering rather than slightly longer exposure.

We developed an automated procedure for choosing the size of the source extraction region that optimizes the signal-to-noise ratio (SNR) in the 24–79 keV band. The algorithm steps through a range of extraction region radii ($r_{\rm ext}$), computing SNR as the ratio of the number of source counts to its uncertainty after background subtraction. The background extraction region is defined as the square area of the detector onto which the target is focused, excluding the circular region 30 % larger than the source extraction region centered on the source and any detected serendipitous sources. The optimum radius is then identified as the the largest radius at which SNR is within 10 % from its broad peak. We show examples of this calculation for several sources of different brightness in Figure 5.3. Applying it to our whole sample, we find that the following empirical scaling relation provides a

[3] `http://heasarc.gsfc.nasa.gov/docs/nustar/analysis/nustar_swguide.pdf`

good estimate of the optimal extraction region radius (±15″) for any short 20-ks *NuSTAR* exposure:

$$r_{\rm ext}\,/\,'' \approx 100 + 45 \times \log {\rm CR}\,.$$

In the expression above, CR is the single-FPM PSF-corrected count rate in the 3–79 keV band. This count rate can be retrieved from the lightcurve downloaded with the raw *NuSTAR* data from the HEASARC archive to quickly choose an appropriate region size without human interference.

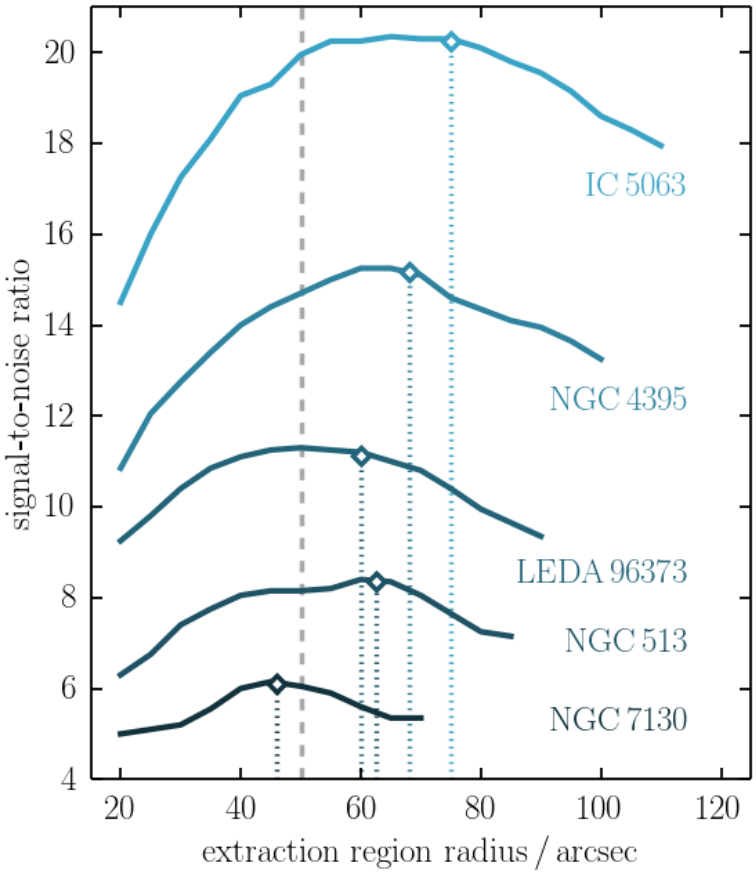

Figure 5.3: Five examples of the optimized source extraction radius calculation. SNR is calculated in the 24–79 keV band (as described in § 5.3.1) and starts decreasing from its broad peak at larger radii for brighter sources. Optimized radius for each example is marked with a diamond symbol and a dotted vertical line of the same color.

The source and background spectra were extracted using the `NuSTARDAS` script `nuproducts`, which generates the calibrated ARF and RMF files. Multiple observations are coadded at this stage and their ARF and RMF files are averaged over. We group the source spectra with a custom built script which distributes the energy bins

so that they have approximately constant SNR per bin. The algorithm first finds the energy around which photon spectral density peaks (which primarily depends on the shape of the source spectrum). Starting from that energy it progresses toward both lower and higher energies adding bin borders until it reaches either the bandpass limits or finds insufficient counts to form more bins. The highest and the lowest bins are then optimized by iteratively shifting the bin borders so that the energy grid covers as much of the bandpass as possible while keeping the SNR of each bin above 3 and close to the median (typically 4–6, and around 10 for very bright sources). In Table C2 we report the median SNR per bin, the minimum number of source counts per bin and the total number of bins for each source.

Swift Data

As described in § 5.2.1, targets are selected for *NuSTAR* observations from the *Swift*/BAT 70-month catalog (Baumgartner et al., 2013) and typically followed-up with a *Swift* observation within approximately one day. We refer to the *Swift* observations taken as part of the survey as quasi-simultaneous (QS) hereafter. *Swift*/BAT 8-channel spectra (14–195 keV) are available for all sources and we use them as published on the *Swift*/BAT 70-month catalog webpage.[4] We generally included *Swift*/BAT spectra in our spectral analysis, except in certain special cases (see notes on individual sources in Appendix A). Data quality indicators such as the count rate, SNR, and median SNR per bin are given in Table C2 for both XRT and BAT data. In this study we did not make use of any *Swift*/UVOT data.

For most targets (104) we used only the QS *Swift*/XRT spectra in combination with *NuSTAR*, in order to minimize the possibility of spectral variability between non-simultaneous observations. However, for some faint targets, the QS *Swift*/XRT data would be insufficient for even the basic spectral analysis, and in some cases the observations were not performed for technical reasons. In those cases, we searched the *Swift*/XRT archive for other observations and select those in which the full-band (0.3–10 keV) background-subtracted source count rate is consistent with the QS observation within photon-counting uncertainties, or those that are consistent with the *NuSTAR*-based 3–7 keV flux in the case where the quasi-simultaneous data were not taken. For 3 targets (Mrk 728, NGC 4388 and NGC 5252) we did not find any *Swift*/XRT data that satisfy these criteria. For 13 we coadded data from multiple *Swift*/XRT observations with consistent count rates in order to increase

[4] `http://swift.gsfc.nasa.gov/results/bs70mon/`

the data quality. We provide the complete list of observations for those sources in Table 5.1. In a few cases, the coadded observations are consecutive (as are *NuSTAR* observations of those targets) and should all be considered QS. All data were taken in the photon-counting mode.

Swift/XRT data were processed using the ASDC XRT Online Analysis service.[5] A range of software versions (`HEASOFT` 6.14–6.19, `XRTDAS` 3.0.1–3.2.0) and editions of the calibration database (20150401–20160909) were employed in data reduction. We did not notice any significant changes between reductions using earlier software versions and those later re-reduced with newer versions. The `xrtpipeline` script was used to perform standard filtering. Source spectra were typically extracted from circular regions $50''$ in radius, unless a smaller radius was needed in order to avoid nearby contaminating sources. Likewise, background spectra were extracted from annular regions around the target taking care that they do not include any contamination. For *Swift*/XRT data processed with the intention of coadding we made certain that the same extraction regions were used, and that the source is no more than $5'$ away from the center of the field of view in order to minimize the effects of the spatially non-uniform sensitivity, since we compared observations by raw (vignetting-uncorrected) count rates.

The `xrtproducts` script was used to produce the ARF and RMF files. For observations suitable for coadding, the source and background spectra were coadded at this stage, and their ARF and RMF files were averaged. Whenever possible, we grouped the spectral files using the same algorithm described in § 5.3.1. However, in the low-count cases it was necessary to lower the SNR criteria to the range between 2 and 4 per energy bin. The lowest-quality *Swift*/XRT spectra consist of only two bins, and as few as 7 photons per bin (see NGC 454 E, ESO 005-G004, and IRAS 07378−3136 in Table C2). In the case of NGC 454 E, for example, the QS observation yielded only $\simeq 15$ source counts. Three other *Swift*/XRT observations all show significantly higher source count rates (by a factor of $\gtrsim 5$, which indicates significant variability and prevents us from combining the QS and additional archival data. The *Swift*/XRT data could be replaced with other non-simultaneous soft X-ray data of higher quality in order to provide better spectral parameter constraints, but we leave that to future studies. Here we emphasize the maximal simultaneity of our broadband X-ray observations for a large number of targets, and deliberately let the *NuSTAR* data dominate the statistical weight in model fitting.

[5] `http://www.asdc.asi.it/mmia/index.php?mission=swiftmastr`

Table 5.1: Information on coadded *Swift*/XRT observations.

Target Name	Observation ID (1)	Observation Start (2)	Exposure (3)	CR_{src} (4)
LEDA 136991 ...	**00080006001**	2014-04-11 03:46	6.9	1.6 ± 0.6
	00036661002	2011-08-07 06:20	11.1	2.1 ± 0.5
NGC 833	00035908003	2007-12-03 10:44	2.8	0.3 ± 0.1
	00035908002	2007-02-24 13:03	5.2	0.26 ± 0.08
	00035908001	2006-11-03 01:33	7.7	0.28 ± 0.06
NGC 835	00035908003	2007-12-03 10:44	2.8	0.4 ± 0.1
	00035908002	2007-02-24 13:03	5.2	0.6 ± 0.1
	00035908001	2006-11-03 01:33	7.7	0.9 ± 0.1
2MFGC 2280 ...	**00080255001**	2013-02-27 12:47	6.6	0.2 ± 0.1
	00036662001	2007-11-22 17:37	6.4	0.11 ± 0.09
	00037106002	2007-07-20 00:38	8.2	0.16 ± 0.06
	00037106001	2007-07-18 00:40	9.8	0.23 ± 0.07
NGC 1229	**00080534001**	2013-07-05 09:52	6.5	0.3 ± 0.1
	00041743001	2010-10-19 06:08	7.5	0.5 ± 0.1
3C 105	**00080328003**	2013-02-16 04:42	2.2	0.4 ± 0.2
	00080328002	2013-02-15 15:43	2.3	0.6 ± 0.2
	00080328001	2013-02-15 02:43	2.2	0.3 ± 0.1
MCG +03-13-001	00041747003	2010-12-23 11:26	3.3	0.7 ± 0.2
	00041747002	2010-12-19 17:09	1.2	1.3 ± 0.3
	00041747001	2010-10-22 19:39	6.4	0.5 ± 0.1
2MASX J0903 ..	**00081040003**	2015-12-02 10:20	1.9	0.5 ± 0.1
	00081040002	2015-11-27 01:23	4.2	0.4 ± 0.1
	00081040001	2015-11-26 23:43	0.9	0.6 ± 0.1
IC 751	**00080064001**	2013-05-25 16:39	5.8	0.5 ± 0.1
	00037374001	2008-02-20 13:13	2.3	0.2 ± 0.1
NGC 5643	**00080731001**	2014-05-24 15:39	4.0	0.8 ± 0.2
	00032724009	2013-02-26 11:55	6.3	1.0 ± 0.1
	00032724004	2013-02-19 14:52	6.1	0.9 ± 0.1
	00037275001	2008-03-16 20:45	3.8	1.2 ± 0.2
NGC 6921	**00080266001**	2013-05-18 07:21	6.6	0.30 ± 0.08
	00035276003	2006-03-28 01:18	0.9	0.3 ± 0.2
	00035276002	2006-03-23 00:21	4.6	0.3 ± 0.1
	00035276001	2005-12-16 01:16	4.5	0.2 ± 0.1
MCG +04-48-002	**00080266001**	2013-05-18 07:21	6.6	0.37 ± 0.08
	00035276003	2006-03-28 01:18	0.9	1.0 ± 0.3

Notes: Columns: (1) observation ID, (2) observation start time in UTC, (3) exposure in ks, (4) background-subtracted source count rate in $10^{-2}\,s^{-1}$. Observation IDs shown in bold are quasi-simultaneous to the *NuSTAR* observations; if they are not shown, such an observation was not performed, or did not yield a clear detection of the source(s). Information regarding the coadded spectra is shown in Table C2.

5.3.2 Spectral Analysis

We perform spectral analysis of the X-ray data for each source in `Xspec` (Arnaud, 1996). Model fitting and error estimation is based on χ^2 statistics. The quoted 68 % confidence intervals on spectral parameters are defined as values for which χ^2 changes by 1 from the best-fit χ^2 while stepping through that parameter and fitting for all other free parameters. In a number of cases with severe degeneracy between spectral parameters, where the best fit places a certain parameter at the edge of the parameter space, `Xspec` is unable to provide a lower or upper limit, so we mimic the error estimation procedure and derive the limit manually. Those limits are shown in parenthesis in Table C3, but treated as normal limits in the rest of our analysis.

In order to evaluate whether a certain model provides a statistically acceptable fit to the data we use a null-probability ($p_{\rm null}$) threshold of 5 %. The null hypothesis here is that the observed data is a random draw from a particular model. $p_{\rm null}$ gives the probability of obtaining a χ^2 value as high (or higher) as that of the best fit under the null hypothesis. By definition, a good model will have $p_{\rm null} \approx 50$ %. Models for which the best fit does not exceed the 5 % threshold are rejected and replaced with more complex ones. It is important to note here that between the models with $p_{\rm null} > 5$ % it is not formally correct to compare which model fits the given observed spectrum better: they are all statistically acceptable representations of the data. In this work, which is focused on the phenomenological description of the spectra observed in our survey, we do not seek to find the best of all possible models for each source. Instead, we first find the simplest possible model for each source. Then we proceed to define a single model that fits all spectra in our main sample with $p_{\rm null} > 5$ %, and quantify how its spectral parameters vary within the sample. This procedure, and the models employed in this work, are described in § 5.4.1.

5.3.3 Bootstrapping the Spectral Parameter Distributions

We use a bootstrapping method in order to include the lower and upper limits into the probability density functions (PDFs) of the parameters of our spectral models. Instead of constructing the cumulative distribution function (CDF) from the best-fit values only, we calculate a large number of CDFs by resampling each parameter constraint according to an approximate PDF that peaks at the best-fit value and contains 68 % of the total probability within the 68 % confidence interval determined from `Xspec`, or that contains 16 % of the probability below an upper limit or above a lower limit determined from `Xspec`. From a collection of typically 10000 such CDFs we calculate the median CDF for each parameter distribution.

From such a CDF we derive a more informed estimate of the median and the 68 % probability interval, along with a measure of uncertainty in these numbers based on the spread of the resampled CDFs.

Our method formally requires a PDF for each spectral parameter constraint and each target in the sample. Since the true posterior PDF for each parameter is beyond the scope of this work,[6] in most cases we approximate it with a sum of two single-sided Gaussians (i.e., a Gaussian with different σ on each side of its peak). We tested a wide range of other simple yet reasonable choices and found that our results do not change significantly with different assumed PDF shapes, or estimated (and otherwise unconstrained) PDF medians for the fits that yielded only limits. The effect of these arbitrary choices may be more significant in smaller subsamples and parameters for which we have a large fraction of limits, but they are in no case driving the shape of any PDFs presented in this chapter. In the cases where the effects of the choice of the PDF functional form are noticeable (see § 5.6.1), we incorporate the estimated systematic uncertainty into the uncertainty quoted on the median and the 68 % interval boundaries.

5.3.4 Notation and Definitions

- Confidence intervals for any PDFs are specified so that they contain 68.27 % of the probability, roughly corresponding to $1\,\sigma$ uncertainties of the PDF approximated by a Gaussian. We denote the PDF median for a parameter x as $M(x)$ and the 68 % interval as $I(x)$. Upper and lower limits are also given at the $1\,\sigma$ level, i.e., so that 15.87 % of the probability stays above or below the limit, respectively. Where a distribution can be well approximated by a Gaussian, we denote the standard deviation with $\sigma(x)$, and the mean equals the median by definition.

- We denote an interval with a pair of numbers enclosed in square brackets. For example, we specify 68 % probability interval for parameter x as $I(x) = [a \pm u_a, b \pm u_b]$, where a and b are boundaries of the interval, and u_a and u_b are estimated $1\,\sigma$ uncertainties on their values. The method of estimation of these uncertainties is described in § 5.3.3.

[6] Ideally, one would use sampling for the marginalized posterior PDF for each parameter derived from a Markov Chain Monte Carlo (MCMC) routine. However, given the number of targets and models considered in this work, and the fact that calculations with the `pexrav` component are time-consuming, we did not rely on MCMC sampling. Where more modern and faster models are used, MCMC sampling is feasible even for large samples – see Chapters IV and VI.

- Any quoted uncertainties and confidence intervals refer only to statistical uncertainties, unless specified otherwise. Some tractable systematic uncertainties are discussed in § 5.6.

- Unless specifically noted otherwise, we quote luminosities in rest-frame energy bands, i.e., $L^{\rm int}_{[E_1,E_2]}$ is the luminosity of the intrinsic coronal continuum in the rest-frame $E_1 - E_2$ keV energy band. We generally use logarithmically equally spaced energy bands delimited by 0.4, 2, 10, 50, and 250 keV.[7] Note that $L_{\rm BAT}$, the luminosity given in the *Swift*/BAT 70-month catalog, is defined in the observer-frame 14-195 keV band.

- The photon index of the intrinsic coronal continuum is consistently marked with Γ without a subscript. As such, it is limited to values reproducible by AGN coronal models (see § 5.6.1), and can only be found from models including all other relevant spectral components. Whenever a photon index is used to describe the slope of an observed spectrum (i.e., neglecting absorption or reprocessed components; see § 5.6.4), we denote it with a subscript. These *effective* photon indices are not limited to any particular range of values.

[7] Note that this arrangement includes the common low-energy end of the bandpass of modern soft X-ray telescopes, the most commonly used 2–10 keV band and the hard 10–50 keV band, optimally suited for *NuSTAR* studies (but generally covering the most sensitive energy range for other hard X-ray instruments with minimal extrapolation). The Compton hump is contained within the 10–50 keV band in a very broad range of physical conditions. The 50–250 keV band, in principle, reaches up to the typical high-energy cutoff in AGN spectra, but the sensitivity of current instruments in that energy range is quite limited (see, e.g., Krivonos et al. 2015).

Table 5.2: Summary of the spectral models used in this chapter

Model Name	Short Description	Xspec Expression	Free Parameters	Number of Good Fits
A	$f(E) \propto E^{-\Gamma} \times e^{-E/E_{\rm cut}}$	c_1×cutoffpl	Γ	9
B	A, with line-of-sight absorption	c_1×phabs×(zphabs×cabs×cutoffpl)	Γ, $N_{\rm H}$	48
C	B, with a 6.4 keV line	c_1 ×phabs×(zphabs×cabs×cutoffpl+zgauss)	Γ, $N_{\rm H}$, $n_{\rm Fe}$	2
D	intrinsic+secondary continuum	c_1 ×phabs×(zphabs×cabs×cutoffpl+c_2×cutoffpl)	Γ, $N_{\rm H}$, $f_{\rm sca}$	19
E	D, with a 6.4 keV line	c_1×phabs×(zphabs×cabs×cutoffpl+c_2×cutoffpl+zgauss)	Γ, $N_{\rm H}$, $f_{\rm sca}$, $n_{\rm Fe}$	16
F	E, with reprocessed continuum	c_1×phabs×(zphabs×cabs×cutoffpl+c_2×cutoffpl+zgauss+pexrav)	Γ, $N_{\rm H}$, $f_{\rm sca}$, $n_{\rm Fe}$, $R_{\rm pex}$	30

Notes: The cross-normalization factor (c_1) is fixed to unity for *NuSTAR*/FPMA, and is fitted for all other instruments. Γ parameters are linked to be equal in all spectral components. All fits include the normalization of the intrinsic continuum as a free parameter. Redshift of each AGN and the intervening Galactic column density are included in all models and the parameters are kept fixed at values listed in Table C1. Unless explicitly stated otherwise, for models that have the following parameters, we keep them fixed at these values: $E_{\rm cut} = 300$ keV (cutoffpl), $E_{\rm Fe} = 6.4$ keV and $\sigma_{\rm Fe} = 1$ eV (zgauss), $\cos\theta_{\rm inc} = 0.45$, and $A_{\rm el} = A_{\rm Fe} = A_{\odot}$ (pexrav). The last column shows the number of sources for which a particular model is the simplest acceptable modeling solution. Note that in Table C3 we append a "−" sign to the model name if any of the default parameters are frozen, a "+" sign if any parameters in addition to the default set are being fitted, or a "±" sign if both situations apply.

5.4 Spectral Modeling

5.4.1 Basic Models

We start our spectral analysis with the simplest power-law model, which fits only 9 sources well according to our acceptance criterion $p_{\rm null} > 5\,\%$ (see § 5.3.2). We immediately replace the power law with a cutoff power law, since a high-energy cutoff in the intrinsic continuum is expected in AGN. For the high-energy cutoff ($E_{\rm cut}$) we choose a fixed value of 300 keV, which is justified post-facto in § 5.6.1. This model is labeled A in Table 5.2, which summarizes the `Xspec` expressions of each model, their main spectral parameters and the number of AGN from our main target list for which they represent the simplest statistically acceptable modeling solution. Next, we add a narrow Gaussian component with unresolved line width ($\sigma = 10^{-3}$ keV) at the energy of the Fe Kα line, 6.4 keV; however, that does not result in any additional acceptable fits.

In model B, we include line-of-sight absorption applied to the intrinsic continuum, parametrized by $N_{\rm H}$. This model represents the simplest well-fitting solution with $p_{\rm null} > 5\,\%$ for 48 sources in our main sample. Addition of a narrow emission line at 6.4 keV (model C) pushes additional 2 sources over the threshold. Models D and E are analogs of models B and C, with addition of a weak secondary power-law continuum component with the same spectral shape as the intrinsic continuum and a relative normalization parametrized by the parameter $f_{\rm sca}$.[8] They represent the simplest models for 19 and 16 sources, respectively. Spectra of the rest of the main sample (30 sources) can only be described well with model F, which includes the reprocessed continuum represented by `pexrav`[9] in addition to the components of model E.

For a small fraction of sources in the main sample the data apparently cannot be fitted well with any of the models described here, but in those cases most of the high χ^2 can be attributed to an issue in the data. We consider those cases in more detail in

[8] Physically, this component is usually interpreted as being due to either Thomson scattering of the intrinsic continuum on free electrons in the NLR, incomplete (partial) covering of the X-ray source by the intervening material, or unresolved non-AGN components due to the host galaxy. We only consider AGN-related origin of this component, hence assuming that its spectral shape is the same as that of the intrinsic continuum. We use the interpretation-neutral label "secondary continuum" hereafter.

[9] For simplicity, throughout this study we use `pexrav`with a fixed inclination angle and Solar elemental abundances. We parametrize the relative strength of the reprocessed continuum with respect to the intrinsic continuum with the parameter $R_{\rm pex}$, defined as $R_{\rm pex} = |R|$, where R is a negative number in the `Xspec` implementation of the model.

§ 5.4.2, showing that model F is in fact sufficient to fit all spectra in our main sample with $p_{\rm null} > 5\,\%$. Although models A through E fit most of our sample (88 sources) well enough to be formally acceptable in terms of fitting statistics, in many cases the data can constrain additional parameters not included in the simplest model. Additional components may not be formally required by the data in all cases, but including them does provide important limits on their contribution and prevalence in the target population. We therefore attempt fitting model F to all spectra in our sample without regard for statistical significance of particular spectral components.

Not all parameters can be constrained for all targets: different groups that share spectral properties also share a number of issues with this modeling approach, so we elaborate them in more detail in the following subsections. Model F lacking one or more parameters due to the issue described here is marked with a minus in the subscript in Table C3 and the rest of the text. Some spectra allow us to constrain one or two additional spectral components, while keeping all the relevant parameters of model F essentially unaffected and therefore comparable to the rest of the sample (see § 5.4.5). For including extra components/parameters in model F, beyond the default listed in Table 5.2, we add a + sign in the subscript or a ± sign if any reduction in the number of spectral parameters was needed at the same time. In Appendix A we provide a brief description of the fitting procedure for a number of sources with best-fit models F_{-}, F_{+} and $\mathrm{F}_{\pm}$. In the remainder of this chapter, we refer to the spectral solution based on model F (with any of the necessary modifications) as the `full` model, and the simplest model (whether it is models A through E, or also model F) as the `simple` model for any given target.

In addition to one row showing the set of parameters of the simplest acceptable model and the set of parameter constraints for the full model (unless the two are the same), Table C3 may contain additional rows for some sources. These extra rows contain sets of model parameters that provide an alternative interpretation of the observed spectra. For example, we flag all objects for which the simplest model suggest CT obscuration ($N_{\rm H}$ consistent with $10^{24}\,\mathrm{cm}^{-2}$ within uncertainties, or Fe Kα EW consistent with 1 keV) and additionally model these sources as described in § 5.4.4 in order to establish their CT nature. As they are of special interest in this study, yet not easy to identify unambiguously, we discuss CT AGN in more detail in § 5.4.4.

5.4.2 Partial Exclusion of Data

Inclusion of *Swift*/BAT data in the fitting does not generally bias the results; however, the *NuSTAR*-based flux can differ significantly from the flux based on the time-averaged *Swift*/BAT data. In order to avoid the possibility that the *Swift*/BAT data drive fits toward a different spectral solutions, we repeat a number of fits using only *NuSTAR* and *Swift*/XRT data. Specifically, we select all targets for which the *NuSTAR*-*Swift*/BAT cross-normalization factor is consistent with an offset by more than a factor of two, and inconsistent with unity within the uncertainty interval for the cross-normalization factor. An analysis of cross-normalization factors and a direct comparison between *Swift*/BAT and *NuSTAR* fluxes is presented in § 5.6.4). Excluded from this analysis are the two pairs of sources not resolved by *Swift*/BAT, for which we do not use the *Swift*/BAT data because the spectrum is clearly a mixture of contributions from both AGN in each of the pairs. For all targets with a non-unity cross-normalization between *NuSTAR* and *Swift*/BAT spectra, we performed fits excluding *Swift*/BAT and found that there are no significant changes to the spectral parameters. They are marked with a note in the last column in Table C3 for completeness.

For a few sources the best-fit spectral parameters of the `full` model do change significantly, i.e., by more than their statistical uncertainties from the fit including *Swift*/BAT data. For example, exclusion of *Swift*/BAT data for MCG +11-11-032 leads to a best-fit model with a rather soft Γ (2.1 ± 0.2) and high $R_{\rm pex}$ (3^{+3}_{-1}), which is likely just a degenerate result due to relatively low data quality. Given the very low $\mathrm{EW}_{\mathrm{Fe\,K}\alpha}$ (< 0.1 keV) and the variability revealed by the fact that the *Swift*/BAT flux is more than a factor of two higher than the one implied by the *NuSTAR* data, we conclude that this is not a RD spectrum of a CT AGN. Fixing $\Gamma = 1.8$ for the fit to *Swift*/XRT and *NuSTAR* data only, we find a model consistent with the initial one (where the *Swift*/BAT data were included), where none of the spectral parameters are outliers in terms of the main spectral parameters. A very similar situation happens with NGC 3786: removal of *Swift*/BAT data results in added degeneracy between Γ and $R_{\rm pex}$, but fixing Γ to a reasonable value essentially recovers the best-fit model derived with *Swift*/BAT data included, despite the relatively large cross-normalization offset. For this reason, in both cases discussed here, we choose to represent these AGN with `full` models based on fits that include *Swift*/BAT.

For some observed spectra it is impossible for any model to fit well according to our $p_{\rm null} > 5\,\%$ criterion. In those cases we were able to identify 1–5 energy

bins clearly offset from the rest of the observed spectrum, without any obvious spectral feature that they could correspond to. We therefore treated them as issues with the data (e.g., imperfect background subtraction) and ignored relevant energy ranges where censorship was necessary in the sense that no model would fit the data without the removal. For example, ignoring a single excessive *Swift*/BAT bin results in a noticeably lower χ^2 for 2MASX J0356 and 2MASX J0923, while for 2MASX J0508 we needed to ignore two highest-energy bins of the *Swift*/BAT spectrum. For NGC 4992, NGC 7582, and Mrk 1498, χ^2 is lowered significantly if we ignore an apparent excess in the *NuSTAR* data below 4 keV. Likewise, ignoring the high-energy end of the *NuSTAR* bandpass reduces χ^2 for NGC 4992 (> 60 keV), 2MASX J1410 (> 50 keV) and NGC 5995 (27–47 keV, *NuSTAR*/FPMA only). For the majority of the sample (95 %) we use the complete *NuSTAR* and *Swift* datasets as described in § 5.3.1 and § 5.3.1.

5.4.3 Unobscured Sources

We find that 12 targets can be considered unobscured given our log $N_{\rm H}/{\rm cm}^{-2} < 22$ criterion, although not all of them are immediately identified by fitting model A to their broadband spectra. IRAS 12074−4619, 2MASX J2119 and PKS 2331−240 are fitted well with model B, which provides full constraints on their $N_{\rm H}$. For each of the 12 sources, we apply model F without the Thomson-scattered continuum (which cannot be constrained because it is simply not observable in these sources) to find upper limits on $N_{\rm H}$ and other spectral parameters. For 6 targets we derive "forced" upper limits by stepping through $N_{\rm H}$ from essentially zero toward higher values.

Application of model F to the spectrum of 2MASX J0756 results in a best fit with log $N_{\rm H}/{\rm cm}^{-2} = 22.1 \pm 0.4$, which is formally above our adopted log $N_{\rm H}/{\rm cm}^{-2} = 22$ threshold for obscured sources. Due to the limited quality of our data for this source and the large statistical uncertainty,[10] we consider this AGN as unobscured, following the modeling results of de Rosa et al. (2012) based on higher-quality soft X-ray data from *XMM-Newton*. For Mrk 728 we are only able to place a relatively high upper limit at log $N_{\rm H}/{\rm cm}^{-2} < 22.3$ because there is no *Swift*/XRT data available. Although this AGN could formally be considered marginally obscured, in a previous study by Vasudevan et al. (2013) its *XMM-Newton* spectrum was modeled as fully unobscured. Of the remaining targets, we find full constraints for three and upper limits for five, all below the log $N_{\rm H}/{\rm cm}^{-2} = 22$ threshold for obscured AGN.

[10] Choosing to fix Γ at a value of 1.8 or lower results in an acceptable fit with log $N_{\rm H}/{\rm cm}^{-2} < 22$; see Table C3.

5.4.4 Heavily Obscured and CT Sources

Difficulties in spectral modeling of AGN with $N_{\rm H}$ near or above the CT threshold are mainly due to the fact that the absorbed power-law component, which dominates the spectrum at non-CT $N_{\rm H}$, becomes commensurate with the reprocessed component. Some of these issues were explored in detail in Chapter III, and we only briefly describe some examples here. One basic problem is whether to classify a source as CT AGN is different models place it both above and below the CT threshold. In the cases of CGCG 420-015 and MCG +04-48-002, for example, we find that our $N_{\rm H}$ constraint is consistent within the 68 % uncertainty with 10^{24} cm^{-2}. Because their $N_{\rm H}$ is slightly lower in the more complex model (`full`, as opposed to `simple`), and the fact that in part of the literature $\log N_{\rm H}/{\rm cm}^{-2} > 24.1$ is taken as the CT threshold, we do not consider them to be CT AGN.

On the other side of the CT threshold, for NGC 3281 we find $\log N_{\rm H}/{\rm cm}^{-2} = 24.1 \pm 0.1$, although the spectrum is clearly dominated by reprocessed light which implies $N_{\rm H}$ far in excess of 10^{24} cm^{-2}. A very similar issue, where a weak transmitted component contributes only a minor amount of flux in the Fe Kα region, was discussed for NGC 424 in Chapter III. We therefore count this AGN securely among CT AGN, despite its previous classification as non-CT source (Vasylenko et al., 2013), which is likely due to real $N_{\rm H}$ variability. Coincidentally, CGCG 420-015 and MCG +04-48-002 discussed in the preceding paragraph, have previously been considered CT AGN, which is also likely due to $N_{\rm H}$ variability (see Severgnini et al. 2011, Koss et al. 2016b, Marinucci et al., in preparation).

For CGCG 164-019 the fits with assumed $\Gamma \leqslant 1.8$ suggest $\log N_{\rm H}/{\rm cm}^{-2} \simeq 23.9$; however, $R_{\rm pex}$ and $f_{\rm sca}$ are high in comparison with the rest of our sample. For $\Gamma > 1.8$ the fits are dramatically different, with $\log N_{\rm H}/{\rm cm}^{-2} \geqslant 24.5$ and very poorly constrained other parameters, as typical for RD spectra. Both extremes of assumed Γ can be interpreted as RD spectral signatures, and the relatively high EW of the Fe Kα line ($\simeq$0.4 keV, up to 0.9 keV within $1\,\sigma$) also agrees with this classification. In order to formally test this solution, we also perform a fit with $\log N_{\rm H}$ fixed at values ranging from 24.1 to 24.5: the $\log N_{\rm H}/{\rm cm}^{-2} = 24.3$ case is shown in Table C3 and other choices of $\log N_{\rm H}$ are consistent with it within parameter uncertainties. As this is the most reasonable spectral solution, we use it as the representative `full` model fit for CGCG 164-019.

For LEDA 96373 we find strong preference for a very hard Γ (1.5 ± 0.1 if fitted with the `full` model), which would imply that the source is not CT ($\log N_{\rm H}/{\rm cm}^{-2} =$

23.7 ± 0.1). However, $EW_{Fe\,K\alpha}$ exceeding 1 keV suggests an RD spectrum and hence a significantly higher log N_H in the CT regime, like in the case of NGC 3281. Forcing Γ against the χ^2 gradient shows that a reasonable CT spectral solution with $\Gamma \approx 2.0$ and $\log N_H/cm^{-2} \approx 24.1$ is formally acceptable. RD model fit with fixed log N_H= 24.1 is shown in Table C3 and considered as the `full` model solution for LEDA 96373.

For CGCG 164-019, LEDA 96373, as well as NGC 7130 and NGC 5643, we show the log N_H parameters as fixed values in Table C3. The reason for that is that constraints on the other spectral parameters strongly depend on the assumed N_H, unlike the cases of other "forced" limits. For unobscured AGN a well-constrained and stable fit can be found while N_H formally tends to zero because the intrinsic luminosity can be defined irrespective of the column. The same cannot be done for CT AGN with N_H essentially going to infinity, because the intrinsic luminosity then cannot be well defined, and parameters f_{sca} and R_{pex} effectively become unbound. We therefore evaluate the RD models at fixed values of log N_H and show those models and constraints on their other parameters in Table C3. However, for all practical purposes in the rest of this study we consider log N_H for these targets as lower limits. When binning the data in log N_H, which we otherwise separate by best-fit values, we consider them to be a part of the $\log N_H/cm^{-2} > 24.5$ bin.

5.4.5 Additional Spectral Components and Complex Models

Examining the residuals with respect to the basic model F, we find that for a number of sources the fit could further be improved by adding a thermal plasma component, fitting for the energy of the Fe Kα line (otherwise kept fixed at 6.4 keV), or fitting for the high-energy cutoff (E_{cut}, otherwise fixed at 300 keV). For the plasma component, we include `mekal`, and fit for the plasma temperature. Fitting for the Fe Kα line energy rarely results in a value inconsistent with 6.4 keV within the 68 % confidence intervals, so we keep it fixed in the majority of cases and make a note in Table C3 for spectra in which fitted line energy does not contain 6.4 keV within the 68 % confidence interval. The EW is given for the line energy fixed at 6.4 keV in all cases, to avoid possible blending of multiple lines in lower-quality spectra. Since fitting for E_{cut} generally adds more degeneracy and weakens constraints on all other parameters, we leave E_{cut} fixed at 300 keV for all fits presented in Table C3. An exception is ESO 103-G035, since fitting for E_{cut} significantly lowers the best-fit χ^2 in that case. We focus specifically on E_{cut} constraints in § 5.6.1.

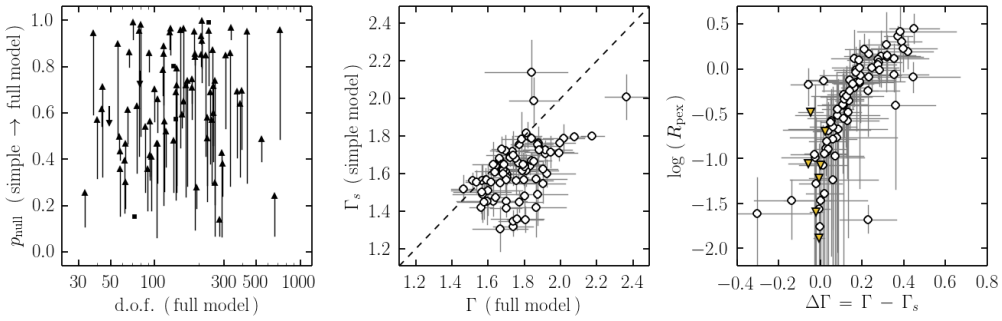

Figure 5.4: Changes in the main spectral parameters between `simple` models (with no reprocessed continuum) and `full` models (including reprocessed continuum). The left panel shows that the fitting statistic generally decreases, increasing $p_{\rm null}$ further above our chosen 5 % threshold. Γ generally changes so that the intrinsic continuum is softer, in order to accommodate a hard reprocessed component. This is further quantified in the right panel, where we show that the change in Γ correlates well with the relative normalization of the reprocessed continuum, parametrized by $R_{\rm pex}$.

In this work we only briefly consider a few possibilities for modifying the reprocessed continuum that provide a better fit or a more reasonable solution for some AGN in our sample (see § 5.6.3 and the Appendix). Although Γ is one the main modifiers, we keep it tied to the intrinsic continuum photon index, as there is no need to break the assumption that these parameters are equal.[11] Presenting the details of these additional solutions for each of our targets is beyond the scope of the present study, as it would increase complexity of the analysis at the expense of its uniformity, while contributing negligibly to physical interpretation. As we argue later in § 5.6.3, neither of these alternative model set-ups, nor the `pexrav`-based model itself, are likely to be good physical models for broadband X-ray spectra of Sy II. Detailed understanding of how they fit the data or fail to do so is therefore of limited practical value.

5.4.6 Differences Between `simple` and `full` Models

We briefly summarize our modeling by considering the differences between the representative `simple` and `full` models for each source. In the rest of the paper we are mostly discussing the `full` model results, as they represent the full spectral

[11] Physically, they could be different because of effects due to the details of structure of the innermost region around the SMBH, or extreme variability combined with time delays between direct and reprocessed emission, but these complex scenarios cannot be tested with neither the data nor the model used here.

characterization of the sample. The `simple` models are mainly employed to show what kind of biases can be expected from the use of this kind of simplification in the literature and in deep X-ray surveys, where data quality severely limits the complexity of spectral analyses.

It should be noted that straightforward application of model F to such a large sample results in a number of different ways in which the spectral solution become unreasonable. For example, in number of non-CT AGN spectra the best fit converges to very high $R_{\rm pex}$, in excess of what `pexrav` can reasonably represent according to the definition of $1/2 \times R_{\rm pex}$ as a sky covering factor. As we will elaborate further in § 5.6.3, $R_{\rm pex} > 1.5$ is also difficult to reconcile with newer geometrical torus models. We therefore investigate further whether the sources for which best-fit $R_{\rm pex}$ exceeds 1.5 can also be fitted well with lower values.

Since `simple` and `full` models are the same for 17 targets (i.e., no model simpler than model F fits the data well), they are not considered in this analysis. Figure 5.4 shows the most important change in going from a `simple` model, which does not include the reprocessed continuum, to the `full` model, which does include a reprocessed component. For nearly all targets[12] $p_{\rm null}$ increases further above our adopted $p_{\rm null} > 5$ % threshold. The photon index, Γ, becomes softer in all but a couple of low-SNR CT AGN spectra in order to accommodate the hard `pexrav` component. Generally, the change in Γ is larger for sources with higher best-fit $R_{\rm pex}$. According to the best-fit values for $R_{\rm pex}$, and the upper limits, the photon index in the `simple` models should in some cases be considered to describe the effective spectral slope (where it approximates both the intrinsic and the reprocessed continuum), while in other cases it likely equals the intrinsic continuum slope (where the reprocessed continuum contribution is negligible).

5.5 Results of Spectral Modeling

5.5.1 Distributions of the Main Spectral Parameters

The method we employ to construct distributions of spectral parameters from the uniform spectral analysis of the main sample is described in § 5.3.3. For each spectral parameter, we first consider the distributions of spectral parameters assuming `simple` models, i.e., models with the lowest number of spectral parameters needed to achieve a statistically acceptable fit for each source. Parts of the sample simply

[12] In two low-SNR cases it happens that due to the change in the number of degrees of freedom, $p_{\rm null}$ actually decreases by a small amount.

do not require some spectral components, which means that the `simple` model distributions are biased as they do not include any upper limits on expected but undetected components.

The `full` model includes all components described in § 5.4.1, even if they are not formally required by the data. Within the framework of the assumed model, all spectral parameters are constrained except for the exceptional cases of low-SNR data, and `full` model parameter distributions provide a complete spectral characterization of the sample. The distributions of best-fit parameters and cumulative probability distributions (CDFs), which account for limits, are shown in Figures 5.5 and 5.6. The medians and 68 % probability intervals of these distributions are summarized in Table 5.3. The table also includes calculations for a subsample of 97 targets with $22 < \log N_{\rm H}/{\rm cm}^{-2} < 24$.

Photon Index

For the `simple` models, owing to their simplicity and the quality of the data, we are unable to constrain the photon index (Γ) for only one target, NGC 7319. With the added complexity of the `full` model, for additional four sources with low-SNR data Γ had to be fixed in order to constrain the other spectral parameters. They are ESO 005-G004, 2MASX J0756, and MCG +06-49-019; all of them have either unobscured or RD spectra discussed in more detail in § 5.4.3 or § 5.4.4. We excluded these sources from computation of the Γ distribution for the `full` model, and NGC 7319 was excluded from both the `simple` and `full` model distribution. Typical 68 % uncertainty on Γ for the rest of the sample is ± 0.1, although it reaches up to ± 0.3 for some of the lowest-SNR spectra. All constraints are two-sided, i.e., there are no lower or upper limits.

The distribution of photon indices for the `simple` model has a median, $M(\Gamma) = 1.65$ and a 68 % interval $I(\Gamma) = [1.49, 1.80]$. Assuming that the distribution is Gaussian, the standard deviation, $\sigma(\Gamma)$, would therefore be approximately 0.16; however, the distribution is not entirely symmetric and has a slightly longer tail toward higher than toward lower values. Excluding the unobscured sources, the Compton-thick sources, or both, has essentially no effect on the distribution: $M(\Gamma)$ remains 1.65, and $\sigma(\Gamma) \approx 0.15$ in all three cases. The uncertainty on these numbers, derived from randomization of measured Γ values within their confidence intervals as described in § 5.3.3, is 0.02. Using the `full` model, the median of the main sample is 1.78 and $I(\Gamma) = [1.62, 1.94]$, as shown in Figure 5.5, panel (a). Sources

with $\log N_{\rm H}/{\rm cm}^{-2} < 22$ or $\log N_{\rm H}/{\rm cm}^{-2} > 24$ do not bias the distribution at all; excluding them results in $m_\Gamma = 1.76$ and $\sigma_\Gamma \approx 0.15$. Given the uncertainty in these numbers, which is the same as for the `simple` models, the differences are negligible. The difference between the `simple` and `full` distributions is systematic, as already pointed out in § 5.4.6.

A straightforward fit with the full model results in well-constrained but atypically steep spectra in three cases ($\Gamma > 2.1$; MCG +08-03-018, IRAS 05189, ESO 033-G022) and atypically hard spectrum in one other case ($\Gamma < 1.5$; LEDA 549777). For three of these sources it is possible to obtain a statistically acceptable model with Γ in the 1.6–1.9 range found for the rest of the sample, except IRAS 05189 for which Γ cannot be lower than 2.4 within the framework of any model considered in this work. These additional models are not used for computing spectral parameters distributions but they are shown in Table C3; we chose to show options with the fixed value of Γ for which these outlying sources appear most similar to the average in term of the spectral parameters other than Γ. The fact that models with more typical parameters are statistically acceptable suggests that these sources are not real outliers, but that the best fit is driven to somewhat extreme values of Γ by minor features in the data. IRAS 05189, which does appear to be significantly different than the rest of the sample and most similar to the excluded source ESO 383-G018, is discussed further in Appendix A and in a dedicated publication based on the same *NuSTAR* data (Xu et al., 2017).

Column Density

Using the `simple` models yields constraints on $N_{\rm H}$ for all targets except for the 9 that can be statistically well represented by a power law with no absorption (model A). We obtain a nearly Gaussian distribution with a median $M(\log N_{\rm H}) = 23.38$ and $I(\log N_{\rm H}) = [22.59, 24.17]$. Excluding spectra at the extreme ends of the $N_{\rm H}$ distribution, where robust constraints are more difficult to obtain from our data, the largest uncertainty range for $\log N_{\rm H}$ is ± 0.3 for the limited-quality NGC 3786 data.

Results of the `full` model fitting include more detailed analyses of the spectra of unobscured and CT sources, resulting in upper limits for 7 and 5 complete constraints for unobscured AGN, and fixed $\log N_{\rm H}$ for 5 CT AGN (as outlined in § 5.4.3 and § 5.4.4). For the latter group, the $N_{\rm H}$ values should generally be regarded as lower limits. The median of the $\log N_{\rm H}$ distribution is 23.22 if only best-fit values are included and 23.33 if lower limits are taken into account using the procedure

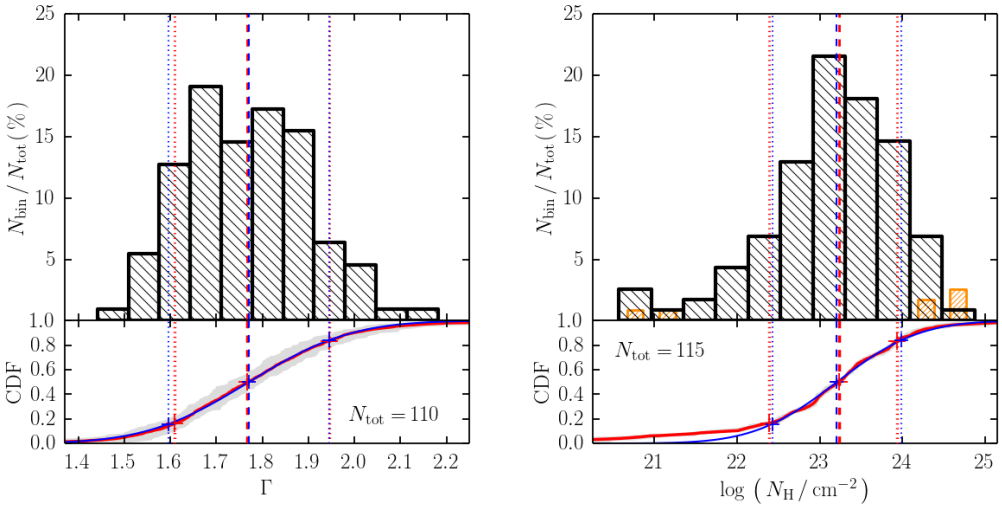

(a) Photon Index (b) Column Density

Figure 5.5: Distributions of the main spectral parameters for the main sample using the `full` model, the photon index (Γ) and the line-of-sight column density ($N_{\rm H}$). In the upper panels, black histograms show the distributions of best-fit values, while the yellow ones show lower or upper limits. For each parameter we calculate the CDF as described in § 5.3.3, taking into account statistical uncertainties and limits. The median CDFs, from which we calculate the median (red dashed vertical lines) and the 68 % probability intervals (red dotted vertical lines), is shown with the solid red curve below the histogram in each panel. The solid blue lines show the best-matching Gaussian CDFs and the dashed and dotted blue vertical lines show their medians and $\pm1\,\sigma$ intervals.

described in § 5.3.3. The corresponding 68 % ranges are 22.40–23.92 and 22.48–24.36, respectively. Despite the latter values likely being closer to the intrinsic distribution because lower and upper limits are taken into account, neither of the distributions is really intrinsic to the Sy II population, as both suffer from the bias that *Swift*/BAT survey has against detecting CT sources. We discuss this further in § 5.6.5. Uncertainties due to the inclusion of lower and upper limits are estimated to be ±0.04 for the median values quoted above, while for the lower and upper bounds of the 68 % ranges they are 0.03 and 0.08, respectively.

Secondary Continuum Normalization

Considering only the `simple` models, we find that a non-zero $f_{\rm sca}$ is required by the data for 48 targets. In all but a few exceptional cases of RD spectra, the secondary power-law component is found to contribute between 0.1 % and 10 % of the flux of the intrinsic continuum. This parameter differs from all others in the `full` model

in that it cannot be constrained for unobscured objects at all, since it is simply not observable. For the remaining 112 targets fitting the `full` model yields 78 full constraints and 34 upper limits. The best-fit values are distributed approximately log-normally, as shown in Figure 5.6, panel (a). From these constraints we derive the distribution median, $M(f_{\rm sca}) = (0.8 \pm 0.1)\,\%$. The upper end of the 68 % probability interval is $(3.2 \pm 0.4)\,\%$. The lower bound of the interval cannot be determined reliably because many of the upper limits are around or even above the median of the PDF and therefore not constraining for the lower part of the distribution of $f_{\rm sca}$ in the sample.

A typical short ≃7-ks *Swift*/XRT observation of a heavily obscured AGN does not produce a soft X-ray spectrum with photon statistics high enough for robust constraints on this parameter, or additional soft components. For many targets in our sample, the sensitivity to the secondary continuum component is limited by the quality of the *Swift*/XRT data. For this reason, our constraints on $f_{\rm sca}$ should generally be considered as upper limits, since the $f_{\rm sca}$ would likely be lower if other soft X-ray components significantly contribute to the soft X-ray flux. With the soft X-ray data already available from other observatories, the constraints on the distribution of $f_{\rm sca}$ can be improved considerably; the data set presented here is simply not ideal for constraining this parameter. Even so, some very tight upper limits can be found for a small number of bright AGN: for example, for NGC 6300, NGC 4992, and ESO 103-G035 we find upper limits at 0.05, 0.1, and 0.02 %, respectively. We note that this is far below the sample distribution median, demonstrating that despite the limited quality of the *Swift*/XRT data, we can identify a some of the so-called "deeply burried" AGN (e.g., Eguchi et al. 2009, Winter et al. 2009).

Fe Kα Line Equivalent Width

Inclusion of the narrow Fe Kα line at 6.4 keV in the `simple` models is not needed to fit the data for 69 targets in our sample, i.e., those spectra can be described well with models A, B, or D. In the rest of the sample, the strong line feature around 6.4 keV requires a narrow line component, and therefore the distribution of line strength for those sources alone will necessarily be biased toward high values. Following the bulk of the literature on X-ray spectroscopy of obscured AGN, we express the relative strength of the Fe Kα line with respect to the observed continuum by computing its equivalent width, $\mathrm{EW}_{\mathrm{Fe\,K}\alpha}$.

The distribution $\mathrm{EW}_{\mathrm{Fe\,K}\alpha}$ for the `simple` models (i.e., excluding any spectra where

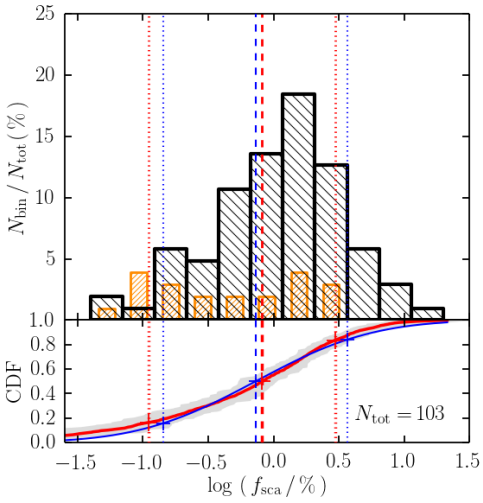

(a) Secondary Continuum Normalization

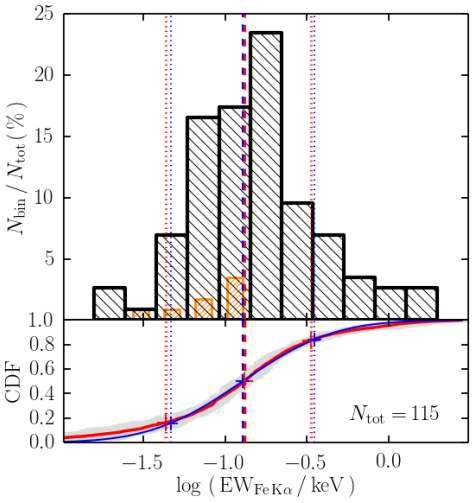

(b) Fe Kα Equivalent Width

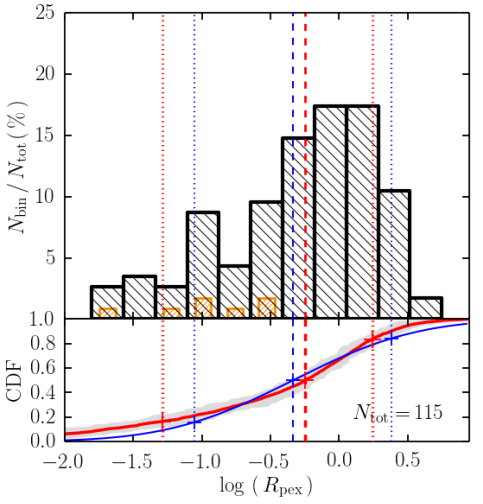

(c) Reprocessed Continuum Normalization

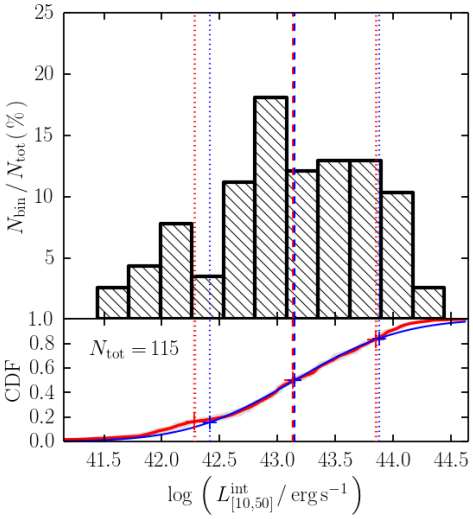

(d) Intrinsic Continuum Luminosity

Figure 5.6: Same as Figure 5.5, for the remainder of the `full` model spectral parameters.

it is not statistically required) has a median at 0.19 keV, and a 68 % interval covering 0.09–0.57 keV. However, meaningful constraints can be found for each source in our sample despite the degeneracy between spectral parameters and the fact that in some sources the line normalization is consistent with zero within the 68 % confidence interval. Taking into account `full` model constraints for all 124 targets, the distribution of Fe Kα equivalent width has a lower median, $M(\mathrm{EW}_{\mathrm{Fe\,K}\alpha}) = 0.13$ keV and $I(\mathrm{EW}_{\mathrm{Fe\,K}\alpha}) = [0.04, 0.33]$ keV (with estimated uncertainty of ±0.04 keV for the upper bound, and ±0.01 keV for the other two numbers). We show the distribution of $\mathrm{EW}_{\mathrm{Fe\,K}\alpha}$ for the `full` model in Figure 5.6, panel (b).

The equivalent width is a purely observational parameter and, by definition, depends on the line-of-sight column density. Indeed, we find that for the sources with $\log N_{\mathrm{H}}/\mathrm{cm}^{-2} < 24$ the 68 % range narrows to 0.04–0.22 keV (the median stays approximately the same as above, since only 16/124 sources are CT), while for $\log N_{\mathrm{H}}/\mathrm{cm}^{-2} > 24$ the distribution shifts to $I(\mathrm{EW}_{\mathrm{Fe\,K}\alpha}) = [0.25, 1.30]$ keV and $M(\mathrm{EW}_{\mathrm{Fe\,K}\alpha}) = 0.68$ keV. Somewhat circularly, this verifies our characterization of sources with high $\mathrm{EW}_{\mathrm{Fe\,K}\alpha}$ as CT in § 5.4.4. We investigate the dependence of $\mathrm{EW}_{\mathrm{Fe\,K}\alpha}$ on N_{H} in more detail in § 5.6.2, where we also consider a more robust measure of the relative strength of the Fe Kα line – the ratio of its luminosity to the luminosity of the intrinsic continuum (e.g., Ricci et al. 2014, Kawamuro et al. 2016a).

Reprocessed Continuum Normalization

A reprocessed continuum, represented in this work with the `pexrav` model, is formally required by the data in the sense that an acceptable fit cannot be found with simpler models (A through E), for 30 out of 124 targets in our sample. For those 30 cases we obtain a distribution of the R_{pex} parameter with $M(R_{\mathrm{pex}}) = 1.29$ and $I(R_{\mathrm{pex}}) = [0.24, 2.80]$ (±0.06 estimated for all three numbers). This distribution is expected to be heavily biased toward high values because only the sources with strong contribution from the reprocessed continuum cannot be fitted well without that component. For the majority of our sample, the data quality is such that it is difficult to statistically distinguish, in terms of χ^2 values and F-tests, whether a given observed spectrum has contributions from both direct and reprocessed components, or just the former with a harder photon index. We simply assumed both components are present in all spectra and proceeded to constrain their parameters wherever this is allowed for by the implicit degeneracy between the spectral parameters of our

assumed model. Both contributions are theoretically expected and present in most spectra where high-quality data are available.

The reprocessed continuum can be constrained to various degrees for most targets in our sample. We find a non-zero best-fit $R_{\rm pex}$ for additional 78 AGN: 19 are constrained only from above, and consistent with zero within the 68 % uncertainty interval, 2 are formally constrained only from below as they have RD CT AGN spectra, and 57 are fully constrained. In 8 cases it is only possible to obtain a "forced" upper limit on $R_{\rm pex}$ from our data, as described in § 5.3.2. For a total of 27 sources the lower bound of the 68 % uncertainty interval for $R_{\rm pex}$ cannot be found from our data, but 19 of those have best-fit $R_{\rm pex} > 0.01$, and all of them have upper limits that clearly distinguish them from spectra with strong reprocessed continuum contribution. As the reprocessed continuum is of special interest in this study, we defer the discussion of these constraints and their reliability to a dedicated section (§ 5.6.3).

Considering the `full` model fits for the whole sample, taking limits into account, we find that the distribution of $R_{\rm pex}$ is broad and peaks at a lower value in comparison to the subsample that statistically requires a reprocessed continuum component, as expected. The distribution (shown in the lower left panel of Figure 5.6) has a notable tail toward low values and is therefore better represented in log-space, contrary to most sample studies that investigated the distribution of this parameter in local AGN (e.g., Rivers et al. 2013, Vasylenko et al. 2015, Kawamuro et al. 2016a). Its median and 68 % probability interval are $M(R_{\rm pex}) = 0.58$ and $I(R_{\rm pex}) = [0.05, 1.81]$, respectively. Other than having a slightly narrower 68 % probability range, $I(R_{\rm pex}) = [0.09, 1.75]$, the distribution does not change significantly if unobscured and CT targets are excluded.

Intrinsic Continuum Luminosity

With both model types we were able to fully constrain the intrinsic luminosity for all sources, although for the RD sources this can be challenging to do robustly as it requires assumptions to be made (see § 5.4.4). The intrinsic 10–50 keV luminosity distributions for the `simple` and `full` models differ very little: their medians are 43.25 and 43.13, and the 68 % probability intervals are $[42.42, 43.91]$ and $[42.26, 43.83]$, respectively, with estimated uncertainty of ± 0.02. These differences can be fully explained with the change in the photon index and the reduction of the transmitted intrinsic continuum contribution to the 10–50 keV flux upon inclusion

of the reprocessed component, as already pointed out in § 5.4.6. Excluding CT AGN does not affect the distribution by more than the estimated uncertainty quoted above. We directly compare the observed luminosities (fluxes) based on *NuSTAR*-only and BAT-only data in § 5.6.4.

Table 5.3: Summary of medians and 68 % probability intervals of the `full` model spectral parameter distributions for the main sample

Parameter	Main Sample	$22 < \log\left(N_{\rm H} \,/\, {\rm cm}^{-2}\right) < 24$
$N_{\rm tot}$	124	97
Γ	1.76 ± 0.02 $[1.61 \pm 0.02, 1.94 \pm 0.02]$	1.75 ± 0.02 $[1.60 \pm 0.02, 1.94 \pm 0.02]$
$\log\left(N_{\rm H} \,/\, {\rm cm}^{-2}\right)$	23.22 ± 0.02 $[22.39 \pm 0.06, 23.94 \pm 0.02]$	23.21 ± 0.02 $[22.60 \pm 0.02, 23.77 \pm 0.03]$
$f_{\rm sca}$ / %	0.8 ± 0.1 $[0.11 \pm 0.03, 3.0 \pm 0.4]$	0.9 ± 0.1 $[0.14 \pm 0.04, 3.0 \pm 0.4]$
$\mathrm{EW}_{\mathrm{Fe\,K}\alpha}$ / keV	0.13 ± 0.01 $[0.04 \pm 0.01, 0.33 \pm 0.04]$	0.13 ± 0.01 $[0.04 \pm 0.01, 0.22 \pm 0.02]$
$R_{\rm pex}$	0.58 ± 0.02 $[0.05 \pm 0.03, 1.81 \pm 0.02]$	0.57 ± 0.02 $[0.09 \pm 0.03, 1.75 \pm 0.03]$
$\log\left(L^{\rm int}_{[10,50]} \,/\, {\rm erg\,s}^{-1}\right)$	43.13 ± 0.02 $[42.26 \pm 0.03, 43.83 \pm 0.02]$	43.17 ± 0.02 $[42.32 \pm 0.03, 43.84 \pm 0.02]$

Notes: The method of calculation of these values and their associated uncertainties is described in § 5.3.3. The distributions are shown in Figures 5.5 and 5.6.

5.5.2 Possible Correlations Between the Main Spectral Parameters

Because of the relatively large number of upper limits, and the lack of any interesting trends, we omit the $f_{\rm sca}$ parameter from Figure 5.7. The figure also does not contain MCG +08-03-018 and IRAS 05089 in the panels with Γ, and NGC 4395 in the panels with $\log L^{\rm int}_{[10,50]}$ simply because they are outliers. In the panels with $\log N_{\rm H}$ on the horizontal axis the unobscured AGN ($\log N_{\rm H} < 22$) are represented with a single point, for which we calculate the median and the 68 % probability interval with the procedure described in § 5.3.3.

The first sample property to note is the rather uniform coverage of the two-dimensional plane spanned by $\log N_{\rm H}$ and $\log L^{\rm int}_{[10,50]}$; any subsamples selected

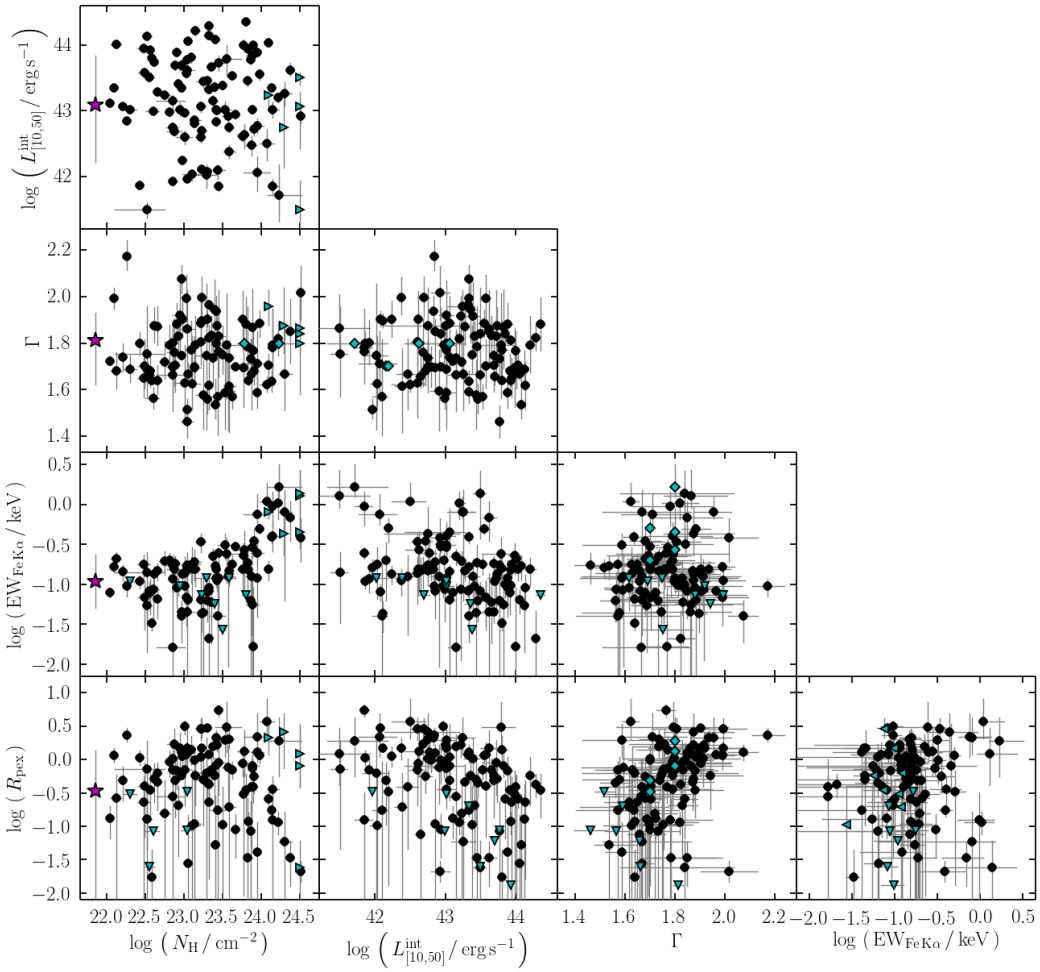

Figure 5.7: Possible correlations between the spectral parameters for the main sample (`full` model). In all panels, lower and upper limits are shown with cyan triangles. Cyan diamonds represent fixed values of Γ for sources with low-quality data. In the leftmost column of panels, the magenta star represents the median (and the errorbars represent 68 % probability interval) for AGN with log $N_{\rm H}/{\rm cm}^{-2} < 22$.

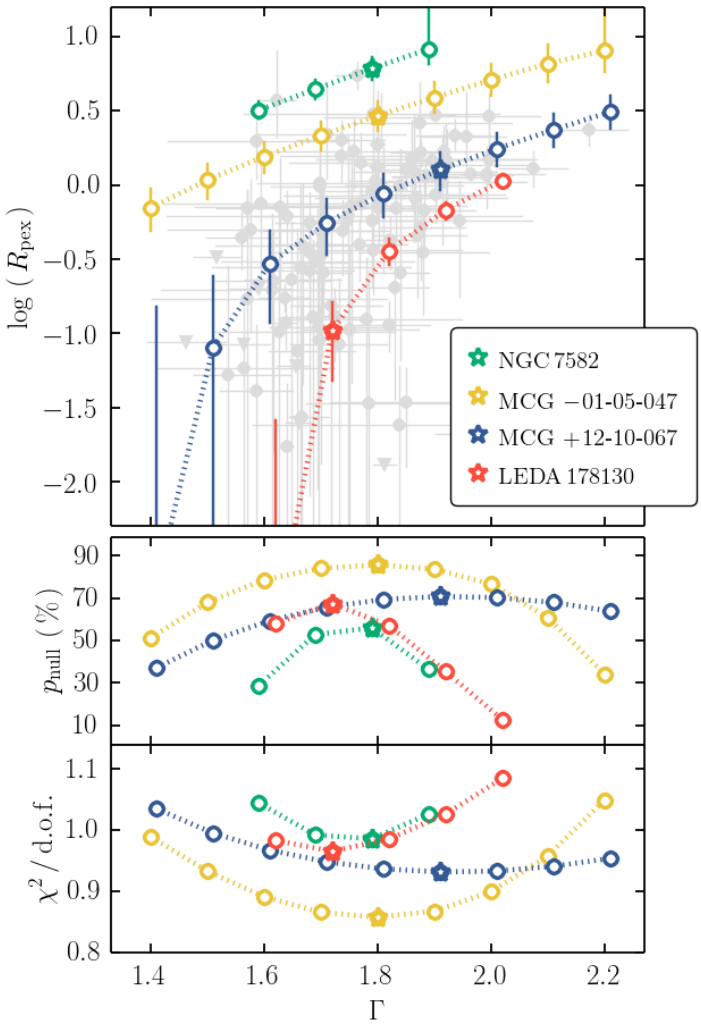

Figure 5.8: Four examples of the degeneracy between `full` model parameters Γ and $R_{\rm pex}$, showing that, even with high-quality *NuSTAR* data (100–350 d.o.f.), a statistically acceptable model can be found for a range of parameters significantly wider than their formal statistical uncertainties. The top panel shows the best-fit $R_{\rm pex}$ parameter and its statistical uncertainty with a vertical errorbar. The grey points with errorbars in the background are constraints from the `full` model for the main sample. The lower two panels show the reduced χ^2 and the associated null-hypothesis probability. The minima of reduced χ^2 (and, conversely, maxima of $p_{\rm null}$) are marked with star symbols; they correspond to the values of Γ closest to the best-fit when that parameter is fitted for. Note that we show only models which are statistically acceptable according to our adopted $p_{\rm null} > 5\,\%$ criterion. Assuming a harder Γ lowers the contribution of the `pexrav` component, as parametrized by $R_{\rm pex}$. However, the fact that in the top panel dotted colored lines generally do not overlap indicates that true differences exist between spectra with high and low $R_{\rm pex}$, i.e., they are not simply a result of the aforementioned model degeneracy.

by intrinsic luminosity therefore cover the full range of log $N_{\rm H}$, and vice versa. Spectral properties of our sample as a function of column density are discussed in more detail in § 5.6.2. Spectral parameters $\mathrm{EW}_{\mathrm{Fe\,K}\alpha}$ and $R_{\rm pex}$ exhibit trends with both column density and luminosity. The former is expected as a natural consequence of the definition of EW with respect to the observed continuum, which becomes increasingly extinguished as $N_{\rm H}$ increases.

The photon index (Γ) appears to be independent of either column density or intrinsic luminosity, which provides a good supporting argument for isotropy in obscured and unobscured AGN once the line-of-sight column density can be effectively modeled out. With soft X-ray telescopes and high obscuration, the energy range over which the slope of the intrinsic continuum could be determined becomes very narrow, sometimes leading to estimates of Γ significantly harder than the typical unobscured AGN.

The strongest correlation in formal mathematical terms is the one between $R_{\rm pex}$ and Γ. A part of the literature considered this to be a physical correlation, e.g., Zdziarski et al. (1999), Dadina (2008), Vasylenko et al. (2015). We argue that at the level of confidence of our constraints, and the previous, poorer measurements, it is mostly due to a model-based degeneracy. This has already been discussed to some extent in a number of other works in the literature in the form of contour plots (see, e.g., Rivers et al. 2013, Kawamuro et al. 2016a). They represent only the statistical uncertainty in a particular fit and do not necessarily reveal the full extent of the regions in the Γ–$R_{\rm pex}$ plane encompassed by all statistically acceptable models. In Figure 5.8 we show 4 examples of how much best-fit $R_{\rm pex}$ (and its uncertainties) depend on the assumed Γ. Note that all spectral solutions shown in the figure represent statistically acceptable models with $p_{\rm null}$>5 %, and that the range of Γ and $R_{\rm pex}$that describe the data well can be significantly wider than what statistical uncertainties imply.

5.6 Discussion

5.6.1 Intrinsic Continuum

In order to find the median photon index for the sample and its typical scatter in the population, we fit for this parameter whenever data quality allows that. For the *simple* model of each source, a fully constrained value can be found in all but two sources with low photon statistics: NGC 7130 and NGC 7319. The median of the distribution based on `full` model fits is 1.78 and the 68 % interval is 1.61–1.92.

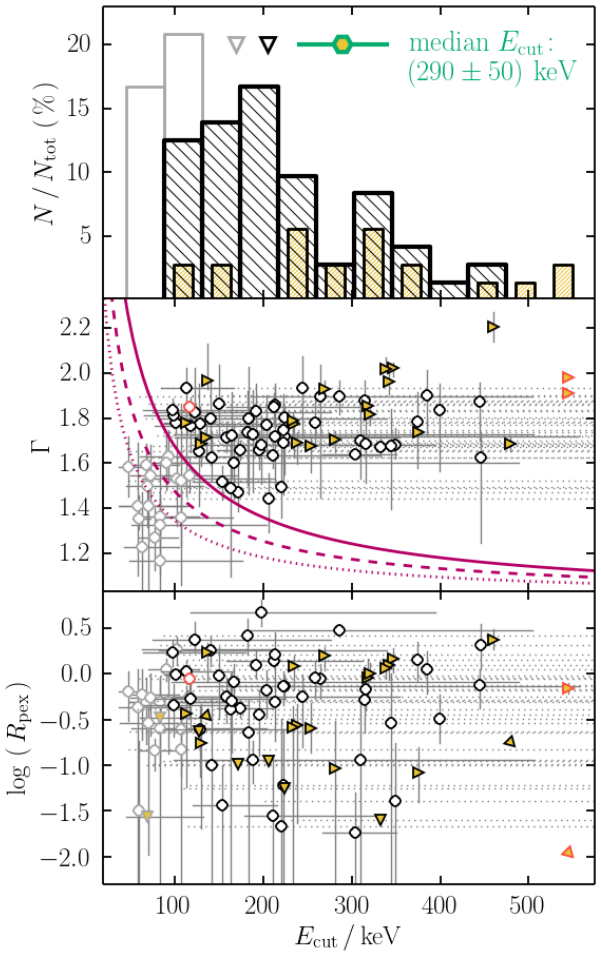

Figure 5.9: Results of the high-energy cutoff ($E_{\rm cut}$) analysis: one-dimensional histogram in the top panel, and distributions in the $E_{\rm cut}$–Γ (middle panel) and $E_{\rm cut}$–$R_{\rm pex}$ planes (bottom panel). The middle panel reveals the model-based degeneracy causing some fits to drift to extremely low values of both $E_{\rm cut}$ and Γ, which is unphysical (see § 5.6.1 for details). The solid purple line marks the $\tau_{\rm e} < 3$ cut that we apply to the results to discard degenerate fits, which are plotted in light grey below that line. Dashed and dotted purple lines mark $\tau_{\rm e} = 4$ and $\tau_{\rm e} = 5$, respectively. In the top panel, the black histogram is for valid best-fit $E_{\rm cut}$ values, the grey additionally includes the discarded values, and the yellow hatched one is for lower limits. The downward pointing triangles above the histograms show corresponding median values of $E_{\rm cut}$, and the green hexagon marks the median and its uncertainty after discarding degenerate results and including all lower limits. The bottom panel reveals no trends, assuring that there are no significant degeneracies between $E_{\rm cut}$ and $R_{\rm pex}$ parameters. In both middle and bottom panels, the long horizontal errorbars that stretch to $E_{\rm cut} > 550$ keV are shown in dotted lines for clarity, and the red symbols mark sources excluded from our main sample.

The uncertainty in these numbers, derived from randomization of measured Γ values within their confidence intervals as described in § 5.3.3, is approximately 0.02.

In comparison with previous work on obscured AGN samples, where the reprocessed continuum was not modeled, the relevant distribution of Γ to compare is the one for the *simple* model. However, the intrinsic distribution is likely closer to the *full* model Γ distribution, since the contribution of the reprocessed light was effectively removed to the extent possible within the framework of our chosen model, allowing us to characterize the intrinsic continuum better then in any previous sample study. Unlike in many previous studies based on limited quality hard X-ray data (e.g., *Swift*/BAT in combination with a soft X-ray spectrum; Winter et al. 2009, Tazaki et al. 2011, Vasudevan et al. 2013), the width of our distribution is not dominated by statistical uncertainty, but actual spread of values in the population. The spread is similar to that of unobscured samples (e.g., Nandra & Pounds 1994, Turner et al. 1997, Rivers et al. 2013).

In setting up our models, we decided to fix the high-energy coronal cutoff, $E_{\rm cut}$, at 300 keV because fitting for it is not required by any of our spectra (in the sense that a satisfactory fit cannot be obtain without it). However, treating $E_{\rm cut}$ as a free parameter, we find 23 targets with fully-constrained $E_{\rm cut}$ in the range between 90 and 500 keV, and additional 19 targets for which $E_{\rm cut}$ is fully constrained but both Γ and $E_{\rm cut}$ so low that the measurement cannot be considered physical, i.e., they are difficult to reconcile with theoretically predicted coronal continua. Furthermore, 30 targets have a best-fit $E_{\rm cut}$ in the 90–500 keV range (one of which is unphysical), but with no upper limit. Data for 21 targets yield only a lower limit on $E_{\rm cut}$ in the same energy range: the best fit is found at the upper end of the parameter space, or above 500 keV. For the remaining targets, all of which have less than 70 d.o.f. and/or are CT AGN, it is impossible to obtain limits on $E_{\rm cut}$ due to severe degeneracy between spectral parameters.

The choice of $E_{\rm cut}$ is an important systematic to consider in comparison to other studies, yet it is often neglected. The Γ distributions discussed above have been derived under the assumption that the intrinsic continuum is proportional to $E^{-\Gamma} \times \exp(E/E_{\rm cut})$, where E is energy and $E_{\rm cut}$= 300 keV. Assuming a finite $E_{\rm cut}$ automatically leads to harder Γ in comparison to a power-law, since the exponential drop-off is gradual but present across any common X-ray band. Fitting in the hard X-ray band will result in a more significant difference from a Γ determined from a pure power-law fit because of this model-induced degeneracy. Figure 5.10 demonstrates

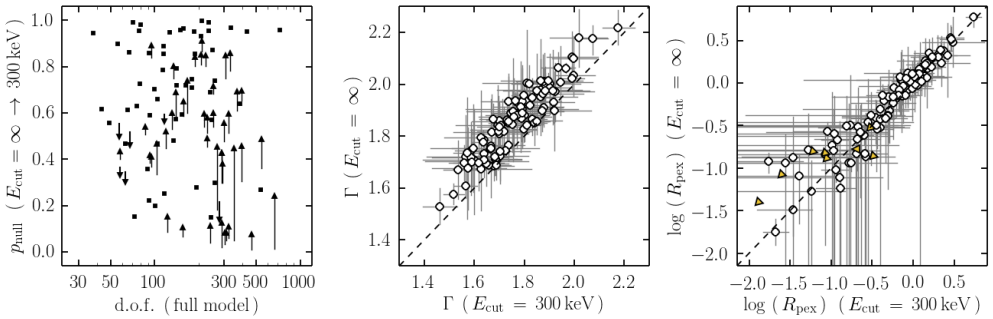

(a) Changes in the key fit parameters assuming no high-energy cutoff ($E_{\rm cut} \rightarrow \infty$)

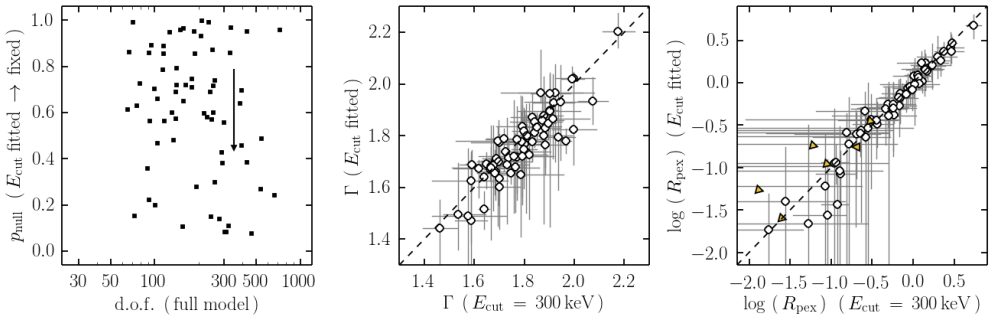

(b) Changes in the key fit parameters with high-energy cutoff included as a free parameter

Figure 5.10: Demonstration of changes in the fitted spectral parameters assuming $E_{\rm cut} \rightarrow \infty$ (formally, $E_{\rm cut} = 10^4$ keV; panel row a) and fitting for $E_{\rm cut}$ (panel row b), instead of assuming a fixed value of 300 keV in our `full` model. The former assumption results in Γ that are on average softer by 0.13 compared to $E_{\rm cut} = 300$ keV, while the $R_{\rm pex}$ parameters do not change significantly. It does not yield an acceptable fit (with $p_{\rm null} < 5\,\%$) for 7 sources with high-SNR spectra. As the leftmost panel shows, the vast majority of fits improve when $E_{\rm cut}$ is lowered to 300 keV, although the improvement is not statistically significant. The lower panel row (b) shows the general lack of significant changes in the fits when $E_{\rm cut}$ is fitted for instead of fixed at 300 keV: except for a single target (ESO 103-G035), there is no appreciable change in $p_{\rm null}$ or $R_{\rm pex}$, while Γ become harder by only 0.05 on average. Results are shown here after applying the $\tau_{\rm e} < 3$ cut that rejects degenerate fits (see Figure 5.9).

that the median Γ in our sample would be softer by approximately 0.13 had we assumed a pure power-law continuum.

5.6.2 Spectral Properties as a Function of the Line-of-sight Column Density

We consider the sources with $\log N_{\rm H}/{\rm cm}^{-2} < 22$ to be unobscured. In our main sample 13/124 (10 %) have unobscured X-ray spectra. Although some of these targets may have been misclassified as type II Seyferts, it is not uncommon to find approximately 10 % of either type I AGN being obscured, or type II AGN being

unobscured (e.g., Malizia et al. 2012, Merloni et al. 2014). Among our unobscured sources there is a mix of objects of optical type 2, 1.9 and 1.8. Other than having low line-of-sight column density, their spectra do not look significantly different than the rest of the sample in terms of other spectral parameters.

Figure 5.11 shows the relevant spectral parameters as a function of $N_{\rm H}$. Binning is employed in order to highlight the overall trends. As noted before, the photon index and the intrinsic luminosity are independent of $N_{\rm H}$. The equivalent width of the Fe Kα line has a strong increasing trend with $N_{\rm H}$. This is expected in a physical scenario in which the continuum is increasingly more absorbed, while the line does not undergo the same amount of absorption, presumably because it is produced via flourescence out of the line of sight to the X-ray source.

However, an interesting trend is observed when the line luminosity is normalized with respect to the intrinsic 10–50 keV continuum, as shown in the upper right panel of Figure 5.11: Fe Kα emission either weakens or becomes more absorbed with increasing $N_{\rm H}$. A similar, but less clear trend has been seen in smaller samples of Ricci et al. (2014) and Kawamuro et al. (2016a), which they interpreted as self-absorption in the torus itself. Another intriguing trend is revealed in terms of $R_{\rm pex}$ as a function of $N_{\rm H}$, or its less model-dependent counterpart $R_{\rm rep}$, defined as the ratio of reprocessed and intrinsic luminosity in the 10–50 keV band. There is a peak in the $\log\ N_{\rm H}/{\rm cm}^{-2} = 23.0 - 23.5$ range, which has been suggested before based on stacked *INTEGRAL* data (Ricci et al., 2011).

Despite its incompleteness (see § 5.6.5) and relatively small size, our sample of 15 CT AGN is the largest collection of high-quality hard X-ray spectra of CT AGN available to date. As the direct continuum is severely attenuated by the large column density in the line of sight, the spectra become dominated by the contributions from scattering in the material surrounding the central SMBH (i.e., out of the direct line of sight). For this, the `pexrav` component employed in this work may only be considered as an approximation, and more advanced models should be used for detailed spectral analyses. Our analysis of this sample will be presented in a companion study (Chapter VI); however, some interesting results are already apparent from this work despite the indirect approach.

With the caveat that for this work we employed `pexrav`, which is not a model representative of the torus reprocessing in detail, we suggest that this separation may be related to existence of two kinds of CT AGN: those that have a relatively thin disk-like or ring-like tori viewed very close to edge-on, and those that have a

nearly spherical (not necessarily uniform) distribution of material around the central engine. The anti-correlation of the torus covering factor with luminosity found for CT AGN by Brightman et al. (2015) suggests that there is a continuum of torus covering factors, so it might be that we are seeing two distinct groups only because of low-number statistics. Using more realistic torus models and larger samples in the future will be crucial for understanding this apparent dichotomy.

The phenomenological models used in the study presented here are already sufficient to provide new insight into the typical and the extreme CT AGN broadband X-ray spectra, and inform searches for the elusive CT AGN population. Here we use the observed *NuSTAR* and *Swift* spectra to further our understanding of the limits of CT AGN selection in two ways: (i) by constructing a completeness correction for the *Swift*/BAT survey, from which our sample is drawn, and (ii) by shifting the observed spectra to higher redshift and examining their hardness ratios, as probed by the significantly deeper *NuSTAR* extragalactic surveys.

5.6.3 Components due to X-ray Reprocessing

Because the reprocessed continuum represented by `pexrav` peaks with a Compton hump at 20–30 keV, model F has a natural degeneracy such that observed hard X-ray spectrum with a given effective slope can be fitted equally well with a hard Γ and low $R_{\rm pex}$ and a soft Γ and high $R_{\rm pex}$, unless the data quality permits to reject a range of solutions based on χ^2 statistics. For most of the AGN in our main sample we are unable to break this degeneracy. While the best-fit Γ and $R_{\rm pex}$ may be interpreted as the most likely trade-off between the reprocessed and intrinsic continua, the reader should keep in mind that fixing $R_{\rm pex}$ at a value lower that the best-fit value simply results in a harder Γ for most of the sources. Models A through E can be seen as limiting cases of model F where $R_{\rm pex}$, and normalizations of other spectral components, tend toward zero. Broadband X-ray spectra of 85 out of 113 AGN in our sample are statistically well represented by models with $R_{\rm pex} \rightarrow 0$, and formally do not require a reprocessed continuum component to be included for a good fit to the data.

The motivation for adding a reprocessed component regardless of whether or not it is required stems from (i) theoretical considerations (e.g., Matt et al. 1991, Nandra & George 1994), (ii) the finding that most spectra do show significant narrow Fe Kα line components thought to arise from reprocessing that would also produce a continuum (here, as well as in the literature, e.g., Fukazawa et al. 2011), and (iii)

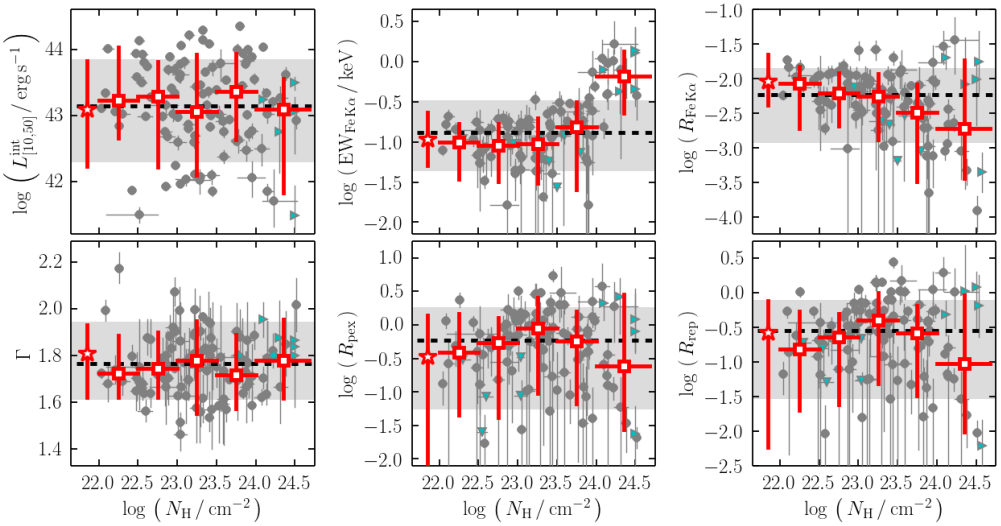

Figure 5.11: Spectral properties of the main sample as a function of column density. Constraints on spectral parameters of individual targets are shown with dark grey, filled circles with errorbars showing 68 % confidence intervals. Upper and lower limits are shown with cyan triangles. The light grey horizontal band shows the 68 % spread in any parameter within the main sample, and the dashed black horizontal line shows the median of each parameter distribution. The red points show the medians and the 68 % spread within narrow bins in log $N_{\rm H}$. Note that the errorbars do not show uncertainty in the median, which is generally negligible. The rightmost column of panels show alternative measures of the reprocessed line emission ($R_{\rm Fe\,K\alpha}$, the ratio of Fe Kα line flux to the 10–50 keV intrinsic continuum; top panel) and reprocessed continuum ($R_{\rm rep}$, the ratio of the reprocessed to intrinsic 10–50 keV continuum; lower panel).

the fact that the reprocessed continuum is a significant component in many high-SNR hard X-ray spectra. In other high-SNR spectra, addition of this component results in upper limits on its contribution, which may still convey useful physical information. However, the reliability of low-$R_{\rm pex}$ measurements depends primarily on data quality: in some cases it is high enough that a flat continuum can clearly be distinguished from a convex continuum with a Compton hump in the 10–50 keV band, but in most cases in our sample, the data quality prevents us from making such a clear distinction.

In order to provide some evidence that despite the data quality and the degeneracy described above it is still possible to distinguish sources with different levels of reprocessed continuum contribution, we show several examples of targets with medium- and high-SNR data in Figure 5.8. As we step through the parameter space

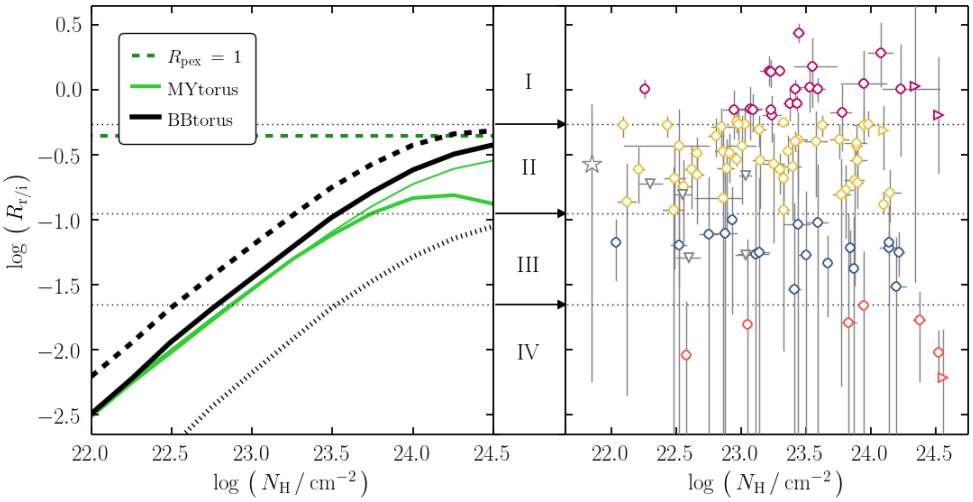

Figure 5.12: Comparison of expectations for the Compton hump strength from spectral models with approximately toroidal geometry, `MYtorus` (Brightman & Nandra, 2011a), and `borus02` (see Chapter IV), with our measurements using the `pexrav`-based `full` model. Compton hump strength is measured with $R_{\rm rep}$: the ratio of reprocessed to intrinsic flux in the 10–50 keV band. In the left panel we show calculations from `MYtorus` in light green (thick line for the edge-on viewing angle and thin line for the line of sight skimming the torus edge) and from `borus02` in black (solid line for the covering factor 50 %, dashed for 90 % and dotted for 10 %). The $R_{\rm pex}$= 1 line based on `pexrav` is show in dark green for comparison. Given the absence of any similar trend in our data, we *decouple* the line-of-sight column density ($N_{\rm H,los}$) and that of the torus ($N_{\rm H,tor}$), and identify four possible groups according to the Compton hump strength: I (purple), AGN with complex and apparently RD spectra; II (yellow), AGN with a torus covering factor of 10–100 % and log $N_{\rm H,tor}/{\rm cm}^{-2}$= [23.5, 24.5]; III (blue), AGN with either a disk-like CT torus (covering factor $\leqslant$ 10 %, log $N_{\rm H,tor}/{\rm cm}^{-2}\approx$ 24) or a 10–100 % covering with log $N_{\rm H,tor}/{\rm cm}^{-2}$= [22.5, 23.5]; and IV (red), AGN with non-CT tori (log $N_{\rm H,tor}/{\rm cm}^{-2}<$ 23.5), possibly obscured only by their host galaxy.

of Γ, $R_{\rm pex}$ converges to different best-fit values in each step, often outside of the 68 % confidence interval determined by the `Xspec` error calculation for the general `full` model fit. In particular, the fits for MCG +12-10-067 show that its spectrum can be equally well described by $R_{\rm pex}$ ranging from zero to $\simeq$ 3, depending on assumed Γ. However, different AGN can still be distinguished by their $R_{\rm pex}$ *for any assumed* Γ.

Another way to understand Figure 5.8 is the following. While one can assume that the whole sample has the same intrinsic photon index (e.g., Γ = 1.77, which is the sample median), fit for the reprocessed continuum contribution and find an acceptable fit for most of the targets, one *cannot* assume a single $R_{\rm pex}$ value for

the whole sample and still find acceptable fits. In other words, the sample is too diverse in terms of reprocessed continuum contributions for this assumption to hold. If our sample is truly representative of the parent Sy II population, as we argue in § 5.2.2, then this implies that hard X-ray spectroscopy can distinguish some physical property that varies significantly across the population.

The spectral model we assumed for the analysis presented here is phenomenological in the sense that the reprocessed continuum, which is thought to be mainly contributed by the AGN torus, is approximated with the disk-reflection model `pexrav`. Because of its nearly invariable spectral shape with a strongly peaked Compton hump (see Figure 5.13), its parameter $R_{\rm pex}$ essentially measures the curvature of the target spectrum around the Compton hump peak at 20–30 keV. However, geometrically more accurate models for the torus (e.g., Ikeda et al. 2009, Murphy & Yaqoob 2009, Liu & Li 2014) show that the Compton hump can be significantly less pronounced.

This leads to the conclusion that AGN with low $R_{\rm pex}$ do not necessarily have a low contribution of the reprocessed continuum – they may instead have a relatively strong reprocessed continuum component of a different shape. From the straightforward model comparison in Figure 5.13 we suggest that at least two physical variables related to the geometry of the torus may be responsible for the observed diversity in the Sy II population: the average column density and inclination. A possible third variable, the covering factor, cannot be changed in the `MYtorus` model, but the `borus02` model introduced in Chapter IV does include that option as well.

Consistency Between the Compton Hump and the Fluorescent Line Emission

`pexmon` (Nandra et al., 2007) is self-consistent model which adds the three main fluorescent lines (Fe Kα, Fe Kβ and Ni Kα) to the `pexrav` continuum. As in the case of `pexrav`, the line strengths were calculated for a flat slab of infinite optical depth illuminated by different cutoff power-law input spectra, for a range of inclinations and elemental abundances (George & Fabian, 1991). Because line normalizations are fixed with respect to the reprocessed continuum, a spectral model employing `pexmon` has fewer degrees of freedom compared to our model F. This is beneficial for spectra with low SNR, where $R_{\rm pex}$ and the normalization of the Fe Kα line can only be poorly constrained. However, some of the highest-SNR spectra are not fitted well by such a model and instead prefer a different relative normalization of the Fe Kα line and the Compton hump that that dictated by `pexmon`. This suggests either a

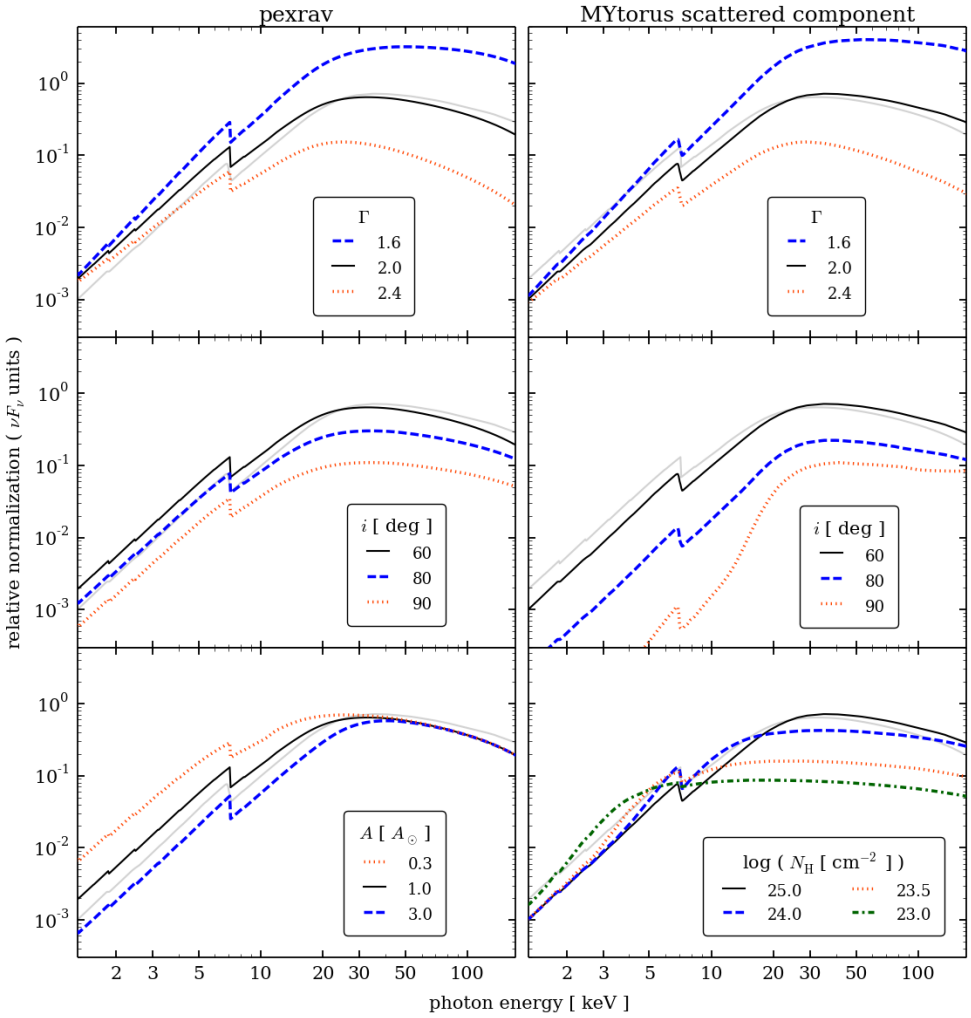

Figure 5.13: Comparison of reprocessed spectra produced by `pexrav` (left column) and `MYtorus` models (right column). In each panel we show a black curve, which corresponds to the spectral component used in fitting in this work, and a grey curve, representing the closest `MYtorus` match to `pexrav` ($\log N_{\rm H} = 10^{25}\,{\rm cm}^{-2}$, $\theta_{\rm inc} = 60°$). Each row of panels shows the effects of variation of a single model parameter.

deviation from Solar abundance of Fe in those cases, or a need for a reprocessed spectrum of a different spectral shape, implying a different geometry. Given the overly simplistic geometry which `pexmon` represents, this should not be surprising.

The high-quality spectra of NGC 5899 and Mrk 3, for example, can be fitted well with a `pexmon`-based model (even with fixed $A_{\rm Fe} = 1$), and neither do the quality of the fit nor the best-fit parameters differ significantly from those presented for model F in Table C3. Contrary to those sources, the high-quality spectra of NGC 262, NGC 2110, NGC 6300, and NGC 1365, to name a few, cannot be fitted well with `pexmon` even when the Fe abundance is fitted for ($p_{\rm null} < 3.5\,\%$ in all cases). This is likely because lowering/increasing the abundance has two effects: the fluorescent lines become weaker/stronger, and the shape of the Compton hump changes as well (see Figure 5.13). The high quality of the *NuSTAR* data constrains the Compton hump to a particular shape and amplitude that is not reproducible with `pexmon` while keeping the line flux consistent with the data. This serves to demonstrate that the combination of Fe line and Compton hump constraints can be a powerful tool for discriminating parameters of the reprocessed spectral component, if a proper model for torus reprocessing is applied instead of `pexrav` or `pexmon`.

Using `pexmon` is particularly illuminating when applied to sources which have excessively low or high $R_{\rm pex}$ (or $R_{\rm rep}$), or atypically weak or strong Fe line emission (or $\mathrm{EW}_{\mathrm{Fe\,K}\alpha}$, or $R_{\rm rep}$). We generally find that, in most cases, forcing the line emission to be consistent with the `pexrav` continuum results in a convergence toward the median $R_{\rm pex}$ and typical relative line normalizations found for the main sample. However, this only holds for the assumption of $A_{\rm Fe} = 1$; when $A_{\rm Fe}$ is fitted for, the best fits are generally found for extreme values of $\simeq 10$ for sources with strong lines and/or low $R_{\rm pex}$, and $\simeq 0.2$ for sources with weak lines and/or high $R_{\rm pex}$. While in most cases it is not formally necessary to fit for $A_{\rm Fe}$ because satisfactory fits can be obtained with $A_{\rm Fe} = 1$, these trends further reinforce our arguments regarding spectral shapes of the reprocessed spectral component other than `pexmon`.

How Robustly Can We Constrain the Reprocessed Spectrum Components?

Given our spectral analysis methodology, the constraints on the reprocessed spectrum components presented as best-fit values and limits based on `full` model fits are not very robust. The true *sensitivity* to the Fe line and the Compton hump is a complex function of many variables, and is plagued with systematic uncertainties. It clearly depends on the data quality and the adopted definition of detection

significance, but also the spectral shape, $N_{\rm H}$ and Γ, the choice of the shape of the reprocessed continuum, whether or not the continuum should be in a fixed relation with line emission, including $A_{\rm Fe}$ as a free parameter or not, and the choice of which other parameters should be fixed or fitted. In Figure 5.8 we have already shown that for spectra with medium-to-high SNR it is possible to find statistically acceptable best-fit models for a range of Γ greatly exceeding the formal uncertainty on Γ based on the best-fit `full` model. For each assumed Γ we found a different $R_{\rm pex}$, covering the full observed range for this parameter in some cases. Although not plotted in Figure 5.8, $\mathrm{EW}_{\mathrm{Fe\,K}\alpha}$ stayed roughly constant in all fits, but the Fe Kα normalization relative to `pexrav` was different for each Γ. Had we assumed that this normalization has to be kept constant, we would constrain $R_{\rm pex}$ to a significantly narrower range of values for which models with $p_{\rm null} > 5\,\%$ can be found.

Robust constraints can perhaps be best demonstrated for sources with apparently extremely low $R_{\rm pex}$, which, at face value, suggests that very low values can be constrained with our data. Focusing on the sources from the higher-quality half of the main sample, the lowest $R_{\rm pex}$ values are found for PKS 2331−240 (< 0.01), NGC 5252 (< 0.03), NGC 2110 (< 0.05), and ESO 416-G002 (< 0.06). These upper limits are defined as points in $R_{\rm pex}$ parameter space at which the fit degrades by $\Delta\chi^2 = 1$ from the best fit ($R_{\rm pex} \rightarrow 0$ in most cases), like in all other 68 % uncertainty interval calculations done in `Xspec`. Forcing $R_{\rm pex}$ to be higher (fixing it at $R_{\rm pex} = 0.2$) still finds an acceptable fit even for the highest-quality spectrum of NGC 2110, but values higher than that do not result in fits with $p_{\rm null} < 5\,\%$, and can therefore be rejected. $R_{\rm pex} < 0.2$ can be considered a more robust upper limit for NGC 2110. Likewise, we derive such upper limits on $R_{\rm pex}$ at 0.35–0.55 for PKS 2331−240, NGC 5252 and ESO 416-G002. This exercise can be repeated with `pexmon` replacing `pexrav` and the Gaussian Fe Kα line in our model F, leading to nearly equal constraints in these four examples.

For the lower-quality half of the sample, in which all sources can be well fitted with models lacking the reprocessed continuum (models A–E), constraints below $R_{\rm pex} \simeq 0.5$ should be considered with due skepticism, since robust limits can only be placed a relatively high $R_{\rm pex}$ ($\leqslant 2$). As we showed in § 5.4.4, the well-constrained low $R_{\rm pex}$ values in the CT regime are a separate issue. Constraints of the order of $R_{\rm pex} \leqslant 2$ are physically not very interesting: Figure 5.12 shows that such a spectrum is consistent with a torus of any covering factor and any average column density. However, more stringent constraints of the order of $R_{\rm pex} \leqslant 0.5$ do disfavor

certain torus models (i.e., high-covering CT tori). Given the caveats regarding the quantification of constraints highlighted above, and the approximate nature of relating them to torus models, we refrain from interpretation of our current results in more physical terms, and postpone that discussion to Chapter VI, where we employ torus models for fitting the X-ray spectra directly.

Limitations of Phenomenological Modeling

We chose to work with this model in order to provide a comparison to the literature, since very similar models have been used in the literature for over 20 years. The model was not chosen to provide physical interpretation of the observed spectra, although we were able to indirectly infer some basic properties of the AGN in our sample, as did many studies before. The `pexrav`-based `full` model most obviously fails in two particular regimes: for apparently RD spectra which do not have CT line-of-sight column density, and CT AGN in general. While there is nothing wrong with using this model for a phenomenological description of the observed spectra, since it clearly fits the data remarkably well for every AGN in our main sample, any interpretation should be considered with care.

A more exact quantification of the biases in inferences made from `pexrav`-based modeling can only be done in comparison with modeling employing more modern torus models and multi-wavelength data for a large and statistically significant sample. Our analyses of this representative sample of Sy II AGN will be presented in a series of follow-up publications (see Chapter VI; also Lanz et al, in preparation). They should provide a bridge between antiquated modeling practices that lack physical interpretation, and newer models that enable constraining some of the basic physical parameters of the AGN torus.

5.6.4 Hard X-ray Flux Variability

It is reasonable to expect that variability will affect most of the results presented here to some extent, as well as those already in the literature. A study of spectral variability in the Sy II population (similar to, e.g., Hernández-García et al. 2015, Connolly et al. 2016) is not possible with the data set presented here, as it consists primarily of single-epoch snapshots. It provides no time-domain information except for the offsets in observed flux between *NuSTAR* observations ($\simeq$20 ks), which are essentially instantaneous compared to *Swift*/BAT integration time of $\simeq$ 11 Ms. From the direct comparison of *NuSTAR* and *Swift*/BAT data, we find that it is not

uncommon to observe a hard X-ray flux offset from the average by a factor of 2–3 at any given time. This agrees well with many studies of variability in unobscured Seyferts, for which it is significantly easier to directly probe the intrinsic continuum in the soft X-ray band.

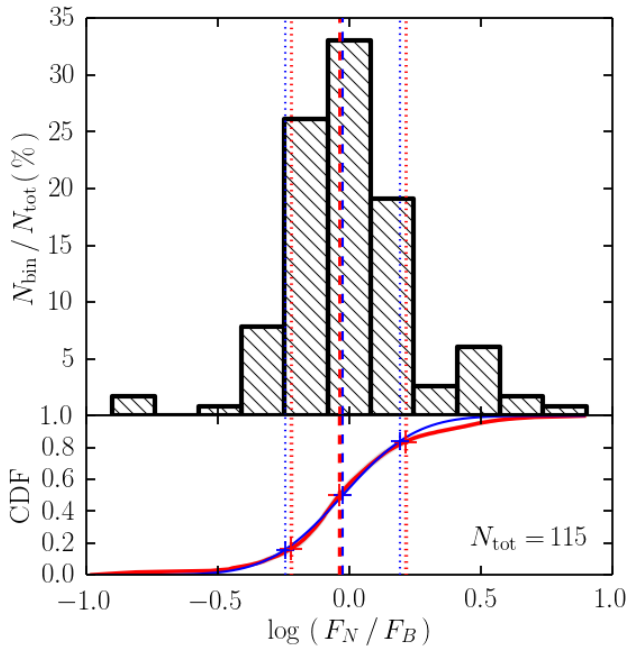

Figure 5.14: Distribution of the flux ratio in the 14–75 keV band between *Swift*/BAT and *NuSTAR*. The flux ratio distribution is centered on unity, and exhibits long tails up to flux ratios of ∼5–7.

In order to compare the *NuSTAR* and *Swift*/BAT fluxes directly, we employ only the overlapping energy band (14–75 keV in the observer frame) and the appropriately simple power-law model. From the two-parameter fit (with free normalization and the power-law photon index) we extract the 14–75 keV fluxes and effective photon indices for the *NuSTAR* observations and the long-term *Swift*/BAT average. We find no significant outliers in the ratio between our calculated 14–75 keV flux and the BAT flux extracted from the *Swift*/BAT 70-month catalog, confirming that the 14–75 keV flux calculated this way is a reliable proxy for the full-band 14–195 keV flux.

The distribution of F_N/F_B is centered around unity (the median is 0.92 ± 0.03) and the 68 % probability interval is $[0.60 \pm 0.03, 0.6 \pm 0.1]$. In Figure 5.14 we show the distribution on the log scale because of a significant number of highly

excessive values. We find $(F_N/F_B) < 0.5$ for 15 sources and $(F_N/F_B) > 1.5$ for 14 sources, where in both groups F_N/F_B is consistent with a 50 % offset and inconsistent with unity within the 68 % uncertainty interval. Because the non-unity flux ratio is most likely due to the natural AGN variability, for these targets we performed spectral modeling both including and excluding the *Swift*/BAT data, as described in § 5.4.2. The cross-normalization factors between *NuSTAR*/FPMA and *Swift*/BAT spectra correlate nearly perfectly with F_N/F_B, as expected. In most cases the spectral solutions with and without *Swift*/BAT data do not differ significantly. It should be noted, however, that flux differences exceeding 50 % between single-epoch observations and the long-term averages are not rare: this occurs for 25 % of our sample. While it may not be an issue when *Swift*/BAT data is used together with *NuSTAR*, because of their overlapping energy range, it could potentially be important for any literature results based on spectral modeling with single-epoch soft X-ray data used in conjunction with *Swift*/BAT data.

This analysis suggests that the *Swift*/BAT data may be unsuitable for spectral modeling in combination with single-epoch soft X-ray data. While some previous studies performed "renormalization" of the *Swift*/BAT spectra based on the 14–195 keV lightcurve (rescaling the flux to the time of the soft X-ray observation; Vasudevan et al. 2013), majority of the literature using *Swift*/BAT data does not consider this issue. The *Swift*/BAT-based luminosity is probably the best indicator of the long-term average once the average contribution of the reprocessed component can be disentangled spectroscopically. The reprocessed continuum component is an important contributor to the hard X-ray band flux, and the extent to which it biases BAT-band flux *on average* can only be probed with high-quality multi-epoch observations with *NuSTAR*. Multi-epoch spectroscopic studies of the brightest AGN in our sample have already shown the reprocessed spectrum components to be less variable (e.g., NGC 2110, Marinucci et al. 2015; NGC 1365, Walton et al. 2014; NGC 7582, Rivers et al. 2015a and Chapter IV; NGC 1068, Marinucci et al. 2016), and the fainter sources show similar behavior, albeit with weaker constraints (e.g., NGC 5643, Annuar et al. 2015; IC 751, Ricci et al. 2016).

5.6.5 *Swift*/BAT Selection Completeness and the Intrinsic $N_{\rm H}$ Distribution

Having a better handle on the typical CT AGN spectra in the hard X-ray band than any large survey performed thus far enables us to make an empirical assessment of the bias against selection of CT AGN with *Swift*/BAT. Other authors have attempted to construct similar completeness corrections for the *Swift*/BAT survey based on

theoretical expectations for broadband X-ray spectra of CT AGN. Burlon et al. (2011) calculated the correction assuming just an absorbed power-law model with increasing $N_{\rm H}$. which results in an exponential decrease the ratio of observed to intrinsic flux, dropping to ≃3 % at log $N_{\rm H}/{\rm cm}^{-2}$= 25 in the 15–55 keV band.

Ricci et al. (2015) used a more appropriate geometrical torus model by Ikeda et al. (2009) to derive the same correction curve; they find that instead of the exponential decrease, the fraction of observed flux levels off at 20 % above log $N_{\rm H}/{\rm cm}^{-2} = 25$. The reason for this is that the reprocessed component starts dominating around log $N_{\rm H}/{\rm cm}^{-2}$ ≈24.5, creating an effective minimum of flux that is not attenuated in the same way as the line-of-sight component. Starting from the parameter distributions derived from our sample, we construct a sequence of models with increasing $N_{\rm H}$ and calculate the ratio of flux observed in the 14–195 keV band between a spectrum with in $N_{\rm H} \rightarrow 0$ and a range of $N_{\rm H}$ between $10^{20}\,{\rm cm}^{-2}$ and $10^{25}\,{\rm cm}^{-2}$. We show the resulting curves, representing the completeness of *Swift*/BAT selection as a function of $N_{\rm H}$, in the lower panel of Figure 5.15.

We first assumed constant $R_{\rm pex}$ fixed at 0.58, the median value for the main sample. However, this assumption disregards the possible dependence of $R_{\rm pex}$ on $N_{\rm H}$ that we presented in § 5.6.2; our results suggest that within the framework of the phenomenological model we employed for this study, the relative normalization of the reprocessed continuum peaks at $23.0 < \log N_{\rm H}/{\rm cm}^{-2} < 23.5$ and decreases toward higher $N_{\rm H}$. This makes CT AGN even harder to detect in a flux-limited hard X-ray survey because it lowers the amount of reprocessed light that can be observed when the source is highly extinguished along the line of sight. We construct a second completeness curve from a series of spectral models assuming that $R_{\rm pex}$ continuously changes as a function of $N_{\rm H}$ by connecting the binned points shown in Figure 5.11, and extrapolating the high-$N_{\rm H}$ end according to the trend seen in the $23.0 < \log N_{\rm H}/{\rm cm}^{-2} < 24.5$ range. This curve features a peak around log $N_{\rm H}/{\rm cm}^{-2} = 23.2$ due to a peak in $R_{\rm pex}$ (see § 5.6.2 and Figure 5.11), and a significantly steeper decline with increasing $N_{\rm H}$. Both curves show that *Swift*/BAT selection is complete up to $N_{\rm H} = 10^{23}\,{\rm cm}^{-2}$. Sy II with $N_{\rm H}$ lower than this value make up 40 % of our sample and 18 % of the *Swift*/BAT-selected sample of local Seyferts.

Using a conservative completeness correction (the average between red and blue lines in Figure 5.15, constructed as described above), we find that the ratio between the number of CT AGN and the number of AGN with $N_{\rm H} < 10^{23}\,{\rm cm}^{-2}$ should be

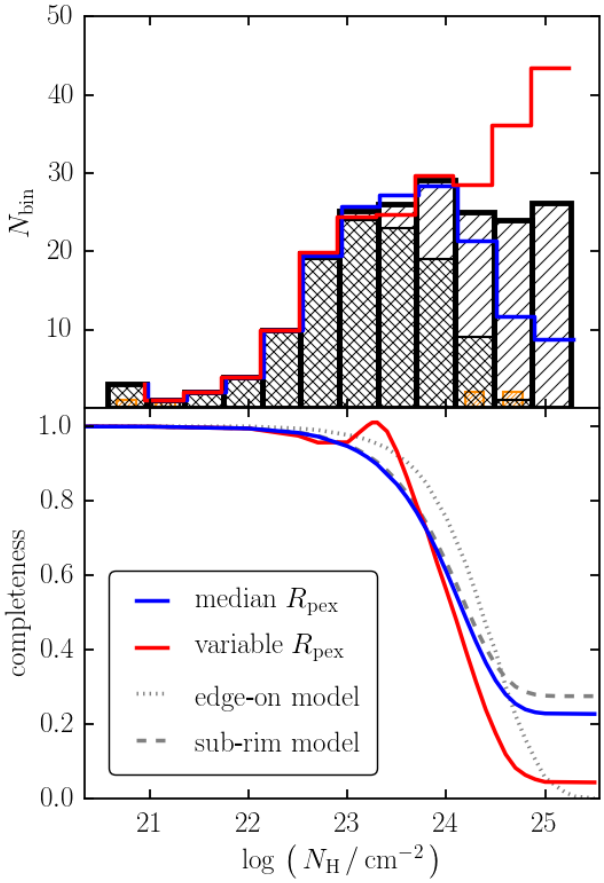

Figure 5.15: *Swift*/BAT selection completeness as a function of $N_{\rm H}$ (lower panel) and the observed and intrinsic distribution of $N_{\rm H}$ in our sample (upper panel). The doubly hatched histogram represents the observed $N_{\rm H}$ distribution, and the orange histogram bars show $N_{\rm H}$ limits for 5 targets. Outlines of the blue and red histograms show the implied intrinsic $N_{\rm H}$ distribution derived using the corresponding completeness curves shown in the lower panel: blue, assuming constant median $R_{\rm pex}$, and red, including $R_{\rm pex}$ trend shown in Figure 5.11. For comparison, we also show two completeness curves based only on theoretical spectral models (`MYtorus` in this case): one assuming edge-on orientation of a torus (dotted grey line), and one assuming viewing angle 10° below the rim of the torus. Adopting the average between the two empirical completeness curves (blue and red) we derive the conservative best-estimate intrinsic $N_{\rm H}$ distribution shown as the singly hatched histogram in the upper panel.

1.5, while the observed ratio is 0.4. This ratio is 1.63 and 1.35, respectively, for $23.0 < \log\ N_{\rm H}/{\rm cm}^{-2} < 24$. We estimate that in absence of incompleteness, CT AGN would account for approximately 49 % of our full sample and consequently, of the Sy II population. In this calculation we assumed that the 4 targets for which we obtain only lower limits on log $N_{\rm H}$ should appear 0.3 dex above the value of their

lower limit. Note that this fraction would be larger if we assumed that their true $N_{\rm H}$ was higher because completeness correction is more severe for higher $N_{\rm H}$. Our main sample excludes a number of well-known *NuSTAR*-observed CT AGN (Circinus Galaxy, NGC 424, NGC 1068, NGC 1192, NGC 4945) because they are not classified as Sy II in the *Swift*/BAT 70-month catalog, or because of the difficulty in modeling their spectra with the simple model uniformly applied to our main sample. However, for population statistics they need to be included together with the other sources observed with *NuSTAR* but excluded from our main sample.

Sy II and Sy I are nearly equally numerous in the *Swift*/BAT 70-month catalog: with $z < 0.1$ and $f_{\rm BAT} > 1 \times 10^{-11}\,{\rm erg\,s^{-1}\,cm^{-2}}$, there are 230 Sy II compared to 240 Sy I. In an unbiased sample we would expect approximately 92 AGN with $\log N_{\rm H}/{\rm cm^{-2}} < 23$, 150 AGN with $23.0 < \log N_{\rm H}/{\rm cm^{-2}} < 24$, and 138 CT AGN (280 Sy II in total). We therefore estimate the intrinsic fraction of CT AGN in the population to be $\gtrsim$27 %. Due to the uncertainty in the exact $N_{\rm H}$ of some of these CT AGN and the systematic uncertainty in the completeness correction, we consider our intrinsic CT AGN fraction estimate to more of a lower limit.

Poissonian uncertainty on this estimate is only about 5 %, but systematics mentioned in the preceding paragraph are the dominant source of uncertainty. In the most recent study of the fraction of CT AGN in the local universe, Ricci et al. (2015) used *Swift*/BAT-selected AGN to arrive at 27 ± 4 % using a completeness correction based on a theoretical model of the torus by Ikeda et al. (2009). Our results are therefore in agreement, but in our derivation there was no need for assumption of a model; our completeness correction is derived entirely empirically from observed (and slightly extrapolated) spectral properties of our sample.

5.6.6 Implications for CXB Modeling and Deep X-ray Surveys

The question of the abundance of CT AGN both in the local universe and at high redshift is still openly debated. An integral constraint on their total numbers is the cosmic X-ray background. Understanding of the components of the cosmic X-ray background (CXB) spectrum relies on synthesis models (e.g., Gilli et al. 2007, Treister et al. 2009, Akylas et al. 2012). These models require a substantial number of CT AGN to reproduce the peak of the CXB spectrum between 20 and 30 keV (e.g., Frontera et al. 2007, Ajello et al. 2008, Moretti et al. 2009). However, the exact number is still unconstrained with the various models predicting a fraction of CT AGN between 10 and 35 % of the total AGN population.

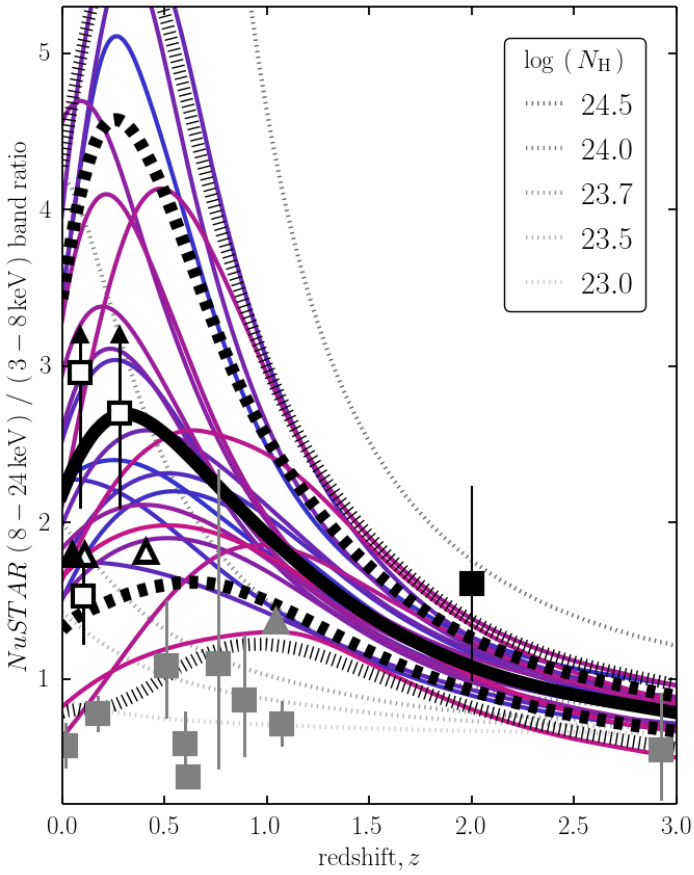

Figure 5.16: Ratio of source counts in the (8–24 keV) and (3–8 keV) *NuSTAR* bands as a function of redshift based on observed spectra of CT AGN within the *Swift*/BAT-selected survey. Purple and magenta lines represent individual AGN, demonstrating considerable diversity. The thick black line is the median curve and the thick dashed and dotted lines represent 68 % and 95 % percent containment. For comparison, the thin, grey, dotted lines in the background show the expected source counts ratio assuming a simple absorbed power-law model typically assumed in deep surveys. The plotted points are detections from early *NuSTAR* studies; see the caption of Figure 3.8 for details.

The CT AGN fraction is directly degenerate with the assumed strength of the Compton hump in non-CT AGN, since a strong Compton hump can produce a similarly peaked non-CT component of the CXB. Synthesis models typically assume $R_{\rm pex} = 1$ for Seyfert nuclei, which contribute most of the CXB. Given that our median $R_{\rm pex}$ for the sample is relatively low (0.58, though the distribution is broad and covers the range 0.05–1.81), our result implies that CT AGN should account for more of the CXB than previously thought. This is in broad agreement with recent findings, including our own estimate in the preceding section, that CT AGN fraction is leaning

toward the upper rather than the lower end of the range of previous constraints (e.g., Koss et al. 2016a, Lansbury et al. 2017, Annuar et al, in preparation).

Regardless of the fact that in this study CT AGN spectra have been analyzed only phenomenologically, we can employ them for an assessment of some techniques for identification of CT AGN in deeper surveys. Following the original calculation of band ratios within the *NuSTAR* bandpass presented in Chapter III, we expand our CT AGN sample to now include a sufficient number of sources to determine the expected band ratios with higher confidence. Indeed, individual tracks of the (8–24 keV)/(3–8 keV) band ratio as a function of redshift (shown with purple and magenta lines in Figure 5.16) display notable diversity. However, we can now construct an area within this diagram that includes approximately the majority of observed sources. The thick black line in Figure 5.16 represents the median curve, and the thick dashed and dotted lines represent 68 % and 95 % percent containment. These regions have already been employed in identifying some of the most extreme sources found in the *NuSTAR* serendipitous survey (Lansbury et al., 2017), confirming their utility for identification of faint, heavily obscured AGN.

CT AGN selection based on observation of the Fe Kα line with high equivalent width ($\simeq$1 keV) is clean and reliable, but its completeness is not known. Both here and in recent studies of particular CT AGN with *NuSTAR* (Gandhi et al., 2017), it is found that AGN unambiguously confirmed as CT do not have such strong Fe Kα emission. Reasons for relatively weak emission line may lie in significantly sub-Solar Fe abundance, self-absorption by the torus (as suggested by Ricci et al. 2014, and supported by our data), or absorption by the host galaxy gas. Because of these effects, some fraction of CT AGN cannot be identified via their Fe Kα emission. However, selecting sources with $\mathrm{EW}_{\mathrm{Fe\,K}\alpha} > 0.5$ keV results in a pure CT AGN sample (11 out of 17 in total get selected) with essentially no contamination from lower-N_{H} AGN. Lowering the threshold to 0.3 keV encompasses all 17 CT AGN in our sample, but also selects 3 non-CT AGN with $\log\ N_{\mathrm{H}}/\mathrm{cm}^{-2}$ as low as 23.1 for MCG −01-05-047.

Finally, we test a new approach for identifying CT AGN in the nearby universe proposed by Koss et al. (2016a). It is based on *spectral curvature* parameters, SC_N and SC_B, defined as follows:

$$\mathrm{SC}_B = -3.42A - 0.82B + 1.65C + 3.58D,$$

and

$$\mathrm{SC}_N = -0.46E + 0.64F + 2.33G.$$

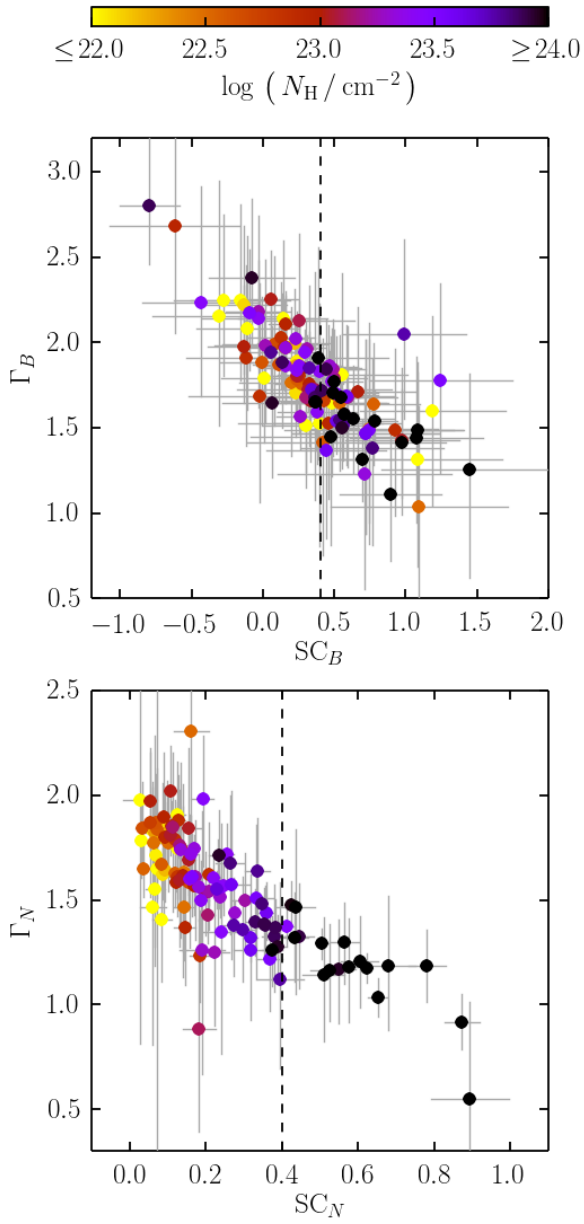

Figure 5.17: Effective photon indices in the 14–75 keV band of *Swift*/BAT (Γ_B) and *NuSTAR* (Γ_N), plotted against spectral curvature parameters SC$_B$ and SC$_N$ defined in § 5.6.6. Colors are assigned according to the best-fit log N_H using the `full` model for each source. Dashed vertical lines mark the SC> 0.4 cut proposed by Koss et al. (2016a) for selection of CT AGN. For both instruments, Γ and SC are clearly correlated, but SC separates CT AGN (darkest points) from the rest of the sample better than Γ. However, while SC$_N > 0.4$ provides a very clean sample of CT AGN, the SC$_B > 0.4$ cut results in significantly higher contamination by hard lower-N_H sources.

In the first equation above, A, B, C and D are fractions of the total 14–50 keV band count rate in the 14–20, 20–24, 24–35, and 35–50 keV subbands of the *Swift*/BAT instrument, respectively. Likewise, E, F and G are fractions of the total 8–30 keV band count rate in the 8–14, 14–20 and 20–30 keV subbands, respectively, averaged between FPMA and FPMB modules of *NuSTAR*. These quantities provide basic information on the amount of curvature in the hard X-ray spectrum in the bands where BAT and *NuSTAR* are most sensitive. Koss et al. (2016a) suggested that this information can be used to select likely heavily obscured AGN for more detailed follow-up based on their *Swift*/BAT data. We note here that in comparing our SC_B values to theirs, it should be taken into account that they used data beyond the 70-month integration time that is currently public (Baumgartner et al., 2013), though differences are negligible in the majority of cases. For three sources (2MASX J0923, J1410 and J1506) we find excessively negative SC_B, which indicates that their *Swift*/BAT spectra are V-shaped (i.e., have an apparently *negative* Compton hump). Similarly to the extreme effective photon indices, this is driven by single-channel excesses or deficits in the *Swift*/BAT spectra.

In Figure 5.17 we show how well Γ_B, Γ_N, SC_B and SC_N trace line-of-sight column density (N_H) determined from broadband spectroscopy described in § 5.4. All four variables are mutually well correlated, in agreement with expectations and Koss et al. (2016a). Large uncertainties in SC_B due to limited data quality make it difficult to establish a clear correlation with N_H: while most heavily obscured sources do have high SC_B, some do not, and many sources with hard spectra and low N_H are consistent with high SC_B values within uncertainties. SC_N has smallest relative uncertainty, since it is partially constrained by the *NuSTAR* data in the highly sensitive 8–14 keV band. The lower panel of Figure 5.17 clearly shows that SC_N is particularly well correlated with log N_H for heavily obscured AGN. This indicates that for sources detected weakly by *NuSTAR*, e.g., in a component of its Extragalactic Legacy Survey program, the SC_N parameter offers a reliable option for identifying faint local CT AGN for which detailed spectral information is not available.

5.7 Summary and Conclusions

The sample of 124 Sy II AGN (covering optical Seyfert types 1.8, 1.9 and 2.0) selected from the *NuSTAR* survey of *Swift*/BAT AGN represents the largest atlas of high-quality hard X-ray spectra of obscured AGN to date. Supplemented with quasi-simultaneous soft X-ray observations with *Swift*/XRT, the survey provides snapshots

of broadband X-ray spectra in the 0.3–79 keV band, allowing us to define the typical spectral parameters and hence better separate extreme spectra. In comparison to previous work, the advantage of our sample is that it is large, representative, and complete up to high levels of obscuration, where the $N_{\rm H}$-dependent selection function of the *Swift*/BAT survey causes only a fraction of CT AGN to be significantly detected. With the empirical constraints on the main spectral components found in this study we are able to account for this incompleteness more robustly than previous studies.

The phenomenological model employed for spectral analysis in this chapter directly corresponds to models used in much of the literature over the past $\simeq$ 20 years, and in synthesis models for the cosmic X-ray background (CXB). In comparison to those studies, we find a number of interesting phenomenological results summarized below.

- The distribution of intrinsic photon indices for type II AGN is not significantly different than that of their type I counterparts. The median and, to smaller extent, the width of the distribution depend on the assumed spectral model. The median is found to be 1.77 ± 0.02 and the spread in the population is $\sigma(\Gamma) = 0.15 \pm 0.02$ for our `full` model, which includes the reprocessed continuum in the form of `pexrav` and the high-energy cutoff fixed at 300 keV. However, neglecting the reprocessed continuum where it is not formally required by the data, modeling the reprocessed continuum with `pexmon` (with fluorescent lines forced to be consistent with the `pexrav` continuum), or assuming no cutoff in the intrinsic spectrum, shifts the median of the Γ distribution between 1.65 and 1.89 (with $\sigma(\Gamma) \approx 0.15$ in each case). Many previous studies of this distribution were based on data which did not allow for tight constraints on Γ in individual Sy II spectra. Furthermore, comparisons between type I and type II distributions were often made without regard to the model assumptions described above, which clearly do contribute systematic uncertainties.

- The median of the distribution of high-energy cutoffs in the intrinsic continua of Sy II is found at 290 ± 50 keV. This value includes lower limits, which comprise a significant fraction of our constraints, and excludes the degenerate cases that do not correspond to physical combinations of Γ and $E_{\rm cut}$ based on physical models of AGN coronae with electron optical depth below 3. In many previous studies limits were excluded and degenerate cases were not,

leading to a range of less reliable measurements of the typical $E_{\rm cut}$ in Seyferts of any type. Our median $E_{\rm cut}$ is very well matched to the previous assumptions folded into CXB synthesis models.

- Parametrized with the popular `pexrav` model and its internal parameter $R_{\rm pex}$, the reprocessed continuum normalization is found to be broadly distributed in log-space, with a median at 0.58 ± 0.04. For many sources we found best-fit values below as well as above $R_{\rm pex} = 1$, which corresponds to a 50 % covering factor by infinitely optically thick material. Most previous studies of obscured AGN samples have found higher average $R_{\rm pex}$ (2–3), however, they only considered AGN for which this component is strongly detected, creating a clear bias toward high values. This is at least in part due to the lack of good-quality coverage in the 5–50 keV range, which critically constrains this component, and where *NuSTAR* data provides the key new spectral information.

- With the lower average $R_{\rm pex}$ in comparison with the CXB models, less of the CXB flux at its peak can be accounted for by obscured non-CT Seyferts. In turn, that implies that the contribution from CT AGN is higher, and that a larger fraction of CT AGN is still missing from the population census.

- The CXB synthesis models also require an unbiased (intrinsic) distribution of $N_{\rm H}$ as input. In this survey the selection function is inherited from *Swift*/BAT, meaning that it is incomplete at the high-$N_{\rm H}$ end. While we cannot remove that lack of completeness, by constraining the spectral shapes of CT AGN we can derive entirely empirical correction factors to estimate the numbers of missing CT sources, without relying on theoretical models. Due to the observed variety of relative normalizations of the reprocessed continua in non-CT Sy II spectra, these correction factors are uncertain by factors of a few. This makes our inferred CT AGN fraction of $\simeq 30$ % broadly consistent with the higher end of the previous estimates with comparable uncertainties (though they are not always explicitly acknowledged, likely because they are dominated by largely unknown systematic uncertainties).

- We investigate some strategies for finding the elusive CT AGN population. In particular, we find that weighted multi-band photometry performed on short *NuSTAR* observations (effectively probing spectral curvature) unambiguously selects CTAGN as proposed by Koss et al. (2016a). Selection by simpler

band ratios, e.g., using the *NuSTAR* 3–8 and 8–24 keV subbands is plagued by the fact that many RD spectra (implying line-of-sight $N_{\rm H}$ in excess of $10^{24.5}\,{\rm cm}^{-2}$) have similar band ratios to more mildly obscured sources with $N_{\rm H}\approx 10^{23.5}\,{\rm cm}^{-2}$. We find evidence that spectral variability, in combination with similarity of spectral shapes in the high-$N_{\rm H}$ regime, likely contributed to a number of misidentifications of CT AGN in the literature. Selection by Fe Kα equivalent width was found to be efficient, though the relatively low value above which all CT AGN in our (notably incomplete) subsample are selected also implies a low level of contamination by lower-$N_{\rm H}$ sources.

Despite the giant leap in sensitivity going from the previous generation of hard X-ray telescopes to *NuSTAR*, it is important to note that the short observations presented here do not have more than a factor of few better photon statistics above 10 keV. The value of the survey is in defining the baseline broadband model from a large and representative sample of Sy II objects without the issue of averaging over a long time period. Follow-up observations aimed at building up data quality in order to better constrain spectra of particular AGN are not implausible; unlike with *Swift*/BAT and *INTEGRAL*, increasing the total photon count by a factor of few can be achieved in reasonable exposure time with *NuSTAR*.

The targets with highest-quality data, our modeling of CT AGN spectra, and the relative normalization of the fluorescent lines with respect to the Compton hump in the main-sample data, all suggest that the Sy II spectra would be statistically better described with reprocessed spectral components with a variety of Compton hump shapes and fluorescent line strengths. We indirectly showed that this can be readily achieved with self-consistently calculated reprocessed spectra for a toroidal geometry with a range of covering factors and average column densities *unrelated* to the observed line-of-sight column density. Spectral analysis of the sample where such models are directly fitted to the X-ray data presented here is the topic of the next chapter.

Acknowledgements

M. B. acknowledges support from NASA Headquarters under the NASA Earth and Space Science Fellowship Program, grant NNX14AQ07H.

This work was supported under NASA Contract No. NNG08FD60C, and made use of data from the *NuSTAR* mission, a project led by the California Institute of Technology, managed by the Jet Propulsion Laboratory, and funded by the National Aero-

nautics and Space Administration. We thank the *NuSTAR* Operations, Software and Calibration teams for support with the execution and analysis of these observations. This research has made use of the *NuSTAR* Data Analysis Software (`NuSTARDAS`) jointly developed by the ASI Science Data Center (ASDC, Italy) and the California Institute of Technology (USA). Part of this work is based on archival data, software, and online services provided by the ASI Science Data Center (ASDC).

Chapter 6

NUSTAR SURVEY OF THE LOCAL SEYFERT II POPULATION: GEOMETRY OF THE OBSCURING TORUS

Abstract

The obscuring torus is one of the main components of the basic unified model of active galactic nuclei (AGN), needed to create anisotropy in obscuration as a function of the viewing angle. We present the first study of the geometrical properties of the AGN torus in a large and representative sample of type II Seyfert nuclei as a continuation of the *NuSTAR* survey of *Swift*/BAT AGN described in Chapter V. The sample consists of 124 AGN selected in the hard X-ray band from the *Swift*/BAT 70-month catalog and observed simultaneously with *NuSTAR* and *Swift*/XRT. These data enable us to explore the constraints that observed spectra place on the properties of the obscuring torus in individual AGN and in the local population of Seyfert II nuclei. We make use of empirically motivated spectral models for X-ray reprocessing in approximately toroidal geometry (`MYtorus` and `borus02`) for constraining the distribution of the average column density of the torus ($N_{\rm H,tor}$), and the distribution of the torus covering factor ($C_{\rm tor}$) within this sample. We find that the average torus column density is independent of the line-of-sight column density, with the median at $\log\ N_{\rm H,tor}/{\rm cm}^{-2} = 24.2$ and the 68 % probability interval spanning $23.5 < \log N_{\rm H,tor}/{\rm cm}^{-2} < 24.7$. The $C_{\rm tor}$ distribution is broad but shows a preference for high covering, peaking around the covering factor 0.9, and with the median at 0.68. We also examine the dependence of $C_{\rm tor}$ on intrinsic luminosity, finding that the median $C_{\rm tor}$ peaks at 10–50 keV intrinsic luminosity $\simeq 3 \times 10^{42}$ erg s^{-1} and decreases toward both lower and higher luminosities.

Material presented in this chapter will be submitted for publication in AAS Journals.

6.1 Introduction

6.1.1 Previous Studies of Obscured AGN in the X-ray Band

Presence of a significant amount of material in between the observer and an X-ray source in an AGN results in line-of-sight absorption, imprinting a photoelectric exponential cutoff at low energies. AGN with line-of-sight column density ($N_{\rm H,los}$, usually referring to absorption by largely neutral gas) exceeding $10^{22}\,{\rm cm}^{-2}$ are considered obscured. We adopt that definition in this work. At optical depth of a few, Compton scattering becomes so efficient at removing photons from our line of sight that the X-ray spectrum becomes dominated by light scattered, or reprocessed, in the material surrounding the X-ray source. Studies of X-ray spectra of obscured AGN have been severely limited by the available instruments in the past. Photoelectric absorption extinguishes the intrinsic continuum in the soft X-ray band, where sensitive focusing X-ray telescopes have been available since the launch of the *Einstein Observatory* in 1978.

There is some confusion in the literature because $N_{\rm H,los}$ may be very different from the column density in directions out of the line of sight (average torus column density, $N_{\rm H,tor}$, hereafter), since some studies make no distinction between the two quantities. The angle-averaged column density outside of the line of sight cannot be measured with phenomenological models used in the bulk of literature on AGN X-ray spectroscopy and Chapter V of this thesis. Ever since it was shown that the commonly observed narrow line(s) of iron can be associated with Compton-thick (CT) matter out of the line of sight in most AGN (e.g., Awaki et al. 1991, George & Fabian 1991, Matt et al. 1991), it became the norm to attribute the fluorescent lines and the Compton hump to a reprocessor approximated by a planar geometry with infinite optical depth (i.e., $N_{\rm H,tor} > 10^{25}\,{\rm cm}^{-2}$). The most popular of such models are `pexrav` (Magdziarz & Zdziarski, 1995), and its update `pexmon` (Nandra et al., 2007). We used them for phenomenological modeling in Chapters II, III, and V in order to better connect our results to the large body of literature on X-ray spectroscopy of AGN.

Reprocessed components of AGN spectra are known to depend on the geometry and the properties of the reprocessing material, as shown by, e.g., Leahy & Creighton (1993), Ghisellini et al. (1994), Krolik et al. (1994), Yaqoob (1997), Matt et al. (1999), Levenson et al. 2002, Murphy & Yaqoob (2009), Ikeda et al. (2009), Brightman & Nandra (2011a), Tatum et al. 2013, Liu & Li (2014), Furui et al. (2016). In the basic unified model, AGN classification is related to orientation of the ob-

server with respect to the structures surrounding the central engine. A large body of observational results in the literature supports a geometry that is in some general sense, toroidal. Many studies (e.g., Pancoast et al. 2014, Elitzur & Netzer 2016) suggest that the broad-line region (BLR) has an approximately toroidal structure as well, and that there may be no distinct boundary between the broad-line region and the classical parsec-scale torus. It is of paramount importance to understand the spectral signatures of reprocessing of X-rays in approximately toroidal geometries in order to use spectral features detectable in X-ray spectra of AGN to constrain the properties of these spatially unresolvable structures. In the following section we compare some of the publicly available spectral models for reprocessing in the AGN torus.

6.1.2 Brief Comparison of Spectral Models for Torus Reprocessing

In this chapter, and this thesis in general, we refer to any approximately toroidal distribution of matter surrounding the central SMBH as the torus, regardless of its actual size or distance from the central engine. None of the currently available spectral models for the torus is restricted to an absolute size scale, so they can be applied to any toroidal distribution of matter that is centrally-illuminated by X-rays. It is important to emphasize that the material contributing to obscuration and reprocessing in the X-ray band does not necessarily have to be the same dusty material observable in the infrared band, which is usually called a torus although its geometry is not believed to be strictly toroidal.

In the § 6.3 we are applying `MYtorus` and `borus02` directly to the broadband spectra of AGN in our large sample, in order to constrain their main spectral parameters. We further discuss the clumpy `Ctorus` model in comparison with our fitted torus models in § 6.5.1.

`MYtorus`

`MYtorus` was the first torus reprocessing model to be made public in a form that is suitable for spectral fitting of X-ray data within the popular spectral analysis tool `Xspec` (Arnaud, 1996). It is also the most widely used in contemporary literature, including many studies based on *NuSTAR* data (e.g., Baloković et al. 2014, Bauer et al. 2015, Boorman et al. 2016, Annuar et al. 2017).

The `MYtorus` model was designed specifically for modeling the X-ray spectra of AGN with a reprocessor that has exactly toroidal geometry. The ratio of the torus

cross-section and its radius is fixed at 2, so that the torus covers 50 % of the sky as seen from the central X-ray source. It has uniform density, so that observers at different inclination angles ($\theta_{\rm inc}$, measured from the axis of symmetry) see different $N_{\rm H,los}$, ranging continuously between the column density at the equator ($N_{\rm H,equ}$) to zero at the rim of the torus (at $\theta_{\rm inc} = 60°$). $N_{\rm H,los}$ is directly related to $\theta_{\rm inc}$ and $N_{\rm H,equ}$ via the following analytic expression:

$$N_{\rm H,los} = N_{\rm H,equ} \times \sqrt{1 - 4\,(\cos\theta_{\rm inc})^2} \tag{6.1}$$

The average column density over the half of the sky covered by the torus, as seen from the center, is lower than $N_{\rm H,equ}$. Integration of Equation 6.1 over all lines of sight though the torus gives the angle-averaged column density equal to $(\pi/4)\,N_{\rm H,equ}$. Although the fitting parameter of the `MYtorus` model is $N_{\rm H,equ}$, for consistency with other models considered in this work, we discuss only the average torus column density defined as $N_{\rm H,tor} = 0.785\,N_{\rm H,equ}$.[1]

In addition to the coupled configuration that represents a torus with a 50 % covering factor, the `MYtorus` tables can be employed to emulate a wider range of spectra that approximate the effects of non-toroidal geometry, torus clumpiness, spectral variability, and covering factors other than 50 %. In order to achieve this, some of the parameters of the reprocessed and line-of-sight components of the model are *decoupled* and used as independent spectral components. In such a decoupled configuration, the model does not have a straightforward geometrical interpretation that the coupled model does, but it is significantly more flexible in terms of the diversity of X-ray spectra it can reproduce. Yaqoob (2012) presented detailed examples of fitting the `MYtorus` model to X-ray data in both configurations, and a possible interpretation of results based on fitting in the decoupled configuration. A number of more recent studies successfully applied this fitting strategy to studies of X-ray spectra of bright AGN: e.g., Braito et al. (2013), Arévalo et al. (2014), Baloković et al. (2014), Puccetti et al. (2014), Bauer et al. (2015), Yaqoob et al. (2015).

`borus02`

The `borus02` model is a part of the new suite of models for reprocessed spectra in various approximately toroidal geometries representing the AGN torus. These calculations are based on a novel Monte Carlo radiative transfer code `BORUS`, and

[1] Equivalently, $\log N_{\rm H,tor}/{\rm cm}^{-2} = \log N_{\rm H,equ}/{\rm cm}^{-2} - 0.105$.

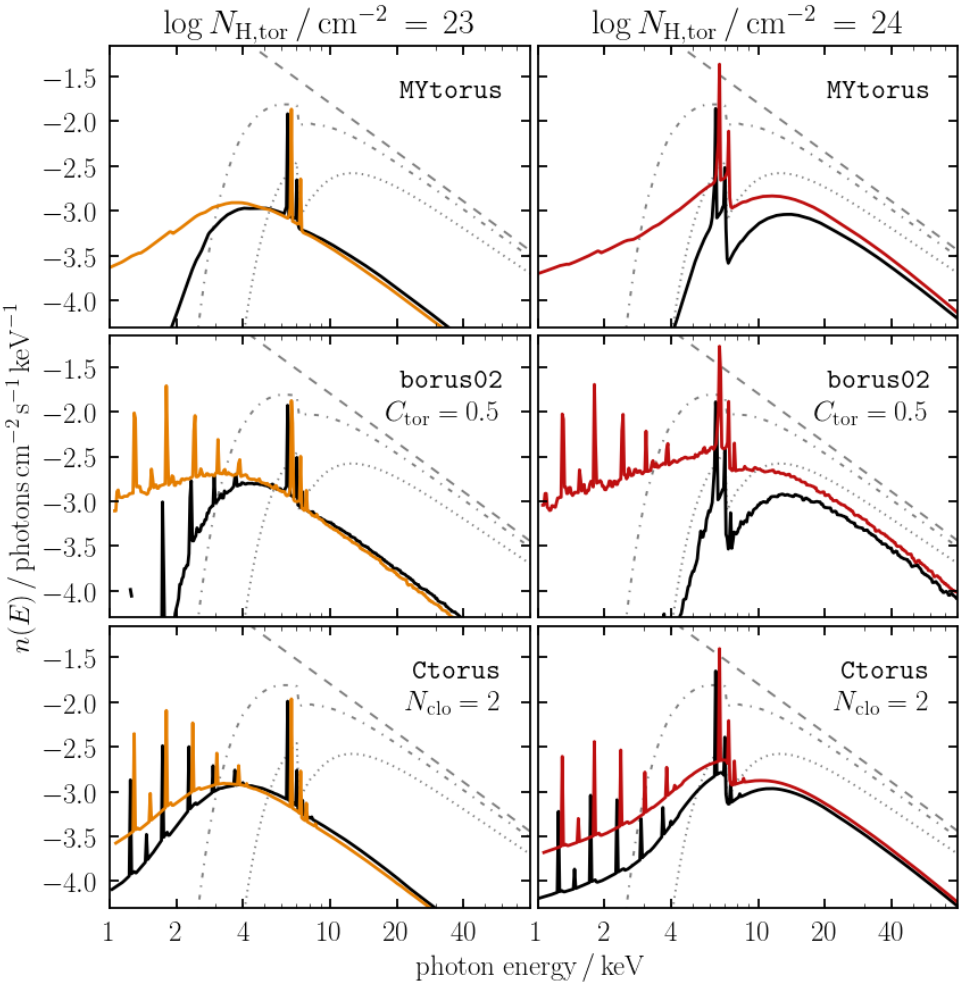

Figure 6.1: Comparison of three publicly available models for reprocessed spectra generated in toroidal and approximately toroidal geometry. The first row shows `MYtorus` (Murphy & Yaqoob, 2009), second row shows `borus02` (Baloković et al., in preparation, see Chapter IV), and the third row shows spectra from the `Ctorus` model (Liu & Li, 2014). All models have a covering factor of 50 %. Two columns show different torus column densities: 10^{23} cm^{-2} on the left, and 10^{24} cm^{-2} on the right. In each panel, the black and colored lines show the reprocessed spectral components for an edge-on and pole-on inclination, respectively. The differences between spectra at these extreme inclinations is primarily due to self-absorption in the torus, while the differences between models are due to different adopted geometry. For context and easier comparison, in each panel we also show the $\Gamma = 1.8$ intrinsic continuum (dashed line) and two absorbed components with log $N_{\rm H,los}$/cm^{-2} = 23.5 (dash-dotted line) and 24.0 (dotted line).

will be presented in detail in Baloković et al., in preparation. Some of its basic assumptions have been outlined in Chapter IV, where the first application of the `borus02` model to observational data was presented. Specifically, for the `borus02` model we adopted the same geometry as Brightman & Nandra (2011a) for their `BNtorus` model: the torus is approximated by a sphere with uniform density and bi-conical cutouts with a range of opening angles. The torus half-opening angle ($\theta_{\rm tor}$), as well as inclination ($\theta_{\rm inc}$), increase away from the symmetry axis of the torus. The covering factor of the torus, as seen from the X-ray source in the center, is simply related to the half-opening angle of the torus, $\theta_{\rm tor}$, as $C_{\rm tor} = \cos\theta_{\rm tor}$.

The physics incorporated in `MYtorus` and `borus02` models is largely equal. Both models include a calculation of fluorescent emission of the Kα and Kβ lines of Fe and the Ni Kα line, together with their down-scattered Compton shoulders. However, `borus02` also includes fluorescent emission of other elements up to atomic number 30 (note the < 4 keV emission lines in Figure 6.1). Unlike `MYtorus`, `borus02` also allows the user to self-consistently vary the relative abundance of Fe in the torus, and include an exponential high-energy coronal cutoff. The main difference between `MYtorus` and `borus02` reprocessed spectra is due to the adopted geometry. In Figure 6.1 we show model spectra, with the covering factor of the `borus02` model set to 50 % so that it matches the (fixed) covering factor of the `MYtorus` model. Changing $C_{\rm tor}$ while keeping all other parameters the same would primarily result in a change of the relative normalization and the prominence of the Compton hump with respect to the intrinsic continuum.

Although we used the same geometry as Brightman & Nandra (2011a) for `borus02`, this newer calculation is more detailed, flexible, includes features that the original calculation lacks, and resolves some known problems. As Liu & Li (2015) recently pointed out, and we confirmed in Chapter IV, there is significant disagreement between `BNtorus` and other radiative transfer calculations for the same geometry. The problem was found to be due to an error in the original code used for the `BNtorus`computation. `borus02` is therefore a replacement for `BNtorus`, which has been a popular choice in many recent spectroscopic studies of obscured AGN (e.g., Gandhi et al. 2014, Ricci et al. 2015, Farrah et al. 2016) as the only publicly available model with a covering factor as a free parameter of the model. While the torus model of Ikeda et al. (2009) has been used for constraining the torus opening angle in a small number of studies (e.g., Eguchi et al. 2011, Tazaki et al. 2011, Tanimoto et al. 2016), the lack of fluorescent emission lines and the limited parameter space of its

publicly available version limit its wider application.

`Ctorus`

`Ctorus` (Liu & Li, 2014) is currently the only publicly available torus model with non-uniform density distribution. It is based on simulations employing the particle interaction simulator GEANT4.[2] The adopted geometry is similar to `BNtorus` (Brightman & Nandra, 2011a) and `borus02` (Baloković et al, in preparation; see Chapter IV): the torus is approximated with a sphere with bi-conical polar cutouts. However, the half-opening angle is fixed at 60° ($C_{\rm tor} = 0.5$), and instead of a uniform density, the torus volume is filled with individual clumps and empty space between them. The number density of clumps can be regulated via the $N_{\rm clo}$ parameter, which specifies the number of clumps along an equatorial line of sight to the X-ray source. This parameter makes `Ctorus` a unique resource for investigating the effects of clumpiness on X-ray reprocessed spectra.

In Figure 6.1 we show model curves computed assuming $N_{\rm clo} = 2$ (the minimum of its domain) in order to show the similarity between reprocessed spectra generated by a porous torus seen edge-on and reprocessed spectra observed pole-on in uniform torus models. This similarity is due to the fact that in a clumpy torus, even edge-on observers have direct lines of sight to the innermost part of the torus between individual clumps that could otherwise obscure it. Reprocessed spectra with relatively strong soft X-ray flux are typical for the inner, directly illuminated walls of the torus. Although we do not fit the `Ctorus` model directly to the X-ray data in this work, this argument will be important for interpretation of our fitting results in § 6.5.

6.2 Sample Selection and Data

The work presented here is a continuation of spectral modeling of the large, hard X-ray selected, flux-limited survey of Seyfert II nuclei (Sy II hereafter) in the local universe ($z < 0.1$). Selection is based on the *Swift*/BAT 70-month catalog (Baumgartner et al., 2013), and the optical classification published therein. We use a broad definition of Sy II that includes AGN optically classed as Sy 1.8, Sy 1.9, and Sy 2.0. In total, 124 targets are included in our sample. We make use of *NuSTAR* data coupled with *Swift*/XRT data taken quasi-simultaneously (typically within 1 day, to minimize issues due to spectral variability), and *Swift*/BAT data averaged over

[2] `http://geant4.cern.ch/`

70 months. Details regarding the target selection, *NuSTAR* and *Swift* observations, data processing procedures, and data quality are given in Chapter V, specifically in § 5.2 and § 5.3.1.

6.3 Spectral Modeling

We perform spectral modeling in `Xspec` (Arnaud, 1996). As in Chapter V, we use a combination of $p_{\rm null} > 5$ % and the visual assessment of the flatness of residuals in order to determine whether a particular model is acceptable as a good description of the observed spectrum. As in the modeling presented in Chapter V, before rejecting any model, we test whether addition of a spectral component (`mekal`, $E_{\rm cut}$, etc.), or censoring small parts of the data, would result in a significantly better fit. In nearly all cases we find that this results in the same modifications described in Chapter V (§ 5.4.2 and § A,).

If a parameter can be limited to a range that is smaller than its domain, so that there is a gradient in χ^2 exceeding $\delta\chi^2 = 1$ from the best fit while all other parameters are free to vary, we consider that parameter constrained. We base our constraints on marginalized probability distributions derived from converged MCMC chains produced with the built-in Goodman & Weare (2010) MCMC algorithm in `Xspec`. They can be two-sided or one-sided. For two-sided constraints uncertainty is quoted as the interval containing 68 % of the total probability, equivalent to 1 σ uncertainty for a Gaussian probability distribution. When $\delta\chi^2$ between the best fit and the edge of the domain is less than unity, we quote a 1 σ limit, so that 84 % of the total probability is enclosed (conversely, 16 % is left out). We verified that the best-fit parameters are always within the uncertainty interval, although they often do not exactly match the distribution medians (e.g., in cases of non-trivial degeneracy between parameters). In constructing distributions of spectral parameters within a sample, we make use of the MCMC-based marginalized probability density functions (PDFs) for each target in our sample, summing them to obtain the joint PDF. In figures throughout the rest of this Chapter, we show PDFs computed in this way with thick lines plotted over the histograms showing the distribution of best-fit values.

In the work presented here, the Fe abundance relative to Solar abundance is kept fixed at unity. This is both due to the fact that including this parameter would result in additional degeneracy between spectral parameters, and the fact that the `MYtorus` model does not feature such a parameter. Except where we note explicitly

that the high-energy cutoff in the intrinsic spectrum ($E_{\rm cut}$) is fitted, we keep it fixed at 300 keV. In finding a best fit for every target in our sample, we follow the same procedure as in Chapter V: if residuals of a model indicate that a component such as photoionized plasma (`mekal`), Thomson-scattered continuum, or $E_{\rm cut}$ would improve the fit, we add it to the basic model. We ignore extraneous bins of data that obviously do not correspond to real spectral features yet cause χ^2 to remain high. For targets with a large cross-normalization offset between *Swift*/BAT and *NuSTAR* data, we test whether best-fit parameters change significantly when *Swift*/BAT are excluded.

For application in uniformly fitting the whole sample with model for the AGN torus we choose the `MYtorus` and `borus02` models. Their basic properties have been described and compared in § 6.1.2. The following subsections are ordered by the complexity of the spectral model. We start with a simpler pair of torus models, in which spectral parameters $N_{\rm H,los}$ and $N_{\rm H,tor}$ are coupled via the geometry assumed for the model. Then, in the following four sections we explore spectral fitting with models which allow for greater flexibility in spectral shapes by having these column density parameters decoupled and fitted separately.

6.3.1 Coupled `borus02` Model

Despite the fact that `borus02` is generally a more flexible model then `MYtorus`, in the coupled configuration used for spectral fitting in this work, it is the simplest torus model to understand and interpret. A basic model may be defined with the following command sequence in `Xspec`:

$$\begin{aligned} \texttt{m} \;&=\; \texttt{c}_1 \times \texttt{phabs} \times (\texttt{atable\{borus02.fits\}} \\ &+\; \texttt{zphabs} \times \texttt{cabs} \times \texttt{cutoffpl} + \texttt{c}_2 \times \texttt{cutoffpl}\,) \end{aligned}$$

In the expression above, $\texttt{c}_1$ and $\texttt{c}_2$ stand for instrument cross-normalization and the relative normalization of a leaked or Thomson-scattered unabsorbed reflection of the intrinsic continuum, respectively. `phabs` accounts for foreground Galactic absorption, while `zphabs`×`cabs` represents line-of-sight absorption at the redshift of the X-ray source, including Compton scattering losses out of the line of sight. `cutoffpl` represents the intrinsic continuum, and its parameters should be linked to the Γ, $E_{\rm cut}$, and normalization parameters of the `borus02` table. For the coupled model, we also link the column density of the `zphabs`×`cabs` component ($N_{\rm H,los}$) to the torus column density in the `borus02` component ($N_{\rm H,tor}$), so that the model only

has a single column density as a free parameter in the fit. The intrinsic continuum is assumed to be a power law with an exponential cutoff, $n(E) \propto E^{-\Gamma} \exp(-E/E_{\rm cut})$.

An acceptable fit can be found for the majority of targets in our sample. However, in some cases with above-average data quality, it can happen that the $p_{\rm null}$ threshold is exceeded, although it is clear from the residuals that the model does not fit the Compton hump well. We do not consider those cases as acceptable. In total, we find that for 93 targets a good fit cannot be found with the assumption that $N_{\rm H,tor} = N_{\rm H,los}$. Excluding sources for which $N_{\rm H,los}/\,{\rm cm}^{-2} < 22$ (i.e., outside of the domain of `borus02`), we find that the assumption is unacceptable for 11/113 (10 %) targets in our sample. For 19 % of the sources for which this model fits well we can derive no constraints on the torus parameters. These are mostly targets with low data quality and targets with low $N_{\rm H,los}$. For the remaining targets we obtain either a full constraint or an upper or lower limit (1 σ equivalent) on $C_{\rm tor}$.

6.3.2 Coupled `MYtorus` Model

The basic properties of the model have been described in § 6.1.2. The tables containing spectral templates arranged in an `Xspec` table model files can be obtained from the Web.[3] Specifically, we used tables with the calculation extending up to 200 keV in order to approximately match our choice of the high-energy cutoff fixed at 300 keV. The fitting model is defined in `Xspec`as:

$$\begin{aligned} \texttt{m} \;&=\; \texttt{c}_1 \times \texttt{phabs} \times (\texttt{atable\{MYtorusS.fits\}} + \texttt{atable\{MYtorusL.fits\}} \\ &+\; \texttt{etable\{MYtorusZ.fits\}} \times \texttt{cutoffpl} + \texttt{c}_2 \times \texttt{cutoffpl}\,) \end{aligned}$$

In the expression above, `MYtorus` tables with appended `S`, `L`, and `Z`, represent the reprocessed (scattered) continuum, reprocessed line emission, and the absorption profile (co-called zeroth-order continuum). In the coupled model, all parameters of the `MYtorus` tables are linked, so that the model corresponds to a solid torus with $C_{\rm tor} = 0.5$. $\texttt{c}_1$ and $\texttt{c}_2$ stand for instrument cross-normalization and the relative normalization of a Thomson-scattered unabsorbed reflection of the intrinsic continuum, respectively, while `phabs` accounts for foreground Galactic absorption.

From this analysis we exclude 10 sources which are known to be unobscured from the modeling presented in Chapter V.[4] We find that the majority of spectra in our

[3] `www.mytorus.org`

[4] This is partly based on the technical limitation of the model to column densities above 10^{22} cm^{-2}. Additionally, with the line of sight not passing through the torus, modeling with the coupled model becomes equivalent to a decoupled model, which is presented in the following section.

sample can be fitted well with this model: 93 targets (82 %, excluding unobscured sources) reach $p_{\rm null} > 5$ % for the best-fit set of parameters. This includes testing for a limited set of additional spectral components where necessary, as described in the previous section. For the remaining targets, the model does not provide a good fit to the data. The most common reason for a poor fit is the unmatched shape of the Compton hump or the strength of the Fe Kα line. Fitting results are listed in Table **??**. An immediate result of the spectral modeling with the coupled `MYtorus` model is a pile-up of best-fit inclinations in a very narrow range close to the rim of the torus, $60^\circ < \theta_{\rm inc} < 61^\circ$. As shown in Figure 6.2, more than 80,% of the sources are found with their inclination constrained to $< 65^\circ$, excluding fully unobscured sources. This is a simple consequence of the fact that for any average column density of the torus in the CT regime, a very large range in $N_{\rm H,los}$ occurs only within that narrow range of angles. This is not unexpected and should not be interpreted physically, since it is just a consequence of the particular geometry chosen from this spectral analysis. That alone is sufficient motivation for exploration of the `MYtorus` model in its decoupled configuration, in which $N_{\rm H,los}$ is not directly related to $\theta_{\rm inc}$, in the following section. We further discuss the results based on the coupled `MYtorus` fits in § 6.4.1.

6.3.3 Decoupled `MYtorus` Model

With high-quality data, such as those used in, e.g., Yaqoob (2012) or Puccetti et al. (2014), one can include both unobscured (pole-on, $\theta_{\rm inc} = 0^\circ$) and obscured (edge-on, $\theta_{\rm inc} = 90^\circ$) components of the reprocessed spectrum. With the lower data quality here, we only aim to identify the primary reprocessed component. In principle, it is also possible to fit for the relative normalization of the reprocessed spectrum with respect to the intrinsic continuum, in which case the torus parameters are constrained from the shape of the reprocessed spectrum alone. That requires exquisite data quality that we do not consider in this work.[5] Henceforth we assume that the relative normalization of the reprocessed component (both the continuum and the lines) is always fixed at unity. In the modeling presented here, *decoupling* refers only to $N_{\rm H,tor}$ being independent of $N_{\rm H,los}$.

For the decoupled setup, in the `Xspec` expression given in § 6.3.2, we replace the tabulated line-of-sight component of `MYtorus` (denoted `MYtorusZ`, the zeroth-

[5] Fitting for the relative normalization of the reprocessed components should generally be allowed because of variability. However, without high-quality multi-epoch data, changing the relative normalization or adding additional components leads to the loss of geometrical interpretation of the model; i.e., it does not correspond to a torus with a 50 % covering factor (Yaqoob, 2012).

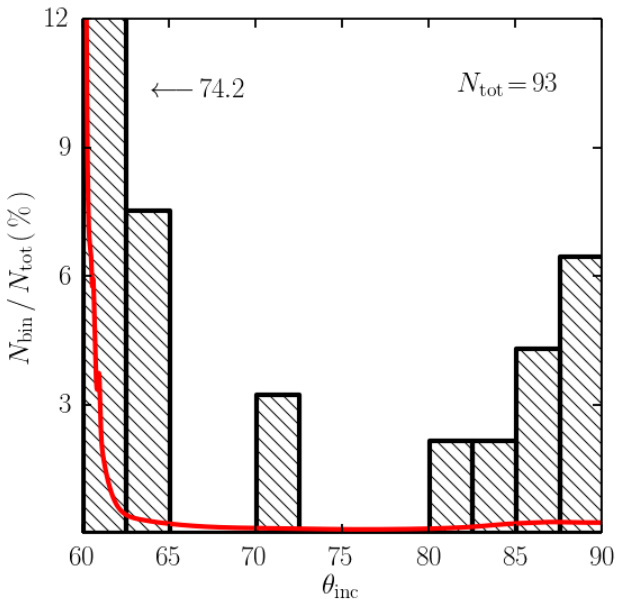

Figure 6.2: Constraints on the inclination parameter ($\theta_{\rm inc}$) using the `MYtorus` model in its coupled configuration. The pile-up at $\theta_{\rm inc} < 65°$ is a consequence of the column density profile, which features a very steep gradient in the line-of-sight column density ($N_{\rm H,los}$) close to the torus rim at $\theta_{\rm inc} = 60°$ whenever the average column density of the torus ($N_{\rm H,tor}$) is in the CT regime.

order continuum) with an absorbed cutoff power-law component, including Compton scattering out of the line of sight. The photon index (Γ) and the normalizations of the intrinsic continuum and both reprocessed components are assumed to be the same. In this configuration, the inclination parameter of the reprocessed components acts as a switch between a reprocessed spectrum being more similar to pole-on (unabsorbed), or more similar to edge-on (absorbed), as discussed in § 6.1.2. We first leave it as a free parameter in our fitting in order to see if the data shows a preference. However, to reduce the amount of degeneracy between spectral parameters, in calculating constraints on the torus column density ($N_{\rm H,tor}$), we fix the inclination to either $\cos\,\theta_{\rm inc} = 0.1$ or $\cos\,\theta_{\rm inc} = 0.9$. The former represents absorbed reprocessed spectra, marked with an "A" in Table C5, and the latter represents unabsorbed reprocessed spectra, marked with a "U".

6.3.4 Decoupled `borus02` Model

Lastly, we employ a model based on `borus02` with $N_{\rm H,tor}$ fitted independently from $N_{\rm H,los}$. In this case, $N_{\rm H,tor}$ (and other torus parameters) are constrained only by spectral features on top of the dominant absorbed intrinsic continuum. In spectra of

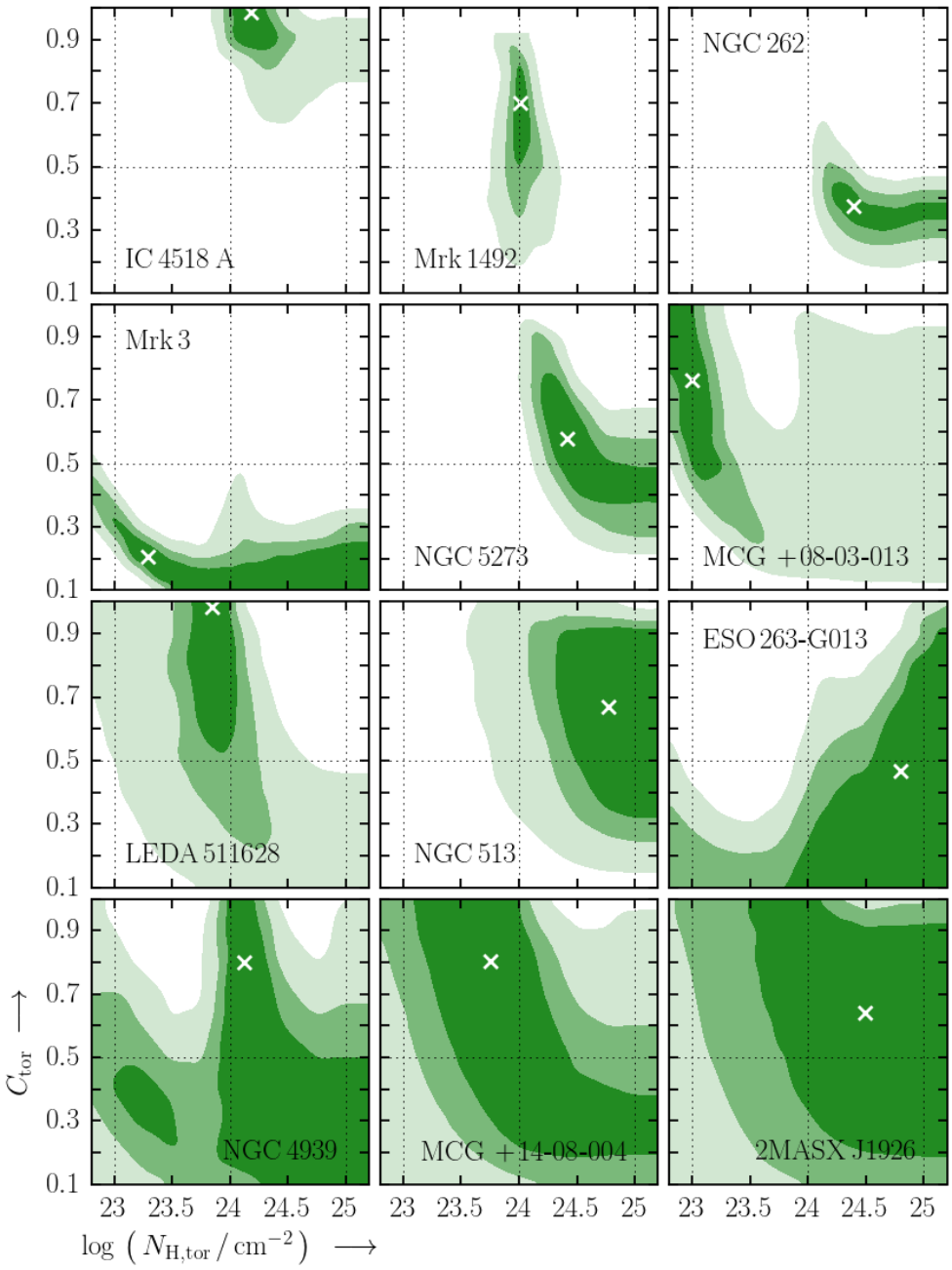

Figure 6.3: Examples of typical two-dimensional constraints in the parameter space spanned by the spectral parameters $N_{\rm H,tor}$ and $C_{\rm tor}$. Green areas show 1, 2, and 3 σ confidence regions (from darker to lighter color, respectively). White crosses mark the best fits. With dotted, black lines we show three values of $N_{\rm H,tor}$ for which we calculate $C_{\rm tor}$ constraints for all targets. We also show $C_{\rm tor} = 0.5$ with a horizontal dotted, black line. In nearly all cases, this line crosses the confidence regions, which means that assuming $C_{\rm tor} = 0.5$ would result in a good fit to the observed spectra for some range of $N_{\rm H,tor}$.

very high quality in terms of photon statistics, these features are relatively easy to distinguish from a featureless continuum, and they provide tight constraints. However, for most of our data these features are hidden by the limited data quality, and the constraints they provide exhibit considerable degeneracy between spectral parameters. In Figure 6.3 we show a number of examples of the degeneracy between $N_{\rm H,tor}$ and $C_{\rm tor}$, covering the full range present in our sample: from tight, non-degenerate constraints (e.g., IC 4518 A, Mrk 1492, NGC 262), to weak, degenerate constraints (e.g., NGC 4939, MCG +14-08-004, 2MASX J1926) that call for assumptions on one or more spectral parameters in order to provide useful constraints on the parameters of interest.

The model is set up in `Xspec` in exactly the same way as the coupled `borus02` model described in § 6.3.1, except that the $N_{\rm H,tor}$ parameter is not linked to $N_{\rm H,los}$. In comparison with that model, the decoupled configuration has one additional free parameter. While it may not seem necessary to release an additional parameter for observed spectra that are well fitted with the coupled model (which is true for 73 % of the sample), we proceed with the decoupled model motivated by results outside of this particular study, and by physical arguments presented in § 6.1.2 and further elaborated in § 6.5.

Due to its additional flexibility in comparison with its coupled counterpart, this model fits all observed spectra in our sample well; we find a set of spectral parameters for each target in our sample that results in a formally acceptable fit with $p_{\rm null} > 5$ %. Instead of simply fitting for all relevant parameters, we first explore the parameter space by stepping through a range of fixed $N_{\rm H,tor}$ values: 10^{23} cm^{-2} as representative of a non-CT torus, 10^{24} cm^{-2} for a borderline CT torus, and 10^{25} cm^{-2} for the heavily CT torus often assumed in the literature (approximated by infinite optical depth to Compton scattering). This set of fits already provides a good qualitative idea of what type of a torus is required by the data. It is notable that spectral modeling with a range of fixed $N_{\rm H,tor}$ values generally shows an anti-correlation between $C_{\rm tor}$ and $N_{\rm H,tor}$ for the majority of sources in our sample, similar to curves shown in Figure 4.3. We find that robust constraints, based on which a part of the parameter space can be excluded via the $p_{\rm null} > 5$ % criterion, are possible for only a small fraction of our sample. This is not surprising since the *NuSTAR* observations used here are predominantly minimal ≃20-ks exposures.

In many cases, the degeneracy between spectral parameters precludes us from obtaining constraints on the main torus parameters without any assumptions. Wherever

possible, we choose to fix only the $N_{\rm H,tor}$ parameter, preferably at its best-fit value (if it can be constrained). Where different assumed $N_{\rm H,tor}$ values all fit equally well (with $\Delta\chi^2 < 1$ across the whole parameter range), we select the fixed value that yields the lowest χ^2, but do not consider $N_{\rm H,tor}$ to be constrained in those cases. Interestingly, the constraining power is not just a simple function of the total number of source counts. As heavy line-of-sight absorption suppresses the transmitted component, reprocessed components become more directly observable in highly obscured (and typically faint) sources. Therefore, despite lower data quality for highly obscured targets, the constraints on their torus parameters are sometimes better than those for a moderately obscured AGN with high-quality data.

In an effort to more accurately represent uncertainties within the sample, we assign our constraints one of three categories according to their quality:

- Q1 (highest): independent constraints on all three relevant torus parameters ($N_{\rm H,tor}$, $C_{\rm tor}$, $\theta_{\rm inc}$);
- Q2: independent constraints on two torus parameters while the third (preferentially $N_{\rm H,tor}$) is kept fixed;
- Q3 (lowest): torus parameters are constrained only if a basic parameter, such as the photon index (Γ), is assumed and kept fixed.

Naturally, Q2 constraints can be obtained from data that provide Q1 constraints by, e.g., fixing one of the torus parameters. In order to remove part of the degeneracy in constraining $C_{\rm tor}$, we calculate those constraints while keeping $N_{\rm H,tor}$ fixed at either the best-fit $N_{\rm H,tor}$ value (for the 99 targets that provide Q1 constraints), or at $\log N_{\rm H,tor}/{\rm cm}^{-2}$ fixed at 23.0, 24.0, or 25.0 (for data that provide Q2 constraints but not Q1), based on which assumption results in the lowest χ^2. In this way we obtain $C_{\rm tor}$ constraints for a greater fraction of the sample, 115 targets in total. The remaining 9 targets only provide Q3 constraints. While it is possible to obtain conditional constraints on the main torus parameters from those data, in the study presented here, this small fraction of the sample (7 % of the total) is simply ignored.

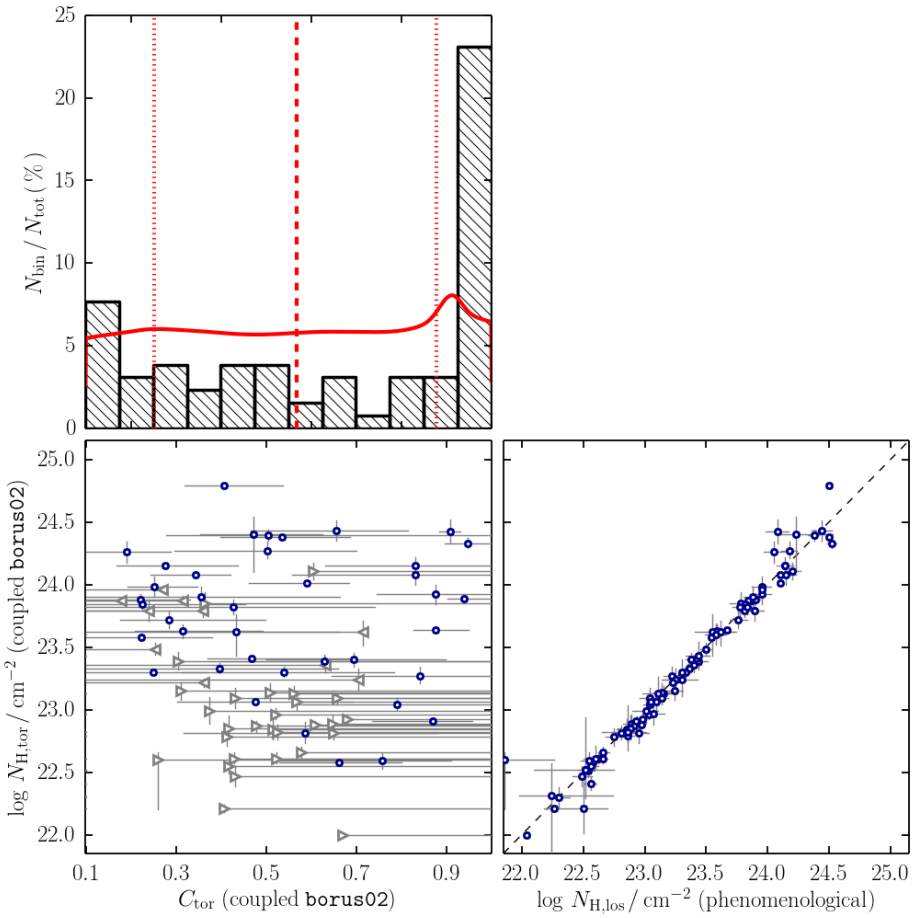

Figure 6.4: Summary of the spectral analysis using the coupled `borus02` model. *Upper left:* Histogram of best-fit values and the probability density function (PDF; red line) of the covering factor of the torus ($C_{\rm tor}$) for the well-fitted sources ($N_{\rm tot}$ = 93). *Lower left:* Scatter plot of $N_{\rm H,tor}$, which is assumed equal to the line-of-sight column density ($N_{\rm H,los}$), and $C_{\rm tor}$ constraints. Best-fit values are plotted with blue circles unless they are at the edge of the domain; in those cases, we mark upper and lower limits with left- and right-pointing grey triangles, respectively. *Lower right:* Relation between $N_{\rm H,los}$ determined from coupled `MYtorus` and $N_{\rm H,los}$ from the phenomenological spectral modeling presented in Chapter V. The dashed line marks the one-to-one proportionality, demonstrating that in this model, $N_{\rm H,tor}$ is entirely determined by the strong photoelectric cutoff in the observed spectra, rather than the more subtle reprocessed spectrum components.

6.4 Results

6.4.1 Models with $N_{\rm H,tor}$ Coupled to $N_{\rm H,los}$

We start our analysis of the spectral modeling results with the coupled `MYtorus` model. Fitting all obscured sources in our sample with the model described in

§ 6.3.2, we find that an overwhelming majority of fits result in $\theta_{\rm inc}$ confined to a very narrow interval between 60° and $\simeq$ 65°. Poor data quality leads to no useful constraint on $\theta_{\rm inc}$ for 5 targets; they are consistent with the full range between 60° and 90° within their 1 σ uncertainties. For 7 targets, mostly with high data quality, the coupled `MYtorus` model does not yield an acceptable fit. More than 85 % of the remaining 93 targets have $\theta_{\rm inc}$ between 60° and 65°. 14 targets (15 %) are found to be consistent with edge-on or intermediate viewing angle. The distribution of $\theta_{\rm inc}$ for our sample, excluding unobscured sources, poor data, and poor fits, is given in Figure 6.2. We stress that this distribution should not be interpreted literally, since the preference for $\theta_{\rm inc}$ around 60° is a simple consequence of choosing a very particular model geometry.

Fitting the coupled `MYtorus` model leads to two qualitatively different types of spectral solutions. The majority of the sample is best fitted with $N_{\rm H,tor}$ in the range between $10^{23.5}\,{\rm cm}^{-2}$and the domain limit at $10^{25}\,{\rm cm}^{-2}$. In order to have $N_{\rm H,los}$ below the CT threshold, it is necessary for the inclination to converge to $\theta_{\rm inc} \approx 60°$ in those cases. The rest of the sample is well fitted with high inclination, mostly consistent with edge-on viewing angle within the 68 % confidence intervals in all but three sources with intermediate inclination. For these sources, fitting indicates that $N_{\rm H,tor} \approx N_{\rm H,los}$. The separation into two groups can clearly be seen in the lower left panel of Figure 6.5: sources with nearly edge-on inclination cluster around the one-to-one proportionality line, while sources with $\theta_{\rm tor}$ close to 60° fill out the region below the line. `MYtorus`-based $N_{\rm H,los}$ values plotted in this figure are calculated using Equation 6.1 and constraints on $N_{\rm H,equ}$ and $\theta_{\rm inc}$ determined from the fits. The lower right panel of the figure shows that these values correlate well with $N_{\rm H,los}$ from phenomenological fits presented in Chapter V. Their uncertainties are considerably wider because they are calculated from two uncertain parameters using a highly non-linear relation.

The lower left panel of Figure 6.5 clearly shows the general tendency for $N_{\rm H,tor}$ to be considerably higher than $N_{\rm H,los}$ by typically more than 0.5 dex. The fact that there appears to be an envelope limiting $N_{\rm H,tor}$ to a line parallel to the one-to-one relation is due to a technical limitation of the model and the fitting procedure. Because the step taken in parameter optimization within `Xspec` is finite, the fitting cannot proceed to inclination value closer to $\theta_{\rm inc}$= 60° than this small but finite step. With the photoelectric cutoff being the strongest feature in any of our spectra (except for unobscured sources, which are excluded from this analysis), this limitation forces

the fitting procedure to lower $N_{\rm H,tor}$ instead of bringing $\theta_{\rm inc}$ closer to 60°, which would have the same net effect on the model spectrum. This also introduces a bias in reconstruction of $N_{\rm H,los}$ from fitted $N_{\rm H,equ}$ and $\theta_{\rm inc}$, making the $N_{\rm H,los}$ values higher than those determined from phenomenological modeling, although the two are consistent in most cases because of wide uncertainties.

The distribution of $N_{\rm H,tor}$ based on coupled `MYtorus` fits (shown in the upper panel of Figure 6.5) is therefore biased, and should not be interpreted in detail. However, this analysis already indicates that $N_{\rm H,tor}$ typically tends to be in the CT regime, although not exclusively so. Approximately 16 % of the total probability is contained below $\log N_{\rm H,tor}/{\rm cm}^{-2} < 23.7$. Examining the low-$N_{\rm H,tor}$ end of the distribution, the fits indicate that NGC 2110, 2MASX J1506, and B2 1204+34 have tori well below the CT threshold: $\log N_{\rm H,tor}/{\rm cm}^{-2} < 23.9$ for the latter two and $\log N_{\rm H,tor}/{\rm cm}^{-2} < 22.9$ for NGC 2110. A common denominator of their X-ray spectra are weak Compton humps and Fe Kα lines. A detailed analysis of *NuSTAR* data for NGC 2110 has already been presented in Chapter IV, making this analysis a good sanity check. Indeed, based on the left panel of Figure 4.5, $C_{\rm tor} \approx 0.5$ implies $\log N_{\rm H,tor}/{\rm cm}^{-2} \approx 22.8 \pm 0.1$, fully consistent with coupled `MYtorus` constraints presented here. The other two examples have considerably lower data quality, but we will return to discussing the nature of their tori following additional constraints from other models considered in this work.

The coupled `MYtorus` model and the coupled `borus02` model, where we assume that any obscured line of sight passes through the torus, share some similarities. Both represent simplifying assumptions that reduce the number of free parameters in spectral modeling. Because the column density profile of `borus02` is a step function, in a coupled configuration, $N_{\rm H,los}$ can only be either equal to $N_{\rm H,tor}$, or equal to zero. The results are therefore simpler and more straightforward than those for the coupled `MYtorus` model. Since the photoelectric absorption profile represents the main driving force in the fitting, in this model $N_{\rm H,los}$ dictates the average column density of the torus ($N_{\rm H,tor}$). The coupled `borus02` model, however, features a variable torus covering factor ($C_{\rm tor}$), which can account for some of the spectral features due to reprocessing within a range of $N_{\rm H,tor}$ narrowly limited by $N_{\rm H,los}$. In order to allow for more flexibility, we additionally fitted for the inclination angle, $\theta_{\rm inc}$, allowing the reprocessed component to have either absorbed or unabsorbed spectral shapes.

In the lower right panel of Figure 6.4 we show the tight correlation between the

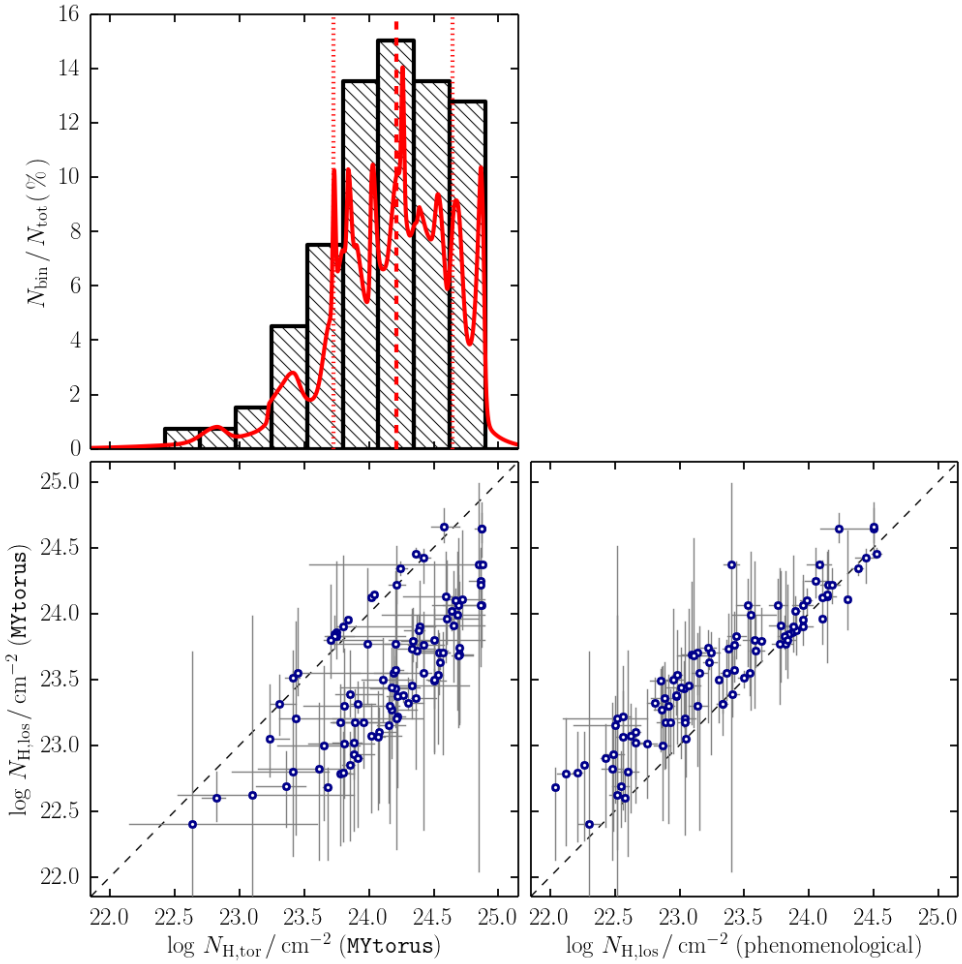

Figure 6.5: Summary of the spectral analysis using the coupled `MYtorus` model. *Upper left:* Histogram of best-fit values and the probability density function (PDF; red line) of the column density of the torus ($N_{\rm H,tor}$) for well-fitted sources ($N_{\rm tot}$ = 97). *Lower left:* Relation between fitted $N_{\rm H,tor}$, and the line-of-sight column density ($N_{\rm H,los}$) calculated from $N_{\rm H,tor}$ and $\theta_{\rm inc}$ determined from the coupled `MYtorus` fits. The dashed line marks the one-to-one proportionality. *Lower right:* Relation between $N_{\rm H,los}$ determined from coupled `MYtorus` and $N_{\rm H,los}$ from the phenomenological spectral modeling presented in Chapter V.

$N_{\rm H,tor}$ constraints from the coupled `borus02` fit and the $N_{\rm H,los}$ determined from phenomenological modeling. The distribution of these $N_{\rm H,tor}$ values is essentially the distribution of $N_{\rm H,los}$, which was discussed extensively in Chapter V. In the same figure we show the two-dimensional constraints in the parameter space spanned by $N_{\rm H,tor}$ (=$N_{\rm H,los}$) and $C_{\rm tor}$, as well as the overall distribution of $C_{\rm tor}$ within the sample (excluding unobscured sources, those with poor data and those fitted badly). Many tori have $N_{\rm H,tor}$ below the CT threshold assuming this model, requiring high $C_{\rm tor}$ in

order to produce the observed Fe Kα fluxes, and, to a smaller extent, the observed Compton humps. Their reprocessed spectra are largely isotropic, therefore providing no constraints on inclination. Despite the large fraction of best fits at 100 % covering, the full PDF of $C_{\rm tor}$ in the sample almost uniformly covers its entire domain.

With both coupled models, we were able to find acceptable spectral fits for the majority of the sample, but a subset of the highest-quality data could not be fitted well. We stress that the AGN with highest-quality (multi-epoch) spectra are not even considered in this work. We draw the motivation for our modeling from analyses of their spectra presented in dedicated publications. There is no reason to believe that fainter AGN would not exhibit similar spectral features, despite them being more difficult to identify in the data.

6.4.2 Decoupled Models: $N_{\rm H,tor}$ Independent from $N_{\rm H,los}$

The decoupled `MYtorus` model is not limited by the clustering of the majority of fits near 60° inclination, and the decoupled `borus02` model is free to explore torus column densities that need not be equal to $N_{\rm H,los}$. With this setup, $N_{\rm H,los}$ is strongly constrained by the photoelectric cutoff, and $N_{\rm H,tor}$ is primarily determined by the more subtle features due to reprocessing. The free inclination parameter simply allows for more flexibility in the shape of the reprocessed spectrum. The main result of spectral modeling using the decoupled `MYtorus` model is the distribution of $N_{\rm H,tor}$ among the AGN in our sample. Likewise, the primary results from fitting the `borus02` model with $N_{\rm H,tor}$ independent from $N_{\rm H,los}$ are the distributions of $N_{\rm H,tor}$ and $C_{\rm tor}$ parameters.

Regarding inclination, here we define two main groups that differ qualitatively in their reprocessed spectral components. If the inclination ($\theta_{\rm inc}$) is constrained in the fitting so that $\cos\,\theta_{\rm inc} \leq C_{\rm tor}$ (recall that $C_{\rm tor} = \cos\,\theta_{\rm tor}$), the reprocessed spectrum is affected by self-absorption. We label this group with the latter A (for "absorbed"). If instead the fitting indicates that $\cos\,\theta_{\rm inc} > C_{\rm tor}$, the reprocessed spectrum is unaffected by self-absorption, and we label to group with the letter U (for "unabsorbed"). As we argue further in § 6.5.1, the exact value of the inclination angle should not be interpreted literally, because of its degeneracy with torus clumpiness, which is not captured by our uniform torus models. For this reason, in the following sections we only distinguish groups A and U according to their qualitatively different reprocessed spectra. If the data shows no preference for either group, as in the case of most low-$N_{\rm H,tor}$ solutions (because of their isotropy) or low data quality, we label

them with the letter N.

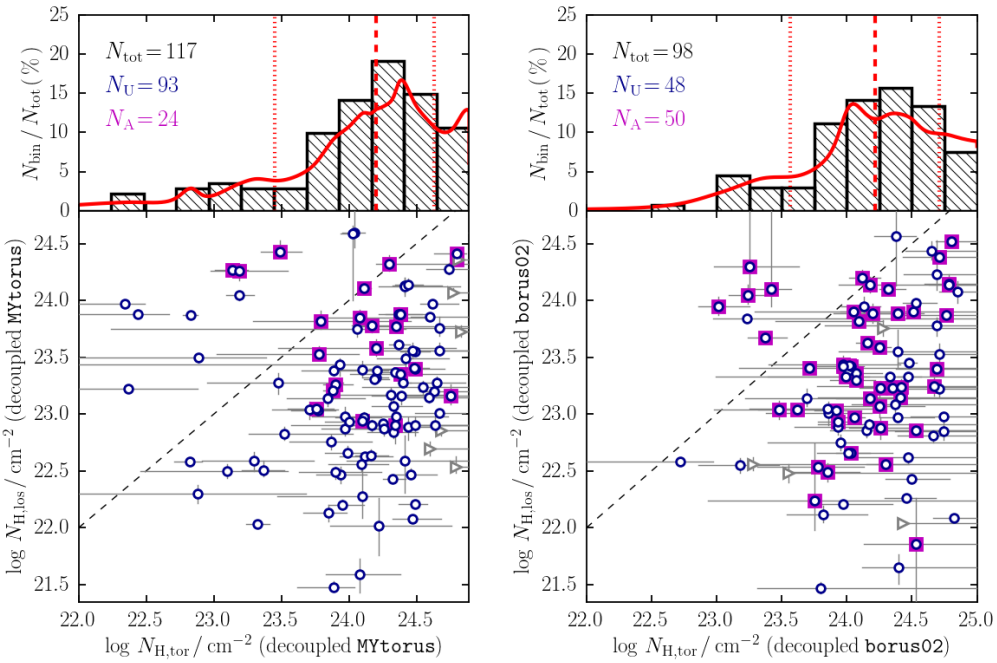

Figure 6.6: Results of modeling the torus column density ($N_{\rm H,tor}$) with decoupled models: `MYtorus` on the left, and `borus02` on the right. For both models we show the histograms of best-fit values as well as the PDF calculated from marginalized PDFs for individual targets (shown with red lines in the upper panels). The vertical dashed and dotted lines mark the median and the central 68 % of the distribution. The lower panels show $N_{\rm H,tor}$ plotted against $N_{\rm H,los}$ determined from the same fit. The dashed lines in the lower panels show a one-to-one relation. Sources for which the inclination is such that the reprocessed component is partly self-absorbed are highlighted with magenta squares.

Distributions of $N_{\rm H,tor}$

Using the `borus02` model, the $N_{\rm H,tor}$ distribution can only be computed for sources that provide an independent constraint on $N_{\rm H,tor}$ (i.e. data which provide Q1 constraints, as defined in the previous section). We find that 97 targets in our sample yield such constraints. For the rest of the sample, without further assumptions, the $1\,\sigma$ equivalent uncertainty ($\Delta\chi^2 < 1$) would include both ends of the $N_{\rm H,tor}$ domain ($22.5 < \log\, N_{\rm H,tor}/{\rm cm}^{-2} < 25.0$). As there is a number of different assumptions that can be made in terms of fixed parameters and their values, each providing different constraints, we do not elaborate them in any detail here. For a range of reasonable assumptions, torus parameters of these sources are consistent with the distribution based on 97 sources (77 % of the sample) with Q1 constraints.

The distributions of $N_{\rm H,tor}$ for decoupled `MYtorus` and `borus02` models are shown in the left panel of Figure 6.6. Both of them are notably skewed toward the CT regime: the medians of the distributions are $\log N_{\rm H,tor}/{\rm cm}^{-2} = 24.20$ and 24.22, respectively. The 68 % probability intervals are $23.45 < \log N_{\rm H,tor}/{\rm cm}^{-2} < 24.63$ for `MYtorus` and $23.57 < \log N_{\rm H,tor}/{\rm cm}^{-2} < 24.71$ for `borus02`, and the distributions are statistically indistinguishable. This result directly confirms the very common assumption that most AGN tori cover at least a part of the sky, as seen from the SMBH, with CT column densities. However, it is also important to note that the data do not prefer extremely high optical depth to Compton scattering (e.g., $> 10^{25}\,{\rm cm}^{-2}$), and that approximately one third of AGN sampled here may have tori that have average column densities below the CT threshold.

Directly comparing $N_{\rm H,tor}$ constraints from `MYtorus` and `borus02` models, we find that they correlate very well, although with some scatter. It is encouraging that either of the models can be used to identify whether a source spectrum is consistent with non-CT, borderline CT, or heavily CT torus, almost without disagreement. We identified only three cases in which spectral solutions qualitatively differ. All of them can be traced to a minor feature in the data that was pivotal in guiding the parameter optimization down a very weak χ^2 gradient. In all three cases it is possible to fix $N_{\rm H,tor}$ to the value determined from the other model, and obtain a good fit the data.

At face value, `MYtorus` suggests that a larger fraction of the sample features unabsorbed reprocessing components. Given that $N_{\rm H,tor}$ is on average above the CT threshold, in many cases the self-absorption has to be partial in order not to completely extinguish the soft X-ray part of the reprocessed continuum. This happens at any inclination ($\theta_{\rm inc}$) that closely matches the half-opening angle of the torus ($\theta_{\rm tor}$). For about a third of `borus02` fits we find inclinations consistent with $\cos\theta_{\rm inc} = \cos\theta_{\rm tor} \pm 0.1$, while such inclinations are rarely obtained from `MYtorus` fits. It is therefore easy to understand the differences with regard to inclination (or rather, the shape of the soft X-ray part of the reprocessed continuum), as we explain in more detail in § 6.5.1.

Distributions of $C_{\rm tor}$

The distribution of $C_{\rm tor}$ can only be derived from `borus02` fits. In principle, it is possible to derive $C_{\rm tor}$ constraints that are entirely independent from $N_{\rm H,tor}$, i.e., allowing it to vary while computing constraints on $C_{\rm tor}$. However, we find that this

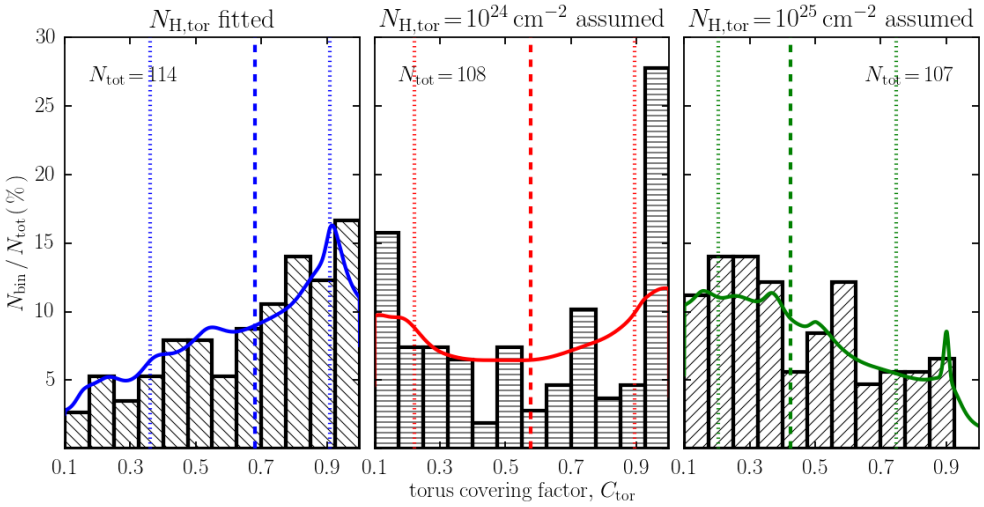

Figure 6.7: Results of modeling the torus covering factor ($C_{\rm tor}$) with the decoupled `borus02` model. The three panels show the histograms of best-fit values as well as probability distributions (shown with thick colored lines) derived from marginalized PDFs for individual sources. The dashed and dotted vertical lines show the median and the central 68 % of the probability distribution. In the left panel we show constraints obtained from fits with $N_{\rm H,tor}$ fixed at either the best-fit value (if the data provides a useful constraint), or at 10^{23}, 10^{24}, or $10^{25}\,{\rm cm}^{-2}$ (whichever yields the lowest χ^2). For the constraints shown in the middle and the right panel, we assume a fixed $N_{\rm H,tor}$ for all sources, and include only those targets that for which this assumption results in an acceptable fit to the data.

results in only a small number of useful constraints. Three AGN providing such constraints have already been analyzed and presented separately in Chapter IV. The targets with highest-quality data generally cover different parts of the parameter space spanned by $N_{\rm H,tor}$ and $C_{\rm tor}$; while there seems to be a preference for $N_{\rm H,tor}$ to be in the CT regime, as opposed to lower column densities, there seems to be no such preference for $C_{\rm tor}$. The distribution of $C_{\rm tor}$ in sources with highest-quality data is nearly uniform over its domain. While this seems uninformative at face value, it does imply that our sample likely contains AGN with a full range of covering factors.

For the majority of spectra in our sample $C_{\rm tor}$ constraints are a function of $N_{\rm H,tor}$: for different assumed values of $N_{\rm H,tor}$, $C_{\rm tor}$ will vary across its entire domain, as shown in all but the top few panels in Figure 6.3. Naturally, the sum of very broad individual probability distributions of $C_{\rm tor}$ derived this way is essentially uniform, and carries very little information. We therefore present only the results based on fits in which $N_{\rm H,tor}$ is kept fixed. Out of 124 sources in our sample, for 99 we were

able to find and constrain a best-fit $N_{\rm H,tor}$. For additional 16 sources it is possible to select $N_{\rm H,tor}$ between assumed values of 10^{23}, 10^{24}, and $10^{25}\,{\rm cm}^{-2}$ based on the lowest χ^2, despite the χ^2 gradients being too weak to yield formal constraints on $N_{\rm H,tor}$. Data for the remaining 9 sources does not provide any useful results due to limited photon statistics.

The probability distribution of $C_{\rm tor}$ within our sample, adopting $N_{\rm H,tor}$ determined from the data but kept fixed, is shown in the leftmost panel in Figure 6.7. It is broad, but it does show a preference for high covering factors. Interestingly, however, if we assume that all tori have column densities of 10^{24} or $10^{25}\,{\rm cm}^{-2}$, the shape of the distribution changes. The distribution of $C_{\rm tor}$ under these two assumptions, which provide statistically good fits for 108 and 107 sources, respectively, are shown in the middle and right panels of Figure 6.7. For assumed $N_{\rm H,tor} = 10^{24}\,{\rm cm}^{-2}$, the distribution is convex, with peaks at both ends of the domain (many of which are upper or lower limits). In the case of assumed $N_{\rm H,tor} = 10^{25}\,{\rm cm}^{-2}$, the distribution is skewed toward low $C_{\rm tor}$: its median is 0.42, compared to 0.68 for fits with $N_{\rm H,tor}$ determined from the data. While the most credible constraints should be those with the least number of assumptions, we present results for assumed $N_{\rm H,tor}$ here in order to point out that they do represent acceptable spectral solutions, yet suggest different preference for $C_{\rm tor}$.

6.4.3 Covering Factor as a Function of Intrinsic Luminosity

Many previous studies suggested that the torus covering factor may depend on AGN luminosity. Formally, the luminosity in question should be bolometric, but it is often approximated with the intrinsic X-ray luminosity. We show our constraints on $C_{\rm tor}$ as a function of the 10–50 keV luminosity of the intrinsic continuum in Figure 6.8. The top two panels show results obtained assuming $N_{\rm H,tor}$ fixed at $10^{24}\,{\rm cm}^{-2}$ and $10^{25}\,{\rm cm}^{-2}$, for each of the targets in the sample. Such constraints are available for all but the sources with lowest data quality (Q3). The lower left panel is made from $C_{\rm tor}$ constraints obtained by fixing $N_{\rm H,tor}$ at its best-fit value for 97 sources with highest quality (Q1) constraints. The colored curves show in each panel are running median curves computed using a window function with a width of 1 dex.[6] The median and the 68 % confidence regions (grey areas) are computed as described in § 6.3, taking into account all upper and lower limits.

The three panels all show similar trends: $C_{\rm tor}$ increases from the lowest intrinsic

[6]The trends persist for other choices of the window function width, or simpler binning into luminosity bins, but clarity is maximized with this particular choice.

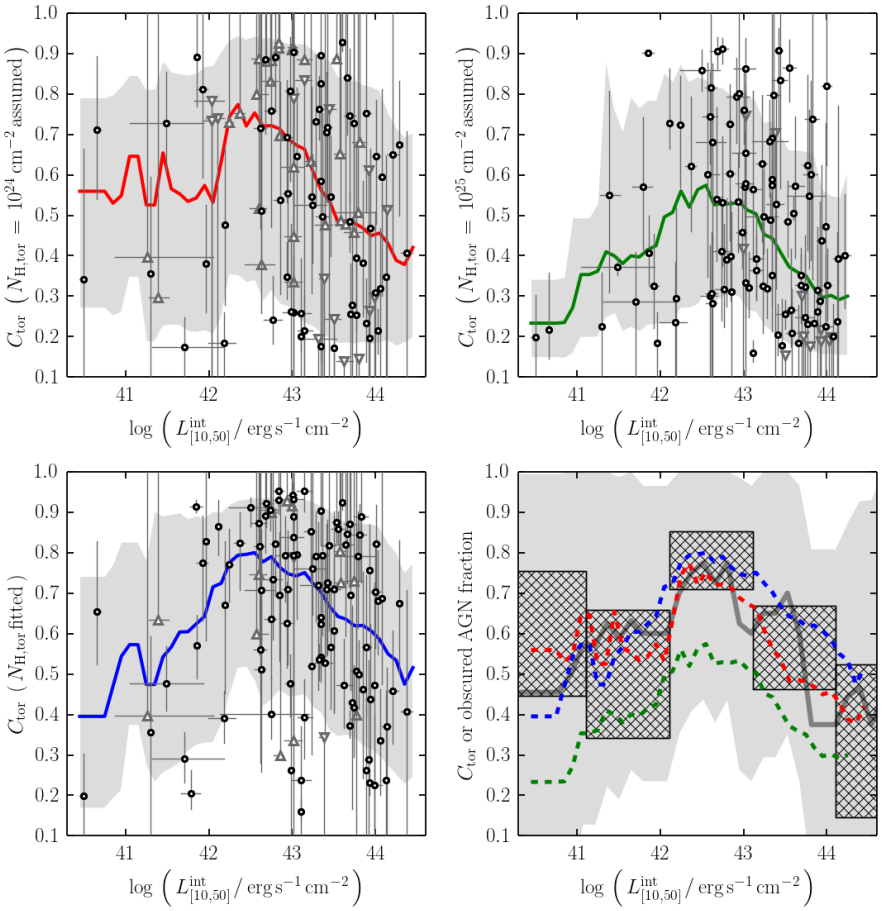

Figure 6.8: The running median of fitted torus covering factors ($C_{\rm tor}$) as a function of the intrinsic luminosity. The top two panels show results obtained assuming $N_{\rm H,tor}$ fixed at $10^{24}\,{\rm cm}^{-2}$ and $10^{25}\,{\rm cm}^{-2}$, for each of the targets in the sample. The lower left panel shows $C_{\rm tor}$ constraints obtained by fixing $N_{\rm H,tor}$ at its best-fit value for a subset 97 sources for which provide a constraint on $N_{\rm H,tor}$. The colored lines show the running median computed with a 1-dex window function, and the grey areas show corresponding 68 % probability interval. In the lower right panel we compared our running median curves (dashed colored lines) to the running median of the obscured AGN fraction from Vasudevan et al. (2013) (thick grey line and grey 68 % uncertainty region) and the binned obscured AGN fraction from Brightman & Nandra (2011a) (hatched boxes covering 68 % uncertainty intervals).

luminosities up to a plateau at $\log L^{\rm int}_{[10,50]} \approx 42.7$, followed by a decrease at even higher luminosities. It is remarkable that the shape of the median $C_{\rm tor}$ curve is similar in all three cases, given that the overall distribution of $C_{\rm tor}$ is different in each case (see Figure 6.7). Clearly, the part of the parameter space at low intrinsic luminosities ($\log L^{\rm int}_{[10,50]} < 42.5$) is not sampled as well as the higher-luminosity part. This is in part due to the faintness of these sources, which only provide Q3

constraints and are therefore not included in Figure 6.8. Though we do not present the details of modeling of their spectra under various assumptions, we note that they do not alter any conclusions qualitatively.

In the bottom right panel of Figure 6.8 we compare our derived dependence of $C_{\rm tor}$ on $L^{\rm int}_{[10,50]}$, under three different assumptions for $N_{\rm H,tor}$, to results from Brightman & Nandra (2011a) and Vasudevan et al. (2013). In both of these studies, the authors investigated the fraction of obscured sources in their samples as a function of luminosity. Naively, the obscured fraction corresponds to a torus covering factor because randomly distributed observers see an obscured AGN with probability that equals the torus covering factor. Their samples are selected differently: while Vasudevan et al. (2013) used a *Swift*/BAT selection similar to ours, Brightman & Nandra (2011a) selected their sample according to their 12 μm flux.

We convert their luminosities from the 2–10 keV band to 10–50 keV band using a conversion factor based on a cutoff power-law continuum with $\Gamma = 1.8$ and $E_{\rm cut} = 300$ keV: $\log L^{\rm int}_{[10,50]} = \log L^{\rm int}_{[10,50]} + 0.11$, basing our choice of the intrinsic continuum parameters from Chapter V (specifically, § 5.5.1 and § 5.6.1). It is important to note that these authors measured the obscured fraction of AGN, and not the covering factor, though the two are thought to be related under some basic assumptions. We further discuss the possible origin and interpretation of this relationship in § 6.5.3.

6.5 Discussion

6.5.1 Inclination Constraints and Torus Clumpiness

Application of the coupled `MYtorus` model leads to an overwhelming majority of AGN in our sample to be fitted with inclination ($\theta_{\rm inc}$) very close to 60° ($\cos\,\theta_{\rm inc} \approx 0.5$). This is a simple consequence of the fixed opening angle and the very narrow range of $\theta_{\rm tor}$ exhibiting a very large range in $N_{\rm H,los}$ for any given $N_{\rm H,tor}$. In order to be able to relate the viewing angle to a particular $N_{\rm H,los}$, future models should feature a less steep transition from heavily obscured to unobscured lines of sight.

In decoupled torus models (either `MYtorus` or `borus02`), the reprocessed component of the spectrum is fitted so that the average torus column density ($N_{\rm H,tor}$) is independent from $N_{\rm H,los}$. The spectral analysis presented here, in agreement with detailed analyses of high-quality broadband spectra (Yaqoob, 2012; Arévalo et al., 2014; Puccetti et al., 2014; Bauer et al., 2015), suggests that decoupled models are

generally preferable. Within our sample, spectra of some AGN with highest-quality data are better fitted with decoupled models (e.g., NGC 6300, NGC 7582). In the decoupled configuration, the inclination does not have a straightforward interpretation, and requires some thought.

As discussed already in Chapter IV, the pole-on, or unobscured, reprocessed component is characteristic for emission from the inner side of the torus, which is directly illuminated by the central X-ray source. Such a component can be seen even if the torus is observed edge-on if the torus is sufficiently porous, so that emission from the inner side of the torus is not significantly absorbed (see Figures 4.1 and 4.2). Indeed, such a component is often observed in spectra of CT AGN, which are thought to be predominantly observed edge-on with respect to their tori (Baloković et al., 2014; Brightman et al., 2015; Annuar et al., 2015; Boorman et al., 2016; Annuar et al., 2017). In the scenario in which the torus is clumpy, unobscured reprocessed component of a uniform-density model cannot be unambiguously associated with pole-on inclination. For this reason, we abstain from a detailed analysis of inclination constraints based on the modeling presented here.

At face value, `MYtorus` suggests that a larger fraction of the sample features unabsorbed reprocessing components. The difference between `MYtorus` and `borus02` results is easy to understand: the reprocessed continua of two models differ in the soft X-ray part of the spectrum (see Figure 6.1) in the sense that `borus02` produces more soft X-ray flux ($\leqslant 4\,\mathrm{keV}$) than `MYtorus`. This difference in spectral shape can be ascribed to the different assumed geometry of the reprocessing material. The spectral shape of the soft X-ray reprocessed continuum produced by `MYtorus` can be reproduced with partial self-absorption (leading to higher θ_{inc}, or higher C_{tor}) in the `borus02` model.

Given that $N_{\mathrm{H,tor}}$ is on average above the CT threshold, in many cases the self-absorption has to be partial in order not to completely extinguish the soft X-ray part of the reprocessed continuum. This happens at any inclination (θ_{inc}) that closely matches the half-opening angle of the torus (θ_{tor}). Indeed, for about a third of `borus02` fits we find inclinations consistent with $\cos\theta_{\mathrm{inc}} = \cos\theta_{\mathrm{tor}} \pm 0.1$. Such inclinations are rarely obtained from `MYtorus` fits, possibly because the transition from self-absorbed to unabsorbed reprocessed continuum is more gradual in `MYtorus` geometry. This can be explained with a "silver lining" effect due to the lower column density at the rim of the torus in this geometry.

6.5.2 Constraints on the Properties of the Seyfert II Torus

Our sample is representative of its parent population of *Swift*/BAT-selected type II Seyferts, so that our results relate more broadly to the Sy II population at least, if not the local Seyfert population in general. Flux-limited hard X-ray selection (14–195 keV band), unlike AGN selection in the optical (e.g., Risaliti et al. 1999, Maiolino et al. 2007) or infrared (e.g., Brightman & Nandra 2011a), almost completely avoids contamination of the sample with star-forming galaxies. It is also less biased against obscuration than selection in a soft X-ray band (e.g., 2–10 keV), although it may still be missing a fraction of AGN with the highest column densities (e.g., Koss et al. 2015, Ricci et al. 2015, also § 5.6.5). It is also not biased toward radio-loud AGN, which get preferentially selected in relatively shallow flux-limited selections in the radio band (e.g., Wilkes et al. 2013, Podigachoski et al. 2015).

Although the dataset we utilize in this work is unique, it consists of spectra that are individually limited in quality when it comes to secondary spectral features that hold the key to constraining the torus structure through X-ray reprocessing. However, its power lies in the sample size, which allows us to probe the average properties of the torus with more confidence then in any previous study. Our main finding is that model spectra that fit our data cover a range of properties and do not naturally lead to some one-parameter family of torus models.

The simpler, coupled models fit most of our data well, but lead to some unphysical results when considering the sample as a whole. For example, the pile-up of $\theta_{\rm inc}$ within 5° from the rim of the torus in the coupled `MYtorus` model is just a consequence of the adopted geometry and the resulting profile of $N_{\rm H,los}$ as a function of $\theta_{\rm inc}$. With the current data it is difficult to fully reject simplified models on purely statistical grounds, although the highest-quality data already suggest that some simplifying assumptions cannot hold in general. In the following sections we examine several common assumptions tested with our modeling in order to better define the basic properties of the AGN torus.

Can We Generally Assume $N_{\rm H,tor} = N_{\rm H,los}$?

This simplifying assumption is often used in the literature when data quality is limited and only $N_{\rm H,los}$ can be measured or estimated from the data. Equating $N_{\rm H,tor}$ to $N_{\rm H,los}$ in our coupled `borus02` model leads to a large number of high $C_{\rm tor}$ values: essentially every spectrum with $\log N_{\rm H,los}/{\rm cm}^{-2} < 23.5$ is consistent with $C_{\rm tor} = 1$. The fits gravitate toward $C_{\rm tor} = 1$ in order to maximize the contribution of fluorescent

line emission and the Compton hump, both of which are weak at low $N_{\rm H,tor}$. The fact that we can find an acceptable fit for the majority of our spectra confirms the results of the phenomenological analysis in Chapter V: most of the observed spectra in our sample can be described with a dominant absorbed power-law component imprinted with subtle features due to reprocessing, which are in many cases not statistically required.

It is reasonable to expect that for at least some obscured AGN, this simplified model represents a good approximation of the actual torus geometry. For example, we find that 15 targets are not consistent with $\theta_{\rm inc} < 65^\circ$ in the coupled `MYtorus` fit. They are also fitted well with the coupled `borus02` model, which is qualitatively very similar to the edge-on coupled `MYtorus`. This group consists of 7 CT AGN and 8 heavily obscured AGN ($23.5 < \log N_{\rm H,los}/{\rm cm}^{-2} < 24.0$). In decoupled model fits most of them converge to $N_{\rm H,tor} \approx N_{\rm H,los}$ (typically within 0.4 dex). Since this range of column densities is entirely within the 68 % interval for $N_{\rm H,tor}$ found in § 6.4.2, we are led to the conclusion that our line of sight passes through a very typical, average part of the torus in these cases.

However, the assumption that Sy II are always viewed through their (uniform) torus, hence justifying $N_{\rm H,tor} = N_{\rm H,los}$, is not generally compatible with our data, nor the literature on detailed modeling of X-ray spectra of bright nearby AGN (e.g., Puccetti et al. 2014, Yaqoob et al. 2015, Marinucci et al. 2016). One straightforward argument is simply that our highest-quality data are not fitted well with the coupled `borus02` model. Second, if the torus material is non-uniform (which is supported by both theory and observations; see, e.g., Hönig 2013, Netzer 2015), $N_{\rm H,los}$ is expected to fluctuate as material of different density passes in and out of our line of sight, while $N_{\rm H,tor}$ can only change due to physical changes in the accretion flow. This has been observed in many local AGN: e.g., Risaliti et al. (2010), Markowitz et al. (2014), Rivers et al. (2015a), Ricci et al. (2016), Masini et al. (2017); also NGC 7582 in Chapter IV.

Finally, one more important argument against the $N_{\rm H,tor} = N_{\rm H,los}$ assumption can be drawn from our sample-based analysis. In the decoupled `MYtorus` and `borus02` model fits, where the inclination parameter ($\theta_{\rm inc}$) was left free to vary, the data showed a lack of preference for self-absorbed reprocessed components. Based on `MYtorus` fitting, 93/117 (79 %) spectra prefer an unabsorbed reprocessed component. `borus02` fits result in 48/98 (49 %) best-fit models with an unabsorbed reprocessed component. Such components are characteristic of reprocessed spectra

emitted from the inner, directly illuminated walls of the torus, which is typically observable at pole-on inclination. In the bottom panel of Figure 6.1 we show reprocessed spectra from the clumpy `Ctorus` model, with a minimum number of clouds making up the torus volume. With such a porous torus, formally obscured lines of sight ($\theta_{\rm inc} > 60°$) receive considerably more soft X-ray reprocessed flux compared to either `MYtorus` or `borus02`, since the innermost regions are directly observable through the holes between individual clumps.

We interpret the high incidence of unabsorbed reprocessed spectra as an indication that in a large fraction of AGN, independently of $N_{\rm H,los}$, we observe direct emission from the inner parts of the torus. This could be due to the inclination being such that our line of sight passes through a puffed-up outer region of the torus (with $N_{\rm H,los} < N_{\rm H,tor}$), missing the denser equatorial region that dominates the average $N_{\rm H,tor}$ and accounts for the bulk of reprocessing. It could also be due to holes in a clumpy torus, which would allow for a view of the innermost regions even at edge-on inclination. Both scenarios require non-uniform density, and imply that $N_{\rm H,los}$ should generally not be expected to match $N_{\rm H,tor}$.

Can We Generally Assume $C_{\rm tor} = 0.5$?

`MYtorus` (as well as `Ctorus`, and the recently published torus model by Furui et al. 2016) features $C_{\rm tor}$ fixed at 0.5. With this assumption, the variety of observed broadband X-ray spectra needs to be accounted for by only $N_{\rm H,tor}$ and $\theta_{\rm inc}$. The main issue with the coupled `MYtorus` model is that, when applied to the sample as a whole, it leads to an apparently unphysical result: the pile-up of $\theta_{\rm inc}$ within 5° from the rim of the torus. However, this is an obvious consequence of the choice of the torus opening angle and its profile of $N_{\rm H,los}$ as a function of $\theta_{\rm inc}$, and should not be interpreted physically. With respect to the fitting statistic, `MYtorus` can fit the majority of spectra in our sample well; using it the decoupled configuration resulted in acceptable fits to the data for 117/124 (94 %) of our sources. Fitting those same sources with the decoupled `borus02` model sometimes leads to a constraint on $C_{\rm tor}$ that formally excludes $C_{\rm tor} = 0.5$ (albeit weakly, given that the confidence interval is equivalent of only $1\,\sigma$). This typically results in the fitted $N_{\rm H,tor}$ being different between `MYtorus` and `borus02` fits, due to a degeneracy between $C_{\rm tor}$ and $N_{\rm H,tor}$.

For example, applying the `MYtorus` model to Mrk 3, Yaqoob et al. (2015) found that its $N_{\rm H,tor}$ is $\simeq 2 \times 10^{23}\,{\rm cm}^{-2}$. The two-dimensional confidence contours shown in Figure 6.3 indicate that our Mrk 3 data is consistent with a non-CT torus if

$C_{\rm tor}$ is assumed to be 0.5. However, the contours also show that a CT torus is equally acceptable if $C_{\rm tor}$ is allowed to be <0.3. Whether that option persists when confronted with additional X-ray data (Guainazzi et al., 2016), remains to be seen in future work. This example, and those investigated in detail in Chapter IV, show that assuming $C_{\rm tor} = 0.5$ is, first of all, unnecessary. It has been shown that high-quality *NuSTAR* data on bright AGN can constrain $C_{\rm tor}$ instead of having it assumed, and that some broadband X-ray spectra are inconsistent with this assumption (e.g., Yaqoob 2012, Bauer et al. 2015). Furthermore, using a model with fixed $C_{\rm tor}$ eliminates the possibility to probe the change of the average torus covering factor with luminosity, which is supported by our data (§ 6.4.3) and many previous studies that constrained this dependence indirectly (see § 6.5.3 for a discussion).

Can We Assume All AGN Tori Are Compton-thick?

One of the main results of this study is the confirmation of the long-held belief that all AGN tori have some fraction of CT covering, although our line of sight does not always cross the torus through its CT part. If all AGN tori can indeed be assumed to have CT tori, then the only way to reproduce the variety of spectral shapes observed in this sample is through variations of the covering factor. We find that 68 % of the probability distribution for $N_{\rm H,tor}$ is enclosed in the interval $23.5 < \log\ N_{\rm H,tor}/{\rm cm}^{-2} < 24.7$. This interval is roughly centered on the CT threshold, and includes non-CT tori. Approximately 15 % of our sources are fitted best with tori with $\log\ N_{\rm H,tor} < 23.5$. However, a closer inspection shows that for nearly all of these spectra, a slightly degraded, yet still statistically acceptable fit can be found by assuming $N_{\rm H,tor} = 10^{24}\,{\rm cm}^{-2}$ or $N_{\rm H,tor} = 10^{25}\,{\rm cm}^{-2}$. Due to the degeneracy between $N_{\rm H,tor}$ and $C_{\rm tor}$ discussed in previous sections, the covering factors are generally lowest for $N_{\rm H,tor} = 10^{25}\,{\rm cm}^{-2}$.

Assumption of $N_{\rm H,tor} = 10^{23}\,{\rm cm}^{-2}$ leads to bad fits in a large fraction of our sample, so $N_{\rm H,tor}$ as low as that can confidently be excluded as a viable assumption for the whole sample. Since a good fit can indeed be found for nearly all sources with fixed $N_{\rm H,tor} = 10^{24}\,{\rm cm}^{-2}$ or $N_{\rm H,tor} = 10^{25}\,{\rm cm}^{-2}$, neither of these options can be ruled out with the X-ray data presented here. Interestingly, they both preserve the shape of the dependence of $C_{\rm tor}$ on the intrinsic luminosity, despite the clear differences in the shape of the marginalized distributions of $C_{\rm tor}$, show in Figure 6.7. Having a range of covering factors within the AGN population may be theoretically better supported than having $C_{\rm tor} = 0.5$.

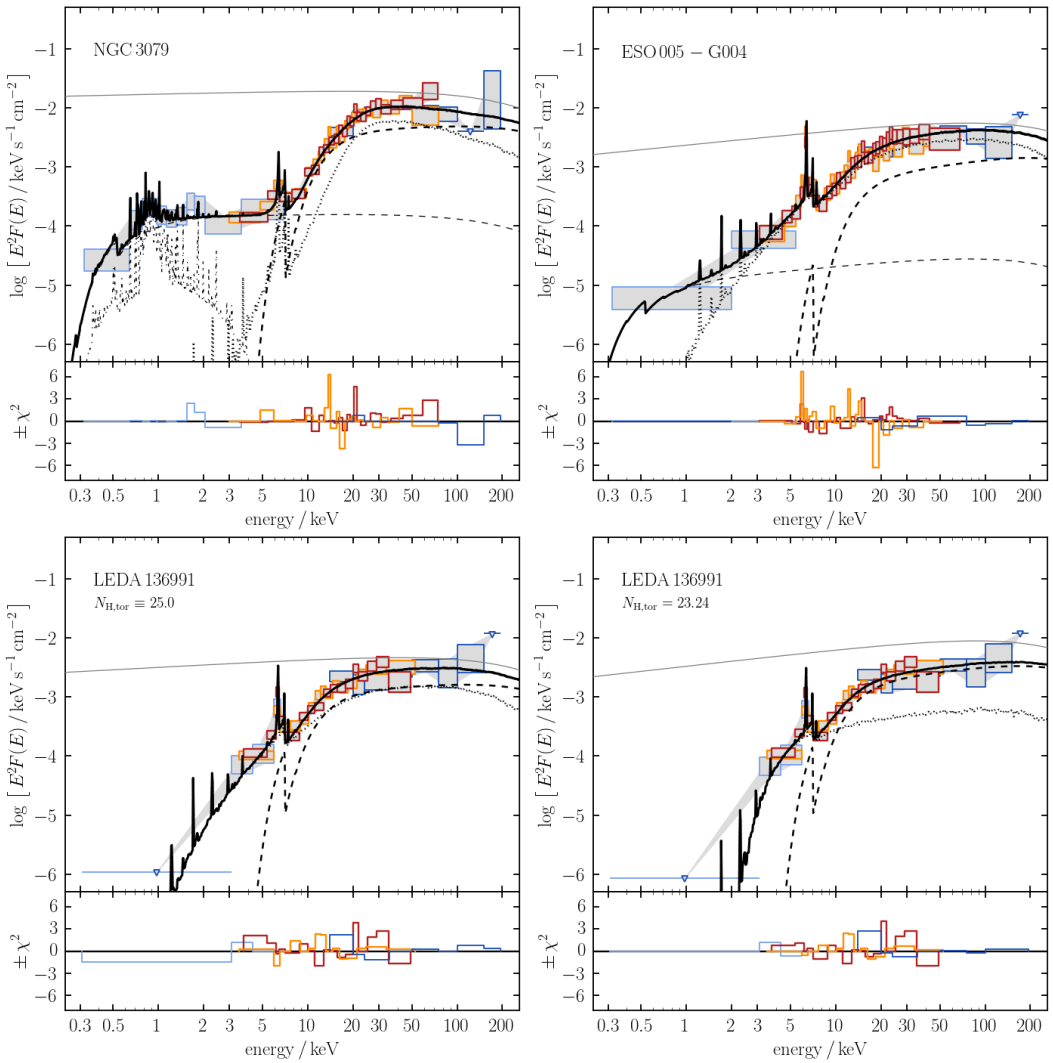

Figure 6.9: Four examples of spectral fits using the `borus02` model with different characteristics, despite all three AGN having $N_{\rm H,los}$ in the CT regime. In each case, the upper panels show the observed data as well as the spectral model with its components, while the lower panels show the χ^2 contributions of each energy bin. *NuSTAR* data is shown with red and orange boxes covering the Poisson uncertainty in each energy bin; light and dark blue boxes show the *Swift* XRT and BAT data, respectively. The thin grey lines show the (unobserved) intrinsic continuum, black dashed lines show the absorbed line-of-sight component, black dotted lines show the reprocessed component, and the thick, black, solid line show the total. The two models for LEDA 136991 demonstrate how the targets with low best-fit $N_{\rm H,tor}$ ($\log\,N_{\rm H,tor}/{\rm cm^{-2}} \approx 23.2$ in this case) can still be fitted well with the assumption that $\log\,N_{\rm H,tor}/{\rm cm^{-2}} = 25$; this simply results in a different spectral decomposition and different constraints on the remaining free parameters.

6.5.3 Comprison with Previous X-ray Studies

No previous studies have been able to directly place constraints on the main parameters of the AGN torus for the whole Sy II population from the X-ray band. X-ray studies of that population have generally focused on studying one object at a time, or rather small samples. Tori of some bright, nearby AGN have been studied in some detail using the `MYtorus` model. They tend to agree that the coupled configuration does not fit the data well, leading to decoupling and a partial loss of accurate geometrical interpretation. Generally, they find a spread in $N_{\rm H,tor}$: e.g., among numerous AGN thought to have CT tori (e.g., NGC 4945; Puccetti et al. 2014), NGC 4507, Braito et al. (2013) and Mrk 3 (Yaqoob et al., 2015) have been suggested not to have CT tori. We find several more AGN that could be similar, though the data quality limits how strong of a claim can be made about the nature of the torus in any particular AGN in our sample. Within our dataset, the non-CT torus in Mrk 3 is supported by the best fit of the decoupled `borus02` model being $\log N_{\rm H,tor}/{\rm cm}^{-2} \approx 23.2$; however, the $1\,\sigma$ uncertainty includes $N_{\rm H,tor}$ up to $10^{25}\,{\rm cm}^{-2}$ with $C_{\rm tor} < 0.2$ (see a contour plot in the leftmost panel in the second row of Figure 6.3).

Regarding sample studies, our measurements of the average properties of the AGN torus may be related to studies of the fraction of obscured AGN and its evolution over cosmic time. It is straightforward is understand the correspondence within the unified model paradigm: if orientation is the only variable determining whether an AGN is observed as obscured or unobscured, than for a large number of random AGN orientations, the obscured fraction will equal to the fraction of random lines of sight passing through the torus, i.e., the torus covering factor. The decrease of the obscured fraction of AGN from the typical Seyfert intrinsic 2–10 keV luminosity of $\sim 10^{43}\,{\rm erg\,s}^{-1}$ toward higher luminosity has been found in many previous studies, both in the local universe (e.g., Brightman & Nandra 2011a, Burlon et al. 2011, Vasudevan et al. 2013) and at moderately high redshift.

X-ray surveys generally show that the fraction of obscured AGN decreases with increasing intrinsic X-ray luminosity (e.g., Hasinger 2008, Merloni et al. 2014, Buchner et al. 2015). The decrease of the covering factor with increasing luminosity can be understood in terms of the idea of a receding torus (Lawrence, 1991), where the inner wall of the torus moves further away from the central engine while its scale height is constant.[7] In recent times, this term was often borrowed to

[7] Strictly speaking, the receding torus model applies to the infrared band, where the emission is

mean that due to greater radiative pressure at higher luminosity, the torus opening angle increases, thus reducing the torus covering factor (see, e.g., Wada 2012). Encouraging agreement with this idea was found by Brightman et al. (2015) from modeling of the covering factor a sample of 10 CT AGN with a range of luminosities. However, given that the model they used (`BNtorus`; Brightman & Nandra 2011a) is now known not to work correctly (see Chapter IV), the decrease of the covering factor with increasing luminosity that they found may rightfully be questioned.

On the other end of the luminosity scale, samples of AGN in the local universe indicate that the obscured AGN fraction decreases towards lower X-ray luminosities from a peak between 10^{42} and 10^{43} erg s^{-1} (e.g., Burlon et al. 2011, Brightman & Nandra 2011a, Vasudevan et al. 2013). The decrease of the covering factor could be an indication of waning ability to radiatively support geometrically thick structures such as the BLR and the torus (Nicastro 2000; Elitzur & Ho 2009). It may also be related to a change in the AGN accretion regime, transitioning from an optically thick, geometrically thin accretion disk (Shakura & Sunyaev, 1973) to a radiatively inefficient accretion flow (e.g., Narayan & Yi 1994, Blandford & Begelman 1999). Kawamuro et al. (2016b) studied a small sample of low-luminosity AGN selected from the *Swift*/BAT AGN catalog, and modeled their tori using the Ikeda et al. (2009) model. They find narrow Fe Kα as a signature of reprocessing in 8 sources, for which they constrain $C_{\rm tor}$ to > 0.3 under the assumption that $N_{\rm H,tor} = N_{\rm H,los}$. They did not consider decoupled models, but our results presented here indicate that $C_{\rm tor}$ would likely be lower for $N_{\rm H,tor}$ in the CT regime.

6.5.4 X-ray Variability

In all of the modeling presented in this work, we assumed that the reprocessed continuum is normalized with respect to the observed intrinsic continuum level, as if there was no variability in time. It is well established that most AGN X-ray intrinsic continua vary both in amplitude and in spectral shape. Indeed, variability exceeding a factor of ~ 2 in amplitude with respect to the long-term (multi-year) average sampled by *Swift*/BAT is observed in a non-negligible fraction of our sample (25 %; § 5.6.4). Given the physical size of the torus, which extends on the size scale of a parsec, the long-term average would be a better normalization for the reprocessed spectrum. The difference may significantly affect torus constraints of single AGN, as we demonstrated with single-epoch and multi-epoch spectral fitting with a torus

dominated by thermal dust emission. The original idea of Lawrence (1991) is based on the increase of the dust sublimation radius with increasing luminosity, which does not influence X-ray obscuration.

model in Chapter IV. For a large sample study such as this, variability of individual AGN averages out, so the average torus properties that we find here may not be biased in any particular way by variability.

At a superficial level, the dependence of the median $C_{\rm tor}$ on intrinsic luminosity (see Figure 6.8), may be affected to a small degree by shifting several sources to the left and to the right by $\simeq$0.5 dex if the average luminosity is used instead of the instantaneous one. More importantly, variability of the intrinsic continuum in the presence of a roughly constant reprocessed spectral component allows the reprocessed component to be better constrained while the intrinsic continuum is low. In the future, within the operational lifetime of *NuSTAR*, the sample of local AGN with good-quality spectra will further increase both in the number of AGN and in the number of epochs per AGN, enabling us to further tie down both the average properties as well as the intrinsic spread within the population.

6.5.5 Comparison with Studies at Other Wavelengths

The torus covering factor have been extensively debated in studies at other wavelengths, and in the infrared in particular. In contrast to the receding torus model, recent studies of extremely luminous infrared-selected AGN at high redshift have found that these AGN are predominantly heavily obscured (Assef et al., 2015). Moreover, their comoving space density is comparable to that of optically bright unobscured quasars, implying a relatively high obscured fraction. As luminous high-redshift AGN are often associated with intensely star-forming and merging host galaxies, it is not unlikely that their obscuration is of a different nature than that of the local Seyferts.

In the local AGN population, an important open question is whether the low-luminosity AGN have higher or lower obscured fraction than the typical Seyferts. While studies of optically selected samples imply that their obscured fraction is nearly 100 % (e.g., Risaliti et al. 1999), studies in the X-ray band have generally suggested a lower obscured fraction (e.g., Brightman & Nandra 2011a, Burlon et al. 2011, Vasudevan et al. 2013). In agreement with most of the X-ray studies, we find that the covering factors at low luminosity tend to be lower on average than those of typically luminous Seyferts. Incompleteness of the sample selection has often been considered as a possible explanation for the disagreement; however, our selection based on hard X-ray flux could be biased toward higher, not lower covering factors. We have shown in Chapter V that a high Compton hump amplitude (which generally

corresponds to higher $C_{\rm tor}$, as shown in § 6.5.3) makes AGN more luminous in the hard X-ray band, making them easier to detect with *Swift*/BAT or other surveying hard X-ray instruments.

It is important to note that the sample presented here consists only of Sy II objects (which we defined as optical types 1.8, 1.9 and 2, see § 5.2 for details). They were selected so that the majority would likely be obscured. While we can look at the relative change of the average covering factor with luminosity, the absolute values may be biased by the absence of type I AGN in the sample. The absolute values are not biased if Sy II are identical in all properties to type I Seyferts, and their apparent differences are only due to observers' orientation, as assumed in the most basic unified model scheme. In a more modern paradigm, relying on weaker unification, it can be expected that type II AGN preferentially have high covering factors (Elitzur, 2012).

In direct comparison with the distribution of covering factors in the Sy II samples of Mateos et al. (2016) and Audibert et al. (2017), we find a similarly broad distribution with a preference for high covering factors (peaking at $C_{\rm tor} \simeq 0.8 \pm 0.2$). A study similar to ours on a sample of type I AGN would be needed in order to see if their covering factors are preferentially lower, as found by, e.g., Ichikawa et al. (2015), Mateos et al. (2016) and Audibert et al. (2017). If true, this would further support the idea that optical classification is not always a good indicator of the viewing angle toward an AGN, as originally thought in the basic unified model paradigm (Antonucci, 1993). Instead, if the torus is clumpy, type II AGN are simply preferentially selected from a pool of AGN with high covering factors, since they have a greater probability of being observed as obscured for a randomly oriented observer (Elitzur, 2012). In this picture it is expected that a small fraction of Sy II will be unobscured in the X-ray band, and that a some fraction of Sy II will have small covering factors. We find that both of these predictions are confirmed in our sample.

In these comparisons it is important to keep in mind that the infrared emission comes from the dust within the torus, while the X-ray reprocessing primarily happens in neutral gas, and the two may not be mixed well enough to trace the same physical structures surrounding SMBHs. Previous studies of $N_{\rm H,los}$ variability have shown that clouds of gas consistent with broad-line region clouds produce relatively short eclipses of the X-ray source as they pass through our line of sight. It was subsequently shown that the eclipse observable in the X-ray band is not accompanied by reddening

of the optical radiation, indicating that the eclipsing cloud may be devoid of dust, again consistent with broad-line region clouds that reside within the dust sublimation radius from the SMBH.

One of the challenges for the future will be to understand which parts of the AGN structure can be probed by detailed observations at different wavelengths, and how different constraints interact in painting a self-consistent picture of this physical system. We further discuss future prospects in § 7.3.

6.6 Summary and Conclusions

In this chapter we performed the first large-scale study of the geometrical properties of the AGN torus based on broadband X-ray data. Our sample consists of 124 Seyfert II targets selected in the hard X-ray band from the *Swift*/BAT all-sky catalog. Short *NuSTAR* observations of these sources produced the largest high-quality hard X-ray dataset to date, enabling us to explore the constraints that these spectra put on the properties of the obscuring torus in individual AGN and in the local population.

In constraining the basic geometric properties of individual AGN we make use of the popular spectral model `MYtorus` (Murphy & Yaqoob, 2009), as well as the more flexible new model `borus02`, presented for the first time in Chapter IV. We first employed these models in their basic *coupled* configurations, where simplifying assumptions are made regarding the torus column density and the line-of-sight column density, finding that this leads to unreasonable results that are difficult to interpret, even if the majority of observed spectra can be described well (in terms of the fitting statistic) with either of the models. Supporting our results based on phenomenological modeling presented in Chapter V, this analysis showed that the data cannot be explained with a single geometrical model applied to the whole sample, and that a variety of torus configurations likely exists in the population.

In agreement with previous studies of bright AGN not included in our sample, we find that *decoupled* configurations of both `MYtorus` and `borus02` models (in which the torus column density is independent of the line-of-sight column density) provide a statistically good representation of the observed spectra for a greater number of AGN, while avoiding some limitations of the coupled configurations. From fitting either of the spectral models, we find that the distribution of the torus column densities ($N_{\rm H,tor}$) in our sample has a median at $\log N_{\rm H,tor}/{\rm cm}^{-2} \approx 24.2$, with the 68 % confidence interval covering $23.5 < \log N_{\rm H,tor}/{\rm cm}^{-2} < 24.7$ (see Figure 6.6).

Furthermore, we find that up to a third of the AGN in our sample could have tori with average column densities below the Compton-thick threshold at 1.4×10^{24} cm^{-2}, and that the data generally do not prefer tori with very high optical depth to Compton scattering.

We also used the `borus02` model to constrain the distribution of torus covering factors ($C_{\rm tor}$) in the sample. The distribution (shown in Figure 6.7, left panel) does not exclude any part of the parameter space between 0.1 and 1.0, but does show a preference for high $C_{\rm tor}$; it peaks around the covering factor 0.9, and has the median at 0.68. We also examine the dependence of $C_{\rm tor}$ on intrinsic luminosity (see Figure 6.8). Despite the large spread at any luminosity, we find that the median increases from 0.5 around the 10–50 keV intrinsic luminosity $\simeq 3 \times 10^{41}$ erg s^{-1} to 0.8 at $\simeq 3 \times 10^{42}$ erg s^{-1}, decreasing back to 0.5 above $\simeq 1 \times 10^{44}$ erg s^{-1}. This agrees well with most previous studies of the obscured AGN fraction, which indirectly probe the average torus covering factor as a function of luminosity. We argue that the low median covering factor at the low-luminosity end is not due to selection incompleteness, further fueling the disagreement between X-ray and optical studies of AGN obscuration at low luminosities.

Chapter 7

SUMMARY, CONCLUSIONS, AND OUTLOOK

7.1 A Unifying Theme

The focus of this thesis is on furthering our understanding of the structure of the accretion flow onto SMBHs. This is achieved though broadband X-ray spectroscopy, with particular emphasis on data from the first focusing hard X-ray telescope, *NuSTAR*. With its unprecedented sensitivity at energies above 10 keV, it provides the key observational diagnostics of the properties of the AGN X-ray source, the corona, and the surrounding gas in the accretion disk, BLR and the torus.[1] From afar, these structures may seem well characterized, since they have been a part of the original unified model constructed ∼20 years ago; however, many details are still unclear.

The modern view of AGN unification has moved beyond the simplistic model described in § 1.1.2, into a regime of increasing diversity. It is therefore important to pin down differences that are as physical as possible, rather than relying on phenomenological classification that may not uniquely correspond to real, physical differences in the structure of the accretion flow. Measuring physical quantities from X-ray spectra, however, is often model-dependent. Confronting various spectral models for AGN X-ray spectra with the unique new data from *NuSTAR*, is a unifying theme of the studies presented in this thesis.

A brief summary of what the data constrains in the framework of these models is given in the following section.

7.2 New Constraints on the Properties of AGN Structures

In the study presented in Chapter II, motivated by our limited knowledge of the geometry and the properties of the AGN corona, I performed a detailed spectroscopic analysis of two *NuSTAR* observations of the obscured Seyfert MCG –05-23-016. The result of spectral modeling using a phenomenological model is the measurement of the exponential high-energy cutoff, $E_{\rm cut} = 116 \pm 6$ keV. Employing a simple

[1] This list is deliberately limited to the structures discussed in this thesis. *NuSTAR* is also very well suited for studying the physics of relativistic jets of blazars; see, e.g., Sbarrato et al. (2013), Baloković et al. (2016), Madejski et al. (2016).

comptonized plasma models to provide independent constraints for both the kinetic temperature of the electrons in the corona and its optical depth, I found $kT_e = 29 \pm 2$ keV and $\tau_e = 1.23 \pm 0.08$ assuming a slab (disk-like) geometry, and $kT_e = 25 \pm 2$ keV and $\tau_e = 3.5 \pm 0.2$ assuming a spherical geometry. Both geometries are found to fit the data equally well and their two principal physical parameters are correlated in both cases.

With the optical depth to Compton scattering in the optically thick regime, the data are pushing the currently available theoretical models of the comptonized plasma to the limits of their validity. Since the spectral features and variability arising from the inner accretion disk have been observed in MCG –05-23-016 (Zoghbi et al., 2014), the inferred high optical depth implies that a spherical or disk-like corona cannot be homogeneous, i.e., it has to be organized into patches that allow us to observe the inner edge of the accretion disk.

Although a part of Chapter III and Chapter IV in its entirety use a phenomenological spectral model, the rest of the thesis is focused on exploration of constraints on the geometry of the obscuring torus that can be extracted from *NuSTAR* data. As there is currently no way to distinguish the physical distance of the matter involved in reprocessing of the intrinsic X-ray continuum (i.e., all models lack a physical scale), the "torus" in this work also includes the BLR and the accretion disk to some extent. However, from previous studies it is known that the BLR has a small volume filling factor, so the bulk of radiation reprocessing is more likely happening in the classical torus. Some ideas regarding the separation of these components in future work are discussed in § 7.3.

Chapter III presents a spectroscopic study of three CT AGN, NGC 424, NGC 1320, and IC 2560, using data from *NuSTAR*, *Swift*, and *XMM-Newton*. The high quality hard X-ray data allowed for detailed modeling of the reprocessed spectral component, which dominates their X-ray spectra above 3 keV. For the first time in these sources, it was possible to constrain the intrinsic photon indices and the average torus column densities through the shape of the reprocessed spectra, which would be impossible without *NuSTAR* data. With the assumption of a 50 % covering factor built into the `MYtorus` model (Murphy & Yaqoob, 2009), the average column density of the tori in these three AGN was found to be $\gtrsim 3 \times 10^{24}$ cm^{-2}. From the fact that pole-on reprocessed spectrum fits the data better, indicating that we may be observing the inner illuminated wall of the torus, we concluded that the torus is likely not uniform.

Conclusions of this early study were echoed in many subsequent studies of CT AGN

with *NuSTAR*, e.g., Annuar et al. (2015), Puccetti et al. 2016, Boorman et al. (2016), and ultimately, the study of the large sample of 124 AGN presented in Chapter VI. However, two intermediate steps had to be taken in order to get to the analysis of the torus parameters in the local obscured AGN population. The chronologically earlier one was the phenomenological study of the large number of obscured AGN spectra obtained though the *NuSTAR* survey of Seyfert II nuclei selected from the *Swift*/BAT catalog. The second step was calculation of a new, more flexible spectral model for X-ray reprocessing in the torus that could be applied to the diverse set of broadband X-ray spectra of *Swift*/BAT-selected AGN.

In this thesis, the new spectral fitting model is presented first, in Chapter IV. Calculation of the new model was based on the Monte Carlo radiative transfer code I wrote from first principles. In calculation of the model spectra I assumed an approximately toroidal geometry (a uniform sphere with conical polar cutouts), following the popular `BNtorus` model of Brightman & Nandra (2011a). The main advantage the new model is its applicability to a wider variety of AGN, and the larger array of free spectral parameters that can be constrained directly from the data; most importantly, the torus average column density, and its covering factor. Also presented in Chapter IV is a spectral analysis performed on four different AGN with good-quality *NuSTAR* data, demonstrating they they cover four different parts of the parameter space spanned by the column density ($22 < \log\ N_{\rm H,tor}/{\rm cm}^{-2} < 25.5$) and the covering factor ($0.1 < C_{\rm tor} < 1.0$).

Chapters V and VI present my work on the large sample of AGN selected in the hard X-ray band (14–195 keV) from the flux-limited all-sky survey with *Swift*/BAT. They were observed nearly simultaneously with short *NuSTAR* and *Swift*/XRT exposures, generating an atlas of good-quality broadband X-ray spectra for over 130 obscured AGN in the local universe. Such a survey provides, for the first time, a complete picture of the spectral diversity exhibited by obscured AGN at the level comparable to that of unobscured AGN. The observations, data, processing, and principles of data analysis for this large survey are all presented in Chapter V. This chapter is also where I present results based on the simplest phenomenological models used ubiquitously in the literature. Despite the very limited interpretation that they offer in terms of constraints on the AGN torus, these models do reveal the typical and the extreme spectral properties of the Seyfert II population, which help us better understand much fainter AGN expected (and found) in deeper surveys (Lansbury et al., 2017).

Finally, Chapter VI presents the first large-scale study of the geometrical constraints on the AGN torus based on broadband X-ray data. For this analysis I used both the popular `MYtorus` model, and my own new model presented in Chapter IV. In agreement with previous studies of bright AGN with *NuSTAR*, we find that the torus column density is generally independent of the line-of-sight column density. Fitting either of the spectral models leads to the finding that torus column densities ($N_{\rm H,tor}$) are mostly constrained to the interval $23.5 < \log\ N_{\rm H,tor}/{\rm cm}^{-2} < 24.7$ (with the median $\log\ N_{\rm H,tor}/{\rm cm}^{-2} \approx 24.2$).

I was also able to constrain the distribution of torus covering factors ($C_{\rm tor}$) in the sample, finding a preference for high $C_{\rm tor}$: the distribution within the Seyfert II population peaks around 0.9, with the median at 0.68. Despite the large spread of $C_{\rm tor}$ constraints at any luminosity, we find that the median $C_{\rm tor}$ does depend on luminosity so that it is lower at both ends of the luminosity range. Remarkably, these results agree with a number of studies based on population statistics and modeling of $C_{\rm tor}$ from the infrared data. These independent constraints should be harnessed in future work in order to further characterize the torus as an integral part of the SMBH accretion flow, and obscured AGN as a population potentially relevant for evolution of galaxies at $z > 0$ (§ 1.2.3).

7.3 Future Prospects

7.3.1 New X-ray Spectral Models and Instruments

The new spectral fitting model presented in Chapter IV is the first in a series of models produced with the Monte Carlo radiative transfer code I developed in order to better understand the formation of reprocessed X-ray spectra in the AGN torus. In future work, this will provide means to investigate the impact of various approximations and arbitrary choices of various nuisance parameters assumed in currently existing spectral templates (see, e.g., § 4.2 and § 6.1.2 for a comparison). A detailed investigation into the effects of different physically-motivated assumptions and simplifications on the ability to constrain basic geometrical and physical parameters of the AGN torus and related structures from broadband X-ray data is currently missing from the literature. Such a study is necessary for understanding the quantitative limits to what can plausibly be constrained with current, as well as future, X-ray instruments under a minimal set of theoretical assumptions.

The choice of geometry for the next generation of spectral models will essentially be

driven by the findings based on *NuSTAR* data (e.g., Chapter VI), rather than assumed a priori. They should also account for the possibility of temporal evolution of X-ray spectra following substantial changes in the luminosity of the central source, i.e. X-ray reverberation from the torus. Detailed studies of particular AGN (e.g., Madejski et al. 2000) have previously shown that tracking X-ray reverberation with multi-epoch observations is a powerful tool for probing the circumnuclear material and its geometry.

Finally, a major driver for further development of torus models will be the availability of very high resolution X-ray data from the planned X-ray calorimetry mission XARM (*Hitomi*/SXS replacement, to be launched in early 2020-ies), and *Athena* further in the future (early 2030-ies; Barret et al. 2016). None of the currently available models have the energy resolution sufficient for fitting those data (with the exception of the Furui et al. 2016 model, which is proprietary). At the energy resolution of these instruments ($\simeq$100 km s^{-1}; Mitsuda et al. 2014, Hitomi Collaboration et al. 2016), it will become possible to resolve dynamics in the innermost regions of the torus and investigate its connection to the BLR, the accretion disk, and outflows.

High energy resolution in the soft X-ray band holds tremendous potential for advancing further toward better understanding of the AGN structure. Relatively strong fluorescent emission lines of Mg, Si and S, which have thus far received little attention in the literature due to the limitations of the current X-ray grating spectrometers, can be used as powerful diagnostics (Shu et al., 2011; Liu et al., 2016). The energy resolution of instruments aboard the XARM and *Athena* will be sufficient for detailed measurements of soft X-ray line profiles and intensities, which contain information on the velocity distribution and therefore distance from the SMBH, as well as relevant densities and ionization structure.

High-resolution spectroscopy will reveal whether material is predominantly inflowing, outflowing, rotating, or moving chaotically, which is of paramount importance for connecting the accretion flow to the AGN host, and characterizing their interaction. Dynamics are encoded in the spatially unresolved soft X-ray spectra of AGN in a nontrivial way, and detailed theoretical studies will be crucial for interpreting them. Additional information may be available in to form of polarization signals in the X-ray band, which could be observable with the proposed X-ray spectropolarimetry mission IXPE (Weisskopf et al., 2016).

7.3.2 Self-consistent Multi-wavelength Spectral Models

Fitting mid-infrared spectra and photometry with spectral templates for emission of dust in the torus can provide constraints on its geometry (e.g., Alonso-Herrero et al. 2011, Hönig 2013, Ichikawa et al. 2015, Netzer 2015). This approach is limited by contamination of the spectra by star formation in the host galaxy, and the fact that assumption of different geometries for the spectral templates can lead to significantly different results (e.g., Feltre et al. 2012). Some of this degeneracy could be remedied by requiring that the torus model of a given geometry fits both the infrared and the X-ray data. Other measurements (e.g., opening angle of the narrow-line cone, megamaser disk detection, mid-infrared interferometry) can be leveraged to provide even tighter constraints. With currently available spectral templates, constraints on the geometry from the X-ray and infrared bands can only be done in an approximate way (e.g., Farrah et al. 2016, Guainazzi et al. 2016), because not a single set of templates for the exact same geometry is available for both bands.

A self-consistent set of X-ray and infrared model spectra would need to include components other than the classical dusty torus (e.g., the broad-line region, the accretion disk) and satisfy some basic physical constraints: e.g., that the gas within the dust sublimation radius contributes negligibly to the dust thermal emission, that the physical scale of the broad line region and the inner "wall" of the torus are consistent with observed scaling relations (e.g., Gandhi et al. 2015, Burtscher et al. 2015), and that the geometry is not inconsistent with recent high-resolution mid-infrared observations (interferometric where possible; Asmus et al. 2016, Wada et al. 2016). This will provide a physical scale for my model, which X-ray models do not need to have. This fact is of utmost importance for making these models physical rather than just geometrical, so that further physical constraints, such as those from resolved dynamics in X-ray data with high energy resolution, can be self-consistently taken into account in the future.

APPENDIX

A Notes on Targets Included in the Main *Swift*/BAT Sample

2MASX J07561963−4137420 — Due to a combination of low photon statistics, significant Galactic absorption, and variability with respect to the average *Swift*/BAT spectrum, this source is described sufficiently well with just a power-law model. However, if we consider the full model, $N_{\rm H,los} > 10^{22}$ cm^{-2} puts it among obscured AGN. If the *Swift*/BAT spectrum is included in the joint fit, its cross-normalization factor is 4 ± 1, but the spectral parameters do not change significantly between fits with and without the *Swift*/BAT data.

NGC 3786 — Due to the large cross-normalization factor between *Swift*/BAT and *NuSTAR* spectra when fitted jointly, in Table C3 we also show parameters derived using only the *NuSTAR* and *Swift*/XRT spectra.

CGCG 164-019 — All models shown in Table C3 for this source have atypically high $f_{\rm sca}$, possibly indicating a need for partial covering multi-layer absorber. The limited photon statistics, however, preclude a more robust evaluation of such a requirement.

NGC 2992 — This bright source with data of very high quality is one of the best examples of a well-constrained full model for a lightly obscured AGN (log $N_{\rm H}$= 22.04 ± 0.02). In-depth study with *Suzaku* (Yaqoob et al., 2007) found $N_{\rm H}$= $8.0 \pm 0.5 \times 10^{21}$ cm^{-2}, which would place the AGN in the unobscured category; however, this could be just a consequence of the lower Γ in their best-fit model. With Sy 1.9 optical classification, this AGN is clearly in between the major classes. It has been documented in the literature that its $N_{\rm H}$ exceeded the 10^{22} cm^{-2} threshold in the past, as summarized most recently by Shu et al. (2010b). The *NuSTAR* observation occurred while the source was a factor of $\simeq 7$ brighter than the average, as evidenced by the significant offset in the *Swift*/BAT cross-normalization factor with respect to *NuSTAR*. Excluding the *Swift*/BAT data does not significantly change any of the spectral parameters.

NGC 4388 – *Swift*/XRT data were not taken simultaneously with the *NuSTAR* observation of this target. Although archival *Swift*/XRT observations do exist, none of those spectra are consistent in flux or shape with the *NuSTAR* spectrum, revealing significant spectral variability. Changes are also evident with respect to the

time-averaged *Swift*/BAT flux (cross-normalization factor, C_B, is 3.33 ± 0.07) and with respect to the literature; e.g., Beckmann et al. (2006) measured log $N_{\rm H}\simeq$ 23.4 and Γ = 1.92 ± 0.09 in comparison to log $N_{\rm H}$= 23.67 ± 0.02 and Γ = 1.70 ± 0.02 here. Excluding the *Swift*/BAT data does not alter the model parameters; it only increases their uncertainties. A summary of X-ray spectral variability of this AGN is presented in a separate publication (Kamraj et al., 2017).

NGC 5252 – Despite the lack of any *Swift*/XRT observation (QS or archival), the very high quality of the *NuSTAR* data enables us to constrain the relatively low $N_{\rm H}$ to $\simeq 3.5 \times 10^{22}\,{\rm cm}^{-2}$. The spectrum is exceptionally featureless and places one of the tightest constraints on the reprocessed continuum contribution ($R_{\rm pex}< 0.03$) in the main sample. The high cross-normalization factor for the *Swift*/BAT spectrum, C_B = 2.40 ± 0.08, points to significant flux variability, but the exclusion of the *Swift*/BAT data does not alter the best-fit model significantly. Fitting the *NuSTAR* and *Swift*/BAT spectra simultaneously with the high-energy cutoff as a free parameter results in the highest well-constrained $E_{\rm cut}$ in the main sample at 330^{+250}_{-90} keV.

NGC 5643 – Annuar et al. (2015) find a lower intrinsic luminosity using the same *NuSTAR* data, which is in part because of more advanced torus models, but also because of the significantly smaller adopted distance (13.9 Mpc, compared to our 17.7 Mpc), which makes all luminosities $\simeq$ 50 % lower regardless of the spectral model.

IRAS 05189+2524 – *NuSTAR* observations of this AGN were previously presented as part of the *NuSTAR* survey of nearby ultraluminous infrared galaxies (Teng et al., 2015). Of the three available observations, two are consecutive, and no variability was observed between those two observations and the third, which is separated by 8 months. We modeled the coadded *NuSTAR* spectrum and the quasi-simultaneous *Swift*/XRT data with the `full` model, finding that the data prefers a very steep photon index (Γ = 2.8 ± 0.1 and a strong `pexrav` component ($R_{\rm pex}$= 3.2 ± 0.7). An acceptable fit can be found for Γ = 2.4 ($p_{\rm null}$= 10 %, see Table C3), but not for any lower values. Dadina (2007) have also found a very steep Γ of $2.9^{+0.3}_{-0.2}$ based on one *BeppoSAX* observation. Teng et al. (2015) used the *NuSTAR* data up to $\simeq$ 22 keV in conjunction with simultaneous *XMM-Newton* data, constraining Γ to 2.55 ± 0.02 with a more complex multi-layer absorption model. The atypicaly steep spectrum led us to explore a range of alternative models including outflowing ionized absorption and reflection from the accretion disk, which is reported in a dedicated publication by Xu et al. (2017).

B Notes on Targets Excluded from the Main *Swift*/BAT Sample

The main spectral parameters used within this paper are described here for some of the sources excluded from our main sample. For most of these sources we simply extract relevant parameters from models discussed in recent literature based on *NuSTAR* data whenever possible. For a few objects for which a dedicated analysis has not been published yet, or the published models significantly differ from the full model used in this paper, we briefly discuss constraints from our own modeling.

SWIFT J0350.1−5019 – As a bright hard X-ray source, this target was identified already in the 9-month *Swift*/BAT catalog (Tueller et al., 2008) and associated with the Sy 2.0 nuclei of either ESO 204-G001 or its companion 2MASX J03502377−5018354 (Parisi et al. 2009, Koss et al., in preparation). Detailed inspection of the *Swift*/XRT images revealed two very close soft X-ray sources at positions of these two optical counterparts. Previous X-ray spectral analyses by Eguchi et al. (2009) and Winter et al. (2009) likely refer to the combined spectrum of both sources, and neither identify a CT AGN in the system. We excluded this target from our main sample due to the difficulty of distinguishing blended nuclei in either *Swift*/XRT or *NuSTAR* data, and because the modeling applied to the main sample is inconclusive with respect to the nature of the observed spectrum: both RD solutions (with intrinsic luminosity $\geqslant 10^{44}$ erg s^{-1}) and Compton-thin models (with intrinsic luminosity $\leqslant 10^{43}$ erg s^{-1}) can be fitted to the *NuSTAR* and *Swift* data equally well. A more detailed spatially-resolved analysis of *XMM-Newton* data on this system will be presented by Ricci et al., in preparation. When considering excluded sources in discussions here, we count 2MASX J0350 as CT, given the results of Ricci et al. (2015) for ESO 204-G001 as the optical counterpart. The spectral curvature parameters for the *NuSTAR* ($SC_N = 0.51 \pm 0.05$) *Swift*/BAT data ($SC_B = 0.6 \pm 0.3$) suggest that the CT AGN dominates in the hard X-ray band.

NGC 7172 – Due to the very high S/N ratio of the data, we are unable to reach our threshold for an acceptable model ($p_{\rm null} > 5$ %) with any modifications of the full model discussed in this paper. The best fit, with χ^2/d.o.f. = 556/493 ($p_{\rm null} = 2.6$ %), is found for $\Gamma = 1.85 \pm 0.01$, $N_{\rm H} = (9.0 \pm 0.2) \times 10^{22}$ cm^{-2} and $R_{\rm pex} = 0.62 \pm 0.04$. This fit already includes the following modifications of the full model: $f_{\rm sca} = 0$ (fixed, with a forced upper limit at 0.07 %), fitted energy of the Fe Kα line ($6.32^{+0.09}_{-0.01}$ keV), fitted energy of the Fe Kβ line (7.3 ± 0.1 keV), very high $E_{\rm cut}$ (> 670 keV), and fitted `pexrav` abundances ($0.7 \pm 0.1\ A_\odot$). This spectral model is broadly consistent with previous studies of the NGC 7172 X-ray spectrum (most recently summarized by

Akylas et al. 2001), given the expected variability in $N_{\rm H}$, Γ and intrinsic luminosity, and the fact that *NuSTAR* data can constrain the contribution of the reprocessed component significantly better than any previously available spectra.

ESO 383-G018 – This source stands out as the most atypical one in our full sample. Despite the data not being of quality as high as the rest of the sources excluded from the main sample, it is extremely difficult to find a modification of our `full` model that would fit the ESO 383-G018 data well. No models with the reprocessed continuum represented by `pexrav` alone get even close to a good fit, but assuming an absorbed `pexrav` does to some extent. Fitting for $R_{\rm pex}$ draws this parameter to infinity, as in the case of lower-quality CT AGN spectra presented here. However, the Fe Kα line is very weak (EW $<$ 0.05 keV) in comparison to any RD spectrum. With $E_{\rm cut}$ fixed at 300 keV as in our default full model, Γ is extremely steep (2.7 ± 0.1), unless `pexrav` abundances are fitted for, in which case Γ decreases to 2.24 ± 0.08. Despite the formally acceptable χ^2 (255.7 for 248 d.o.f.; $p_{\rm null}$= 36 %), it is difficult to understand the relation between the spectral components of this model, and to quantify spectral parameters $f_{\rm sca}$ and $L^{\rm int}$. Such a solution is also inconsistent with the high-quality *XMM-Newton* data presented by Ricci et al. (2010). Their preferred model includes two-layer partial absorption, and our preliminary study of the longer 100-ks *NuSTAR* observation of ESO 383-G018 points to a similar model (Kosec et al., in preparation). For a direct comparison with the rest of our main sample, we use a model with Γ and $R_{\rm pex}$ fixed at 1.7 and 1.0, respectively. It does not fit the data very well, but the spectral parameters are comparable to the rest of our sample, and are roughly consistent with the more detailed modeling by Ricci et al. (2010). In this model $E_{\rm cut}$ has to remain extremely low (55 ± 5 keV) in order to match the data reasonably well. As this is only a phenomenological model with a limited scope, we defer physical interpretation of this exceptional spectrum to Kosec et al., in preparation.

NGC 5506 – Due to very high SNR of both *NuSTAR* and *Swift* data, even the `full` model does not fit the observed spectrum well. Matt et al. (2015) analyzed the same *NuSTAR* and *Swift*/XRT data, but used the `xillver` model to represent the reprocessed component due to the torus, instead of `pexrav`. They found that no relativistic broadening was required by those data alone. However, using 11 epochs of archival data (including *NuSTAR*), Sun et al. (2017) recently found evidence for a relativistic disk component as well as ionized absorption. Using a modified full model with components similar to their best-fit model, we do indeed find a good fit for

the *NuSTAR* and *Swift*/XRT spectrum (excluding the *Swift*/BAT data). The Compton hump is then contributed by both the disk and the torus components, reducing the torus contribution from $R_{\rm pex} \approx 1.7$ (from the `full` model fit) to $R_{\rm pex} \approx 0.5$. Most other parameters change very little with respect to the `full` model fit, except that the column density in the line of sight refers to partially ionized instead of neutral gas.

C Long Tables

In order to minimize disruption in reading of Chapters V and VI, tables containing numerical data and exceeding one page in length are placed in this appendix.

Table C1: Basic information on each target in the main sample

Target Name	R.A. (1)	Dec. (2)	z (3)	$N_{\rm H,Gal}$ (4)	*Swift*/BAT Source (5)	Type (6)	Notes (7)
LEDA 136991	00 25 32.87	+68 21 44.2	0.0120	55.0	J0025.8+6818	Sy 2.0	a
NGC 262	00 48 47.14	+31 57 25.1	0.0150	5.79	J0048.8+3155	Sy 2.0, RL	—
ESO 195-IG021	01 00 36.53	−47 52 02.7	0.0494	1.93	J0100.9−4750	Sy 1.8, Sy 2.0	—
IC 1663	01 14 07.02	−32 39 03.2	0.0119	2.40	J0114.5−3236	Sy 2.0	—
NGC 454 E	01 14 24.93	−55 23 49.5	0.0121	2.25	J0114.4−5522	Sy 2.0	—
MCG +08-03-018	01 22 34.43	+50 03 18.0	0.0204	15.0	J0122.8+5003	Sy 2.0	a
NGC 513	01 24 26.85	+33 47 58.0	0.0195	5.25	J0124.5+3350	Sy 2.0	—
NGC 612	01 33 57.74	−36 29 35.7	0.0298	2.07	J0134.1−3625	Sy 2.0, RL	—
2MASX J01402676−5319389	01 40 26.79	−53 19 39.7	0.0716	2.63	J0140.6−5321	Sy 2.0	—
MCG −01-05-047	01 52 49.00	−03 26 48.6	0.0172	2.78	J0152.8−0329	Sy 2.0	—
NGC 788	02 01 06.45	−06 48 55.9	0.0136	2.12	J0201.0−0648	Sy 2.0	—
NGC 833	02 09 20.84	−10 07 59.1	0.0129	2.53	J0209.5−1010	LINER, Sy 2.0	b
NGC 835	02 09 24.60	−10 08 09.3	0.0136	2.53	J0209.5−1010	Sy 2.0, LINER	b
ESO 416-G002	02 35 13.46	−29 36 17.0	0.0591	1.70	J0235.3−2934	Sy 1.9	—
NGC 1052	02 41 04.80	−08 15 20.7	0.0050	2.78	J0241.3−0816	Sy 2.0, LINER, RL	—
2MFGC 2280	02 50 42.59	+54 42 17.6	0.0152	40.6	J0251.3+5441	Sy 2.0	a
NGC 1229	03 08 10.79	−22 57 38.9	0.0363	1.72	J0308.2−2258	Sy 2.0	—
MGC +00-09-042	03 17 02.19	+01 15 17.9	0.0238	6.94	J0317.2+0116	Sy 2.0, LINER	—
NGC 1365	03 33 36.37	−36 08 25.4	0.0055	1.34	J0333.6−3607	Sy 1.8	—
2MASX J03565655−4041453	03 56 56.54	−40 41 46.7	0.0748	1.86	J0356.9−4041	Sy 1.9	—

Continued on the next page...

Target Name	R.A. (1)	Dec. (2)	z (3)	$N_{\rm H,Gal}$ (4)	*Swift*/BAT Source (5)	Type (6)	Notes (7)
3C 105	04 07 16.48	+03 42 25.8	0.0890	10.9	J0407.4+0339	Sy 2.0, RL	—
2MASX J04234080+0408017	04 23 40.77	+04 08 01.8	0.0450	12.6	J0423.5+0414	Sy 2.0	—
MCG +03-13-001	04 46 29.67	+18 27 39.2	0.0154	16.2	J0446.4+1828	Sy 2.0	—
CGCG 420-015	04 53 25.75	+04 03 41.7	0.0294	6.59	J0453.4+0404	Sy 2.0	—
ESO 033-G002	04 55 58.96	−75 32 28.2	0.0181	8.77	J0456.3−7532	Sy 2.0	—
LEDA 178130	05 05 45.73	−23 51 14.0	0.0350	2.16	J0505.8−2351	Sy 2.0	b?
2MASX J05081967+1721483	05 08 19.69	+17 21 48.1	0.0175	18.4	J0508.1+1727	Sy 2.0, Sy 1.9	a
ESO 553-G043	05 26 27.25	−21 17 11.7	0.0278	3.38	J0526.1−2118	Sy 2.0	—
NGC 2110	05 52 11.38	−07 27 22.3	0.0078	16.6	J0552.2−0727	Sy 2.0	—
ESO 005-G004	06 05 41.63	−86 37 54.7	0.0062	10.2	J0601.9−8636	Sy 2.0	—
Mrk 3	06 15 36.36	+71 02 15.1	0.0135	9.67	J0615.8+7101	Sy 2.0, Sy 1.9	—
ESO 121-IG028	06 23 45.57	−60 58 44.4	0.0405	3.87	J0623.9−6058	Sy 2.0	—
LEDA 549777	06 40 37.99	−43 21 21.0	0.0610	5.67	J0640.1−4328	Sy 2.0	—
LEDA 511628	07 08 43.26	−46 42 49.3	0.0469	6.42	J0709.0−4642	Sy 2.0	—
MCG +06-16-028	07 14 03.86	+35 16 45.4	0.0157	5.55	J0714.2+3518	Sy 2.0, Sy 1.9	—
LEDA 96373	07 26 26.35	−35 54 21.7	0.0294	27.7	J0726.6−3552	Sy 2.0	a
IRAS 07378−3136	07 39 44.68	−31 43 02.5	0.0258	4.31	J0739.7−3142	Sy 2.0	—
UGC 3995 A	07 44 06.97	+29 14 56.9	0.0158	3.83	J0744.0+2914	Sy 2.0	b?
2MASX J07561963−4137420	07 56 19.63	−41 37 42.2	0.0210	40.0	J0756.3−4137	Sy 2.0	—
Mrk 1210	08 04 05.86	+05 06 49.8	0.0135	3.62	J0804.2+0507	Sy 2.0	—
MCG −01-22-006	08 23 01.10	−04 56 05.5	0.0218	4.40	J0823.4−0457	Sy 2.0	—
CGCG 150-014	08 40 02.37	+29 49 02.6	0.0647	4.61	J0840.2+2947	Sy 2.0	c?
MCG +11-11-032	08 55 12.54	+64 23 45.6	0.0363	4.74	J0855.6+6425	Sy 2.0	—

Continued on the next page...

Target Name	R.A. (1)	Dec. (2)	z (3)	$N_{\rm H,Gal}$ (4)	*Swift*/BAT Source (5)	Type (6)	Notes (7)
NGC 2655	08 55 37.73	+78 13 23.1	0.0047	2.18	J0856.0+7812	Sy 2.0, LINER	—
Mrk 18	09 01 58.39	+60 09 06.2	0.0111	4.37	J0902.0+6007	Sy 2.0	—
2MASX J09034285−7414170	09 03 42.89	−74 14 17.2	0.0910	8.91	J0902.8−7414	Sy 2.0	—
2MASX J09112999+4528060	09 11 29.97	+45 28 06.0	0.0268	1.23	J0911.2+4533	Sy 2.0	—
IC 2461	09 19 58.03	+37 11 28.5	0.0075	1.08	J0920.1+3712	Sy 1.9	—
MCG −01-24-012	09 20 46.25	−08 03 22.1	0.0196	3.02	J0920.8−0805	Sy 2.0	—
2MASX J09235371−3141305	09 23 53.73	−31 41 30.7	0.0424	13.3	J0924.2−3141	Sy 1.9	a
NGC 2992	09 45 42.05	−14 19 34.9	0.0077	4.86	J0945.6−1420	Sy 2.0, Sy 1.9	—
NGC 3079	10 01 57.80	+55 40 47.2	0.0037	0.89	J1001.7+5543	Sy 2.0, Sy 1.9	—
ESO 263-G013	10 09 48.21	−42 48 40.4	0.0335	10.2	J1009.3−4250	Sy 2.0	a
NGC 3281	10 31 52.09	−34 51 13.3	0.0107	6.71	J1031.7−3451	Sy 2.0	—
MCG +12-10-067	10 44 08.54	+70 24 19.3	0.0336	2.46	J1044.1+7024	Sy 2.0	—
MCG +06-24-008	10 44 48.97	+38 10 51.6	0.0259	1.26	J1044.8+3812	Sy 1.9	—
UGC 5881	10 46 42.52	+25 55 53.6	0.0206	2.51	J1046.8+2556	Sy 2.0, LINER	—
NGC 3393	10 48 23.46	−25 09 43.4	0.0125	6.35	J1048.4−2511	Sy 2.0	—
Mrk 417	10 49 30.93	−22 57 52.4	0.0328	1.88	J1049.4−2258	Sy 2.0	—
Mrk 728	11 01 01.78	+11 02 48.9	0.0357	2.02	J1100.9+1104	Sy 1.9	—
2MASX J11364205−6003070	11 36 42.05	−60 03 06.7	0.0140	63.4	J1136.7−6007	Sy 2.0, LINER	a
NGC 3786	11 39 42.55	+31 54 33.4	0.0089	2.03	J1139.8+3157	Sy 1.8	—
NGC 3822	11 42 11.11	+10 16 40.0	0.0209	3.67	J1142.2+1021	Sy 2.0	—
IC 751	11 58 52.60	+42 34 13.2	0.0312	1.22	J1158.9+4234	Sy 2.0	—
2MASX J12055599+4959561	12 05 56.02	+49 59 56.2	0.0631	1.98	J1205.8+4959	Sy 1.8	—
B2 1204+34	12 07 32.91	+33 52 40.0	0.0791	1.36	J1207.5+3355	Sy 2.0, RL	—

Continued on the next page...

Target Name	R.A. (1)	Dec. (2)	z (3)	$N_{\rm H,Gal}$ (4)	*Swift*/BAT Source (5)	Type (6)	Notes (7)
IRAS 12074−4619	12 10 04.03	−46 36 27.3	0.0315	7.53	J1210.1−4637	Sy 1.8	—
WAS 49	12 14 17.81	+29 31 43.4	0.0610	1.68	J1214.3+2933	Sy 2.0	b?
NGC 4258	12 18 57.50	+47 18 14.3	0.0015	1.60	J1219.4+4720	LINER, Sy 1.9	—
NGC 4388	12 25 46.75	+12 39 43.5	0.0084	2.58	J1225.8+1240	Sy 2.0	—
NGC 4395	12 25 48.86	+33 32 48.9	0.0011	1.85	J1202.5+3332	Sy 1.9	—
NGC 4507	12 35 36.63	−39 54 33.4	0.0118	7.04	J1235.6−3954	Sy 2.0	—
LEDA 170194	12 39 06.28	−16 10 47.1	0.0367	3.02	J1239.3−1611	Sy 2.0	—
NGC 4941	13 04 13.14	−05 33 05.8	0.0037	2.17	J1304.3−0532	Sy 2.0	—
NGC 4939	13 04 14.39	−10 20 22.5	0.0104	3.30	J1304.3−1022	Sy 2.0	—
NGC 4992	13 09 05.60	+11 38 03.0	0.0251	1.93	J1309.2+1139	Sy 2.0	—
Mrk 248	13 15 17.27	+44 24 25.6	0.0366	1.47	J1315.8+4420	Sy 2.0	b?
ESO 509-IG066	13 34 40.40	−23 26 46.0	0.0446	6.91	J1334.8−2328	Sy 2.0	b
NGC 5252	13 38 15.96	+04 32 33.3	0.0230	2.14	J1338.2+0433	Sy 1.9	—
NGC 5273	13 42 08.34	+35 39 15.2	0.0036	0.92	J1341.9+3537	Sy 1.9	—
2MASX J14104482−4228325	14 10 44.82	−42 28 32.9	0.0339	5.57	J1410.9−4229	Sy 2.0	—
NGC 5610	14 24 22.94	+24 36 50.9	0.0169	1.90	J1424.2−2435	Sy 2.0	—
NGC 5643	14 32 40.74	−44 10 27.9	0.0040	8.01	J1432.8−4412	Sy 2.0	—
NGC 5674	14 33 52.24	+05 27 29.6	0.0249	2.48	J1433.9+0528	Sy 1.9	—
NGC 5728	14 42 23.90	−17 15 11.1	0.0094	7.61	J1442.5−1715	Sy 2.0	—
CGCG 164-019	14 45 36.84	+27 02 05.2	0.0299	2.50	J1445.6+2702	Sy 1.9	—
IC 4518 A	14 57 41.18	−43 07 55.6	0.0163	8.87	J1457.8−4308	Sy 2.0	a
2MASX J15064412+0351444	15 06 44.13	+03 51 44.4	0.0377	3.73	J1506.7+0353B	Sy 2.0	b
NGC 5899	15 15 03.22	+42 02 59.5	0.0086	1.80	J1515.0+4205	Sy 2.0, LINER?	—

Continued on the next page...

Target Name	R.A. (1)	Dec. (2)	z (3)	$N_{\rm H,Gal}$ (4)	*Swift*/BAT Source (5)	Type (6)	Notes (7)
MCG +11-19-006	15 19 33.69	+65 35 58.5	0.0440	2.69	J1519.6+6538	Sy 1.9, Sy 2.0	—
MCG −01-40-001	15 33 20.71	−08 42 01.9	0.0227	8.17	J1533.2−0836	Sy 2.0	—
NGC 5995	15 48 24.96	−13 45 27.9	0.0252	10.2	J1548.5−1344	Sy 2.0	—
MCG +14-08-004	16 19 19.26	+81 02 48.6	0.0239	4.55	J1621.2+8104	Sy 2.0	—
Mrk 1498	16 28 04.06	+51 46 31.4	0.0547	1.83	J1628.1+5145	Sy 1.9, RL	—
IRAS 16288+3929	16 30 32.66	+39 23 03.2	0.0306	0.94	J1630.5+3925	Sy 2.0	—
ESO 137-G034	16 35 14.11	−58 04 48.1	0.0090	22.8	J1635.0−5804	Sy 2.0	a
LEDA 214543	16 50 42.87	+04 36 18.0	0.0321	6.16	J1650.5+0434	Sy 2.0	—
NGC 6240	16 52 58.87	+02 24 03.3	0.0245	4.87	J1652.9+0223	Sy 2.0	b
NGC 6300	17 16 59.47	−62 49 14.0	0.0037	7.79	J1717.1−6249	Sy 2.0	—
MCG +07-37-031	18 16 11.55	+42 39 37.2	0.0412	3.14	J1816.0+4236	Sy 2.0	b?
2MASX J18241083+1846088	18 24 10.83	+18 46 08.7	0.0670	17.4	J1824.2+1845	Sy 2.0, Sy 1.9	a
IC 4709	18 24 19.39	−56 22 09.0	0.0169	7.23	J1824.3−5624	Sy 2.0	—
LEDA 3097193	18 26 32.40	+32 51 30.0	0.0220	6.30	J1826.8+3254	Sy 2.0	—
ESO 103-G035	18 38 20.34	−65 25 39.2	0.0133	5.71	J1838.4−6524	Sy 2.0, Sy 1.9	—
CGCG 341-006	18 45 26.20	+72 11 01.7	0.0463	5.61	J1845.4+7211	Sy 2.0	—
ESO 231-G026	19 13 14.76	−50 10 58.5	0.0625	5.28	J1913.3−5010	Sy 2.0	—
2MASX J19263018+4133053	19 26 30.20	+41 33 05.1	0.0710	8.93	J1926.9+4140	Sy 2.0	a
2MASX J19471938+4449425	19 47 19.36	+44 49 42.3	0.0539	17.3	J1947.3+4447	Sy 2.0	a
3C 403	19 52 15.81	+02 30 24.2	0.0590	12.2	J1952.4+0237	Sy 2.0, RL	a
2MASX J20063331+5620364	20 06 33.33	+56 20 36.7	0.0430	17.5	J2006.5+5619	Sy 2.0	a
2MASX J20183871+4041003	20 18 38.72	+40 41 00.2	0.0144	105	J2018.8+4041	Sy 2.0	a
2MASX J20214907+4400399	20 21 49.05	+44 00 39.6	0.0170	87.7	J2021.9+4400	Sy 2.0	a

Continued on the next page...

Target Name	R.A. (1)	Dec. (2)	z (3)	$N_{\rm H,Gal}$ (4)	*Swift*/BAT Source (5)	Type (6)	Notes (7)
NGC 6921	20 28 28.86	+25 43 24.3	0.0145	20.7	J2028.5+2543B	Sy 2.0	a, b
MCG +04-48-002	20 28 35.06	+25 44 00.0	0.0139	20.7	J2028.5+2543A	Sy 2.0	a, b
IC 5063	20 52 02.34	−57 04 07.6	0.0114	6.10	J2052.0−5704	Sy 2.0, RL	—
2MASX J21192912+3332566	21 19 29.14	+33 32 56.9	0.0506	13.3	J2118.9+3336	Sy 1.8, Sy 1.5	a
NGC 7130	21 48 19.52	−34 57 04.5	0.0162	1.93	J2148.3−3454	Sy 2.0, Sy 1.9	—
MCG +06-49-019	22 27 05.78	+36 21 41.7	0.0213	9.28	J2226.8+3628	Sy 2.0	—
NGC 7319	22 36 03.55	+33 58 32.6	0.0225	6.15	J2235.9+3358	Sy 2.0	—
MCG +01-57-016	22 40 17.05	+08 03 14.1	0.0250	6.39	J2240.2+0801	Sy 1.8	—
NGC 7582	23 18 23.50	−42 22 14.0	0.0053	1.33	J2318.4−4223	Sy 2.0	—
2MASX J23303771+7122464	23 30 37.69	+71 22 46.5	0.0370	27.7	J2330.5+7124	Sy 2.0	a
PKS 2331−240	23 33 55.24	−23 43 40.66	0.0477	4.77	J2333.9−2342	Sy 2.0, RL	—
PKS 2356−61	23 59 04.36	−60 54 59.3	0.0963	1.51	J2359.3−6058	Sy 2.0, RL	—

Notes: Full target name is given here, but shortened versions (only the first four digits of a 2MASX source number are retained) are used in the rest of the tables and text. In addition to the information extracted from the parent *Swift*/BAT 70-month catalog, in column (6) we also provide alternative and updated optical classification where possible, mainly from the BASS survey (Koss et al., in prep.). Columns: (1-2) sky coordinates of the optical counterpart identified in the *Swift*/BAT 70-month catalog; (3) redshift of the optical counterpart; (4) Galactic column density in the line of sight to the target in 10^{20} cm^{-2}, from Kalberla et al. (2005); (5) *Swift*/BAT 70-month catalog source designation; (6) optical classification from the *Swift*/BAT 70-month catalog and BASS; (7) notes: (a) $b < 15°$ (within Galactic plane); (b) binary or (possibly) blended source, or AGN pair.

Table C2: Information regarding observations and data quality for the main sample targets

Target Name	Observation ID	Observation Start	Exp.	CR_{src}	$N^{tot}_{src\ ph}$	Band SNR	Med. SNR/bin	$N^{min/bin}_{src\ ph}$	N_{bin}	Notes
	(1)	(2)	(3)	(4)	(5)	(6)	(7)	(8)	(9)	(10)
LEDA 136991	60061003002	2014-04-11 03:51	26.0	2.9 / 2.5	1396	7.1 / 6.4	4.6 / 4.0	19	62	—
	coadded	2011–2014	18.0	0.18 / 2.3	34	5.0 / 9.1	2.9 / 3.0	9	3	b
NGC 262	60160026002	2015-10-28 06:56	20.9	144.8 / 134.7	58387	38.3 / 36.8	13.0 / 10.6	50	356	—
	00080866001	2015-10-28 09:09	6.7	17.8 / 22.3	1192	34.2 / 81.4	5.1 / 33.2	23	44	—
ESO 195-IG021 ..	60061344002	2014-08-13 06:51	23.0	18.0 / 16.4	7887	8.9 / 7.1	5.6 / 5.6	23	213	—
	00080679001	2014-08-13 07:46	6.6	5.5 / 2.4	366	18.9 / 9.7	4.2 / 4.3	17	20	—
IC 1663	60061008002+3	2013-01-26 14:30	12.9	2.6 / 2.8	592	3.9 / 3.4	3.9 / 3.8	16	39	f
	00080015001	2013-01-26 13:12	6.5	0.5 / 2.1	29	5.0 / 7.8	2.8 / 2.7	8	3	—
NGC 454 E	60061009002	2016-02-14 05:16	23.1	4.0 / 3.2	1674	7.5 / 5.0	4.3 / 4.4	18	78	—
	00080016001	2016-02-14 06:47	5.2	0.3 / 2.4	14	3.3 / 9.7	2.2 / 3.8	6	2	—
MCG +08-03-018	60061010002	2014-01-27 19:36	31.7	4.6 / 4.6	2915	6.5 / 8.3	4.5 / 4.9	20	118	—
	00080019001	2014-01-27 00:06	6.6	1.3 / 2.2	88	9.1 / 8.3	3.5 / 2.2	10	7	—
NGC 513	60061012002	2013-02-16 07:01	16.0	10.0 / 9.5	3132	9.2 / 7.6	4.6 / 4.7	20	125	—
	00080021001	2013-02-16 07:47	6.8	2.1 / 3.0	144	11.8 / 10.7	3.7 / 3.7	13	10	—
NGC 612	60061014002	2012-09-14 07:41	16.7	9.2 / 8.6	2970	12.8 / 11.1	4.6 / 4.9	20	121	—
	00035627001	2006-06-02 01:53	6.7	0.7 / 6.6	46	6.3 / 26.0	3.2 / 9.6	10	4	c
2MASX J0140 ...	60160072002	2015-03-03 11:06	22.6	14.0 / 13.1	6097	7.7 / 7.1	5.3 / 5.1	22	203	—

Continued on the next page...

Target Name	Observation ID	Observation Start	Exp.	CR_{src}	$N^{tot}_{src\ ph}$	Band SNR	Med. SNR/bin	$N^{min/bin}_{src\ ph}$	N_{bin}	Notes
	(1)	(2)	(3)	(4)	(5)	(6)	(7)	(8)	(9)	(10)
	00080892001	2015-03-03 11:08	6.3	5.3 / 2.1	330	18.0 / 8.6	4.1 / 3.2	16	19	—
MCG −01-05-047	60061016002	2012-11-30 00:06	11.1	10.7 / 9.8	2278	8.9 / 7.0	4.7 / 4.5	20	96	—
	00080027001	2012-12-05 01:05	6.8	2.6 / 3.4	174	13.0 / 11.9	3.7 / 4.3	14	12	—
NGC 788	60061018002	2013-01-28 05:21	15.4	12.3 / 11.7	3695	13.5 / 12.5	4.8 / 4.8	21	140	—
	00080238001	2013-01-28 05:11	6.3	1.5 / 11.0	93	9.4 / 39.2	3.5 / 16.5	11	7	—
NGC 833	60061346002	2015-09-13 05:11	17.4	1.8 / 1.6	581	3.8 / 2.9	3.8 / 3.9	15	33	—
	coadded	2006–2015	15.5	0.28 / 1.8	43	6.2 / 6.5	3.0 / 2.4	9	4	d
NGC 835	60061346002	2015-09-13 05:11	17.4	2.2 / 2.0	728	4.9 / 4.9	3.9 / 4.0	16	40	—
	coadded	2006–2015	15.5	0.73 / 1.8	113	10.3 / 6.5	3.6 / 2.4	12	8	d
ESO 416-G002 ...	60061340002	2015-01-08 19:41	20.6	9.7 / 8.8	3810	7.0 / 6.2	5.4 / 4.7	21	137	—
	00032052002	2011-08-10 07:29	1.2	14.8 / 2.8	177	13.4 / 11.0	3.9 / 3.9	14	12	c
NGC 1052	60061027002	2013-02-14 09:51	15.6	18.3 / 18.3	5706	9.7 / 10.0	5.2 / 5.6	22	169	—
	00036365002	2009-06-08 05:12	10.3	4.0 / 4.0	417	20.1 / 14.4	4.1 / 5.5	16	23	c
2MFGC 2280	60061030002	2013-02-16 15:01	15.9	1.9 / 1.9	603	6.8 / 6.2	3.9 / 3.9	16	33	—
	coadded	2007–2013	30.9	0.19 / 3.1	58	6.4 / 11.0	3.2 / 3.9	13	4	b
NGC 1229	60061325002	2013-07-05 09:16	24.9	4.2 / 3.9	2016	8.2 / 6.8	4.3 / 4.2	19	94	—
	coadded	2010–2013	13.9	0.37 / 1.5	51	6.6 / 5.7	3.3 / 1.3	11	4	b
NGC 1365	60002046002	2012-07-25 22:21	36.3	39.3 / 36.3	27419	30.0 / 26.7	7.5 / 7.1	27	422	—
	00035458003	2012-07-26 01:11	4.5	5.6 / 9.5	252	15.8 / 38.5	4.0 / 14.7	15	16	—

Continued on the next page...

Target Name	Observation ID	Observation Start	Exp.	CR_{src}	$N^{tot}_{src\ ph}$	Band SNR	Med. SNR/bin	$N^{min/bin}_{src\ ph}$	N_{bin}	Notes
	(1)	(2)	(3)	(4)	(5)	(6)	(7)	(8)	(9)	(10)
2MASX J0350 ...	60061331002	2014-08-09 03:01	23.2	2.1 / 2.1	982	6.8 / 5.7	4.0 / 4.0	17	52	—
	00080666001	2014-08-09 03:12	6.0	0.5 / 2.6	28	5.1 / 11.1	3.3 / 4.3	11	2	—
2MASX J0356 ...	60061341002	2015-04-13 23:56	21.4	8.5 / 7.7	3464	7.4 / 6.0	5.0 / 4.6	20	139	—
	00080675001	2015-04-14 01:21	5.8	2.8 / 2.6	160	12.5 / 10.9	4.1 / 3.6	16	9	—
3C 105	60061044002+4+6	2013-02-15 02:05	16.6	5.9 / 5.7	1915	7.7 / 6.5	4.4 / 4.5	19	88	f
	00080328001+2+3	2013-02-15 02:43	6.8	0.45 / 4.2	30	5.1 / 13.2	2.7 / 5.1	8	3	a
2MASX J0423 ...	60006005001+2+3	2012-07-24 20:23	17.7	8.0 / 7.5	2753	10.7 / 11.5	4.7 / 4.7	20	115	f
	00037305001	2008-03-28 00:05	4.9	1.0 / 3.6	48	6.8 / 11.1	3.2 / 4.2	10	4	c
MCG +03-13-001	60061051002	2014-03-18 00:41	19.5	4.3 / 4.5	1725	7.6 / 7.1	4.4 / 4.4	18	80	—
	00041747001+2+3	2010-10–12	10.1	0.69 / 2.2	75	8.3 / 6.1	3.4 / 1.9	11	6	d
CGCG 420-015 ..	60061053002+4	2013–2014	33.2	10.3 / 9.4	6550	16.7 / 14.6	5.3 / 4.8	22	233	g
	00080344003	2013-01-27 00:25	6.4	2.0 / 4.0	126	11.0 / 11.7	3.6 / 5.1	13	9	—
ESO 033-G002 ...	60061054002	2014-05-04 00:46	23.6	32.6 / 30.6	14903	13.4 / 11.2	6.4 / 5.8	25	332	—
	00080345001	2014-05-04 02:20	6.9	15.5 / 3.1	1072	32.6 / 12.7	4.7 / 5.2	19	48	—
LEDA 178130	60061056002	2013-08-21 09:16	21.2	51.3 / 49.8	21394	19.3 / 17.2	7.0 / 6.8	26	344	—
	00080347001	2013-08-21 15:49	4.7	9.0 / 8.1	424	20.4 / 30.4	4.3 / 12.3	17	23	—
2MASX J0508 ...	60006011002	2012-07-23 21:46	15.5	32.6 / 31.0	9873	11.4 / 10.9	6.8 / 5.7	25	220	—
	00049706002	2013-07-28 04:11	8.4	13.3 / 4.1	1113	33.1 / 11.2	4.5 / 4.2	19	54	c
IRAS 05189−2524	60002027002+4+5	2013-02–10	56.7	10.5 / 9.9	11579	6.9 / 4.4	5.5 / 5.3	24	168	f, g

Continued on the next page...

Target Name	Observation ID	Observation Start	Exp.	CR_{src}	$N^{tot}_{src\ ph}$	Band SNR	Med. SNR/bin	$N^{min/bin}_{src\ ph}$	N_{bin}	Notes
	(1)	(2)	(3)	(4)	(5)	(6)	(7)	(8)	(9)	(10)
	00080353001+2	2013-02–10	3.7	3.8 / 1.7	142	11.7 / 6.5	3.6 / 2.4	13	10	a
NGC 2110	60061061002	2012-10-05 05:31	15.5	765.4 / 731.4	232602	70.6 / 68.2	26.3 / 21.7	177	348	—
	00080364001	2012-10-05 11:16	7.1	60.1 / 43.8	4267	65.2 / 132.8	5.3 / 53.9	24	148	—
ESO 005-G004 ...	60061063002	2015-11-10 13:16	23.0	3.1 / 2.9	1385	8.1 / 5.1	4.4 / 4.4	18	61	—
	00080367002	2015-11-10 15:22	5.7	0.4 / 4.0	19	4.1 / 15.3	2.6 / 5.0	7	2	—
Mrk 3	60002048008	2014-10-09 04:36	26.5	87.8 / 83.8	45474	48.9 / 48.9	8.3 / 7.6	34	530	—
	00080368004	2014-10-23 12:04	2.0	5.5 / 17.6	110	10.5 / 65.0	3.7 / 24.7	14	8	—
ESO 121-IG028 ..	60061065002	2014-08-08 02:56	22.1	12.9 / 12.7	5640	11.3 / 9.7	5.2 / 5.3	22	175	—
	00080370001	2014-08-08 03:22	6.6	1.6 / 4.0	102	9.7 / 15.8	4.6 / 6.4	17	4	—
LEDA 549777	60061070002	2014-01-21 00:51	22.0	6.2 / 6.0	2697	5.7 / 5.8	5.6 / 4.7	20	96	—
	00080376001	2014-01-21 03:22	5.2	1.2 / 2.1	60	7.5 / 8.0	3.4 / 2.9	11	5	—
LEDA 511628	60160284002	2015-07-18 17:46	24.5	11.3 / 10.2	5280	8.2 / 6.8	4.9 / 5.0	22	189	—
	00081003001	2015-07-18 18:47	5.6	3.5 / 2.0	198	13.9 / 7.7	3.9 / 3.3	15	12	—
MCG +06-16-028	60061072002	2013-12-03 07:06	23.6	4.2 / 3.9	1917	8.7 / 8.4	4.3 / 4.4	19	86	—
	00080381001	2013-12-03 07:52	7.4	0.7 / 2.1	53	7.0 / 6.5	3.4 / 2.1	12	4	—
LEDA 96373	60061073002	2014-07-31 20:46	22.0	6.8 / 6.6	2957	11.3 / 11.0	4.7 / 4.5	21	123	—
	00080382001	2014-07-31 21:04	3.3	1.2 / 2.6	38	6.0 / 9.7	2.9 / 2.9	9	4	—
IRAS 07378−3136	60061351002	2014-04-20 22:41	23.9	13.0 / 11.9	5968	13.7 / 11.2	4.9 / 4.8	22	226	—
	00080686001	2014-04-21 07:20	1.9	1.0 / 3.7	18	4.0 / 13.3	2.7 / 5.2	7	2	—

Continued on the next page...

Target Name	Observation ID	Observation Start	Exp.	CR_{src}	$N^{tot}_{src\ ph}$	Band SNR	Med. SNR/bin	$N^{min/bin}_{src\ ph}$	N_{bin}	Notes
	(1)	(2)	(3)	(4)	(5)	(6)	(7)	(8)	(9)	(10)
UGC 3995 A	60061352002	2014-11-08 17:36	23.3	9.8 / 9.6	4543	13.4 / 13.2	5.0 / 4.7	21	180	—
	00080687002	2014-11-08 14:55	6.6	1.2 / 2.4	81	8.7 / 7.5	3.4 / 2.7	12	6	—
2MASX J0756 ...	60061076002	2014-07-29 15:26	21.2	1.8 / 1.7	744	1.9 / 1.4	3.9 / 3.9	16	41	—
	00080385001	2014-07-30 00:22	6.8	1.0 / 1.6	68	8.0 / 5.9	3.2 / 2.3	11	6	—
Mrk 1210	60061078002	2012-10-05 15:21	15.4	39.3 / 38.1	11949	17.9 / 17.6	6.5 / 5.7	24	258	—
	00080387001	2012-10-05 19:33	6.0	4.7 / 8.3	282	16.6 / 25.5	4.2 / 9.7	17	15	—
MCG −01-22-006	60061080002	2014-01-10 08:06	24.3	28.2 / 24.4	12784	18.0 / 17.5	5.9 / 5.2	24	356	—
	00080391001	2014-01-10 11:34	3.8	3.0 / 6.0	115	10.6 / 19.0	3.7 / 7.0	13	8	—
CGCG 150-014 ..	60061083002	2013-11-08 06:11	21.0	5.3 / 4.8	2132	6.6 / 7.4	4.4 / 4.2	19	100	—
	00080398001	2013-11-08 08:34	6.8	0.6 / 2.3	41	6.0 / 7.9	2.8 / 2.8	9	4	—
MCG +11-11-032	60061086002	2016-02-18 19:11	3.5	20.8 / 20.5	1428	6.1 / 4.8	4.5 / 4.4	18	58	—
	00080403001	2016-02-18 19:29	1.8	3.5 / 2.4	62	7.9 / 9.9	3.2 / 4.3	10	5	—
Mrk 18	60061088002	2013-12-15 05:16	17.8	3.3 / 3.4	1184	4.7 / 3.9	4.2 / 4.3	17	58	—
	00080406001	2013-12-15 07:49	6.6	0.6 / 1.4	42	6.1 / 5.6	3.1 / 2.1	9	4	—
2MASX J0903 ...	60160346002	2015-11-26 23:36	14.1	4.1 / 3.7	1101	6.3 / 4.2	4.5 / 4.1	17	54	—
	00081040001+2+3	2015-11–12	6.9	0.44 / 1.5	31	5.1 / 5.8	1.8 / 1.9	8	3	a
2MASX J0911 ...	60061089002	2014-12-23 23:41	20.2	10.8 / 10.0	4195	8.8 / 10.0	4.8 / 6.9	21	130	—
	00080412001	2014-12-23 20:01	4.9	0.5 / 2.6	26	4.9 / 10.3	3.1 / 3.5	9	2	—
IC 2461	60061353002	2014-06-13 23:16	32.9	10.3 / 9.7	6582	9.7 / 8.0	5.0 / 5.1	22	235	—

Continued on the next page...

Target Name	Observation ID	Observation Start	Exp.	CR_{src}	$N^{tot}_{src\ ph}$	Band SNR	Med. SNR/bin	$N^{min/bin}_{src\ ph}$	N_{bin}	Notes
	(1)	(2)	(3)	(4)	(5)	(6)	(7)	(8)	(9)	(10)
	00080688002	2014-06-15 02:33	4.7	2.3 / 3.0	109	10.3 / 11.3	3.7 / 4.1	13	8	—
MCG −01-24-012	60061091010	2013-05-12 12:31	15.3	60.1 / 58.8	18224	15.5 / 14.5	7.4 / 6.7	25	303	—
	00080415005	2013-05-12 18:06	1.8	14.1 / 6.6	253	15.8 / 21.3	4.4 / 7.8	18	12	—
2MASX J0923 ...	60061339002	2014-04-19 17:36	17.7	7.1 / 6.8	2448	11.9 / 9.6	4.5 / 5.0	20	100	—
	00080674001	2014-04-19 14:16	6.6	0.6 / 3.8	37	5.0 / 12.8	3.2 / 4.1	11	3	—
NGC 2992	60160371002	2015-12-02 13:46	20.5	176.7 / 165.1	70137	37.3 / 35.5	13.7 / 12.5	62	357	—
	00081055001	2015-12-02 13:57	6.5	79.8 / 3.9	5184	71.9 / 12.2	5.6 / 4.9	27	159	—
NGC 3079	60061097002	2013-11-12 04:01	18.0	5.3 / 5.6	1962	14.6 / 13.7	4.3 / 4.3	19	94	—
	00080030001	2013-11-12 05:30	6.7	1.6 / 4.3	106	9.9 / 18.6	3.7 / 7.1	12	6	—
ESO 263-G013 ...	60061098002	2015-10-13 12:36	20.8	8.3 / 7.7	3334	11.6 / 9.6	4.9 / 4.5	20	136	—
	00080032001	2015-10-13 13:48	6.5	0.4 / 4.8	27	5.0 / 16.4	3.2 / 5.6	10	2	—
NGC 3281	60061201002	2016-01-22 22:46	19.1	14.2 / 12.8	5185	19.8 / 19.2	5.0 / 4.7	22	191	—
	00080037001	2016-01-22 23:15	6.4	1.1 / 12.4	71	8.0 / 40.2	3.4 / 16.1	12	5	—
MCG +12-10-067	60061204002	2015-01-15 11:01	24.8	6.5 / 6.0	3092	6.4 / 5.6	4.5 / 4.4	20	132	—
	00080040001	2-15-01-15 11:48	6.5	1.3 / 1.7	81	8.6 / 7.5	3.5 / 3.2	11	6	—
MCG +06-24-008	60061359002	2014-11-02 19:46	24.1	7.3 / 7.2	3505	5.2 / 7.1	4.7 / 5.0	21	137	—
	00080694001	2014-11-02 23:11	6.3	2.5 / 1.5	156	12.3 / 6.3	3.9 / 2.5	15	9	—
UGC 5881	60160409002	2015-05-17 05:01	21.0	4.7 / 4.4	1908	5.2 / 5.7	4.4 / 4.4	19	89	—
	00081073001	2015-05-17 06:13	5.4	0.9 / 2.8	50	6.8 / 11.4	3.2 / 4.4	11	4	—

Continued on the next page...

Target Name	Observation ID	Observation Start	Exp.	CR_{src}	$N^{tot}_{src\ ph}$	Band SNR	Med. SNR/bin	$N^{min/bin}_{src\ ph}$	N_{bin}	Notes
	(1)	(2)	(3)	(4)	(5)	(6)	(7)	(8)	(9)	(10)
NGC 3393	60061205002	2013-01-28 14:06	15.7	4.8 / 4.2	1409	11.8 / 10.7	4.3 / 4.2	17	70	—
	00080042001	2013-01-28 14:03	7.1	1.3 / 3.1	88	9.2 / 9.7	3.4 / 3.2	11	7	—
Mrk 728	60061338002	2014-02-17 18:36	23.3	11.5 / 10.7	5182	5.2 / 5.7	5.0 / 4.9	22	186	—
	—	—	—	— / 1.7	—	— / 6.1	— / 2.1	—	—	e
2MASX J1136 ...	60061213002	2014-10-29 22:16	21.6	13.4 / 13.8	5869	8.4 / 6.6	4.8 / 4.7	22	210	—
	00080058002	2014-10-30 02:37	4.9	10.4 / 3.0	508	22.4 / 9.8	4.1 / 4.0	16	28	—
NGC 3786	60061349002	2014-06-09 14:26	22.0	2.5 / 2.4	1081	2.5 / 2.2	4.3 / 4.1	17	53	—
	00080684001	2014-06-09 15:34	3.8	0.9 / 2.3	34	5.7 / 9.3	3.0 / 3.8	9	3	—
NGC 3822	60061332002	2016-01-12 09:51	19.5	6.6 / 6.4	2520	5.0 / 3.8	4.8 / 4.5	20	106	—
	00080667002	2016-01-15 00:06	0.9	11.5 / 2.2	103	10.3 / 8.0	3.8 / 2.8	14	7	—
IC 751	60061217006	2013-05-23 05:36	25.1	2.4 / 2.3	1164	6.2 / 4.5	4.3 / 4.1	18	58	—
	coadded	2008–2013	8.1	0.46 / 1.7	37	5.7 / 7.4	2.9 / 2.3	9	3	b
2MASX J1205 ...	60061357002	2014-10-23 19:26	22.4	4.1 / 3.9	1796	3.2 / 2.6	4.6 / 4.7	19	75	—
	00080692001	2014-04-18 07:41	6.5	6.6 / 1.3	427	20.5 / 6.1	4.2 / 1.8	16	22	—
B2 1204+34	60061356002	2014-12-16 07:56	21.9	13.9 / 13.4	6000	7.1 / 6.8	5.1 / 5.8	22	179	—
	00080691001	2014-12-16 09:22	6.4	4.6 / 1.4	291	16.9 / 6.2	4.3 / 2.1	18	15	—
IRAS 12074−4619	60061345002	2014-05-28 00:26	19.9	8.2 / 7.9	3195	5.6 / 3.7	4.8 / 4.7	20	128	—
	00080680001	2014-05-28 01:10	6.9	7.9 / 2.0	546	23.1 / 6.1	4.4 / 1.7	18	27	—
WAS 49	60061335002	2014-07-15 15:56	17.1	5.9 / 6.2	2064	5.6 / 5.5	4.4 / 5.1	19	86	—

Continued on the next page...

Target Name	Observation ID	Observation Start	Exp.	CR_{src}	$N^{tot}_{src\ ph}$	Band SNR	Med. SNR/bin	$N^{min/bin}_{src\ ph}$	N_{bin}	Notes
	(1)	(2)	(3)	(4)	(5)	(6)	(7)	(8)	(9)	(10)
	coadded	2013–2014	9.2	1.4 / 2.3	129	10.9 / 9.5	3.9 / 3.8	14	8	b
NGC 4388	60061228002	2013-12-27 06:46	21.4	40.6 / 38.3	16866	21.4 / 19.6	6.8 / 6.1	25	310	—
	—	—	—	— / 37.1	—	— / 138.1	— / 56.8	—	—	e
NGC 4395	60061322002	2013-05-10 02:31	19.3	31.3 / 29.5	11696	14.5 / 12.8	6.8 / 5.6	24	265	—
	00080514001	2013-05-10 03:24	6.8	5.9 / 3.6	402	19.7 / 15.6	4.8 / 7.0	17	18	—
LEDA 170194	60061232002	2016-01-15 07:06	19.7	8.2 / 7.6	3112	5.2 / 4.1	4.8 / 4.5	20	127	—
	00080086001	2016-01-15 08:02	6.9	1.9 / 5.6	131	11.2 / 16.3	3.7 / 6.8	14	9	—
NGC 4941	60061236002	2016-01-19 01:31	16.9	3.4 / 2.9	1066	8.2 / 7.2	4.2 / 4.0	17	54	—
	00080100002	2016-01-23 16:53	5.8	0.6 / 2.7	34	5.5 / 8.7	2.9 / 3.7	8	3	—
NGC 4992	60061239002	2015-01-27 05:01	20.3	16.3 / 15.4	6424	17.1 / 17.1	5.0 / 5.0	23	239	—
	00080106001	2015-01-27 05:02	6.8	1.1 / 6.8	74	8.1 / 25.4	3.7 / 10.2	13	5	—
Mrk 248	60061241002	2013-04-21 20:31	12.9	24.3 / 22.0	5981	9.1 / 8.1	6.0 / 5.6	22	138	—
	00080109001	2013-04-21 18:57	6.6	4.5 / 2.8	295	17.0 / 12.7	4.1 / 4.2	16	16	—
ESO 509-IG066 ..	60061244002	2014-09-02 23:11	20.9	15.5 / 14.5	6281	9.1 / 8.7	5.5 / 5.0	22	208	—
	00080115002	2014-09-03 00:21	6.1	2.6 / 2.6	158	12.3 / 7.3	3.7 / 3.1	13	11	—
NGC 5252	60061245002	2013-05-11 01:16	19.0	41.3 / 38.4	15160	14.0 / 12.1	7.9 / 6.0	25	289	—
	—	—	—	— / 15.7	—	— / 53.3	— / 22.3	—	—	e
NGC 5273	60061350002	2014-07-14 02:56	21.1	51.7 / 50.5	21582	20.7 / 20.5	6.7 / 6.5	26	431	—
	00080685001	2014-07-14 04:00	6.4	17.4 / 1.6	1114	33.3 / 6.9	4.9 / 2.6	21	47	—

Continued on the next page...

Target Name	Observation ID	Observation Start	Exp.	CR_{src}	$N^{tot}_{src\ ph}$	Band SNR	Med. SNR/bin	$N^{min/bin}_{src\ ph}$	N_{bin}	Notes
	(1)	(2)	(3)	(4)	(5)	(6)	(7)	(8)	(9)	(10)
2MASX J1410 ...	60160571002	2015-05-14 11:06	21.4	6.3 / 5.8	2593	7.3 / 5.8	4.5 / 4.5	20	113	—
	00081157003	2015-05-14 16:17	5.5	1.3 / 2.3	72	8.1 / 6.3	3.4 / 1.7	11	6	—
NGC 5643	60061362002+4	2014-05–06	42.1	2.5 / 2.3	1984	8.8 / 8.0	4.4 / 4.3	19	103	g
	coadded	2008–2014	20.2	1.1 / 2.3	221	14.2 / 6.1	3.8 / 2.3	14	14	b
NGC 5674	60061337002	2014-07-10 14:56	20.7	19.6 / 18.4	7844	8.4 / 10.1	5.6 / 5.5	23	220	—
	00080672001	2014-07-10 15:20	6.2	6.3 / 2.4	391	19.7 / 7.7	4.3 / 2.7	17	21	—
NGC 5728	60061256002	2013-01-02 04:21	24.4	20.6 / 19.0	9644	26.0 / 25.3	5.3 / 5.1	25	264	—
	00080137001	2013-01-02 05:03	6.6	0.9 / 11.8	58	7.2 / 28.7	3.5 / 10.4	13	4	—
CGCG 164-019 ..	60061327002	2013-09-13 23:46	24.3	2.0 / 2.0	970	5.3 / 4.2	4.0 / 3.9	16	51	—
	00080536002	2013-09-14 01:14	5.4	0.5 / 1.5	28	4.9 / 6.0	3.2 / 2.3	10	2	—
IC 4518A	60061260002	2013-08-02 11:51	7.8	18.0 / 18.5	2844	8.8 / 8.6	4.8 / 4.7	20	108	—
	00080141001	2013-08-02 12:50	7.1	2.9 / 4.6	205	14.1 / 12.3	3.9 / 5.0	14	13	—
2MASX J1506 ...	60061261002	2014-09-08 08:31	21.3	3.7 / 3.9	1616	3.6 / 3.5	4.3 / 4.2	18	78	—
	00080144001	2014-09-08 09:56	6.0	2.1 / 2.3	124	10.9 / 6.4	3.7 / 2.1	12	9	—
NGC 5899	60061348002	2014-04-08 02:46	21.4	19.1 / 18.2	7989	13.3 / 10.6	6.1 / 5.6	24	219	—
	00080683001	2014-04-08 02:58	6.5	3.1 / 2.8	200	14.0 / 11.5	4.0 / 5.0	16	12	—
MCG +11-19-006	60061264002	2014-05-01 12:36	15.0	4.6 / 4.7	1401	6.4 / 6.2	4.4 / 4.3	19	66	—
	00080147001	2014-05-01 12:40	6.8	0.9 / 1.9	59	7.4 / 8.4	3.3 / 2.8	11	3	—
MCG −01-40-001	60061265002	2015-08-07 02:41	20.7	14.9 / 14.3	6030	9.6 / 9.4	5.2 / 5.9	22	178	—

Continued on the next page...

Target Name	Observation ID (1)	Observation Start (2)	Exp. (3)	CR_{src} (4)	$N^{tot}_{src\ ph}$ (5)	Band SNR (6)	Med. SNR/bin (7)	$N^{min/bin}_{src\ ph}$ (8)	N_{bin} (9)	Notes (10)
	00080150001	2015-08-07 03:40	6.9	4.6 / 4.9	319	17.7 / 10.9	4.1 / 4.3	15	19	—
NGC 5995	60061267002	2014-08-28 04:41	21.2	41.6 / 39.0	17060	16.8 / 12.0	7.1 / 7.1	25	263	—
	00080153001	2014-08-28 08:41	6.7	22.9 / 6.4	1531	38.8 / 13.5	4.9 / 5.0	22	62	—
MCG +14-08-004	60061270002	2014-12-21 05:46	29.8	3.9 / 3.6	2220	3.9 / 3.9	4.5 / 4.6	20	94	—
	00080158002	2014-12-21 05:47	5.9	0.7 / 3.1	43	6.3 / 12.5	3.2 / 4.6	10	4	—
Mrk 1498	60160640002	2015-05-11 15:31	21.8	33.4 / 31.9	14215	17.4 / 16.8	6.8 / 6.3	26	277	—
	00081194001	2015-05-11 18:00	6.7	4.7 / 6.6	312	17.5 / 26.1	4.0 / 10.0	15	19	—
IRAS 16288+3929	60061271002	2012-09-19 00:21	16.1	4.1 / 3.9	1275	4.4 / 5.6	4.3 / 4.1	18	63	—
	00080164001	2012-09-19 00:03	7.0	0.3 / 1.6	23	4.2 / 5.9	2.9 / 2.3	8	2	—
NGC 6240	60002040002	2014-03-30 13:41	30.9	17.4 / 16.2	10362	25.6 / 24.6	5.9 / 5.3	24	295	—
	00080175001	2014-03-30 14:17	6.5	4.2 / 9.5	270	16.0 / 23.0	3.9 / 7.9	14	17	—
NGC 6300	60061277002	2013-02-25 21:31	17.7	73.5 / 70.4	25481	26.2 / 26.2	8.8 / 8.3	26	268	—
	00080182001	2013-02-25 21:39	3.4	10.3 / 15.0	348	18.4 / 44.4	4.0 / 16.8	16	21	—
MCG +07-37-031	60061283002	2015-06-24 15:46	11.1	34.1 / 31.5	7279	11.2 / 11.5	6.8 / 5.7	23	154	—
	00080208001	2015-06-25 04:38	5.3	7.4 / 2.7	391	19.6 / 9.6	4.4 / 3.3	18	20	—
2MASX J1824 ...	60160686002	2015-09-07 02:01	22.0	9.5 / 9.1	4083	8.5 / 8.3	4.9 / 4.9	21	155	—
	00081219002	2015-09-07 03:42	5.5	1.4 / 2.7	74	8.4 / 8.1	3.4 / 2.8	12	6	—
IC 4709	60061284002	2013-07-24 18:06	19.9	17.9 / 16.5	6854	12.8 / 12.5	5.6 / 5.2	23	211	—
	00080211003	2013-07-25 00:22	3.2	1.9 / 6.2	59	7.5 / 18.0	3.2 / 7.1	10	5	—

Continued on the next page...

Target Name	Observation ID	Observation Start	Exp.	CR_{src}	$N^{tot}_{src\ ph}$	Band SNR	Med. SNR/bin	$N^{min/bin}_{src\ ph}$	N_{bin}	Notes
	(1)	(2)	(3)	(4)	(5)	(6)	(7)	(8)	(9)	(10)
LEDA 3097193 ..	60061354002+4	2014-05-19 21:35	24.5	33.2 / 30.4	15581	17.1 / 13.4	6.8 / 5.8	25	347	f
	00080689001	2014-05-21 07:50	7.0	6.4 / 2.4	450	21.1 / 8.1	4.2 / 3.1	17	22	—
ESO 103-G035 ...	60061288002	2013-02-24 21:26	27.4	90.6 / 85.7	48313	25.9 / 25.4	12.2 / 12.5	47	288	—
	00080219001	2013-02-24 21:50	6.7	9.7 / 17.3	648	25.2 / 53.9	4.6 / 20.6	17	31	—
ESO 231-G026 ...	60160706002	2015-03-13 06:06	24.4	13.7 / 13.0	6516	10.9 / 10.5	5.0 / 5.0	22	224	—
	00081229001	2015-03-13 06:48	6.1	1.6 / 2.2	100	9.6 / 6.2	3.6 / 2.2	13	7	—
2MASX J1926 ...	60061334002	2014-05-21 14:06	21.4	4.1 / 4.3	1793	2.7 / 2.1	4.3 / 4.6	19	80	—
	00080669001	2014-05-21 15:57	2.1	4.4 / 2.1	92	9.5 / 7.4	3.4 / 2.3	11	7	—
2MASX J1947 ...	60061292002	2012-11-06 08:16	17.0	19.6 / 18.1	6394	8.2 / 9.0	5.1 / 5.0	22	223	—
	00802320010	2012-11-06 15:42	6.9	4.2 / 3.7	289	16.8 / 13.1	4.9 / 5.6	15	9	—
3C 403	60061293002	2013-05-25 18:06	20.0	12.2 / 11.5	4746	8.7 / 8.8	5.0 / 4.7	22	174	—
	00080233001	2013-05-25 14:32	5.9	0.9 / 4.3	56	7.1 / 11.9	3.4 / 4.3	12	4	—
2MASX J2006 ...	60061355002	2014-06-30 22:51	21.4	5.6 / 5.1	2278	6.4 / 4.2	4.5 / 4.4	19	106	—
	00080690001	2014-07-01 00:03	6.5	0.9 / 1.7	57	7.3 / 6.5	3.5 / 2.3	12	4	—
2MASX J2018 ...	60061297002	2013-12-21 12:21	21.0	18.4 / 17.8	7601	14.9 / 12.0	5.3 / 5.0	23	245	—
	00080262002	2013-12-21 15:29	3.7	1.9 / 4.0	72	8.1 / 13.8	3.3 / 5.0	11	6	—
2MASX J2021 ...	60061298002	2014-10-03 15:46	21.1	7.6 / 6.9	3057	7.4 / 7.0	4.7 / 4.5	21	127	—
	00080263001	2014-10-03 21:12	5.3	0.8 / 1.8	41	5.8 / 6.4	3.3 / 2.2	11	3	—
NGC 6921	60061300002	2013-05-18 06:26	19.5	3.2 / 2.9	1204	9.6 / 7.8	4.1 / 4.1	17	64	—

Continued on the next page...

Target Name	Observation ID	Observation Start	Exp.	CR_{src}	$N^{tot}_{src\ ph}$	Band SNR	Med. SNR/bin	$N^{min/bin}_{src\ ph}$	N_{bin}	Notes
	(1)	(2)	(3)	(4)	(5)	(6)	(7)	(8)	(9)	(10)
	coadded	2005-2013	16.6	0.30 / 10.1	49	6.5 / 33.0	3.3 / 12.3	11	4	b
MCG +04-48-002	60061300002	2013-05-18 06:26	19.5	4.0 / 3.7	1489	9.0 / 7.0	4.3 / 4.4	18	72	—
	coadded	2006–2013	7.5	0.45 / 10.1	33	5.4 / 33.0	3.2 / 12.3	11	2	b
IC 5063	60061302002	2013-07-08 07:51	18.4	43.8 / 40.8	15614	20.6 / 18.7	7.2 / 6.4	25	257	—
	00080269001	2013-07-08 07:35	7.1	4.3 / 10.2	303	17.2 / 32.3	5.6 / 13.6	18	8	—
2MASX J2119 . . .	60061358002	2015-01-17 16:21	21.5	23.8 / 23.7	10190	8.7 / 9.0	7.7 / 5.8	24	215	—
	00080693001	2015-01-17 16:56	6.6	20.6 / 2.3	1357	36.8 / 8.1	4.7 / 2.6	20	59	—
NGC 7130	60061347002	2014-08-17 23:31	21.2	1.0 / 1.1	449	5.4 / 5.3	3.7 / 3.7	14	26	—
	00080682001	2014-08-17 21:53	6.3	1.2 / 2.2	75	8.4 / 6.5	3.3 / 2.2	11	6	—
MCG +06-49-019	60061311002	2014-11-29 18:11	21.4	2.2 / 2.0	914	2.5 / 1.2	4.0 / 4.2	17	45	—
	00080285001	2014-11-30 00:49	6.8	1.9 / 2.4	126	11.0 / 8.7	3.6 / 3.1	12	9	—
NGC 7319	60061313002	2012-11-09 14:01	14.7	2.2 / 2.0	617	5.3 / 4.9	4.1 / 3.7	15	34	—
	00080287001	2012-11-09 14:08	6.6	0.6 / 4.6	37	5.6 / 16.8	2.8 / 6.6	9	4	—
MCG +01-57-016	60061343002	2014-11-18 11:06	21.4	11.0 / 10.2	4519	6.5 / 4.8	6.3 / 4.8	21	143	—
	00080678001	2014-11-18 11:16	7.2	14.0 / 2.6	1008	31.7 / 8.2	5.2 / 2.9	24	37	—
NGC 7582	60061318002	2012-08-31 16:46	16.5	28.5 / 26.2	9001	21.3 / 19.4	5.2 / 5.3	23	273	—
	00032534001	2012-09-01 17:07	6.5	4.3 / 11.2	278	16.4 / 39.7	4.0 / 16.0	15	16	—
2MASX J2330 . . .	60061320002	2014-10-26 15:41	16.1	5.6 / 4.8	1677	4.5 / 3.8	4.6 / 4.1	19	74	—
	00080302001	2014-10-26 16:54	4.1	1.1 / 1.6	43	6.4 / 6.1	3.1 / 2.0	9	4	—

Continued on the next page...

Target Name	Observation ID	Observation Start	Exp.	CR_{src}	$N^{tot}_{src\,ph}$	Band SNR	Med. SNR/bin	$N^{min/bin}_{src\,ph}$	N_{bin}	Notes
	(1)	(2)	(3)	(4)	(5)	(6)	(7)	(8)	(9)	(10)
PKS 2331-240 ...	60160832002	2015-07-30 00:06	17.9	29.6 / 27.5	10211	9.4 / 9.1	7.5 / 6.5	25	197	—
	00081308002	2015-07-30 01:28	6.2	36.3 / 2.0	2248	47.1 / 6.8	5.3 / 2.0	22	79	—
PKS 2356-61	60061330002	2014-08-10 17:16	23.1	8.2 / 7.7	3673	6.9 / 6.6	4.9 / 4.7	21	144	—
	00080665001	2014-08-10 17:27	7.1	1.8 / 1.9	124	10.7 / 7.6	3.6 / 3.1	13	9	—

Notes: For each source, the first row refers to the *NuSTAR* data, and the second refers to *Swift* (both XRT and BAT) data. For *NuSTAR*, "/" in columns (4), (6), and (7) separates values for FPMA and FPMB, while for *Swift* it separates XRT and BAT values. Column descriptions: (1) observation ID, if *Swift*/XRT data is coadded, details can be found in Table 5.1; (2) start of observation in UT; (3) total exposure in ks; (4) source count rate in $10^{-2}\,s^{-1}$ for *NuSTAR* and *Swift*/XRT, and in $10^{-6}\,s^{-1}$ for *Swift*/BAT; (5) total number of source counts, both modules for *NuSTAR*, and XRT for *Swift*; (6) full-band SNR; (7) median SNR per bin; (8) minimum number of source counts per bin, either of the *NuSTAR* modules, and XRT for *Swift*; (9) total number of energy bins; (10) notes: (a) consecutive quasi-simultaneous *Swift*/XRT observations coadded; (b) archival data coadded with quasi-simultaneous *Swift*/XRT observation; (c) single archival *Swift*/XRT observation (no usable quasi-simultaneous data); (d) archival *Swift*/XRT observations coadded; (e) no usable *Swift*/XRT data; (f) consecutive *NuSTAR* observations coadded; (g) multi-epoch *NuSTAR* observations coadded.

Table C3: Results of phenomenological spectral fitting for targets in the main sample

Target Name	Model	χ^2/ d.o.f.	$p_{\rm null}$	Γ	$\log N_{\rm H}/{\rm cm}^{-2}$	$f_{\rm sca}$	$EW_{\rm Fe\,K\alpha}$	$R_{\rm pex}$	$\log L^{\rm int}_{[10,50]}$	Notes
	(1)	(2)	(3)	(4)	(5)	(6)	(7)	(8)	(9)	(10)
LEDA 136991	**F**$_-$	68.5 / 68	46	1.7 ± 0.1	23.9 ± 0.2	($<$ 1)	$0.8^{+0.6}_{-0.2}$	2^{+3}_{-1}	42.1 ± 0.3	e
NGC 262	**F**	509.0 / 465	8	1.75 ± 0.02	22.97 ± 0.01	0.21 ± 0.09	0.04 ± 0.01	0.58 ± 0.08	43.69 ± 0.01	—
ESO 195-IG021 ..	B	247.5 / 253	59	1.76 ± 0.03	22.59 ± 0.04	—	—	—	43.83 ± 0.01	—
	F	224.7 / 250	87	1.88 ± 0.08	22.62 ± 0.05	0.5 ± 0.4	0.14 ± 0.04	0.5 ± 0.4	43.74 ± 0.05	—
IC 1663	B	44.3 / 46	54	1.5 ± 0.2	$23.39^{+0.09}_{-0.11}$	—	—	—	42.14 ± 0.04	h
	F	39.6 / 43	62	1.6 ± 0.2	$23.44^{+0.09}_{-0.11}$	$1.6^{+2.2}_{-1.0}$	$0.04^{+0.15}_{-u}$	$0.2^{+0.7}_{-u}$	$42.10^{+0.08}_{-0.14}$	h
NGC 454 E	B	82.3 / 83	50	1.3 ± 0.1	23.60 ± 0.08	—	—	—	42.50 ± 0.03	—
	F	56.0 / 80	98	1.7 ± 0.2	23.88 ± 0.08	5 ± 2	0.13 ± 0.11	$0.4^{+0.6}_{-0.3}$	42.5 ± 0.2	—
MCG +08-03-018	E	112.3 / 129	85	2.0 ± 0.1	23.89 ± 0.05	6 ± 2	$0.32^{+0.10}_{-0.08}$	—	43.04 ± 0.04	—
	F	100.4 / 128	97	2.4 ± 0.1	23.95 ± 0.08	$1.6^{+1.4}_{-0.8}$	$0.24^{+0.11}_{-0.07}$	$1.3^{+0.6}_{-0.4}$	42.8 ± 0.1	e
	F$_-$	110.7 / 129	88	1.9 (f)	$23.80^{+0.05}_{-0.07}$	8 ± 1	0.33 ± 0.08	$0.4^{+0.5}_{-0.3}$	42.9 ± 0.1	—
NGC 513	B	154.6 / 144	26	1.45 ± 0.05	22.73 ± 0.09	—	—	—	42.93 ± 0.02	—
	F	127.2 / 141	79	1.7 ± 0.1	22.85 ± 0.08	$2.5^{+1.2}_{-0.9}$	0.17 ± 0.06	1.0 ± 0.6	$42.75^{+0.06}_{-0.08}$	—
NGC 612	B	111.8 / 130	87	1.57 ± 0.06	23.93 ± 0.03	—	—	—	43.89 ± 0.02	—
	F	102.3 / 127	95	1.59 ± 0.06	23.95 ± 0.03	0.2 ± 0.1	0.12 ± 0.08	$0.04^{+0.07}_{-u}$	43.89 ± 0.04	—
2MASX J0140 ...	B	226.0 / 239	72	1.63 ± 0.03	22.09 ± 0.06	—	—	—	44.07 ± 0.02	—

Continued on the next page...

Target Name	Model	χ^2 / d.o.f.	$p_{\rm null}$	Γ	$\log N_{\rm H}/{\rm cm}^{-2}$	$f_{\rm sca}$	$EW_{\rm Fe\,K\alpha}$	$R_{\rm pex}$	$\log L^{\rm int}_{[10,50]}$	Notes
	(1)	(2)	(3)	(4)	(5)	(6)	(7)	(8)	(9)	(10)
	F	200.3 / 236	96	1.68 ± 0.08	22.12 ± 0.07	$1.1^{+1.4}_{-u}$	0.21 ± 0.05	$0.27^{+0.33}_{-u}$	44.01 ± 0.05	—
MCG −01-05-047	E	128.4 / 116	20	1.36 ± 0.07	23.18 ± 0.06	$3.1^{+1.1}_{-0.8}$	0.37 ± 0.09	—	42.97 ± 0.03	—
	F	99.1 / 115	86	1.8 ± 0.1	23.22 ± 0.07	1.3 ± 0.7	0.34 ± 0.09	$2.9^{+1.3}_{-0.9}$	42.60 ± 0.09	—
NGC 788	E	152.4 / 151	45	1.75 ± 0.05	23.94 ± 0.03	2.1 ± 0.4	0.32 ± 0.08	—	43.25 ± 0.03	h
	F	121.2 / 150	96	1.77 ± 0.05	23.89 ± 0.04	1.3 ± 0.5	0.29 ± 0.08	0.7 ± 0.2	43.01 ± 0.06	h
NGC 833	B	37.6 / 34	31	1.4 ± 0.2	23.1 ± 0.2	—	—	—	42.16 ± 0.05	c
	F_	38.8 / 39	48	1.6 ± 0.2	23.2 ± 0.1	3^{+4}_{-2}	(< 0.1)	$0.2^{+0.8}_{-u}$	$42.11^{+0.09}_{-0.14}$	h
	F_	35.0 / 32	33	1.8 ± 0.3	23.3 ± 0.2	3^{+3}_{-2}	(< 0.1)	$0.6^{+1.4}_{-u}$	42.0 ± 0.2	c
NGC 835	D	47.1 / 51	63	1.5 ± 0.1	23.58 ± 0.08	3 ± 1	—	—	42.43 ± 0.04	—
	F	46.9 / 49	56	1.6 ± 0.2	23.59 ± 0.08	2^{+2}_{-1}	< 0.1	$0.2^{+0.6}_{-u}$	$42.38^{+0.09}_{-0.12}$	—
ESO 416-G002 ...	A	160.6 / 159	45	1.63 ± 0.03	—	—	—	—	43.50 ± 0.02	d
	F_	149.6 / 157	65	1.66 ± 0.03	(< 20.8)	—	0.11 ± 0.05	(< 0.1)	43.70 ± 0.02	d
NGC 1052	D	199.7 / 213	73	1.56 ± 0.04	23.08 ± 0.04	7 ± 1	—	—	41.97 ± 0.02	—
	F_	184.7 / 212	91	1.52 ± 0.04	23.04 ± 0.05	8 ± 2	0.16 ± 0.04	(< 0.3)	41.96 ± 0.01	—
2MFGC 2280	D	37.3 / 40	59	1.5 ± 0.1	24.12 ± 0.05	$0.23^{+0.22}_{-0.11}$	—	—	43.4 ± 0.1	e
	F	25.2 / 38	94	1.6 ± 0.2	24.20 ± 0.07	$0.22^{+0.23}_{-0.13}$	$1.3^{+1.0}_{-0.8}$	$0.06^{+0.09}_{-u}$	43.1 ± 0.1	e
NGC 1229	**F**	112.8 / 101	20	1.6 ± 0.2	23.53 ± 0.09	3 ± 2	0.3 ± 0.1	$2.0^{+1.4}_{-0.9}$	43.0 ± 0.2	—

Continued on the next page...

Target Name	Model	χ^2 / d.o.f.	$p_{\rm null}$	Γ	$\log N_{\rm H}/{\rm cm}^{-2}$	$f_{\rm sca}$	$EW_{\rm Fe\,K\alpha}$	$R_{\rm pex}$	$\log L^{\rm int}_{[10,50]}$	Notes
	(1)	(2)	(3)	(4)	(5)	(6)	(7)	(8)	(9)	(10)
NGC 1365	$\mathbf{F}_{+}$	436.9 / 429	39	1.90 ± 0.03	23.30 ± 0.02	4 ± 1	0.08 ± 0.02	3.0 ± 0.4	42.07 ± 0.03	b, f
	$F_{\pm}$	473.0 / 430	8	1.7 (f)	23.25 ± 0.03	6 ± 1	0.11 ± 0.02	1.6 ± 0.1	42.07 ± 0.03	b, f
2MASX J0356 ...	**F**	178.5 / 156	10	1.65 ± 0.09	22.48 ± 0.08	(< 2)	0.18 ± 0.06	$0.2^{+0.4}_{-u}$	43.94 ± 0.06	c
3C 105	B	99.0 / 95	37	1.74 ± 0.09	23.74 ± 0.05	—	—	—	44.43 ± 0.03	h
	$\mathbf{F}_{-}$	89.3 / 93	59	1.9 ± 0.1	23.80 ± 0.05	0.5 ± 0.4	(< 0.1)	$0.27^{+0.26}_{-0.21}$	44.35 ± 0.06	h
2MASX J0423 ...	E	125.6 / 121	37	1.66 ± 0.09	23.89 ± 0.04	1.8 ± 0.5	< 0.1	—	44.12 ± 0.03	—
	F	118.6 / 120	52	1.77 ± 0.09	23.90 ± 0.04	$1.1^{+0.6}_{-0.4}$	< 0.1	0.4 ± 0.2	44.00 ± 0.06	—
MCG +03-13-001	E	102.1 / 90	18	1.5 ± 0.1	23.65 ± 0.05	$0.8^{+0.5}_{-0.3}$	0.19 ± 0.09	—	42.79 ± 0.03	—
	F	93.3 / 89	36	1.9 ± 0.1	23.76 ± 0.07	$0.2^{+0.2}_{-u}$	0.15 ± 0.09	0.9 ± 0.4	42.61 ± 0.07	—
CGCG 420-015 ..	$\mathbf{F}_{+}$	268.1 / 245	15	1.89 ± 0.06	23.98 ± 0.05	0.5 ± 0.4	0.49 ± 0.08	1.1 ± 0.4	43.55 ± 0.08	e, f
ESO 033-G002 ...	E	445.1 / 430	30	1.80 ± 0.02	22.15 ± 0.03	0.9 ± 0.6	0.11 ± 0.02	—	43.12 ± 0.01	—
	F	382.0 / 429	95	2.17 ± 0.07	22.26 ± 0.03	0.5 ± 0.3	0.09 ± 0.02	2.3 ± 0.6	42.84 ± 0.05	—
	F_{-}	406.8 / 430	78	1.9 (f)	22.17 ± 0.03	0.7 ± 0.5	0.12 ± 0.02	0.62 ± 0.09	43.04 ± 0.02	—
LEDA 178130	B	400.2 / 388	32	1.67 ± 0.02	23.06 ± 0.03	—	—	—	44.07 ± 0.02	—
	F	374.6 / 385	64	$1.67^{+0.05}_{-0.02}$	23.05 ± 0.03	0.7 ± 0.2	0.06 ± 0.02	$0.03^{+0.12}_{-u}$	$44.06^{+0.01}_{-0.03}$	—
2MASX J0508 ...	**F**	353.5 / 322	11	1.74 ± 0.06	22.21 ± 0.04	1.2 ± 0.9	0.14 ± 0.03	0.5 ± 0.3	43.06 ± 0.04	c
NGC 2110	D	718.7 / 664	7	1.642 ± 0.005	22.59 ± 0.01	0.5 ± 0.2	—	—	43.80 ± 0.01	h

Continued on the next page...

Target Name	Model	χ^2 / d.o.f.	$p_{\rm null}$	Γ	$\log N_{\rm H}/{\rm cm}^{-2}$	$f_{\rm sca}$	$EW_{\rm Fe\,K\alpha}$	$R_{\rm pex}$	$\log L^{\rm int}_{[10,50]}$	Notes
	(1)	(2)	(3)	(4)	(5)	(6)	(7)	(8)	(9)	(10)
	F	687.2 / 662	24	$1.640^{+0.010}_{-0.008}$	22.58 ± 0.01	0.5 ± 0.2	0.033 ± 0.006	$0.02^{+0.03}_{-u}$	43.80 ± 0.02	h
ESO 005-G004 ...	E	76.5 / 65	16	1.5 ± 0.1	24.09 ± 0.06	5 ± 2	$2.1^{+1.0}_{-0.6}$	—	42.13 ± 0.08	e
	F$_-$	72.5 / 65	25	1.7 ± 0.1	24.5 (f)	1^{+23}_{-1}	$1.8^{+2.1}_{-0.5}$	$1.1^{+u}_{-0.7}$	$41.5^{+0.3}_{-0.5}$	e
Mrk 3	E	551.4 / 543	39	1.61 ± 0.02	23.85 ± 0.01	2.2 ± 0.1	0.16 ± 0.02	—	43.97 ± 0.02	—
	F	542.3 / 542	49	1.64 ± 0.02	23.84 ± 0.01	1.9 ± 0.2	0.15 ± 0.02	0.12 ± 0.04	43.93 ± 0.02	—
ESO 121-IG028 ..	B	168.5 / 189	86	1.64 ± 0.05	23.33 ± 0.04	—	—	—	43.80 ± 0.02	—
	F$_-$	156.4 / 187	95	1.83 ± 0.09	23.36 ± 0.04	(< 0.2)	0.06 ± 0.04	0.7 ± 0.3	43.66 ± 0.05	—
LEDA 549777	B	104.7 / 106	52	1.52 ± 0.07	23.10 ± 0.08	—	—	—	43.77 ± 0.02	—
	F$_-$	98.5 / 105	66	1.46 ± 0.07	23.04 ± 0.08	(< 1.8)	0.17 ± 0.07	(< 0.1)	43.77 ± 0.02	—
	F$_-$	104.2 / 105	50	1.7 (f)	23.17 ± 0.06	< 1.8	0.12 ± 0.06	0.4 ± 0.2	43.68 ± 0.04	—
LEDA 511628	B	194.3 / 212	80	1.59 ± 0.03	22.41 ± 0.07	—	—	—	43.66 ± 0.02	—
	F	187.8 / 209	85	$1.70^{+0.11}_{-0.09}$	22.49 ± 0.08	$1.4^{+1.1}_{-1.0}$	0.07 ± 0.04	$0.4^{+0.5}_{-0.3}$	43.58 ± 0.07	—
MCG +06-16-028	**F**	102.0 / 92	22	1.8 ± 0.2	$24.15^{+0.08}_{-0.06}$	0.9 ± 0.6	0.4 ± 0.2	0.4 ± 0.2	43.0 ± 0.1	e
LEDA 96373	E	118.8 / 129	73	1.3 ± 0.1	23.82 ± 0.07	13 ± 4	0.9 ± 0.2	—	43.53 ± 0.05	e, i
	F	114.4 / 128	80	1.5 ± 0.1	23.7 ± 0.1	13 ± 4	0.8 ± 0.2	$0.9^{+0.9}_{-0.5}$	43.3 ± 0.1	i
	F$_-$	133.0 / 128	36	1.96 ± 0.08	24.1 (f)	3 ± 2	$0.8^{+0.4}_{-0.1}$	$2.1^{+2.1}_{-0.9}$	43.2 ± 0.2	e, i
IRAS 07378−3136	C	247.4 / 231	22	1.32 ± 0.05	23.29 ± 0.05	—	0.28 ± 0.05	—	43.43 ± 0.02	—
	F	229.8 / 230	49	1.7 ± 0.1	23.38 ± 0.06	(< 2)	0.22 ± 0.05	$1.6^{+0.8}_{-0.6}$	43.15 ± 0.09	—

Continued on the next page...

Target Name	Model	χ^2 / d.o.f.	$p_{\rm null}$	Γ	$\log N_{\rm H}/{\rm cm}^{-2}$	$f_{\rm sca}$	$EW_{\rm Fe\,K\alpha}$	$R_{\rm pex}$	$\log L^{\rm int}_{[10,50]}$	Notes
	(1)	(2)	(3)	(4)	(5)	(6)	(7)	(8)	(9)	(10)
	F_	232.4 / 231	46	1.6 (f)	23.34 ± 0.04	(< 2)	0.25 ± 0.05	1.0 ± 0.2	43.24 ± 0.04	—
UGC 3995 A	D	217.1 / 191	10	1.35 ± 0.06	23.54 ± 0.04	1.4 ± 0.6	—	—	43.10 ± 0.02	h
	F	169.5 / 189	84	1.74 ± 0.08	23.59 ± 0.06	0.7 ± 0.5	0.15 ± 0.05	$2.0^{+0.7}_{-0.5}$	42.75 ± 0.08	h
	F_	172.8 / 188	78	1.6 (f)	23.54 ± 0.04	$1.3^{+0.8}_{-0.6}$	0.16 ± 0.05	1.4 ± 0.3	42.83 ± 0.05	h
2MASX J0756 ...	A	49.8 / 46	32	1.57 ± 0.09	—	—	—	—	42.24 ± 0.05	d, h
	F_	41.6 / 50	80	2.1 ± 0.4	22.1 ± 0.4	—	$0.1^{+0.2}_{-u}$	3 ± 2	$41.9^{+0.2}_{-0.6}$	c, d
	F_	38.4 / 44	71	1.7 (f)	21.9 ± 0.3	—	0.2 ± 0.1	0.5 ± 0.4	42.16 ± 0.04	c, d
Mrk 1210	**F**	290.7 / 287	43	1.88 ± 0.05	23.43 ± 0.03	1.7 ± 0.4	0.11 ± 0.03	1.6 ± 0.3	43.00 ± 0.04	—
	F_	296.2 / 275	18	1.7 (f)	23.37 ± 0.02	2.4 ± 0.4	0.14 ± 0.03	0.9 ± 0.1	43.10 ± 0.02	—
MCG −01-22-006	B	376.8 / 371	41	1.42 ± 0.03	23.26 ± 0.03	—	—	—	43.56 ± 0.02	—
	F	353.8 / 368	69	1.56 ± 0.06	23.30 ± 0.03	0.6 ± 0.3	0.06 ± 0.03	0.4 ± 0.2	43.46 ± 0.04	—
CGCG 150-014 ..	D	114.3 / 107	30	1.6 ± 0.1	23.75 ± 0.05	$2.4^{+1.5}_{-0.9}$	—	—	44.07 ± 0.03	—
	F	105.6 / 105	47	1.7 ± 0.2	23.77 ± 0.07	2 ± 2	0.2 ± 0.1	0.3 ± 0.4	43.99 ± 0.09	—
MCG +11-11-032	B	67.3 / 67	47	1.57 ± 0.08	23.03 ± 0.09	—	—	—	43.85 ± 0.03	h
	F_	61.1 / 65	61	1.9 ± 0.2	23.07 ± 0.09	(< 1)	$0.04^{+0.09}_{-u}$	$1.4^{+1.3}_{-0.8}$	43.6 ± 0.1	h
	F_	53.4 / 59	68	1.8 (f)	23.05 ± 0.07	(< 1)	$0.05^{+0.09}_{-u}$	1.1 ± 0.4	43.68 ± 0.05	c
Mrk 18	B	75.9 / 66	19	1.7 ± 0.1	$23.12^{+0.09}_{-0.11}$	—	—	—	42.06 ± 0.04	—
	F	68.3 / 63	30	1.6 ± 0.2	23.1 ± 0.1	2^{+3}_{-1}	0.2 ± 0.1	$0.1^{+0.6}_{-u}$	$42.03^{+0.06}_{-0.10}$	—

Continued on the next page...

Target Name	Model	χ^2 / d.o.f.	$p_{\rm null}$	Γ	$\log N_{\rm H}/{\rm cm}^{-2}$	$f_{\rm sca}$	$EW_{\rm Fe\,K\alpha}$	$R_{\rm pex}$	$\log L^{\rm int}_{[10,50]}$	Notes
	(1)	(2)	(3)	(4)	(5)	(6)	(7)	(8)	(9)	(10)
2MASX J0903 ...	**F**	62.1 / 58	33	1.8 ± 0.2	23.6 ± 0.2	1^{+2}_{-u}	0.2 ± 0.1	3^{+4}_{-2}	43.8 ± 0.3	i
2MASX J0911 ...	B	123.7 / 137	78	1.68 ± 0.06	23.46 ± 0.04	—	—	—	43.40 ± 0.02	—
	$\mathbf{F}_-$	120.9 / 135	80	$1.75^{+0.12}_{-0.08}$	23.50 ± 0.05	$0.7^{+0.7}_{-0.5}$	(< 0.03)	$0.1^{+0.3}_{-u}$	$43.38^{+0.03}_{-0.06}$	—
IC 2461	B	261.6 / 250	29	1.65 ± 0.04	22.84 ± 0.05	—	—	—	42.04 ± 0.02	—
	$\mathbf{F}_-$	243.4 / 248	57	1.8 ± 0.1	22.86 ± 0.06	(< 0.3)	0.12 ± 0.04	0.7 ± 0.4	41.92 ± 0.06	—
MCG −01-24-012	D	344.2 / 330	28	1.80 ± 0.02	22.91 ± 0.03	0.3 ± 0.2	—	—	43.53 ± 0.02	—
	F	300.7 / 328	86	2.07 ± 0.06	22.97 ± 0.03	$0.1^{+0.1}_{-u}$	0.04 ± 0.02	1.3 ± 0.4	43.34 ± 0.04	—
2MASX J0923 ...	E	95.2 / 87	26	1.4 ± 0.2	23.76 ± 0.07	2 ± 1	0.11 ± 0.09	—	44.01 ± 0.03	b, c
	F	84.0 / 86	54	1.9 ± 0.2	23.89 ± 0.09	$0.2^{+0.5}_{-u}$	$0.06^{+0.08}_{-u}$	0.8 ± 0.4	43.83 ± 0.09	b, c
NGC 2992	B	723.5 / 723	49	1.695 ± 0.008	22.02 ± 0.01	—	—	—	43.14 ± 0.02	h
	F	655.9 / 720	96	1.72 ± 0.02	22.04 ± 0.02	0.7 ± 0.3	0.08 ± 0.01	0.13 ± 0.07	43.11 ± 0.02	h
NGC 3079	E	130.0 / 107	6	1.79 ± 0.07	24.41 ± 0.03	$0.41^{+0.11}_{-0.08}$	0.7 ± 0.3	—	42.68 ± 0.07	e
	$\mathbf{F}_+$	103.5 / 103	47	2.0 ± 0.1	24.52 ± 0.04	$0.07^{+0.06}_{-0.04}$	0.4 ± 0.3	$0.021^{+0.009}_{-0.006}$	42.9 ± 0.1	e, f
	$F_\pm$	107.2 / 104	39	1.8 (f)	24.46 ± 0.03	0.18 ± 0.07	0.4 ± 0.2	0.04 ± 0.01	42.9 ± 0.1	e, f
ESO 263-G013 ...	D	137.8 / 142	58	1.72 ± 0.08	23.87 ± 0.04	1.5 ± 0.5	—	—	43.80 ± 0.03	—
	F	136.3 / 140	57	1.73 ± 0.08	23.87 ± 0.04	1.3 ± 0.7	$0.06^{+0.07}_{-u}$	$0.1^{+0.1}_{-u}$	$43.77^{+0.04}_{-0.06}$	—
NGC 3281	$\mathbf{F}_-$	217.3 / 200	19	1.62 ± 0.03	24.1 ± 0.1	(< 0.1)	$1.1^{+0.8}_{-0.1}$	4^{+4}_{-2}	42.5 ± 0.3	e
	F_+	190.1 / 198	64	2.01 ± 0.09	24.13 ± 0.06	$0.05^{+0.12}_{-u}$	$1.0^{+0.3}_{-0.1}$	2.4 ± 0.7	42.86 ± 0.09	e, g

Continued on the next page...

Target Name	Model	χ^2 / d.o.f.	$p_{\rm null}$	Γ	$\log N_{\rm H}/{\rm cm}^{-2}$	$f_{\rm sca}$	$EW_{\rm Fe\,K\alpha}$	$R_{\rm pex}$	$\log L^{\rm int}_{[10,50]}$	Notes
	(1)	(2)	(3)	(4)	(5)	(6)	(7)	(8)	(9)	(10)
MCG +12-10-067	B	154.4 / 142	23	1.60 ± 0.07	23.15 ± 0.07	—	—	—	43.25 ± 0.03	—
	F	130.4 / 139	69	1.9 ± 0.2	23.24 ± 0.07	$1.8^{+1.1}_{-0.8}$	0.08 ± 0.06	$1.4^{+1.0}_{-0.7}$	$43.02^{+0.09}_{-0.11}$	—
MCG +06-24-008	B	153.7 / 156	54	1.56 ± 0.04	22.55 ± 0.08	—	—	—	42.99 ± 0.02	—
	F$_-$	149.2 / 154	59	1.56 ± 0.05	$22.60^{+0.08}_{-0.10}$	1.1 ± 0.9	0.09 ± 0.05	(< 0.1)	42.99 ± 0.02	i
UGC 5881	B	110.7 / 98	18	1.45 ± 0.08	22.9 ± 0.1	—	—	—	42.74 ± 0.03	h
	F	97.4 / 95	41	1.6 ± 0.2	23.0 ± 0.1	4 ± 3	0.14 ± 0.08	$0.7^{+0.8}_{-0.5}$	$42.60^{+0.09}_{-0.11}$	h
	F$_-$	91.8 / 89	40	1.7 (f)	23.02 ± 0.09	3 ± 2	0.13 ± 0.08	1.1 ± 0.4	42.55 ± 0.05	c
NGC 3393	E	83.1 / 81	41	2.0 ± 0.1	24.38 ± 0.04	$0.28^{+0.10}_{-0.08}$	0.9 ± 0.5	—	43.67 ± 0.08	e
	F$_+$	58.0 / 78	96	1.9 ± 0.1	24.38 ± 0.05	$0.2^{+0.2}_{-0.1}$	0.7 ± 0.4	0.03 ± 0.02	$43.62^{+0.11}_{-0.09}$	e, f
Mrk 728	A	180.6 / 192	71	1.55 ± 0.03	—	—	—	—	43.09 ± 0.02	a, d
	F$_-$	169.5 / 190	86	1.59 ± 0.05	< 22.3	—	0.08 ± 0.05	(< 0.2)	43.34 ± 0.02	a, d
2MASX J1136 ...	A	297.7 / 263	7	1.76 ± 0.03	—	—	—	—	42.56 ± 0.02	d
	F$_-$	271.6 / 260	30	$2.00^{+0.09}_{-0.07}$	20.6 ± 0.6	—	0.11 ± 0.04	$1.5^{+0.7}_{-0.5}$	42.37 ± 0.07	d
NGC 3786	B	60.7 / 60	45	1.56 ± 0.07	22.2 ± 0.2	—	—	—	41.64 ± 0.04	h
	F	56.4 / 57	50	1.8 ± 0.2	$22.5^{+0.2}_{-0.4}$	7^{+7}_{-u}	$0.14^{+0.10}_{-0.11}$	$0.7^{+1.2}_{-0.6}$	41.5 ± 0.1	h
NGC 3822	A	112.0 / 118	64	1.62 ± 0.04	—	—	—	—	42.67 ± 0.03	d
	F$_-$	96.9 / 115	89	$1.69^{+0.10}_{-0.07}$	21.2 ± 0.2	—	0.15 ± 0.07	$0.2^{+0.5}_{-u}$	$42.63^{+0.05}_{-0.08}$	d
IC 751	D	67.5 / 65	39	1.5 ± 0.1	23.60 ± 0.08	7 ± 4	—	—	43.08 ± 0.04	—

Continued on the next page...

Target Name	Model	χ^2 / d.o.f.	$p_{\rm null}$	Γ	$\log N_{\rm H}/{\rm cm}^{-2}$	$f_{\rm sca}$	$EW_{\rm Fe\,K\alpha}$	$R_{\rm pex}$	$\log L^{\rm int}_{[10,50]}$	Notes
	(1)	(2)	(3)	(4)	(5)	(6)	(7)	(8)	(9)	(10)
	F	63.2 / 63	47	1.6 ± 0.2	23.58 ± 0.09	6 ± 4	$0.1^{+0.1}_{-u}$	$0.8^{+0.9}_{-0.5}$	42.9 ± 0.1	—
2MASX J1205 ...	A	128.4 / 119	26	1.71 ± 0.05	—	—	—	—	43.41 ± 0.03	d
	F$_-$	114.0 / 117	56	1.92 ± 0.08	(< 20.0)	—	0.09 ± 0.08	$1.7^{+0.8}_{-0.6}$	43.22 ± 0.07	d
B2 1204+34	B	185.4 / 211	90	1.65 ± 0.03	22.47 ± 0.06	—	—	—	44.16 ± 0.01	—
	F	178.3 / 208	93	$1.69^{+0.08}_{-0.06}$	22.52 ± 0.06	1.6 ± 0.8	0.05 ± 0.04	$0.1^{+0.3}_{-u}$	$44.13^{+0.03}_{-0.05}$	—
IRAS 12074−4619	E	174.4 / 182	64	1.67 ± 0.04	21.5 ± 0.2	20^{+9}_{-19}	0.33 ± 0.07	—	$43.05^{+0.07}_{-0.04}$	d
	F	170.1 / 181	71	1.8 ± 0.1	21.6 ± 0.1	18 ± 9	0.32 ± 0.07	$1.0^{+0.8}_{-0.6}$	42.94 ± 0.08	d
WAS 49	D	101.2 / 95	31	1.62 ± 0.08	23.43 ± 0.06	4 ± 2	—	—	43.90 ± 0.03	—
	F	95.1 / 93	42	1.8 ± 0.2	23.44 ± 0.07	3 ± 2	0.12 ± 0.08	$0.8^{+0.9}_{-0.6}$	43.7 ± 0.1	—
NGC 4388	**F**	347.1 / 312	8	1.70 ± 0.02	23.67 ± 0.02	6.8 ± 0.6	0.30 ± 0.03	0.09 ± 0.06	42.94 ± 0.02	a, h
NGC 4395	B	306.2 / 309	54	1.48 ± 0.02	22.57 ± 0.04	—	—	—	40.78 ± 0.01	—
	F	280.4 / 306	85	1.64 ± 0.06	22.66 ± 0.05	1.6 ± 0.6	0.07 ± 0.03	0.6 ± 0.3	40.66 ± 0.04	—
LEDA 170194	B	152.9 / 144	29	1.69 ± 0.05	22.69 ± 0.07	—	—	—	43.27 ± 0.02	—
	F	130.9 / 141	72	$1.72^{+0.09}_{-0.07}$	22.75 ± 0.07	4 ± 2	0.19 ± 0.06	0.2 ± 0.3	43.23 ± 0.05	—
NGC 4941	E	61.1 / 59	40	1.7 ± 0.2	24.13 ± 0.06	$1.6^{+0.7}_{-0.4}$	$1.0^{+0.6}_{-0.4}$	—	41.89 ± 0.07	e
	F	59.1 / 58	44	1.7 ± 0.2	24.14 ± 0.07	$1.0^{+0.8}_{-0.5}$	$0.9^{+0.6}_{-0.3}$	$0.21^{+0.19}_{-0.15}$	41.8 ± 0.1	e
NGC 4992	**F**$_-$	266.6 / 240	11	1.57 ± 0.05	23.63 ± 0.03	(< 0.1)	0.18 ± 0.05	0.7 ± 0.2	43.53 ± 0.05	b

Continued on the next page...

Target Name	Model	χ^2 / d.o.f.	$p_{\rm null}$	Γ	$\log N_{\rm H}/{\rm cm}^{-2}$	$f_{\rm sca}$	$EW_{\rm Fe\,K\alpha}$	$R_{\rm pex}$	$\log L^{\rm int}_{[10,50]}$	Notes
	(1)	(2)	(3)	(4)	(5)	(6)	(7)	(8)	(9)	(10)
Mrk 248	B	180.0 / 170	29	1.71 ± 0.04	22.94 ± 0.05	—	—	—	43.76 ± 0.02	—
	F	154.9 / 167	74	2.0 ± 0.1	23.03 ± 0.05	0.3 ± 0.2	0.07 ± 0.04	1.2 ± 0.6	43.57 ± 0.07	—
ESO 509-IG066 ..	B	232.0 / 228	41	1.58 ± 0.04	22.84 ± 0.06	—	—	—	43.79 ± 0.01	—
	F	203.2 / 225	85	1.7 ± 0.1	22.89 ± 0.07	1.3 ± 0.8	0.18 ± 0.05	$0.5^{+0.5}_{-0.4}$	43.69 ± 0.07	—
NGC 5252	B	310.5 / 294	24	1.68 ± 0.02	22.60 ± 0.06	—	—	—	43.50 ± 0.02	a, h
	$\mathbf{F}_-$	299.8 / 293	38	1.66 ± 0.02	22.55 ± 0.07	—	0.08 ± 0.03	(< 0.03)	43.50 ± 0.02	a, h
NGC 5273	**F**	554.7 / 535	27	1.80 ± 0.05	22.43 ± 0.04	3.6 ± 0.6	0.11 ± 0.02	1.1 ± 0.3	41.86 ± 0.03	h
2MASX J1410 ...	$\mathbf{F}_-$	138.0 / 122	15	1.9 ± 0.2	22.95 ± 0.09	(< 0.5)	(< 0.1)	$1.5^{+1.1}_{-0.7}$	43.0 ± 0.1	b
NGC 5643	F_+	120.8 / 115	34	1.7 ± 0.1	23.9 ± 0.2	10^{+10}_{-5}	$1.3^{+0.9}_{-0.2}$	3 ± 2	41.1 ± 0.3	e, f
	$\mathbf{F}_\pm$	125.8 / 116	25	1.9 ± 0.1	24.5 (f)	$2.1^{+4.2}_{-1.6}$	$1.3^{+1.4}_{-0.4}$	1.2 ± 0.8	41.5 ± 0.4	e, f
NGC 5674	B	280.6 / 262	21	1.75 ± 0.03	22.59 ± 0.04	—	—	—	43.36 ± 0.02	h
	F	244.1 / 259	74	1.87 ± 0.09	22.66 ± 0.05	1.4 ± 0.5	0.15 ± 0.04	0.5 ± 0.4	43.28 ± 0.06	h
NGC 5728	$\mathbf{F}_+$	271.0 / 269	46	1.64 ± 0.05	24.14 ± 0.02	$0.05^{+0.10}_{-u}$	0.39 ± 0.07	0.17 ± 0.04	43.34 ± 0.03	e, f
	F_+	262.1 / 268	59	1.79 ± 0.08	24.14 ± 0.02	$0.07^{+0.08}_{-u}$	0.36 ± 0.07	0.36 ± 0.09	43.32 ± 0.03	e, f, g
CGCG 164-019 ..	D	56.4 / 57	50	1.5 ± 0.2	24.0 ± 0.1	8 ± 4	—	—	43.19 ± 0.09	e
	F	41.0 / 55	92	1.7 ± 0.2	23.7 ± 0.4	7^{+13}_{-5}	0.4 ± 0.3	5^{+u}_{-4}	$42.4^{+0.4}_{-0.6}$	e
	$\mathbf{F}_-$	43.0 / 56	90	1.9 ± 0.2	24.3 (f)	2^{+14}_{-2}	$0.4^{+0.5}_{-0.2}$	3^{+u}_{-2}	42.8 ± 0.5	e

Continued on the next page...

Target Name	Model	χ^2 / d.o.f.	$p_{\rm null}$	Γ	$\log N_{\rm H}/{\rm cm}^{-2}$	$f_{\rm sca}$	$EW_{\rm Fe\,K\alpha}$	$R_{\rm pex}$	$\log L^{\rm int}_{[10,50]}$	Notes
	(1)	(2)	(3)	(4)	(5)	(6)	(7)	(8)	(9)	(10)
IC 4518A	**F**$_-$	126.3 / 131	60	2.00 ± 0.09	23.23 ± 0.06	1.5 ± 0.6	(< 0.1)	$2.9^{+1.2}_{-0.8}$	42.69 ± 0.09	—
	F$_-$	139.4 / 123	15	1.6 (f)	23.14 ± 0.05	$3.8^{+1.0}_{-0.8}$	0.07 ± 0.06	0.7 ± 0.2	42.95 ± 0.04	—
2MASX J1506 ...	B	78.5 / 95	89	1.69 ± 0.06	22.30 ± 0.09	—	—	—	43.02 ± 0.03	h, i
	F$_-$	78.5 / 95	89	1.69 ± 0.06	22.30 ± 0.08	(< 2.0)	(< 0.1)	(< 0.3)	43.01 ± 0.03	h, i
NGC 5899	E	247.1 / 241	38	1.63 ± 0.04	22.90 ± 0.04	0.6 ± 0.4	0.16 ± 0.04	—	42.42 ± 0.02	—
	F	228.7 / 240	69	1.90 ± 0.08	22.98 ± 0.04	$0.25^{+0.26}_{-0.23}$	0.13 ± 0.04	$1.1^{+0.5}_{-0.3}$	42.24 ± 0.05	—
MCG +11-19-006	D	87.5 / 75	15	1.45 ± 0.09	23.24 ± 0.09	$1.6^{+1.1}_{-0.8}$	—	—	43.54 ± 0.03	—
	F	85.4 / 73	15	1.6 ± 0.1	23.25 ± 0.09	$1.3^{+1.1}_{-0.7}$	< 0.1	$0.5^{+0.6}_{-0.4}$	$43.44^{+0.08}_{-0.10}$	—
MCG −01-40-001	D	195.7 / 213	80	1.62 ± 0.04	22.81 ± 0.06	6 ± 1	—	—	43.12 ± 0.02	—
	F	159.8 / 211	100	1.79 ± 0.09	22.81 ± 0.06	4 ± 1	0.20 ± 0.04	0.9 ± 0.5	42.98 ± 0.06	—
NGC 5995	**F**	396.2,/ 394	46	1.98 ± 0.05	22.08 ± 0.04	2.7 ± 0.8	0.17 ± 0.02	1.1 ± 0.3	43.35 ± 0.04	b
MCG +14-08-004	B	99.1 / 102	56	1.73 ± 0.08	23.18 ± 0.07	—	—	—	42.88 ± 0.03	h
	F$_-$	92.0 / 100	70	$1.70^{+0.13}_{-0.09}$	23.14 ± 0.08	(< 0.7)	0.19 ± 0.08	$0.1^{+0.4}_{-u}$	$42.86^{+0.04}_{-0.08}$	h
Mrk 1498	**F**$_+$	314.5 / 287	13	1.82 ± 0.05	23.33 ± 0.04	1.0 ± 0.3	$0.02^{+0.03}_{-u}$	0.4 ± 0.2	44.29 ± 0.04	b, f
IRAS 16288+3929	B	60.0 / 70	80	1.8 ± 0.1	23.81 ± 0.06	—	—	—	43.44 ± 0.04	—
	F	54.5 / 67	86	1.8 ± 0.2	23.83 ± 0.06	$0.4^{+0.5}_{-0.3}$	0.2 ± 0.1	$0.03^{+0.23}_{-0.03}$	$43.45^{+0.05}_{-0.08}$	—
NGC 6240	F	346.0 / 322	17	1.67 ± 0.05	24.12 ± 0.02	1.7 ± 0.3	0.26 ± 0.05	0.14 ± 0.05	44.09 ± 0.03	e

Continued on the next page...

Target Name	Model (1)	χ^2 / d.o.f. (2)	$p_{\rm null}$ (3)	Γ (4)	$\log N_{\rm H}/{\rm cm}^{-2}$ (5)	$f_{\rm sca}$ (6)	$EW_{\rm Fe\,K\alpha}$ (7)	$R_{\rm pex}$ (8)	$\log L^{\rm int}_{[10,50]}$ (9)	Notes (10)
	$\mathbf{F}_{\pm}$	313.1 / 320	60	1.71 ± 0.05	24.10 ± 0.02	(< 0.1)	0.15 ± 0.04	0.26 ± 0.07	$44.03^{+0.04}_{-0.02}$	e, f, g
NGC 6300	$\mathbf{F}_{-}$	339.0 / 304	8	1.90 ± 0.03	23.23 ± 0.02	(< 0.05)	0.04 ± 0.02	1.5 ± 0.2	42.11 ± 0.02	—
MCG +07-37-031	D	212.2 / 195	19	1.60 ± 0.03	22.56 ± 0.06	2.9 ± 0.8	—	—	43.98 ± 0.01	h
	F	204.1 / 193	28	1.68 ± 0.07	22.56 ± 0.06	2.6 ± 0.8	0.08 ± 0.04	0.4 ± 0.3	43.92 ± 0.05	h
2MASX J1824 ...	B	178.6 / 166	24	1.45 ± 0.05	23.01 ± 0.07	—	—	—	44.04 ± 0.02	—
	F	152.2 / 163	72	1.8 ± 0.1	23.09 ± 0.07	$1.0^{+1.1}_{-0.9}$	0.16 ± 0.06	$1.4^{+0.8}_{-0.6}$	43.81 ± 0.09	—
IC 4709	$\mathbf{F}_{-}$	216.6 / 218	51	1.93 ± 0.07	23.42 ± 0.05	(< 0.4)	0.15 ± 0.04	2.1 ± 0.6	42.84 ± 0.06	—
	F_{-}	226.1 / 219	36	1.7 (f)	23.34 ± 0.03	(< 0.4)	0.19 ± 0.04	1.0 ± 0.2	42.98 ± 0.03	—
LEDA 3097193 ..	B	398.2 / 395	44	1.79 ± 0.02	22.93 ± 0.03	—	—	—	43.45 ± 0.02	h
	$\mathbf{F}_{-}$	378.0 / 393	70	1.83 ± 0.06	22.93 ± 0.03	(< 0.1)	0.10 ± 0.02	$0.20^{+0.20}_{-0.16}$	43.41 ± 0.04	h
ESO 103-G035 ...	F_{-}	352.8 / 350	45	1.97 ± 0.02	23.33 ± 0.01	(< 0.01)	0.08 ± 0.01	1.2 ± 0.1	43.32 ± 0.02	—
	$\mathbf{F}_{\pm}$	327.9 / 349	78	1.78 ± 0.05	23.27 ± 0.02	(< 0.02)	0.11 ± 0.01	1.0 ± 0.1	43.35 ± 0.02	g
ESO 231-G026 ...	B	194.9 / 238	98	1.56 ± 0.05	23.32 ± 0.03	—	—	—	44.19 ± 0.01	—
	F	186.8 / 235	99	1.6 ± 0.1	23.33 ± 0.04	$0.2^{+0.4}_{-u}$	0.09 ± 0.04	$0.23^{+0.26}_{-0.21}$	44.14 ± 0.06	—
2MASX J1926 ...	A	88.0 / 94	65	1.78 ± 0.05	—	—	—	—	$43.41^{+0.01}_{-0.03}$	d, h
	$\mathbf{F}_{-}$	76.8 / 91	86	1.9 ± 0.1	< 21.1	—	0.13 ± 0.08	$1.0^{+1.0}_{-0.6}$	$43.39^{+0.09}_{-0.12}$	d, h
2MASX J1947 ...	B	260.5 / 255	39	1.73 ± 0.04	22.89 ± 0.04	—	—	—	44.01 ± 0.01	—

Continued on the next page...

Target Name	Model	χ^2 / d.o.f.	$p_{\rm null}$	Γ	$\log N_{\rm H}/{\rm cm}^{-2}$	$f_{\rm sca}$	$EW_{\rm Fe\,K\alpha}$	$R_{\rm pex}$	$\log L^{\rm int}_{[10,50]}$	Notes
	(1)	(2)	(3)	(4)	(5)	(6)	(7)	(8)	(9)	(10)
	F$_-$	246.7 / 253	60	1.88 ± 0.09	22.91 ± 0.05	(< 0.4)	0.09 ± 0.04	0.7 ± 0.4	43.89 ± 0.06	—
3C 403	B	179.9 / 184	57	1.56 ± 0.06	23.41 ± 0.04	—	—	—	44.10 ± 0.02	—
	F	168.0 / 181	75	$1.54^{+0.11}_{-0.06}$	23.41 ± 0.05	1^{+1}_{-u}	0.17 ± 0.06	$0.05^{+0.23}_{-u}$	$44.08^{+0.03}_{-0.05}$	—
2MASX J2006 ...	B	108.6 / 116	68	1.72 ± 0.08	23.31 ± 0.05	—	—	—	43.47 ± 0.02	—
	F$_-$	101.9 / 114	78	1.9 ± 0.1	23.40 ± 0.06	$1.2^{+0.9}_{-0.7}$	(< 0.1)	0.6 ± 0.5	43.36 ± 0.08	—
2MASX J2018 ...	E	255.5 / 254	46	1.42 ± 0.04	23.08 ± 0.06	1^{+3}_{-u}	0.19 ± 0.04	—	42.97 ± 0.02	—
	F$_-$	240.7 / 254	72	1.70 ± 0.09	23.14 ± 0.05	(< 3)	0.15 ± 0.04	1.0 ± 0.4	42.80 ± 0.06	—
2MASX J2021 ...	C	144.2 / 134	26	1.36 ± 0.06	22.7 ± 0.1	—	0.20 ± 0.07	—	42.71 ± 0.02	—
	F$_-$	134.2 / 134	48	1.8 ± 0.1	22.9 ± 0.1	(< 0.08)	0.15 ± 0.07	$1.7^{+1.2}_{-0.8}$	42.7 ± 0.1	—
NGC 6921	E	56.1 / 72	92	1.80 ± 0.07	$24.17^{+0.05}_{-0.03}$	0.4 ± 0.3	1.2 ± 0.5	—	$43.22^{+0.08}_{-0.06}$	e, h
	F	45.9 / 71	99	1.82 ± 0.07	24.22 ± 0.04	$0.18^{+0.13}_{-0.08}$	1.0 ± 0.4	0.11 ± 0.05	43.20 ± 0.08	e, h
MCG +04-48-002	E	80.5 / 76	34	1.73 ± 0.06	24.00 ± 0.05	1.9 ± 0.6	0.4 ± 0.1	—	42.95 ± 0.05	e, h
	F	70.3 / 75	63	$1.67^{+0.07}_{-0.05}$	23.90 ± 0.07	$0.5^{+0.7}_{-u}$	0.3 ± 0.1	0.7 ± 0.3	$42.69^{+0.09}_{-0.10}$	h
IC 5063	E	325.8 / 289	7	1.57 ± 0.03	23.38 ± 0.02	1.0 ± 0.2	0.14 ± 0.03	—	43.18 ± 0.02	—
	F	291.6 / 288	43	1.80 ± 0.05	23.42 ± 0.03	0.5 ± 0.2	0.12 ± 0.03	0.8 ± 0.2	43.02 ± 0.03	—
2MASX J2119 ...	B	298.6 / 334	92	1.79 ± 0.02	21.45 ± 0.04	—	—	—	43.90 ± 0.02	d
	F$_-$	285.6 / 332	97	1.84 ± 0.05	21.47 ± 0.05	—	0.10 ± 0.03	0.3 ± 0.2	43.85 ± 0.03	d

Continued on the next page...

Target Name	Model	χ^2 / d.o.f.	$p_{\rm null}$	Γ	$\log N_{\rm H}/{\rm cm}^{-2}$	$f_{\rm sca}$	$EW_{\rm Fe\,K\alpha}$	$R_{\rm pex}$	$\log L^{\rm int}_{[10,50]}$	Notes
	(1)	(2)	(3)	(4)	(5)	(6)	(7)	(8)	(9)	(10)
NGC 7130	E	45.5 / 35	11	2.1 ± 0.2	24.54 ± 0.06	$0.20^{+0.15}_{-0.09}$	$1.8^{+1.8}_{-1.3}$	—	43.7 ± 0.2	e
	$\mathbf{F}_-$	37.9 / 33	26	1.8 ± 0.3	24.5 (f)	0.3 ± 0.2	$1.4^{+1.2}_{-1.0}$	$0.02^{+0.04}_{-0.02}$	$43.50^{+0.08}_{-0.11}$	e, f
MCG +06-49-019	A	73.7 / 63	17	1.57 ± 0.06	—	—	—	—	42.30 ± 0.04	d, h
	$\mathbf{F}_-$	64.4 / 62	39	1.7 (f)	(< 21.0)	—	0.5 ± 0.2	$0.33^{+0.35}_{-0.31}$	42.19 ± 0.03	d, h
NGC 7319	E	43.7 / 40	32	1.6 ± 0.1	23.92 ± 0.08	5 ± 2	0.4 ± 0.2	—	$42.99^{+0.09}_{-0.07}$	h
	$\mathbf{F}_\pm$	37.8 / 40	57	1.8 (f)	$23.78^{+0.07}_{-0.09}$	(< 4)	0.3 ± 0.2	$1.3^{+1.4}_{-0.8}$	42.6 ± 0.2	f, h
MCG +01-57-016	A	255.7 / 232	14	$1.68^{+0.02}_{-0.04}$	—	—	—	—	42.83 ± 0.02	d
	$\mathbf{F}_-$	224.0 / 229	58	1.85 ± 0.05	< 20.1	—	0.08 ± 0.04	1.3 ± 0.4	42.85 ± 0.04	d
NGC 7582	$\mathbf{F}_+$	294.8 / 299	56	1.76 ± 0.04	23.45 ± 0.05	$1.8^{+1.0}_{-0.9}$	0.25 ± 0.04	5 ± 1	41.85 ± 0.07	f
2MASX J2330 ...	B	71.9 / 82	78	1.55 ± 0.08	22.7 ± 0.1	—	—	—	43.22 ± 0.03	—
	F	71.1 / 79	72	1.7 ± 0.2	22.9 ± 0.2	3^{+3}_{-u}	$0.02^{+0.08}_{-u}$	$0.3^{+0.7}_{-u}$	$43.15^{+0.08}_{-0.11}$	—
PKS 2331-240 ...	B	403.9 / 373	13	1.82 ± 0.02	20.84 ± 0.07	—	—	—	43.93 ± 0.01	d, h
	$\mathbf{F}_-$	392.6 / 372	22	1.81 ± 0.02	20.83 ± 0.07	—	0.10 ± 0.03	(< 0.013)	43.93 ± 0.01	d, h
PKS 2356-61	B	155.6 / 161	61	1.65 ± 0.06	23.10 ± 0.06	—	—	—	44.33 ± 0.02	—
	F	127.8 / 158	96	1.8 ± 0.1	23.15 ± 0.06	$2.1^{+1.0}_{-0.8}$	0.15 ± 0.06	0.6 ± 0.5	44.21 ± 0.07	—

Continued on the next page...

Target Name	Model	χ^2/ d.o.f.	$p_{\rm null}$	Γ	$\log N_{\rm H}/{\rm cm}^{-2}$	$f_{\rm sca}$	$EW_{\rm Fe\,K\alpha}$	$R_{\rm pex}$	$\log L^{\rm int}_{[10,50]}$	Notes
	(1)	(2)	(3)	(4)	(5)	(6)	(7)	(8)	(9)	(10)

Notes: For each source we list the simplest statistically acceptable model ($p_{\rm null} > 5\,\%$) in the first row. Full model fits used in population analysis are marked with boldface font in the second column. For sources with ambiguous spectra, we also include additional fits discussed in the text. Uncertainties and limits are given as $1\,\sigma$ (68 % confidence interval, i.e. $\Delta\chi^2 = 1$ from the best fit); limits in parentheses are derived as described in § 5.3.2, and are considered equivalent to limits produced by `Xspec`. Fixed parameters are marked with (f) following the parameter value. Columns: (1) model, as listed in Table 5.2; (2) χ^2 and the number of degrees of freedom; (3) null-hypothesis probability in percent; (4) intrinsic continuum photon index, assuming $E_{\rm cut} = 300\,{\rm keV}$; (5) logarithm of the line-of-sight column density in ${\rm cm}^{-2}$; (6) relative normalization of the Thomson-scattered continuum in percent; (7) observed equivalent width of the Fe Kα line (fixed at 6.4 keV) in keV; (8) reprocessed continuum relative normalization from `pexrav`; (9) logarithm of the intrinsic continuum luminosity in the 10–50 keV band; (10) notes (see text and § A for details): (a) *Swift*/XRT data not available; (b) part of *NuSTAR* data ignored; (c) *Swift*/BAT data partly or fully ignored; (d) candidate unobscured source; (e) candidate Compton-thick source; (f) `mekal` component included in fit; (h) non-unity cross-normalization factor(s);

Table C4: Spectral parameters obtained from fitting the coupled and the decoupled `borus02` models

Target Name	Model [a]	χ^2 / d.o.f.	$p_{\rm null}$ / %	Γ	$\log N_{\rm H,los}/{\rm cm}^{-2}$ [b]	$\log N_{\rm H,tor}/{\rm cm}^{-2}$	$\theta_{\rm inc}$ / deg. [c]
LEDA 136991	C	68.69 / 67	42	2.0 ± 0.1	$24.3^{+0.3}_{-0.1}$	$24.86^{+0.03}_{-0.09}$	$60.60^{+1.09}_{-0.09}$
	D	64.88 / 69	61	$1.75^{+0.11}_{-0.07}$	24.27 ± 0.04	23.1 ± 0.1	O
NGC 262	C	518.29 / 464	4	1.767 ± 0.006	$23.38^{+0.03}_{-0.05}$	24.26 ± 0.01	60.18 ± 0.03
	D	506.08 / 465	9.0	1.63 ± 0.03	22.94 ± 0.02	$24.10^{+0.06}_{-0.09}$	O
ESO 195-IG021 ..	C	227.66 / 249	83	1.87 ± 0.02	$23.1^{+0.2}_{-0.6}$	$24.02^{+0.23}_{-0.03}$	60.1 ± 0.1
	D	227.48 / 251	85	1.89 ± 0.05	22.63 ± 0.05	24.1 ± 0.2	U
NGC 454 E	C	57.36 / 80	97	1.6 ± 0.2	$23.9^{+0.5}_{-0.2}$	$23.80^{+0.53}_{-0.05}$	87^{+3}_{-18}
	D	56.36 / 81	98	$1.6^{+0.3}_{-0.1}$	23.85 ± 0.07	$24.1^{+0.6}_{-0.3}$	O
MCG +08-03-018	C	104.42 / 126	92	$2.36^{+0.06}_{-0.11}$	24.1 ± 0.2	24.69 ± 0.03	$60.6^{+0.8}_{-0.2}$
	D	99.85 / 129	97	2.3 ± 0.1	$24.05^{+0.03}_{-0.05}$	23.2 ± 0.1	U
NGC 513	C	125.01 / 140	81	1.68 ± 0.03	$23.49^{+0.09}_{-0.54}$	$24.50^{+0.09}_{-0.04}$	$60.10^{+0.00}_{-0.09}$
NGC 612	C	105.64 / 127	91	$1.57^{+0.08}_{-0.06}$	$23.95^{+0.01}_{-0.03}$	23.84 ± 0.02	88^{+2}_{-4}
2MASX J0140 ...	C	208.26 / 235	89	1.71 ± 0.03	22.8 ± 0.5	$23.78^{+0.10}_{-0.03}$	$60.10^{+0.35}_{-0.09}$
	D	205.40 / 237	93	1.71 ± 0.04	22.13 ± 0.07	23.9 ± 0.2	U
MCG −01-05-047	C	120.26 / 114	32	$1.64^{+0.03}_{-0.19}$	$23.7^{+0.1}_{-0.6}$	24.70 ± 0.03	$60.12^{+0.07}_{-0.11}$
	D	117.11 / 116	45	1.67 ± 0.07	$23.28^{+0.05}_{-0.03}$	24.6 ± 0.2	U
NGC 788	C	118.97 / 147	95	$1.86^{+0.03}_{-0.05}$	24.0 ± 0.1	24.64 ± 0.02	60.6 ± 0.3

Continued on the next page...

Target Name	Model [a]	χ^2 / d.o.f.	$p_{\rm null}$ / %	Γ	$\log N_{\rm H,los}/{\rm cm}^{-2}$ [b]	$\log N_{\rm H,tor}/{\rm cm}^{-2}$	$\theta_{\rm inc}$ / deg. [c]
NGC 1052	C	178.24 / 206	91	$1.62^{+0.05}_{-0.03}$	$23.2^{+0.3}_{-0.1}$	$23.78^{+0.14}_{-0.08}$	$60.6^{+0.6}_{-0.2}$
	D	184.94 / 212	91	1.59 ± 0.05	23.03 ± 0.04	23.8 ± 0.2	U
NGC 1229	C	108.64 / 99	23	$1.66^{+0.08}_{-0.21}$	$24.1^{+0.2}_{-0.5}$	$24.86^{+0.03}_{-0.37}$	$60.26^{+0.29}_{-0.09}$
2MASX J0356 ...	C	190.40 / 156	3.0	1.67 ± 0.05	$22.8^{+0.5}_{-0.7}$	$23.6^{+0.2}_{-0.5}$	$60.3^{+0.8}_{-0.2}$
3C 105	C	93.59 / 92	43	$1.83^{+0.08}_{-0.13}$	23.8 ± 0.2	$23.73^{+0.15}_{-0.07}$	88^{+2}_{-9}
2MASX J0423 ...	C	125.51 / 119	32	$1.75^{+0.07}_{-0.11}$	23.9 ± 0.2	$24.38^{+0.05}_{-0.11}$	61.0 ± 0.4
	D	117.35 / 121	57	$1.83^{+0.07}_{-0.05}$	23.88 ± 0.04	24.4 ± 0.2	O
MCG +03-13-001	C	90.95 / 89	42	1.9 ± 0.1	24.1 ± 0.3	$24.87^{+0.02}_{-0.30}$	60.25 ± 0.01
CGCG 420-015 ..	C	274.36 / 244	8.0	2.07 ± 0.04	$24.10^{+0.09}_{-0.10}$	24.67 ± 0.03	60.8 ± 0.2
	D	277.85 / 248	9.0	$2.05^{+0.09}_{-0.06}$	$23.97^{+0.04}_{-0.02}$	$24.62^{+0.19}_{-0.09}$	U
ESO 033-G002 ...	C	437.79 / 427	34	1.92 ± 0.03	$22.9^{+0.3}_{-0.6}$	$23.85^{+0.04}_{-0.06}$	$60.10^{+0.17}_{-0.09}$
	D	398.70 / 430	85	1.96 ± 0.02	22.21 ± 0.03	$24.49^{+0.09}_{-0.12}$	U
LEDA 178130	C	373.80 / 384	63	1.67 ± 0.02	23.1 ± 0.4	$23.23^{+0.15}_{-0.01}$	65^{+15}_{-3}
	D	372.80 / 386	67	1.74 ± 0.04	23.05 ± 0.03	23.8 ± 0.2	O
2MASX J0508 ...	C	364.81 / 323	5.0	1.72 ± 0.03	$22.8^{+0.3}_{-0.5}$	$23.80^{+0.05}_{-0.02}$	$60.10^{+0.23}_{-0.09}$
	D	348.33 / 319	12	1.74 ± 0.04	$22.20^{+0.05}_{-0.03}$	23.9 ± 0.2	U
NGC 2110	C	685.36 / 660	24	1.642 ± 0.005	22.6 ± 0.2	$22.82^{+0.07}_{-0.11}$	64^{+3}_{-1}
	D	691.85 / 663	21	$1.637^{+0.004}_{-0.006}$	22.58 ± 0.02	$22.82^{+0.09}_{-0.11}$	U
ESO 005-G004 ...	C	80.34 / 64	8.0	$2.05^{+0.03}_{-0.07}$	24.6 ± 0.1	24.87 ± 0.03	64 ± 2

Continued on the next page...

Target Name	Model [a]	χ^2 / d.o.f.	$p_{\rm null}$ / %	Γ	$\log N_{\rm H,los}/{\rm cm}^{-2}$ [b]	$\log N_{\rm H,tor}/{\rm cm}^{-2}$	$\theta_{\rm inc}$ / deg. [c]
	D	62.67 / 65	55	1.61 ± 0.08	$24.6^{+0.4}_{-0.1}$	24.04 ± 0.09	U
Mrk 3	C	563.23 / 540	23	1.61 ± 0.02	23.84 ± 0.01	23.73 ± 0.01	87^{+3}_{-1}
	D	550.18 / 543	40	$1.62^{+0.03}_{-0.01}$	23.87 ± 0.01	22.83 ± 0.06	U
ESO 121-IG028 ..	C	152.19 / 186	96	$1.81^{+0.06}_{-0.08}$	23.6 ± 0.3	24.2 ± 0.2	$60.5^{+0.6}_{-0.1}$
	D	153.83 / 188	96	1.77 ± 0.05	23.32 ± 0.04	$24.20^{+0.09}_{-0.10}$	U
LEDA 549777	C	98.33 / 103	61	$1.55^{+0.08}_{-0.10}$	$23.2^{+0.7}_{-0.9}$	$23.4^{+0.5}_{-0.1}$	64^{+7}_{-4}
	D	97.31 / 105	69	$1.52^{+0.09}_{-0.07}$	23.04 ± 0.08	23.7 ± 0.3	U
LEDA 511628	C	182.45 / 209	90	1.70 ± 0.02	$22.9^{+0.2}_{-0.6}$	$23.88^{+0.16}_{-0.03}$	$60.13^{+0.05}_{-0.12}$
	D	182.52 / 210	91	1.70 ± 0.05	22.47 ± 0.08	23.9 ± 0.2	U
MCG +06-16-028	C	92.29 / 90	41	$1.79^{+0.06}_{-0.08}$	24.22 ± 0.26	$24.86^{+0.01}_{-0.03}$	$60.54^{+1.18}_{-0.06}$
LEDA 96373	C	149.72 / 127	8.0	1.7 ± 0.1	$24.0^{+0.4}_{-0.2}$	$24.60^{+0.25}_{-0.09}$	$60.5^{+0.8}_{-0.2}$
	D	111.68 / 129	86	1.7 ± 0.2	$24.43^{+0.10}_{-0.04}$	23.5 ± 0.2	O
IRAS 07378−3136	C	228.67 / 229	49	1.75 ± 0.09	23.7 ± 0.3	24.3 ± 0.2	$60.6^{+0.4}_{-0.2}$
	D	239.14 / 231	34	$1.53^{+0.08}_{-0.03}$	$23.31^{+0.05}_{-0.02}$	$24.19^{+0.11}_{-0.08}$	U
UGC 3995 A	C	180.78 / 189	65	$1.56^{+0.04}_{-0.06}$	$23.7^{+0.3}_{-0.1}$	$24.37^{+0.24}_{-0.07}$	$60.52^{+0.05}_{-0.12}$
	D	178.54 / 190	71	$1.60^{+0.09}_{-0.06}$	23.55 ± 0.04	24.5 ± 0.1	U
2MASX J0756 ...	C	41.32 / 49	77	$1.95^{+0.06}_{-0.16}$	$23.1^{+0.2}_{-0.6}$	$24.15^{+0.13}_{-0.09}$	$60.10^{+0.05}_{-0.09}$
	D	43.11 / 51	77	1.81 ± 0.09	22.0 ± 0.3	24.2 ± 0.5	U
MCG −01-22-006	C	356.01 / 368	66	$1.59^{+0.05}_{-0.15}$	23.5 ± 0.3	24.1 ± 0.2	60.6 ± 0.3

Continued on the next page...

Target Name	Model [a]	χ^2 / d.o.f.	$p_{\rm null}$ / %	Γ	$\log N_{\rm H,los}/{\rm cm}^{-2}$ [b]	$\log N_{\rm H,tor}/{\rm cm}^{-2}$	$\theta_{\rm inc}$ / deg. [c]
	D	354.74 / 369	69	1.51 ± 0.05	23.26 ± 0.03	$23.90^{+0.13}_{-0.09}$	O
CGCG 150-014 ..	C	103.69 / 104	49	1.7 ± 0.2	23.8 ± 0.6	24.0 ± 0.3	64^{+20}_{-2}
	D	104.42 / 106	52	1.7 ± 0.2	$23.75^{+0.11}_{-0.07}$	$24.1^{+0.4}_{-1.8}$	U
MCG +11-11-032	C	66.55 / 65	42	1.73 ± 0.05	$23.4^{+0.6}_{-0.3}$	$24.3^{+0.4}_{-0.1}$	$60.18^{+0.16}_{-0.08}$
	D	66.84 / 67	48	$1.71^{+0.10}_{-0.09}$	22.98 ± 0.09	24.4 ± 0.4	U
Mrk 18	C	67.97 / 63	31	$1.81^{+0.11}_{-0.09}$	$23.7^{+0.9}_{-0.5}$	$24.69^{+0.11}_{-0.05}$	$60.10^{+3.49}_{-0.09}$
2MASX J0903 ...	C	62.76 / 58	31	1.7 ± 0.2	$24.0^{+0.5}_{-0.7}$	$24.7^{+0.2}_{-0.6}$	$60.4^{+1.0}_{-0.2}$
	D	69.15 / 60	19	1.5 ± 0.2	23.49 ± 0.08	24.4 ± 0.3	U
2MASX J0911 ...	C	127.85 / 134	63	$1.70^{+0.05}_{-0.07}$	$23.51^{+0.05}_{-0.07}$	23.41 ± 0.06	89^{+1}_{-5}
IC 2461	C	244.61 / 247	53	1.79 ± 0.02	$23.3^{+0.3}_{-0.1}$	$24.17^{+0.20}_{-0.02}$	$60.16^{+0.12}_{-0.06}$
	D	243.23 / 249	59	$1.81^{+0.05}_{-0.07}$	22.87 ± 0.06	24.3 ± 0.2	U
MCG −01-24-012	C	306.69 / 328	79	1.96 ± 0.03	$23.37^{+0.07}_{-0.14}$	$24.22^{+0.04}_{-0.08}$	$60.20^{+0.03}_{-0.05}$
	D	308.13 / 329	79	1.96 ± 0.04	22.92 ± 0.03	$24.25^{+0.12}_{-0.08}$	U
NGC 2992	C	643.63 / 707	95	$1.771^{+0.008}_{-0.012}$	$22.7^{+0.1}_{-0.6}$	23.68 ± 0.04	60.10 ± 0.09
	D	665.27 / 721	93	$1.716^{+0.011}_{-0.008}$	22.03 ± 0.01	23.32 ± 0.09	U
NGC 3079	C	99.85 / 102	54	$1.94^{+0.10}_{-0.09}$	$24.45^{+0.05}_{-0.03}$	24.36 ± 0.04	85 ± 1
	D	91.60 / 104	80	1.99 ± 0.09	24.41 ± 0.04	$24.80^{+0.07}_{-0.17}$	O
ESO 263-G013 ...	C	139.70 / 140	49	1.68 ± 0.08	23.86 ± 0.04	23.75 ± 0.03	88^{+2}_{-4}
NGC 3281	C	200.71 / 198	43	2.02 ± 0.02	24.37 ± 0.03	24.88 ± 0.02	60.99 ± 0.06

Continued on the next page...

Target Name	Model [a]	χ^2 / d.o.f.	$p_{\rm null}$ / %	Γ	$\log N_{\rm H,los}/{\rm cm}^{-2}$ [b]	$\log N_{\rm H,tor}/{\rm cm}^{-2}$	$\theta_{\rm inc}$ / deg. [c]
MCG +12-10-067	C	126.52 / 135	68	1.84 ± 0.04	$23.7^{+0.2}_{-0.8}$	24.57 ± 0.05	60.2 ± 0.2
MCG +06-24-008	C	148.98 / 153	57	1.62 ± 0.05	$22.8^{+0.9}_{-0.6}$	$23.4^{+0.3}_{-0.5}$	$60.6^{+13.4}_{-0.3}$
	D	149.17 / 154	59	$1.58^{+0.06}_{-0.04}$	22.59 ± 0.09	23.3 ± 0.4	U
UGC 5881	C	96.21 / 95	44	1.69 ± 0.18	$23.4^{+0.3}_{-0.5}$	$24.2^{+0.2}_{-0.4}$	60.3 ± 0.2
	D	96.64 / 96	46	$1.55^{+0.14}_{-0.09}$	$22.98^{+0.08}_{-0.11}$	$24.0^{+0.4}_{-0.2}$	U
NGC 3393	C	54.05 / 75	96	1.8 ± 0.2	24.34 ± 0.05	24.24 ± 0.05	85^{+5}_{-3}
NGC 3786	C	57.22 / 57	46	1.77 ± 0.05	23 ± 1	$24.2^{+0.2}_{-0.5}$	$60.10^{+29.90}_{-0.09}$
IC 751	C	63.14 / 62	43	1.6 ± 0.1	23.8 ± 0.6	24.5 ± 0.4	$60.4^{+0.6}_{-0.2}$
B2 1204+34	C	177.26 / 208	94	$1.68^{+0.10}_{-0.03}$	$22.6^{+1.4}_{-0.9}$	$23.1^{+0.8}_{-0.6}$	$61.1^{+28.9}_{-0.9}$
	D	178.93 / 209	93	$1.66^{+0.05}_{-0.03}$	22.50 ± 0.06	$23.1^{+0.4}_{-0.6}$	U
WAS 49	C	79.04 / 89	76	$1.98^{+0.05}_{-0.08}$	$23.8^{+0.6}_{-0.2}$	$23.75^{+0.53}_{-0.08}$	81^{+9}_{-10}
	D	95.37 / 94	44	1.7 ± 0.1	$23.39^{+0.08}_{-0.06}$	24.1 ± 0.3	U
NGC 4395	C	280.22 / 305	84	1.61 ± 0.02	$23.1^{+0.2}_{-0.5}$	$24.08^{+0.12}_{-0.02}$	$60.11^{+0.04}_{-0.10}$
	D	283.23 / 307	83	1.63 ± 0.04	22.64 ± 0.05	24.2 ± 0.1	U
LEDA 170194	C	134.57 / 140	61	$1.76^{+0.07}_{-0.04}$	23.0 ± 0.4	23.8 ± 0.3	$60.3^{+0.3}_{-0.1}$
	D	134.16 / 142	66	$1.78^{+0.09}_{-0.06}$	22.76 ± 0.07	23.9 ± 0.3	U
NGC 4941	C	55.22 / 57	54	1.9 ± 0.1	$24.1^{+0.3}_{-0.5}$	$24.59^{+0.07}_{-0.33}$	$61.2^{+3.2}_{-0.7}$
	D	62.47 / 59	35	$1.85^{+0.20}_{-0.08}$	$24.12^{+0.08}_{-0.06}$	$24.4^{+0.4}_{-0.2}$	U
NGC 4992	C	268.73 / 248	17	1.63 ± 0.05	$23.8^{+0.3}_{-0.1}$	$24.34^{+0.16}_{-0.09}$	$60.8^{+0.4}_{-0.2}$

Continued on the next page...

Target Name	Model [a]	χ^2 / d.o.f.	$p_{\rm null}$ / %	Γ	$\log N_{\rm H,los}/{\rm cm}^{-2}$ [b]	$\log N_{\rm H,tor}/{\rm cm}^{-2}$	$\theta_{\rm inc}$ / deg. [c]
	D	265.33 / 242	14	1.59 ± 0.05	23.61 ± 0.03	24.37 ± 0.08	U
Mrk 248	C	149.62 / 166	81	$1.93^{+0.04}_{-0.07}$	23.4 ± 0.3	24.2 ± 0.2	60.3 ± 0.1
	D	155.91 / 168	73	$1.85^{+0.06}_{-0.08}$	$22.97^{+0.05}_{-0.02}$	24.1 ± 0.2	U
ESO 509-IG066 ..	C	208.59 / 225	77	1.69 ± 0.06	23.2 ± 0.3	24.0 ± 0.2	60.3 ± 0.2
	D	206.21 / 226	82	$1.69^{+0.09}_{-0.06}$	$22.87^{+0.08}_{-0.06}$	24.0 ± 0.3	U
NGC 5252	C	300.23 / 291	34	1.68 ± 0.03	22.7 ± 0.3	23.4 ± 0.2	$60.5^{+0.3}_{-0.1}$
	D	299.47 / 293	38	1.67 ± 0.02	$22.51^{+0.08}_{-0.06}$	23.4 ± 0.2	U
NGC 5273	C	561.73 / 528	15	1.68 ± 0.02	$22.9^{+0.3}_{-0.5}$	$23.91^{+0.04}_{-0.02}$	$60.10^{+0.17}_{-0.09}$
	D	557.43 / 536	25	1.74 ± 0.02	$22.43^{+0.02}_{-0.04}$	$24.32^{+0.10}_{-0.07}$	U
2MASX J1410 ...	C	144.90 / 122	7.0	$1.73^{+0.03}_{-0.08}$	23.5 ± 0.6	24.50 ± 0.06	$60.10^{+0.83}_{-0.09}$
NGC 5643	C	114.56 / 108	31	$2.18^{+0.03}_{-0.05}$	24.6 ± 0.2	$24.87^{+0.02}_{-0.05}$	64^{+5}_{-2}
	D	117.97 / 115	40	$1.71^{+0.03}_{-0.13}$	24.6 ± 1.3	$24.03^{+0.04}_{-0.09}$	U
NGC 5674	C	245.37 / 258	70	1.86 ± 0.04	$23.0^{+0.1}_{-0.3}$	$23.88^{+0.06}_{-0.16}$	60.19 ± 0.08
	D	244.23 / 260	75	$1.88^{+0.06}_{-0.04}$	$22.66^{+0.06}_{-0.04}$	24.0 ± 0.2	U
NGC 5728	C	278.97 / 270	34	$1.69^{+0.03}_{-0.07}$	24.14 ± 0.03	24.04 ± 0.02	85^{+5}_{-3}
	D	277.95 / 272	38	1.68 ± 0.05	24.11 ± 0.03	24.11 ± 0.05	O
CGCG 164-019 ..	C	42.29 / 55	89	1.8 ± 0.2	$24.1^{+0.5}_{-0.2}$	24.7 ± 0.2	$60.6^{+2.5}_{-0.3}$
	D	40.61 / 56	93	1.7 ± 0.2	$24.26^{+0.06}_{-0.08}$	$23.2^{+0.4}_{-0.2}$	O
IC 4518A	C	136.29 / 128	29	1.72 ± 0.03	23.63 ± 0.06	24.55 ± 0.03	60.15 ± 0.02

Continued on the next page...

Target Name	Model [a]	χ^2 / d.o.f.	$p_{\rm null}$ / %	Γ	$\log N_{\rm H,los}/{\rm cm}^{-2}$ [b]	$\log N_{\rm H,tor}/{\rm cm}^{-2}$	$\theta_{\rm inc}$ / deg. [c]
2MASX J1506 ...	C	78.24 / 92	84	1.70 ± 0.07	$22.4^{+1.3}_{-0.7}$	$22.6^{+1.0}_{-0.5}$	64^{+26}_{-3}
NGC 5899	C	232.76 / 240	61	1.84 ± 0.03	$23.5^{+0.3}_{-0.5}$	$24.53^{+0.04}_{-0.02}$	$60.10^{+0.30}_{-0.09}$
	D	228.65 / 241	70	1.88 ± 0.04	23.01 ± 0.04	24.7 ± 0.2	U
MCG −01-40-001	C	169.53 / 209	97	1.77 ± 0.02	$23.32^{+0.19}_{-0.05}$	24.30 ± 0.03	$60.11^{+0.04}_{-0.01}$
	D	167.84 / 212	98	1.79 ± 0.05	22.84 ± 0.05	24.3 ± 0.2	U
MCG +14-08-004	C	91.43 / 99	69	1.8 ± 0.1	23.3 ± 0.5	23.8 ± 0.3	$61.0^{+2.1}_{-0.4}$
	D	91.40 / 101	74	$1.75^{+0.11}_{-0.08}$	23.14 ± 0.07	23.8 ± 0.3	U
Mrk 1498	C	342.58 / 305	6.0	1.70 ± 0.04	23.31 ± 0.17	23.91 ± 0.05	$60.66^{+0.07}_{-0.04}$
	D	346.12 / 309	7.0	1.71 ± 0.03	$23.21^{+0.03}_{-0.01}$	23.88 ± 0.07	O
IRAS 16288+3929	C	52.85 / 67	89	1.8 ± 0.1	23.8 ± 0.4	$23.70^{+0.41}_{-0.05}$	86^{+4}_{-20}
	D	53.77 / 68	89	1.8 ± 0.2	$23.82^{+0.09}_{-0.07}$	$23.8^{+0.7}_{-0.5}$	O
NGC 6240	C	313.27 / 317	54	1.72 ± 0.05	24.12 ± 0.02	24.02 ± 0.02	88 ± 2
	D	323.01 / 320	44	$1.74^{+0.02}_{-0.06}$	24.15 ± 0.01	25^{+u}_{-2}	U
MCG +07-37-031	C	202.20 / 192	29	$1.76^{+0.02}_{-0.04}$	23.2 ± 0.5	$24.22^{+0.06}_{-0.03}$	$60.10^{+0.36}_{-0.09}$
	D	204.92 / 194	28	$1.72^{+0.06}_{-0.12}$	$22.56^{+0.04}_{-0.06}$	24.1 ± 0.2	U
2MASX J1824 ...	C	158.83 / 163	57	$1.68^{+0.03}_{-0.06}$	23.7 ± 0.5	$24.70^{+0.10}_{-0.04}$	60.10 ± 0.09
	D	156.67 / 164	64	$1.65^{+0.11}_{-0.05}$	$23.07^{+0.11}_{-0.05}$	24.3 ± 0.2	U
IC 4709	C	223.12 / 218	39	1.88 ± 0.07	23.8 ± 0.3	24.4 ± 0.2	60.5 ± 0.2
	D	231.97 / 220	27	$1.74^{+0.07}_{-0.05}$	23.37 ± 0.04	24.3 ± 0.1	U
LEDA 3097193 ..	C	372.93 / 392	74	$1.88^{+0.03}_{-0.05}$	23.2 ± 0.3	23.9 ± 0.2	60.37 ± 0.09

Continued on the next page...

Target Name	Model [a]	χ^2 / d.o.f.	$p_{\rm null}$ / %	Γ	$\log N_{\rm H,los}/{\rm cm}^{-2}$ [b]	$\log N_{\rm H,tor}/{\rm cm}^{-2}$	$\theta_{\rm inc}$ / deg. [c]
	D	375.84 / 394	73	1.89 ± 0.05	22.93 ± 0.03	24.0 ± 0.2	U
ESO 231-G026 ...	C	187.82 / 235	99	$1.54^{+0.03}_{-0.05}$	23.3 ± 0.2	$23.31^{+0.12}_{-0.07}$	72^{+18}_{-7}
2MASX J1947 ...	C	247.80 / 252	56	1.87 ± 0.04	$23.3^{+0.2}_{-0.9}$	$24.16^{+0.07}_{-0.24}$	60.2 ± 0.2
	D	247.24 / 254	60	1.86 ± 0.07	22.90 ± 0.05	24.2 ± 0.2	U
3C 403	C	161.81 / 181	84	$1.59^{+0.08}_{-0.06}$	23.4 ± 0.3	$23.9^{+0.3}_{-0.1}$	$61.2^{+0.6}_{-0.3}$
	D	166.35 / 182	79	$1.57^{+0.12}_{-0.07}$	23.38 ± 0.05	23.9 ± 0.3	U
2MASX J2006 ...	C	97.96 / 113	84	1.89 ± 0.05	$24.4^{+0.6}_{-2.3}$	$24.85^{+0.03}_{-1.31}$	61^{+29}_{-1}
	D	101.31 / 114	79	$1.89^{+0.09}_{-0.11}$	23.40 ± 0.05	24.5 ± 0.3	O
2MASX J2018 ...	C	241.16 / 253	69	$1.73^{+0.07}_{-0.05}$	23.7 ± 0.3	$24.54^{+0.08}_{-0.15}$	$60.21^{+0.08}_{-0.11}$
	D	244.08 / 255	67	$1.69^{+0.05}_{-0.09}$	$23.16^{+0.03}_{-0.07}$	24.4 ± 0.2	U
2MASX J2021 ...	C	138.68 / 133	35	$1.58^{+0.03}_{-0.05}$	$23.4^{+0.3}_{-0.5}$	$24.36^{+0.16}_{-0.04}$	$60.10^{+0.07}_{-0.09}$
	D	137.27 / 135	42	$1.64^{+0.05}_{-0.09}$	$22.89^{+0.08}_{-0.12}$	24.4 ± 0.2	U
NGC 6921	C	44.30 / 71	99	1.85 ± 0.07	24.2 ± 0.1	24.21 ± 0.07	72 ± 5
	D	48.66 / 72	98	1.76 ± 0.07	24.14 ± 0.05	24.4 ± 0.1	U
MCG +04-48-002	C	71.96 / 76	61	1.76 ± 0.06	$23.9^{+0.4}_{-0.1}$	24.39 ± 0.12	61.0 ± 0.4
	D	74.27 / 77	56	1.73 ± 0.07	23.88 ± 0.06	24.4 ± 0.2	U
IC 5063	C	292.77 / 287	39	1.77 ± 0.03	$23.57^{+0.10}_{-0.09}$	$24.20^{+0.06}_{-0.03}$	60.5 ± 0.1
	D	292.44 / 289	43	1.74 ± 0.04	23.38 ± 0.02	$24.21^{+0.08}_{-0.03}$	U
NGC 7130	C	34.81 / 31	29	2.1 ± 0.4	24.7 ± 0.1	24.6 ± 0.1	81 ± 4

Continued on the next page...

Target Name	Model [a]	χ^2 / d.o.f.	$p_{\rm null}$ / %	Γ	$\log N_{\rm H,los}/{\rm cm}^{-2}$ [b]	$\log N_{\rm H,tor}/{\rm cm}^{-2}$	$\theta_{\rm inc}$ / deg. [c]
NGC 7319	C	28.86 / 37	82	1.6 ± 0.1	23.9 ± 0.4	24.6 ± 0.3	$60.4^{+0.4}_{-0.2}$
PKS 2356-61	C	129.84 / 157	94	1.84 ± 0.06	23.6 ± 0.3	$24.42^{+0.06}_{-0.56}$	$60.2^{+0.5}_{-0.2}$
	D	128.78 / 159	96	$1.83^{+0.08}_{-0.13}$	$23.17^{+0.06}_{-0.08}$	24.3 ± 0.4	U

[a] (C)oupled or (D)ecoupled `MYtorus` model. Only well-fitting parameter sets are listed.

[b] For the coupled model, $N_{\rm H,los}$ is calculated from $N_{\rm H,tor}$ and $\theta_{\rm inc}$.

[c] For the decoupled model, we only list the inclination bin, depending on whether the reprocessed spectrum is (O)bscured or (U)nobscured.

Table C5: Spectral parameters obtained from fitting the coupled and the decoupled `MYtorus` models

Target Name	Model [a]	χ^2 / d.o.f.	$p_{\rm null}$ / %	Γ	$\log N_{\rm H,los}/{\rm cm}^{-2}$ [b]	$\log N_{\rm H,tor}/{\rm cm}^{-2}$	$\theta_{\rm inc}$ / deg. [c]
LEDA 136991	C	68.69 / 67	42	2.0 ± 0.1	$24.3^{+0.3}_{-0.1}$	$24.86^{+0.03}_{-0.09}$	$60.60^{+1.09}_{-0.09}$
	D	64.88 / 69	61	$1.75^{+0.11}_{-0.07}$	24.27 ± 0.04	23.1 ± 0.1	O
NGC 262	C	518.29 / 464	4	1.767 ± 0.006	$23.38^{+0.03}_{-0.05}$	24.26 ± 0.01	60.18 ± 0.03
	D	506.08 / 465	9.0	1.63 ± 0.03	22.94 ± 0.02	$24.10^{+0.06}_{-0.09}$	O
ESO 195-IG021 ..	C	227.66 / 249	83	1.87 ± 0.02	$23.1^{+0.2}_{-0.6}$	$24.02^{+0.23}_{-0.03}$	60.1 ± 0.1
	D	227.48 / 251	85	1.89 ± 0.05	22.63 ± 0.05	24.1 ± 0.2	U
NGC 454 E	C	57.36 / 80	97	1.6 ± 0.2	$23.9^{+0.5}_{-0.2}$	$23.80^{+0.53}_{-0.05}$	87^{+3}_{-18}
	D	56.36 / 81	98	$1.6^{+0.3}_{-0.1}$	23.85 ± 0.07	$24.1^{+0.6}_{-0.3}$	O
MCG +08-03-018	C	104.42 / 126	92	$2.36^{+0.06}_{-0.11}$	24.1 ± 0.2	24.69 ± 0.03	$60.6^{+0.8}_{-0.2}$
	D	99.85 / 129	97	2.3 ± 0.1	$24.05^{+0.03}_{-0.05}$	23.2 ± 0.1	U
NGC 513	C	125.01 / 140	81	1.68 ± 0.03	$23.49^{+0.09}_{-0.54}$	$24.50^{+0.09}_{-0.04}$	$60.10^{+0.00}_{-0.09}$
NGC 612	C	105.64 / 127	91	$1.57^{+0.08}_{-0.06}$	$23.95^{+0.01}_{-0.03}$	23.84 ± 0.02	88^{+2}_{-4}
2MASX J0140 ...	C	208.26 / 235	89	1.71 ± 0.03	22.8 ± 0.5	$23.78^{+0.10}_{-0.03}$	$60.10^{+0.35}_{-0.09}$
	D	205.40 / 237	93	1.71 ± 0.04	22.13 ± 0.07	23.9 ± 0.2	U
MCG −01-05-047	C	120.26 / 114	32	$1.64^{+0.03}_{-0.19}$	$23.7^{+0.1}_{-0.6}$	24.70 ± 0.03	$60.12^{+0.07}_{-0.11}$
	D	117.11 / 116	45	1.67 ± 0.07	$23.28^{+0.05}_{-0.03}$	24.6 ± 0.2	U
NGC 788	C	118.97 / 147	95	$1.86^{+0.03}_{-0.05}$	24.0 ± 0.1	24.64 ± 0.02	60.6 ± 0.3

Continued on the next page...

Target Name	Model [a]	χ^2 / d.o.f.	$p_{\rm null}$ / %	Γ	$\log N_{\rm H,los}/{\rm cm}^{-2}$ [b]	$\log N_{\rm H,tor}/{\rm cm}^{-2}$	$\theta_{\rm inc}$ / deg. [c]
NGC 1052	C	178.24 / 206	91	$1.62^{+0.05}_{-0.03}$	$23.2^{+0.3}_{-0.1}$	$23.78^{+0.14}_{-0.08}$	$60.6^{+0.6}_{-0.2}$
	D	184.94 / 212	91	1.59 ± 0.05	23.03 ± 0.04	23.8 ± 0.2	U
NGC 1229	C	108.64 / 99	23	$1.66^{+0.08}_{-0.21}$	$24.1^{+0.2}_{-0.5}$	$24.86^{+0.03}_{-0.37}$	$60.26^{+0.29}_{-0.09}$
2MASX J0356 ...	C	190.40 / 156	3.0	1.67 ± 0.05	$22.8^{+0.5}_{-0.7}$	$23.6^{+0.2}_{-0.5}$	$60.3^{+0.8}_{-0.2}$
3C 105	C	93.59 / 92	43	$1.83^{+0.08}_{-0.13}$	23.8 ± 0.2	$23.73^{+0.15}_{-0.07}$	88^{+2}_{-9}
2MASX J0423 ...	C	125.51 / 119	32	$1.75^{+0.07}_{-0.11}$	23.9 ± 0.2	$24.38^{+0.05}_{-0.11}$	61.0 ± 0.4
	D	117.35 / 121	57	$1.83^{+0.07}_{-0.05}$	23.88 ± 0.04	24.4 ± 0.2	O
MCG +03-13-001	C	90.95 / 89	42	1.9 ± 0.1	24.1 ± 0.3	$24.87^{+0.02}_{-0.30}$	60.25 ± 0.01
CGCG 420-015 ..	C	274.36 / 244	8.0	2.07 ± 0.04	$24.10^{+0.09}_{-0.10}$	24.67 ± 0.03	60.8 ± 0.2
	D	277.85 / 248	9.0	$2.05^{+0.09}_{-0.06}$	$23.97^{+0.04}_{-0.02}$	$24.62^{+0.19}_{-0.09}$	U
ESO 033-G002 ...	C	437.79 / 427	34	1.92 ± 0.03	$22.9^{+0.3}_{-0.6}$	$23.85^{+0.04}_{-0.06}$	$60.10^{+0.17}_{-0.09}$
	D	398.70 / 430	85	1.96 ± 0.02	22.21 ± 0.03	$24.49^{+0.09}_{-0.12}$	U
LEDA 178130	C	373.80 / 384	63	1.67 ± 0.02	23.1 ± 0.4	$23.23^{+0.15}_{-0.01}$	65^{+15}_{-3}
	D	372.80 / 386	67	1.74 ± 0.04	23.05 ± 0.03	23.8 ± 0.2	O
2MASX J0508 ...	C	364.81 / 323	5.0	1.72 ± 0.03	$22.8^{+0.3}_{-0.5}$	$23.80^{+0.05}_{-0.02}$	$60.10^{+0.23}_{-0.09}$
	D	348.33 / 319	12	1.74 ± 0.04	$22.20^{+0.05}_{-0.03}$	23.9 ± 0.2	U
NGC 2110	C	685.36 / 660	24	1.642 ± 0.005	22.6 ± 0.2	$22.82^{+0.07}_{-0.11}$	64^{+3}_{-1}
	D	691.85 / 663	21	$1.637^{+0.004}_{-0.006}$	22.58 ± 0.02	$22.82^{+0.09}_{-0.11}$	U
ESO 005-G004 ...	C	80.34 / 64	8.0	$2.05^{+0.03}_{-0.07}$	24.6 ± 0.1	24.87 ± 0.03	64 ± 2

Continued on the next page...

Target Name	Model [a]	χ^2 / d.o.f.	$p_{\rm null}$ / %	Γ	$\log N_{\rm H,los}/{\rm cm}^{-2}$ [b]	$\log N_{\rm H,tor}/{\rm cm}^{-2}$	$\theta_{\rm inc}$ / deg. [c]
	D	62.67 / 65	55	1.61 ± 0.08	$24.6^{+0.4}_{-0.1}$	24.04 ± 0.09	U
Mrk 3	C	563.23 / 540	23	1.61 ± 0.02	23.84 ± 0.01	23.73 ± 0.01	87^{+3}_{-1}
	D	550.18 / 543	40	$1.62^{+0.03}_{-0.01}$	23.87 ± 0.01	22.83 ± 0.06	U
ESO 121-IG028 ..	C	152.19 / 186	96	$1.81^{+0.06}_{-0.08}$	23.6 ± 0.3	24.2 ± 0.2	$60.5^{+0.6}_{-0.1}$
	D	153.83 / 188	96	1.77 ± 0.05	23.32 ± 0.04	$24.20^{+0.09}_{-0.10}$	U
LEDA 549777	C	98.33 / 103	61	$1.55^{+0.08}_{-0.10}$	$23.2^{+0.7}_{-0.9}$	$23.4^{+0.5}_{-0.1}$	64^{+7}_{-4}
	D	97.31 / 105	69	$1.52^{+0.09}_{-0.07}$	23.04 ± 0.08	23.7 ± 0.3	U
LEDA 511628	C	182.45 / 209	90	1.70 ± 0.02	$22.9^{+0.2}_{-0.6}$	$23.88^{+0.16}_{-0.03}$	$60.13^{+0.05}_{-0.12}$
	D	182.52 / 210	91	1.70 ± 0.05	22.47 ± 0.08	23.9 ± 0.2	U
MCG +06-16-028	C	92.29 / 90	41	$1.79^{+0.06}_{-0.08}$	24.22 ± 0.26	$24.86^{+0.01}_{-0.03}$	$60.54^{+1.18}_{-0.06}$
LEDA 96373	C	149.72 / 127	8.0	1.7 ± 0.1	$24.0^{+0.4}_{-0.2}$	$24.60^{+0.25}_{-0.09}$	$60.5^{+0.8}_{-0.2}$
	D	111.68 / 129	86	1.7 ± 0.2	$24.43^{+0.10}_{-0.04}$	23.5 ± 0.2	O
IRAS 07378−3136	C	228.67 / 229	49	1.75 ± 0.09	23.7 ± 0.3	24.3 ± 0.2	$60.6^{+0.4}_{-0.2}$
	D	239.14 / 231	34	$1.53^{+0.08}_{-0.03}$	$23.31^{+0.05}_{-0.02}$	$24.19^{+0.11}_{-0.08}$	U
UGC 3995 A	C	180.78 / 189	65	$1.56^{+0.04}_{-0.06}$	$23.7^{+0.3}_{-0.1}$	$24.37^{+0.24}_{-0.07}$	$60.52^{+0.05}_{-0.12}$
	D	178.54 / 190	71	$1.60^{+0.09}_{-0.06}$	23.55 ± 0.04	24.5 ± 0.1	U
2MASX J0756 ...	C	41.32 / 49	77	$1.95^{+0.06}_{-0.16}$	$23.1^{+0.2}_{-0.6}$	$24.15^{+0.13}_{-0.09}$	$60.10^{+0.05}_{-0.09}$
	D	43.11 / 51	77	1.81 ± 0.09	22.0 ± 0.3	24.2 ± 0.5	U
MCG −01-22-006	C	356.01 / 368	66	$1.59^{+0.05}_{-0.15}$	23.5 ± 0.3	24.1 ± 0.2	60.6 ± 0.3

Continued on the next page...

Target Name	Model [a]	χ^2 / d.o.f.	$p_{\rm null}$ / %	Γ	$\log N_{\rm H,los}/{\rm cm}^{-2}$ [b]	$\log N_{\rm H,tor}/{\rm cm}^{-2}$	$\theta_{\rm inc}$ / deg. [c]
	D	354.74 / 369	69	1.51 ± 0.05	23.26 ± 0.03	$23.90^{+0.13}_{-0.09}$	O
CGCG 150-014 ..	C	103.69 / 104	49	1.7 ± 0.2	23.8 ± 0.6	24.0 ± 0.3	64^{+20}_{-2}
	D	104.42 / 106	52	1.7 ± 0.2	$23.75^{+0.11}_{-0.07}$	$24.1^{+0.4}_{-1.8}$	U
MCG +11-11-032	C	66.55 / 65	42	1.73 ± 0.05	$23.4^{+0.6}_{-0.3}$	$24.3^{+0.4}_{-0.1}$	$60.18^{+0.16}_{-0.08}$
	D	66.84 / 67	48	$1.71^{+0.10}_{-0.09}$	22.98 ± 0.09	24.4 ± 0.4	U
Mrk 18	C	67.97 / 63	31	$1.81^{+0.11}_{-0.09}$	$23.7^{+0.9}_{-0.5}$	$24.69^{+0.11}_{-0.05}$	$60.10^{+3.49}_{-0.09}$
2MASX J0903 ...	C	62.76 / 58	31	1.7 ± 0.2	$24.0^{+0.5}_{-0.7}$	$24.7^{+0.2}_{-0.6}$	$60.4^{+1.0}_{-0.2}$
	D	69.15 / 60	19	1.5 ± 0.2	23.49 ± 0.08	24.4 ± 0.3	U
2MASX J0911 ...	C	127.85 / 134	63	$1.70^{+0.05}_{-0.07}$	$23.51^{+0.05}_{-0.07}$	23.41 ± 0.06	89^{+1}_{-5}
IC 2461	C	244.61 / 247	53	1.79 ± 0.02	$23.3^{+0.3}_{-0.1}$	$24.17^{+0.20}_{-0.02}$	$60.16^{+0.12}_{-0.06}$
	D	243.23 / 249	59	$1.81^{+0.05}_{-0.07}$	22.87 ± 0.06	24.3 ± 0.2	U
MCG −01-24-012	C	306.69 / 328	79	1.96 ± 0.03	$23.37^{+0.07}_{-0.14}$	$24.22^{+0.04}_{-0.08}$	$60.20^{+0.03}_{-0.05}$
	D	308.13 / 329	79	1.96 ± 0.04	22.92 ± 0.03	$24.25^{+0.12}_{-0.08}$	U
NGC 2992	C	643.63 / 707	95	$1.771^{+0.008}_{-0.012}$	$22.7^{+0.1}_{-0.6}$	23.68 ± 0.04	60.10 ± 0.09
	D	665.27 / 721	93	$1.716^{+0.011}_{-0.008}$	22.03 ± 0.01	23.32 ± 0.09	U
NGC 3079	C	99.85 / 102	54	$1.94^{+0.10}_{-0.09}$	$24.45^{+0.05}_{-0.03}$	24.36 ± 0.04	85 ± 1
	D	91.60 / 104	80	1.99 ± 0.09	24.41 ± 0.04	$24.80^{+0.07}_{-0.17}$	O
ESO 263-G013 ...	C	139.70 / 140	49	1.68 ± 0.08	23.86 ± 0.04	23.75 ± 0.03	88^{+2}_{-4}
NGC 3281	C	200.71 / 198	43	2.02 ± 0.02	24.37 ± 0.03	24.88 ± 0.02	60.99 ± 0.06

Continued on the next page...

Target Name	Model [a]	χ^2 / d.o.f.	$p_{\rm null}$ / %	Γ	$\log N_{\rm H,los}/{\rm cm}^{-2}$ [b]	$\log N_{\rm H,tor}/{\rm cm}^{-2}$	$\theta_{\rm inc}$ / deg. [c]
MCG +12-10-067	C	126.52 / 135	68	1.84 ± 0.04	$23.7^{+0.2}_{-0.8}$	24.57 ± 0.05	60.2 ± 0.2
MCG +06-24-008	C	148.98 / 153	57	1.62 ± 0.05	$22.8^{+0.9}_{-0.6}$	$23.4^{+0.3}_{-0.5}$	$60.6^{+13.4}_{-0.3}$
	D	149.17 / 154	59	$1.58^{+0.06}_{-0.04}$	22.59 ± 0.09	23.3 ± 0.4	U
UGC 5881	C	96.21 / 95	44	1.69 ± 0.18	$23.4^{+0.3}_{-0.5}$	$24.2^{+0.2}_{-0.4}$	60.3 ± 0.2
	D	96.64 / 96	46	$1.55^{+0.14}_{-0.09}$	$22.98^{+0.08}_{-0.11}$	$24.0^{+0.4}_{-0.2}$	U
NGC 3393	C	54.05 / 75	96	1.8 ± 0.2	24.34 ± 0.05	24.24 ± 0.05	85^{+5}_{-3}
NGC 3786	C	57.22 / 57	46	1.77 ± 0.05	23 ± 1	$24.2^{+0.2}_{-0.5}$	$60.10^{+29.90}_{-0.09}$
IC 751	C	63.14 / 62	43	1.6 ± 0.1	23.8 ± 0.6	24.5 ± 0.4	$60.4^{+0.6}_{-0.2}$
B2 1204+34	C	177.26 / 208	94	$1.68^{+0.10}_{-0.03}$	$22.6^{+1.4}_{-0.9}$	$23.1^{+0.8}_{-0.6}$	$61.1^{+28.9}_{-0.9}$
	D	178.93 / 209	93	$1.66^{+0.05}_{-0.03}$	22.50 ± 0.06	$23.1^{+0.4}_{-0.6}$	U
WAS 49	C	79.04 / 89	76	$1.98^{+0.05}_{-0.08}$	$23.8^{+0.6}_{-0.2}$	$23.75^{+0.53}_{-0.08}$	81^{+9}_{-10}
	D	95.37 / 94	44	1.7 ± 0.1	$23.39^{+0.08}_{-0.06}$	24.1 ± 0.3	U
NGC 4395	C	280.22 / 305	84	1.61 ± 0.02	$23.1^{+0.2}_{-0.5}$	$24.08^{+0.12}_{-0.02}$	$60.11^{+0.04}_{-0.10}$
	D	283.23 / 307	83	1.63 ± 0.04	22.64 ± 0.05	24.2 ± 0.1	U
LEDA 170194	C	134.57 / 140	61	$1.76^{+0.07}_{-0.04}$	23.0 ± 0.4	23.8 ± 0.3	$60.3^{+0.3}_{-0.1}$
	D	134.16 / 142	66	$1.78^{+0.09}_{-0.06}$	22.76 ± 0.07	23.9 ± 0.3	U
NGC 4941	C	55.22 / 57	54	1.9 ± 0.1	$24.1^{+0.3}_{-0.5}$	$24.59^{+0.07}_{-0.33}$	$61.2^{+3.2}_{-0.7}$
	D	62.47 / 59	35	$1.85^{+0.20}_{-0.08}$	$24.12^{+0.08}_{-0.06}$	$24.4^{+0.4}_{-0.2}$	U
NGC 4992	C	268.73 / 248	17	1.63 ± 0.05	$23.8^{+0.3}_{-0.1}$	$24.34^{+0.16}_{-0.09}$	$60.8^{+0.4}_{-0.2}$

Continued on the next page...

Target Name	Model [a]	χ^2 / d.o.f.	$p_{\rm null}$ / %	Γ	$\log N_{\rm H,los}/{\rm cm}^{-2}$ [b]	$\log N_{\rm H,tor}/{\rm cm}^{-2}$	$\theta_{\rm inc}$ / deg. [c]
	D	265.33 / 242	14	1.59 ± 0.05	23.61 ± 0.03	24.37 ± 0.08	U
Mrk 248	C	149.62 / 166	81	$1.93^{+0.04}_{-0.07}$	23.4 ± 0.3	24.2 ± 0.2	60.3 ± 0.1
	D	155.91 / 168	73	$1.85^{+0.06}_{-0.08}$	$22.97^{+0.05}_{-0.02}$	24.1 ± 0.2	U
ESO 509-IG066 ..	C	208.59 / 225	77	1.69 ± 0.06	23.2 ± 0.3	24.0 ± 0.2	60.3 ± 0.2
	D	206.21 / 226	82	$1.69^{+0.09}_{-0.06}$	$22.87^{+0.08}_{-0.06}$	24.0 ± 0.3	U
NGC 5252	C	300.23 / 291	34	1.68 ± 0.03	22.7 ± 0.3	23.4 ± 0.2	$60.5^{+0.3}_{-0.1}$
	D	299.47 / 293	38	1.67 ± 0.02	$22.51^{+0.08}_{-0.06}$	23.4 ± 0.2	U
NGC 5273	C	561.73 / 528	15	1.68 ± 0.02	$22.9^{+0.3}_{-0.5}$	$23.91^{+0.04}_{-0.02}$	$60.10^{+0.17}_{-0.09}$
	D	557.43 / 536	25	1.74 ± 0.02	$22.43^{+0.02}_{-0.04}$	$24.32^{+0.10}_{-0.07}$	U
2MASX J1410 ...	C	144.90 / 122	7.0	$1.73^{+0.03}_{-0.08}$	23.5 ± 0.6	24.50 ± 0.06	$60.10^{+0.83}_{-0.09}$
NGC 5643	C	114.56 / 108	31	$2.18^{+0.03}_{-0.05}$	24.6 ± 0.2	$24.87^{+0.02}_{-0.05}$	64^{+5}_{-2}
	D	117.97 / 115	40	$1.71^{+0.03}_{-0.13}$	24.6 ± 1.3	$24.03^{+0.04}_{-0.09}$	U
NGC 5674	C	245.37 / 258	70	1.86 ± 0.04	$23.0^{+0.1}_{-0.3}$	$23.88^{+0.06}_{-0.16}$	60.19 ± 0.08
	D	244.23 / 260	75	$1.88^{+0.06}_{-0.04}$	$22.66^{+0.06}_{-0.04}$	24.0 ± 0.2	U
NGC 5728	C	278.97 / 270	34	$1.69^{+0.03}_{-0.07}$	24.14 ± 0.03	24.04 ± 0.02	85^{+5}_{-3}
	D	277.95 / 272	38	1.68 ± 0.05	24.11 ± 0.03	24.11 ± 0.05	O
CGCG 164-019 ..	C	42.29 / 55	89	1.8 ± 0.2	$24.1^{+0.5}_{-0.2}$	24.7 ± 0.2	$60.6^{+2.5}_{-0.3}$
	D	40.61 / 56	93	1.7 ± 0.2	$24.26^{+0.06}_{-0.08}$	$23.2^{+0.4}_{-0.2}$	O
IC 4518A	C	136.29 / 128	29	1.72 ± 0.03	23.63 ± 0.06	24.55 ± 0.03	60.15 ± 0.02

Continued on the next page...

Target Name	Model [a]	χ^2 / d.o.f.	$p_{\rm null}$ / %	Γ	$\log N_{\rm H,los}/{\rm cm}^{-2}$ [b]	$\log N_{\rm H,tor}/{\rm cm}^{-2}$	$\theta_{\rm inc}$ / deg. [c]
2MASX J1506 ...	C	78.24 / 92	84	1.70 ± 0.07	$22.4^{+1.3}_{-0.7}$	$22.6^{+1.0}_{-0.5}$	64^{+26}_{-3}
NGC 5899	C	232.76 / 240	61	1.84 ± 0.03	$23.5^{+0.3}_{-0.5}$	$24.53^{+0.04}_{-0.02}$	$60.10^{+0.30}_{-0.09}$
	D	228.65 / 241	70	1.88 ± 0.04	23.01 ± 0.04	24.7 ± 0.2	U
MCG −01-40-001	C	169.53 / 209	97	1.77 ± 0.02	$23.32^{+0.19}_{-0.05}$	24.30 ± 0.03	$60.11^{+0.04}_{-0.01}$
	D	167.84 / 212	98	1.79 ± 0.05	22.84 ± 0.05	24.3 ± 0.2	U
MCG +14-08-004	C	91.43 / 99	69	1.8 ± 0.1	23.3 ± 0.5	23.8 ± 0.3	$61.0^{+2.1}_{-0.4}$
	D	91.40 / 101	74	$1.75^{+0.11}_{-0.08}$	23.14 ± 0.07	23.8 ± 0.3	U
Mrk 1498	C	342.58 / 305	6.0	1.70 ± 0.04	23.31 ± 0.17	23.91 ± 0.05	$60.66^{+0.07}_{-0.04}$
	D	346.12 / 309	7.0	1.71 ± 0.03	$23.21^{+0.03}_{-0.01}$	23.88 ± 0.07	O
IRAS 16288+3929	C	52.85 / 67	89	1.8 ± 0.1	23.8 ± 0.4	$23.70^{+0.41}_{-0.05}$	86^{+4}_{-20}
	D	53.77 / 68	89	1.8 ± 0.2	$23.82^{+0.09}_{-0.07}$	$23.8^{+0.7}_{-0.5}$	O
NGC 6240	C	313.27 / 317	54	1.72 ± 0.05	24.12 ± 0.02	24.02 ± 0.02	88 ± 2
	D	323.01 / 320	44	$1.74^{+0.02}_{-0.06}$	24.15 ± 0.01	25^{+u}_{-2}	U
MCG +07-37-031	C	202.20 / 192	29	$1.76^{+0.02}_{-0.04}$	23.2 ± 0.5	$24.22^{+0.06}_{-0.03}$	$60.10^{+0.36}_{-0.09}$
	D	204.92 / 194	28	$1.72^{+0.06}_{-0.12}$	$22.56^{+0.04}_{-0.06}$	24.1 ± 0.2	U
2MASX J1824 ...	C	158.83 / 163	57	$1.68^{+0.03}_{-0.06}$	23.7 ± 0.5	$24.70^{+0.10}_{-0.04}$	60.10 ± 0.09
	D	156.67 / 164	64	$1.65^{+0.11}_{-0.05}$	$23.07^{+0.11}_{-0.05}$	24.3 ± 0.2	U
IC 4709	C	223.12 / 218	39	1.88 ± 0.07	23.8 ± 0.3	24.4 ± 0.2	60.5 ± 0.2
	D	231.97 / 220	27	$1.74^{+0.07}_{-0.05}$	23.37 ± 0.04	24.3 ± 0.1	U
LEDA 3097193 ..	C	372.93 / 392	74	$1.88^{+0.03}_{-0.05}$	23.2 ± 0.3	23.9 ± 0.2	60.37 ± 0.09

Continued on the next page...

Target Name	Model [a]	χ^2 / d.o.f.	$p_{\rm null}$ / %	Γ	$\log N_{\rm H,los}/{\rm cm}^{-2}$ [b]	$\log N_{\rm H,tor}/{\rm cm}^{-2}$	$\theta_{\rm inc}$ / deg. [c]
	D	375.84 / 394	73	1.89 ± 0.05	22.93 ± 0.03	24.0 ± 0.2	U
ESO 231-G026 ...	C	187.82 / 235	99	$1.54^{+0.03}_{-0.05}$	23.3 ± 0.2	$23.31^{+0.12}_{-0.07}$	72^{+18}_{-7}
2MASX J1947 ...	C	247.80 / 252	56	1.87 ± 0.04	$23.3^{+0.2}_{-0.9}$	$24.16^{+0.07}_{-0.24}$	60.2 ± 0.2
	D	247.24 / 254	60	1.86 ± 0.07	22.90 ± 0.05	24.2 ± 0.2	U
3C 403	C	161.81 / 181	84	$1.59^{+0.08}_{-0.06}$	23.4 ± 0.3	$23.9^{+0.3}_{-0.1}$	$61.2^{+0.6}_{-0.3}$
	D	166.35 / 182	79	$1.57^{+0.12}_{-0.07}$	23.38 ± 0.05	23.9 ± 0.3	U
2MASX J2006 ...	C	97.96 / 113	84	1.89 ± 0.05	$24.4^{+0.6}_{-2.3}$	$24.85^{+0.03}_{-1.31}$	61^{+29}_{-1}
	D	101.31 / 114	79	$1.89^{+0.09}_{-0.11}$	23.40 ± 0.05	24.5 ± 0.3	O
2MASX J2018 ...	C	241.16 / 253	69	$1.73^{+0.07}_{-0.05}$	23.7 ± 0.3	$24.54^{+0.08}_{-0.15}$	$60.21^{+0.08}_{-0.11}$
	D	244.08 / 255	67	$1.69^{+0.05}_{-0.09}$	$23.16^{+0.03}_{-0.07}$	24.4 ± 0.2	U
2MASX J2021 ...	C	138.68 / 133	35	$1.58^{+0.03}_{-0.05}$	$23.4^{+0.3}_{-0.5}$	$24.36^{+0.16}_{-0.04}$	$60.10^{+0.07}_{-0.09}$
	D	137.27 / 135	42	$1.64^{+0.05}_{-0.09}$	$22.89^{+0.08}_{-0.12}$	24.4 ± 0.2	U
NGC 6921	C	44.30 / 71	99	1.85 ± 0.07	24.2 ± 0.1	24.21 ± 0.07	72 ± 5
	D	48.66 / 72	98	1.76 ± 0.07	24.14 ± 0.05	24.4 ± 0.1	U
MCG +04-48-002	C	71.96 / 76	61	1.76 ± 0.06	$23.9^{+0.4}_{-0.1}$	24.39 ± 0.12	61.0 ± 0.4
	D	74.27 / 77	56	1.73 ± 0.07	23.88 ± 0.06	24.4 ± 0.2	U
IC 5063	C	292.77 / 287	39	1.77 ± 0.03	$23.57^{+0.10}_{-0.09}$	$24.20^{+0.06}_{-0.03}$	60.5 ± 0.1
	D	292.44 / 289	43	1.74 ± 0.04	23.38 ± 0.02	$24.21^{+0.08}_{-0.03}$	U
NGC 7130	C	34.81 / 31	29	2.1 ± 0.4	24.7 ± 0.1	24.6 ± 0.1	81 ± 4

Continued on the next page...

Target Name	Model [a]	χ^2 / d.o.f.	$p_{\rm null}$ / %	Γ	$\log N_{\rm H,los}/{\rm cm}^{-2}$ [b]	$\log N_{\rm H,tor}/{\rm cm}^{-2}$	$\theta_{\rm inc}$ / deg. [c]
NGC 7319	C	28.86 / 37	82	1.6 ± 0.1	23.9 ± 0.4	24.6 ± 0.3	$60.4^{+0.4}_{-0.2}$
PKS 2356-61	C	129.84 / 157	94	1.84 ± 0.06	23.6 ± 0.3	$24.42^{+0.06}_{-0.56}$	$60.2^{+0.5}_{-0.2}$
	D	128.78 / 159	96	$1.83^{+0.08}_{-0.13}$	$23.17^{+0.06}_{-0.08}$	24.3 ± 0.4	U

[a] (C)oupled or (D)ecoupled `MYtorus` model. Only well-fitting parameter sets are listed.

[b] For the coupled model, $N_{\rm H,los}$ is calculated from $N_{\rm H,tor}$ and $\theta_{\rm inc}$.

[c] For the decoupled model, we only list the inclination bin, depending on whether the reprocessed spectrum is (A)bsorbed or (U)nabsorbed.

BIBLIOGRAPHY

Abbott, B. P., Abbott, R., Abbott, T. D., et al., 2016, Phys. Rev. Lett., 116 (6), 061102

Aird, J., Nandra, K., Laird, E. S., et al., 2010, MNRAS, 401, 2531

Aird, J., Coil, A. L., Georgakakis, A., et al., 2015, MNRAS, 451, 1892

Ajello, M., Greiner, J., Sato, G., et al., 2008, ApJ, 689, 666

Akylas, A., Georgantopoulos, I., & Comastri, A., 2001, MNRAS, 324, 521

Akylas, A., Georgakakis, A., Georgantopoulos, I., Brightman, M., & Nandra, K., 2012, A&A, 546, A98

Akylas, A., Georgantopoulos, I., Ranalli, P., et al., 2016, A&A, 594, A73

Alef, W., Goetz, M. M. A., Preuss, E., & Kellermann, K. I., 1988, A&A, 192, 53

Alexander, D. M., Chary, R.-R., Pope, A., et al., 2008, ApJ, 687, 835

Alexander, D. M., Stern, D., Del Moro, A., et al., 2013, ApJ, 773, 125

Alonso-Herrero, A., Ramos Almeida, C., Mason, R., et al., 2011, ApJ, 736, 82

Anders, E., & Grevesse, N., 1989, GeoCoA, 53, 197

Annuar, A., Gandhi, P., Alexander, D. M., et al., 2015, ApJ, 815, 36

Annuar, A., Alexander, D. M., Gandhi, P., et al., 2017, ApJ, 836, 165

Antonucci, R., 1993, ARA&A, 31, 473

Antonucci, R. R. J., & Miller, J. S., 1985, ApJ, 297, 621

Arévalo, P., Bauer, F. E., Puccetti, S., et al., 2014, ApJ, 791, 81

Arnaud, K. A., 1996, in Astronomical Society of the Pacific Conference Series, Astronomical Data Analysis Software and Systems V, ed. G. H. Jacoby, & J. Barnes, Vol. 101, 17

Asmus, D., Hönig, S. F., & Gandhi, P., 2016, ApJ, 822, 109

Assef, R. J., Stern, D., Kochanek, C. S., et al., 2013, ApJ, 772, 26

Assef, R. J., Eisenhardt, P. R. M., Stern, D., et al., 2015, ApJ, 804, 27

Audibert, A., Riffel, R., Sales, D. A., Pastoriza, M. G., & Ruschel-Dutra, D., 2017, MNRAS, 464, 2139

Awaki, H., Koyama, K., Inoue, H., & Halpern, J. P., 1991, PASJ, 43, 195

Baade, W., & Minkowski, R., 1954, ApJ, 119, 206

Balestra, I., Bianchi, S., & Matt, G., 2004, A&A, 415, 437

Ballantyne, D. R., 2007, Modern Physics Letters A, 22, 2397

—, 2014, MNRAS, 437, 2845

Ballantyne, D. R., Everett, J. E., & Murray, N., 2006, ApJ, 639, 740

Ballantyne, D. R., Draper, A. R., Madsen, K. K., Rigby, J. R., & Treister, E., 2011, ApJ, 736, 56

Ballantyne, D. R., Bollenbacher, J. M., Brenneman, L. W., et al., 2014, ApJ, 794, 62

Baloković, M., Smolčić, V., Ivezić, Ž., et al., 2012, ApJ, 759, 30

Baloković, M., Comastri, A., Harrison, F. A., et al., 2014, ApJ, 794, 111

Baloković, M., Matt, G., Harrison, F. A., et al., 2015, ApJ, 800, 62

Baloković, M., Paneque, D., Madejski, G., et al., 2016, ApJ, 819, 156

Barret, D., Lam Trong, T., den Herder, J.-W., et al., 2016, in Proc. SPIE, Space Telescopes and Instrumentation 2016: Ultraviolet to Gamma Ray, Vol. 9905, 99052F

Barthelmy, S. D., Barbier, L. M., Cummings, J. R., et al., 2005, Space Sci. Rev., 120, 143

Bauer, F. E., Arévalo, P., Walton, D. J., et al., 2015, ApJ, 812, 116

Baumgartner, W. H., Tueller, J., Markwardt, C. B., et al., 2013, ApJS, 207, 19

Beckmann, V., Gehrels, N., Shrader, C. R., & Soldi, S., 2006, ApJ, 638, 642

Beckmann, V., Courvoisier, T. J.-L., Gehrels, N., et al., 2008, A&A, 492, 93

Bell, E. F., 2003, ApJ, 586, 794

Bendo, G. J., Joseph, R. D., Wells, M., et al., 2002, AJ, 124, 1380

Berger, M., & Hubbell, J. 1987, XCOM: Photon cross sections on a personal computer

Best, P. N., & Heckman, T. M., 2012, MNRAS, 421, 1569

Bian, W., & Gu, Q., 2007, ApJ, 657, 159

Bird, A. J., Bazzano, A., Malizia, A., et al., 2016, ApJS, 223, 15

Blandford, R. D., & Begelman, M. C., 1999, MNRAS, 303, L1

Boorman, P. G., Gandhi, P., Alexander, D. M., et al., 2016, ApJ, 833, 245

Bottacini, E., Ajello, M., & Greiner, J., 2012, ApJS, 201, 34

Braatz, J. A., Wilson, A. S., & Henkel, C., 1996, ApJS, 106, 51

Braito, V., Reeves, J. N., Dewangan, G. C., et al., 2007, ApJ, 670, 978

Braito, V., Ballo, L., Reeves, J. N., et al., 2013, MNRAS, 428, 2516

Brandt, W. N., & Hasinger, G., 2005, ARA&A, 43, 827

Brandt, W. N., & Alexander, D. M., 2015, A&A Rev., 23, 1

Brenneman, L. W., & Reynolds, C. S., 2006, ApJ, 652, 1028

Brenneman, L. W., Reynolds, C. S., Nowak, M. A., et al., 2011, ApJ, 736, 103

Brenneman, L. W., Madejski, G., Fuerst, F., et al., 2014a, ApJ, 781, 83

—, 2014b, ApJ, 788, 61

Brightman, M., & Nandra, K., 2011a, MNRAS, 413, 1206

—, 2011b, MNRAS, 414, 3084

Brightman, M., & Ueda, Y., 2012, MNRAS, 423, 702

Brightman, M., & Nandra, K., 2012, MNRAS, 422, 1166

Brightman, M., Silverman, J. D., Mainieri, V., et al., 2013, MNRAS, 433, 2485

Brightman, M., Nandra, K., Salvato, M., et al., 2014, MNRAS, 443, 1999

Brightman, M., Baloković, M., Stern, D., et al., 2015, ApJ, 805, 41

Buchner, J., Georgakakis, A., Nandra, K., et al., 2014, A&A, 564, A125

Buchner, J., Georgakakis, A., Nandra, K., et al., 2015, ApJ, 802, 89

Buchner, J., & Bauer, F. E., 2017, MNRAS, 465, 4348

Burbidge, E. M., Burbidge, G. R., & Prendergast, K. H., 1959, ApJ, 130, 26

Burlon, D., Ajello, M., Greiner, J., et al., 2011, ApJ, 728, 58

Burrows, D. N., Hill, J. E., Nousek, J. A., et al., 2005, Space Sci. Rev., 120, 165

Burtscher, L., Meisenheimer, K., Tristram, K. R. W., et al., 2013, A&A, 558, A149

Burtscher, L., Orban de Xivry, G., Davies, R. I., et al., 2015, A&A, 578, A47

Cash, W., 1979, ApJ, 228, 939

Chiaberge, M., Capetti, A., & Celotti, A., 1999, A&A, 349, 77

Churazov, E., Sunyaev, R., Revnivtsev, M., et al., 2007, A&A, 467, 529

Cicone, C., Maiolino, R., Sturm, E., et al., 2014, A&A, 562, A21

Civano, F., Hickox, R. C., Puccetti, S., et al., 2015, ApJ, 808, 185

Collinge, M. J., & Brandt, W. N., 2000, MNRAS, 317, L35

Comastri, A., 2004, in Astrophysics and Space Science Library, Supermassive Black Holes in the Distant Universe, ed. A. J. Barger, Vol. 308, 245

Comastri, A., Iwasawa, K., Gilli, R., et al., 2010, ApJ, 717, 787

Condon, J. J., Cotton, W. D., Greisen, E. W., et al., 1998, AJ, 115, 1693

Connolly, S. D., McHardy, I. M., Skipper, C. J., & Emmanoulopoulos, D., 2016, MNRAS

Cowie, L. L., Barger, A. J., Bautz, M. W., Brandt, W. N., & Garmire, G. P., 2003, ApJL, 584, L57

Cusumano, G., La Parola, V., Segreto, A., et al., 2010, A&A, 524, A64

Dadina, M., 2007, A&A, 461, 1209

—, 2008, A&A, 485, 417

Dai, X., Kochanek, C. S., Chartas, G., et al., 2010, ApJ, 709, 278

Dauser, T., Garcia, J., Wilms, J., et al., 2013, MNRAS, 430, 1694

de Rosa, A., Panessa, F., Bassani, L., et al., 2012, MNRAS, 420, 2087

Del Moro, A., Mullaney, J. R., Alexander, D. M., et al., 2014, ApJ, 786, 16

Detmers, R. G., Kaastra, J. S., Steenbrugge, K. C., et al., 2011, A&A, 534, A38

Di Matteo, T., Springel, V., & Hernquist, L., 2005, Nature, 433, 604

Dickey, J. M., & Lockman, F. J., 1990, ARA&A, 28, 215

Dietrich, M., Peterson, B. M., Grier, C. J., et al., 2012, ApJ, 757, 53

Doeleman, S. S., Weintroub, J., Rogers, A. E. E., et al., 2008, Nature, 455, 78

Ebrero, J., Carrera, F. J., Page, M. J., et al., 2009, A&A, 493, 55

Eckart, A., Hüttemann, A., Kiefer, C., et al., 2017, Foundations of Physics

Efstathiou, A., Christopher, N., Verma, A., & Siebenmorgen, R., 2013, MNRAS, 436, 1873

Eguchi, S., Ueda, Y., Terashima, Y., Mushotzky, R., & Tueller, J., 2009, ApJ, 696, 1657

Eguchi, S., Ueda, Y., Awaki, H., et al., 2011, ApJ, 729, 31

Elitzur, M., 2012, ApJL, 747, L33

Elitzur, M., & Shlosman, I., 2006, ApJL, 648, L101

Elitzur, M., & Netzer, H., 2016, MNRAS, 459, 585

Elvis, M., 2000, ApJ, 545, 63

Elvis, M., Maccacaro, T., Wilson, A. S., et al., 1978, MNRAS, 183, 129

Esposito, V., & Walter, R., 2016, A&A, 590, A49

Evans, I. N., Ford, H. C., Kinney, A. L., et al., 1991, ApJL, 369, L27

Ezhikode, S. H., Gandhi, P., Done, C., et al., 2016, ArXiv e-prints

Fabian, A. C., 2012, ARA&A, 50, 455

Fabian, A. C., Rees, M. J., Stella, L., & White, N. E., 1989, MNRAS, 238, 729

Fabian, A. C., Lohfink, A., Kara, E., et al., 2015, MNRAS, 451, 4375

Fanaroff, B. L., & Riley, J. M., 1974, MNRAS, 167, 31P

Farrah, D., Baloković, M., Stern, D., et al., 2016, ApJ, 831, 76

Faucher-Giguère, C.-A., & Quataert, E., 2012, MNRAS, 425, 605

Feltre, A., Hatziminaoglou, E., Fritz, J., & Franceschini, A., 2012, MNRAS, 426, 120

Ferrarese, L., & Merritt, D., 2000, ApJL, 539, L9

Fiore, F., Puccetti, S., Brusa, M., et al., 2009, ApJ, 693, 447

Fischer, T. C., Crenshaw, D. M., Kraemer, S. B., & Schmitt, H. R., 2013, ApJS, 209, 1

Flohic, H. M. L. G., & Eracleous, M., 2008, ApJ, 686, 138

Fossati, G., Maraschi, L., Celotti, A., Comastri, A., & Ghisellini, G., 1998, MNRAS, 299, 433

Frontera, F., Orlandini, M., Landi, R., et al., 2007, ApJ, 666, 86

Fukazawa, Y., Hiragi, K., Mizuno, M., et al., 2011, ApJ, 727, 19

Furui, S., Fukazawa, Y., Odaka, H., et al., 2016, ApJ, 818, 164

Gandhi, P., Horst, H., Smette, A., et al., 2009, A&A, 502, 457

Gandhi, P., Lansbury, G. B., Alexander, D. M., et al., 2014, ApJ, 792, 117

Gandhi, P., Hönig, S. F., & Kishimoto, M., 2015, ApJ, 812, 113

Gandhi, P., Annuar, A., Lansbury, G. B., et al., 2017, MNRAS, 467, 4606

Garcia, J., Dauser, T., Lohfink, A., et al., 2014, ApJ, 782, 76

García, J., Dauser, T., Reynolds, C. S., et al., 2013, ApJ, 768, 146

Garcia-Burillo, S., Combes, F., Ramos Almeida, C., et al., 2016, ArXiv e-prints

Gardner, E., & Done, C., 2014, MNRAS, 442, 2456

Gaskell, C. M., Shields, G. A., & Wampler, E. J., 1981, ApJ, 249, 443

Gebhardt, K., Bender, R., Bower, G., et al., 2000, ApJL, 539, L13

Gehrels, N., Chincarini, G., Giommi, P., et al., 2004, ApJ, 611, 1005

Georgantopoulos, I., Rovilos, E., Akylas, A., et al., 2011, A&A, 534, A23

George, I. M., & Fabian, A. C., 1991, MNRAS, 249, 352

Ghisellini, G., 2016, Galaxies, 4, 36

Ghisellini, G., Haardt, F., & Matt, G., 1994, MNRAS, 267, 743

Gilli, R., Comastri, A., & Hasinger, G., 2007, A&A, 463, 79

Gilli, R., Vignali, C., Mignoli, M., et al., 2010, A&A, 519, A92

González-Martín, O., Hernández-García, L., Masegosa, J., et al., 2016, A&A, 587, A1

Goodman, J., & Weare, J., 2010, Comm. App. Math. Comp. Sci., 5, 65

Goulding, A. D., Alexander, D. M., Mullaney, J. R., et al., 2011, MNRAS, 411, 1231

Greenhill, L. J., Tilak, A., & Madejski, G., 2008, ApJL, 686, L13

Gu, Q., Melnick, J., Cid Fernandes, R., et al., 2006, MNRAS, 366, 480

Guainazzi, M., Risaliti, G., Awaki, H., et al., 2016, ArXiv e-prints

Haardt, F., & Maraschi, L., 1991, ApJL, 380, L51

—, 1993, ApJ, 413, 507

Haardt, F., Maraschi, L., & Ghisellini, G., 1994, ApJL, 432, L95

Harrison, F. A., Craig, W. W., Christensen, F. E., et al., 2013, ApJ, 770, 103

Harrison, F. A., Aird, J., Civano, F., et al., 2016, ApJ, 831, 185

Hasinger, G., 2008, A&A, 490, 905

Heckman, T. M., & Best, P. N., 2014, ARA&A, 52, 589

Hernández-García, L., Masegosa, J., González-Martín, O., & Márquez, I., 2015, A&A, 579, A90

Hitomi Collaboration, Aharonian, F., Akamatsu, H., et al., 2016, Nature, 535, 117

Ho, L. C., 2008, ARA&A, 46, 475

Hönig, S. F., 2013, ArXiv e-prints

Hönig, S. F., & Beckert, T., 2007, MNRAS, 380, 1172

Hönig, S. F., Kishimoto, M., Antonucci, R., et al., 2012, ApJ, 755, 149

Hopkins, P. F., Hernquist, L., Cox, T. J., et al., 2006, ApJS, 163, 1

Hopkins, P. F., & Elvis, M., 2010, MNRAS, 401, 7

Hoyle, F., & Fowler, W. A., 1963, Nature, 197, 533

Hunter, J. D., 2007, Computing In Science & Engineering, 9.3, 90

Ichikawa, K., Packham, C., Ramos Almeida, C., et al., 2015, ApJ, 803, 57

Ikeda, S., Awaki, H., & Terashima, Y., 2009, ApJ, 692, 608

Inglis, M. D., Brindle, C., Hough, J. H., et al., 1993, MNRAS, 263, 895

Ishihara, Y., Nakai, N., Iyomoto, N., et al., 2001, PASJ, 53, 215

Iwasawa, K., Matt, G., Fabian, A. C., et al., 2001, MNRAS, 326, 119

Iwasawa, K., Maloney, P. R., & Fabian, A. C., 2002, MNRAS, 336, L71

Iwasawa, K., Gilli, R., Vignali, C., et al., 2012, A&A, 546, A84

Jaffe, W., Ford, H. C., Ferrarese, L., van den Bosch, F., & O'Connell, R. W., 1993, Nature, 364, 213

Jiang, L., Fan, X., Ivezić, Ž., et al., 2007, ApJ, 656, 680

Kalberla, P. M. W., Burton, W. B., Hartmann, D., et al., 2005, A&A, 440, 775

Kamraj, N., Rivers, E., Harrison, F. A., Brightman, M., & Baloković, M., 2017, ArXiv e-prints

Kara, E., Zoghbi, A., Marinucci, A., et al., 2015a, MNRAS, 446, 737

Kara, E., Fabian, A. C., Lohfink, A. M., et al., 2015b, MNRAS, 449, 234

Kawamuro, T., Ueda, Y., Tazaki, F., Ricci, C., & Terashima, Y., 2016a, ApJS, 225, 14

Kawamuro, T., Ueda, Y., Tazaki, F., Terashima, Y., & Mushotzky, R., 2016b, ArXiv e-prints

King, A., 2003, ApJL, 596, L27

Kinney, A. L., Antonucci, R. R. J., Ward, M. J., Wilson, A. S., & Whittle, M., 1991, ApJ, 377, 100

Kondratko, P. T. 2007, "Search for and follow-up imaging of subparsec accretion disks in AGN", PhD thesis (Harvard University)

Koss, M. J., Romero-Cañizales, C., Baronchelli, L., et al., 2015, ApJ, 807, 149

Koss, M. J., Assef, R., Baloković, M., et al., 2016a, ApJ, 825, 85

Koss, M. J., Glidden, A., Baloković, M., et al., 2016b, ApJL, 824, L4

Kraemer, S. B., Schmitt, H. R., Crenshaw, D. M., et al., 2011, ApJ, 727, 130

Krause, M. O., 1979, Journal of Physical and Chemical Reference Data, 8.2, 307

Krivonos, R., Tsygankov, S., Lutovinov, A., et al., 2015, MNRAS, 448, 3766

Krolik, J. H., Madau, P., & Zycki, P. T., 1994, ApJL, 420, L57

La Franca, F., Fiore, F., Comastri, A., et al., 2005, ApJ, 635, 864

LaMassa, S. M., Heckman, T. M., Ptak, A., et al., 2010, ApJ, 720, 786

Lamer, G., Uttley, P., & McHardy, I. M., 2003, MNRAS, 342, L41

Lansbury, G. B., Alexander, D. M., Del Moro, A., et al., 2014, ApJ, 785, 17

Lansbury, G. B., Gandhi, P., Alexander, D. M., et al., 2015, ApJ, 809, 115

Lansbury, G. B., Stern, D., Aird, J., et al., 2017, ApJ, 836, 99

Lawrence, A., 1991, MNRAS, 252, 586

Leahy, D. A., & Creighton, J., 1993, MNRAS, 263, 314

Levenson, N. A., Krolik, J. H., Życki, P. T., et al., 2002, ApJL, 573, L81

Lira, P., Videla, L., Wu, Y., et al., 2013, ApJ, 764, 159

Liu, Y., & Li, X., 2014, ApJ, 787, 52

—, 2015, MNRAS, 448, L53

Liu, J., Liu, Y., Li, X., et al., 2016, MNRAS, 459, L100

Lohfink, A. M., Ogle, P., Tombesi, F., et al., 2015, ApJ, 814, 24

Longinotti, A. L., Krongold, Y., Kriss, G. A., et al., 2013, ApJ, 766, 104

Lopez-Rodriguez, E., Packham, C., Jones, T. J., et al., 2015, MNRAS, 452, 1902

Lusso, E., Comastri, A., Simmons, B. D., et al., 2012, MNRAS, 425, 623

Lutz, D., Maiolino, R., Spoon, H. W. W., & Moorwood, A. F. M., 2004, A&A, 418, 465

Madau, P., Ghisellini, G., & Fabian, A. C., 1994, MNRAS, 270, L17

Madejski, G., Życki, P., Done, C., et al., 2000, ApJL, 535, L87

Madejski, G., Done, C., Życki, P. T., & Greenhill, L., 2006, ApJ, 636, 75

Madejski, G. M., Nalewajko, K., Madsen, K. K., et al., 2016, ApJ, 831, 142

Madsen, K. K., Fürst, F., Walton, D. J., et al., 2015a, ApJ, 812, 14

Madsen, K. K., Harrison, F. A., Markwardt, C. B., et al., 2015b, ApJS, 220, 8

Magdziarz, P., & Zdziarski, A. A., 1995, MNRAS, 273, 837

Maiolino, R., Salvati, M., Bassani, L., et al., 1998, A&A, 338, 781

Maiolino, R., Shemmer, O., Imanishi, M., et al., 2007, A&A, 468, 979

Maksym, W. P., Fabbiano, G., Elvis, M., et al., 2016, ArXiv e-prints

Malizia, A., Bassani, L., Stephen, J. B., et al., 2003, ApJL, 589, L17

Malizia, A., Stephen, J. B., Bassani, L., et al., 2009, MNRAS, 399, 944

Malizia, A., Bassani, L., Bazzano, A., et al., 2012, MNRAS, 426, 1750

Malizia, A., Molina, M., Bassani, L., et al., 2014, ApJL, 782, L25

Marchese, E., Braito, V., Della Ceca, R., Caccianiga, A., & Severgnini, P., 2012, MNRAS, 421, 1803

Marconi, A., Risaliti, G., Gilli, R., et al., 2004, MNRAS, 351, 169

Marin, F., 2016, ArXiv e-prints

Marinucci, A., Bianchi, S., Matt, G., et al., 2011, A&A, 526, A36

Marinucci, A., Bianchi, S., Nicastro, F., Matt, G., & Goulding, A. D., 2012, ApJ, 748, 130

Marinucci, A., Miniutti, G., Bianchi, S., Matt, G., & Risaliti, G., 2013, MNRAS, 436, 2500

Marinucci, A., Matt, G., Kara, E., et al., 2014, MNRAS, 440, 2347

Marinucci, A., Matt, G., Bianchi, S., et al., 2015, MNRAS, 447, 160

Marinucci, A., Bianchi, S., Matt, G., et al., 2016, MNRAS, 456, L94

Markowitz, A. G., Krumpe, M., & Nikutta, R., 2014, MNRAS, 439, 1403

Marshall, N., Warwick, R. S., & Pounds, K. A., 1981, MNRAS, 194, 987

Masini, A., Comastri, A., Baloković, M., et al., 2016, A&A, 589, A59

Masini, A., Comastri, A., Puccetti, S., et al., 2017, A&A, 597, A100

Mason, R. E., Geballe, T. R., Packham, C., et al., 2006, ApJ, 640, 612

Mason, R. E., Lopez-Rodriguez, E., Packham, C., et al., 2012, AJ, 144, 11

Mateos, S., Carrera, F. J., Alonso-Herrero, A., et al., 2016, ApJ, 819, 166

Matt, G., 2002, MNRAS, 337, 147

Matt, G., Perola, G. C., & Piro, L., 1991, A&A, 247, 25

Matt, G., Pompilio, F., & La Franca, F., 1999, New Astronomy, 4, 191

Matt, G., Fabian, A. C., Guainazzi, M., et al., 2000, MNRAS, 318, 173

Matt, G., Bianchi, S., Guainazzi, M., et al., 2003a, A&A, 399, 519

Matt, G., Guainazzi, M., & Maiolino, R., 2003b, MNRAS, 342, 422

Matt, G., Bianchi, S., Guainazzi, M., & Molendi, S., 2004, A&A, 414, 155

Matt, G., Marinucci, A., Guainazzi, M., et al., 2014, MNRAS, 439, 3016

Matt, G., Baloković, M., Marinucci, A., et al., 2015, MNRAS, 447, 3029

Mattson, B. J., & Weaver, K. A., 2004, ApJ, 601, 771

McConnell, N. J., & Ma, C.-P., 2013, ApJ, 764, 184

Merloni, A., Bongiorno, A., Brusa, M., et al., 2014, MNRAS, 437, 3550

Middleton, M., Done, C., & Gierliński, M., 2007, MNRAS, 381, 1426

Miller, L., Turner, T. J., & Reeves, J. N., 2008, A&A, 483, 437

Miller, L., & Turner, T. J., 2013, ApJL, 773, L5

Miniutti, G., Sanfrutos, M., Beuchert, T., et al., 2014, MNRAS, 437, 1776

Mitsuda, K., Kelley, R. L., Akamatsu, H., et al., 2014, in Proc. SPIE, Space Telescopes and Instrumentation 2014: Ultraviolet to Gamma Ray, Vol. 9144, 91442A

Molina, M., Bassani, L., Malizia, A., et al., 2013, MNRAS, 433, 1687

Moran, E. C., Barth, A. J., Kay, L. E., & Filippenko, A. V., 2000, ApJL, 540, L73

Moretti, A., Pagani, C., Cusumano, G., et al., 2009, A&A, 493, 501

Mosquera, A. M., Kochanek, C. S., Chen, B., et al., 2013, ApJ, 769, 53

Mulchaey, J. S., Mushotzky, R. F., & Weaver, K. A., 1992, ApJL, 390, L69

Mulchaey, J. S., Koratkar, A., Ward, M. J., et al., 1994, ApJ, 436, 586

Mullaney, J. R., Del-Moro, A., Aird, J., et al., 2015, ApJ, 808, 184

Murayama, T., Taniguchi, Y., & Iwasawa, K., 1998, AJ, 115, 460

Murphy, K. D., & Yaqoob, T., 2009, MNRAS, 397, 1549

Nandra, K., & Pounds, K. A., 1994, MNRAS, 268, 405

Nandra, K., & George, I. M., 1994, MNRAS, 267, 974

Nandra, K., O'Neill, P. M., George, I. M., & Reeves, J. N., 2007, MNRAS, 382, 194

Narayan, R., & Yi, I., 1994, ApJL, 428, L13

Nemmen, R. S., Storchi-Bergmann, T., & Eracleous, M., 2014, MNRAS, 438, 2804

Nenkova, M., Sirocky, M. M., Nikutta, R., Ivezić, Ž., & Elitzur, M., 2008a, ApJ, 685, 160

Nenkova, M., Sirocky, M. M., Ivezić, Ž., & Elitzur, M., 2008b, ApJ, 685, 147

Netzer, H., 2015, ARA&A, 53, 365

Osterbrock, D. E., 1978, Proceedings of the National Academy of Science, 75, 540

O'Sullivan, E., Zezas, A., Vrtilek, J. M., et al., 2014, ApJ, 793, 73

Padovani, P., 2016, A&A Rev., 24, 13

Pancoast, A., Brewer, B. J., Treu, T., et al., 2014, MNRAS, 445, 3073

Panessa, F., Bassani, L., Cappi, M., et al., 2006, A&A, 455, 173

Parisi, P., Masetti, N., Jiménez-Bailón, E., et al., 2009, A&A, 507, 1345

Perola, G. C., Matt, G., Cappi, M., et al., 2002, A&A, 389, 802

Podigachoski, P., Barthel, P., Haas, M., Leipski, C., & Wilkes, B., 2015, ApJL, 806, L11

Podigachoski, P., Rocca-Volmerange, B., Barthel, P., Drouart, G., & Fioc, M., 2016, MNRAS, 462, 4183

Pogge, R. W., 1988, ApJ, 328, 519

Poutanen, J., & Svensson, R., 1996, ApJ, 470, 249

Puccetti, S., Comastri, A., Fiore, F., et al., 2014, ApJ, 793, 26

Puccetti, S., Comastri, A., Bauer, F. E., et al., 2016, A&A, 585, A157

Ramos Almeida, C., Martínez González, M. J., Asensio Ramos, A., et al., 2016, MNRAS, 461, 1387

Reeves, J. N., Awaki, H., Dewangan, G. C., et al., 2007, PASJ, 59, 301

Reis, R. C., & Miller, J. M., 2013, ApJL, 769, L7

Reunanen, J., Prieto, M. A., & Siebenmorgen, R., 2010, MNRAS, 402, 879

Reynolds, C. S., 2014, Space Science Reviews, 183, 277

Reynolds, C. S., & Nowak, M. A., 2003, PhR, 377, 389

Ricci, C., Beckmann, V., Audard, M., & Courvoisier, T. J.-L., 2010, A&A, 518, A47

Ricci, C., Walter, R., Courvoisier, T. J.-L., & Paltani, S., 2011, A&A, 532, A102

Ricci, C., Ueda, Y., Paltani, S., et al., 2014, MNRAS, 441, 3622

Ricci, C., Ueda, Y., Koss, M. J., et al., 2015, ApJL, 815, L13

Ricci, C., Bauer, F. E., Arevalo, P., et al., 2016, ApJ, 820, 5

Risaliti, G., 2002, A&A, 386, 379

Risaliti, G., Maiolino, R., & Salvati, M., 1999, ApJ, 522, 157

Risaliti, G., Elvis, M., & Nicastro, F., 2002, ApJ, 571, 234

Risaliti, G., Elvis, M., Fabbiano, G., Baldi, A., & Zezas, A., 2005, ApJL, 623, L93

Risaliti, G., Elvis, M., Bianchi, S., & Matt, G., 2010, MNRAS, 406, L20

Risaliti, G., Harrison, F. A., Madsen, K. K., et al., 2013, Nature, 494, 449

Rivers, E., Markowitz, A., & Rothschild, R., 2011, ApJL, 742, L29

—, 2013, ApJ, 772, 114

Rivers, E., Baloković, M., Arévalo, P., et al., 2015a, ApJ, 815, 55

Rivers, E., Risaliti, G., Walton, D. J., et al., 2015b, ApJ, 804, 107

Roseboom, I. G., Lawrence, A., Elvis, M., et al., 2013, MNRAS, 429, 1494

Ross, R. R., & Fabian, A. C., 2005, MNRAS, 358, 211

Rybicki, G. B., & Lightman, A. P. 1979, Radiative Processes in Astrophysics (Wiley)

Salpeter, E. E., 1964, ApJ, 140, 796

Sandage, A., 1965, ApJ, 141, 1560

Sazonov, S. Y., & Revnivtsev, M. G., 2004, A&A, 423, 469

Sbarrato, T., Tagliaferri, G., Ghisellini, G., et al., 2013, ApJ, 777, 147

Schartmann, M., Meisenheimer, K., Camenzind, M., et al., 2008, A&A, 482, 67

Schmidt, M., 1963, Nature, 197, 1040

Schmitt, H. R., Donley, J. L., Antonucci, R. R. J., Hutchings, J. B., & Kinney, A. L., 2003, ApJS, 148, 327

Severgnini, P., Caccianiga, A., Della Ceca, R., et al., 2011, A&A, 525, A38

Severgnini, P., Caccianiga, A., & Della Ceca, R., 2012, A&A, 542, A46

Seyfert, C. K., 1943, ApJ, 97, 28

Shakura, N. I., & Sunyaev, R. A., 1973, A&A, 24, 337

Shappee, B. J., Prieto, J. L., Grupe, D., et al., 2014, ApJ, 788, 48

Shu, X. W., Yaqoob, T., & Wang, J. X., 2010a, ApJS, 187, 581

Shu, X. W., Yaqoob, T., Murphy, K. D., et al., 2010b, ApJ, 713, 1256

Shu, X. W., Yaqoob, T., & Wang, J. X., 2011, ApJ, 738, 147

Silk, J., & Rees, M. J., 1998, A&A, 331, L1

Silverman, J. D., Green, P. J., Barkhouse, W. A., et al., 2008, ApJ, 679, 118

Smolčić, V., 2009, ApJL, 699, L43

Stern, D., Lansbury, G. B., Assef, R. J., et al., 2014, ApJ, 794, 102

Storchi-Bergmann, T., Wilson, A. S., & Baldwin, J. A., 1992a, ApJ, 396, 45

Storchi-Bergmann, T., Mulchaey, J. S., & Wilson, A. S., 1992b, ApJL, 395, L73

Sturm, E., González-Alfonso, E., Veilleux, S., et al., 2011, ApJL, 733, L16

Sun, S., Guainazzi, M., Ni, Q., et al., 2017, ArXiv e-prints

Tanaka, Y., Nandra, K., Fabian, A. C., et al., 1995, Nature, 375, 659

Tanimoto, A., Ueda, Y., Kawamuro, T., & Ricci, C., 2016, PASJ, 68, S26

Tatum, M. M., Turner, T. J., Miller, L., & Reeves, J. N., 2013, ApJ, 762, 80

Tazaki, F., Ueda, Y., Terashima, Y., & Mushotzky, R. F., 2011, ApJ, 738, 70

Teng, S. H., Rigby, J. R., Stern, D., et al., 2015, ApJ, 814, 56

Terashima, Y., & Wilson, A. S., 2003, ApJ, 583, 145

Tilak, A., Greenhill, L. J., Done, C., & Madejski, G., 2008, ApJ, 678, 701

Titarchuk, L., 1994, ApJ, 434, 570

Tombesi, F., Cappi, M., Reeves, J. N., & Braito, V., 2012, MNRAS, 422, L1

Tombesi, F., Meléndez, M., Veilleux, S., et al., 2015, Nature, 519, 436

Torricelli-Ciamponi, G., Pietrini, P., Risaliti, G., & Salvati, M., 2014, MNRAS, 442, 2116

Tozzi, P., Gilli, R., Mainieri, V., et al., 2006, A&A, 451, 457

Tran, H. D., Miller, J. S., & Kay, L. E., 1992, ApJ, 397, 452

Treister, E., & Urry, C. M., 2006, ApJL, 652, L79

Treister, E., Krolik, J. H., & Dullemond, C., 2008, ApJ, 679, 140

Treister, E., Urry, C. M., & Virani, S., 2009, ApJ, 696, 110

Tueller, J., Mushotzky, R. F., Barthelmy, S., et al., 2008, ApJ, 681, 113

Turner, T. J., George, I. M., Nandra, K., & Mushotzky, R. F., 1997, ApJS, 113, 23

Turner, T. J., & Miller, L., 2009, A&A Rev., 17, 47

Ueda, Y., Akiyama, M., Hasinger, G., Miyaji, T., & Watson, M. G., 2014, ApJ, 786, 104

Urry, C. M., & Padovani, P., 1995, PASP, 107, 803

Vasudevan, R. V., & Fabian, A. C., 2009, MNRAS, 392, 1124

Vasudevan, R. V., Brandt, W. N., Mushotzky, R. F., et al., 2013, ApJ, 763, 111

Vasudevan, R. V., Mushotzky, R. F., Reynolds, C. S., et al., 2014, ApJ, 785, 30

Vasylenko, A. A., Fedorova, E., & Zhdanov, V. I., 2013, Advances in Astronomy and Space Physics, 3, 120

Vasylenko, A. A., Zhdanov, V. I., & Fedorova, E. V., 2015, Astrophysics and Space Sciencev, 360, 37

Véron, P., Lindblad, P. O., Zuiderwijk, E. J., Véron, M. P., & Adam, G., 1980, A&A, 87, 245

Wada, K., 2012, ApJ, 758, 66

Wada, K., Schartmann, M., & Meijerink, R., 2016, ApJL, 828, L19

Wagner, A. Y., Umemura, M., & Bicknell, G. V., 2013, ApJL, 763, L18

Walton, D. J., Nardini, E., Fabian, A. C., Gallo, L. C., & Reis, R. C., 2013, MNRAS, 428, 2901

Walton, D. J., Risaliti, G., Harrison, F. A., et al., 2014, ApJ, 788, 76

Wandel, A., & Mushotzky, R. F., 1986, ApJL, 306, L61

Weaver, K. A., Yaqoob, T., Mushotzky, R. F., et al., 1997, ApJ, 474, 675

Wegner, G., Bernardi, M., Willmer, C. N. A., et al., 2003, AJ, 126, 2268

Weisskopf, M. C., Ramsey, B., O'Dell, S., et al., 2016, in Proc. SPIE, Space Telescopes and Instrumentation 2016: Ultraviolet to Gamma Ray, Vol. 9905, 990517

Wilkes, B. J., Kuraszkiewicz, J., Haas, M., et al., 2013, ApJ, 773, 15

Wilms, J., Allen, A., & McCray, R., 2000, ApJ, 542, 914

Winkler, C., Courvoisier, T. J.-L., Di Cocco, G., et al., 2003, A&A, 411, L1

Winter, L. M., Mushotzky, R. F., Reynolds, C. S., & Tueller, J., 2009, ApJ, 690, 1322

Xu, Y., Baloković, M., Walton, D. J., et al., 2017, ApJ, 837, 21

Yaqoob, T., 1997, ApJ, 479, 184

—, 2012, MNRAS, 423, 3360

Yaqoob, T., & Padmanabhan, U., 2004, ApJ, 604, 63

Yaqoob, T., Murphy, K. D., Griffiths, R. E., et al., 2007, PASJ, 59, 283

Yaqoob, T., & Murphy, K. D., 2011, MNRAS, 412, 277

Yaqoob, T., Tatum, M. M., Scholtes, A., Gottlieb, A., & Turner, T. J., 2015, MNRAS, 454, 973

Zdziarski, A. A., Lubiński, P., & Smith, D. A., 1999, MNRAS, 303, L11

Zdziarski, A. A., Poutanen, J., & Johnson, W. N., 2000, ApJ, 542, 703

Zhang, J. S., Henkel, C., Guo, Q., Wang, H. G., & Fan, J. H., 2010, ApJ, 708, 1528

Zoghbi, A., Reynolds, C., Cackett, E. M., et al., 2013, ApJ, 767, 121

Zoghbi, A., Cackett, E. M., Reynolds, C., et al., 2014, ApJ, 789, 56

Zoghbi, A., Matt, G., Miller, J. M., et al., 2017, ApJ, 836, 2

Zubovas, K., & Nayakshin, S., 2014, MNRAS, 440, 2625